In-Situ Backplane Inspection of Fiber Optic Ferrules

by

Andrew K. Wilson

B.S.M.E., Santa Clara University (1999)
S.M., Massachusetts Institute of Technology (2001)

Submitted to the Department of Mechanical Engineering
in partial fulfillment of the requirements for the degree of

Doctor of Philosophy

at the

MASSACHUSETTS INSTITUTE OF TECHNOLOGY

January 2006

Author_____
Department of Mechanical Engineering
January 13, 2006

Certified by_____
Samir Nayfeh
Associate Professor
Thesis Supervisor

Accepted by_____
Lallit Anand
Chairman, Department Committee on Graduate Students

In-Situ Backplane Inspection of Fiber Optic Ferrules

by

Andrew K. Wilson

Submitted to the Department of Mechanical Engineering
on January 13, 2006, in partial fulfillment of the
requirements for the degree of
Doctor of Philosophy

Abstract

The next generation of supercomputers, routers, and switches are envisioned to have hundreds and thousands of optical interconnects among components. An optical interconnect attains a bandwidth-distance product as high as 90 GHz.km, about 200 times higher than can be attained by a copper interconnect. But defects (such as dust or scratches) as small as 1 micron on the connector endfaces can seriously degrade performance. Therefore, for every mate and de-mate, optical connectors must be inspected to ensure high performance data transmission capabilities. The tedious and time consuming task of manually inspecting each connector is one of the barriers to adoption of optics in the backplanes of large card-based machines.

This thesis provides a framework and method for in-situ automatic inspection of backplane optical connectors. We develop an inspection system that fits into the envelope of a single daughter card, moves a custom microscope objective in three degrees of freedom to image the connector endfaces, and detects and classifies defects with major diameter of one micron or larger.

The inspection machine mounts to the backplane in the same manner as a daughter card, and positions the microscope with better than 0.2 micron resolution and 15 micron repeatability in three degrees of freedom. Despite tight packaging constraints, the ultra-long working distance custom microscope objective attains 1 micron Rayleigh resolution via deconvolution. Several images taken at different exposures and focus settings are fused to extend the imaging sensor's limited dynamic range and depth of field. A set of machine-vision algorithms are developed to process the resulting image and detect and classify the fiber core, cladding and their defects.

Thesis Supervisor: Samir Nayfeh
Title: Associate Professor

Acknowledgments

This research was supported by Tom Pitten, John Lehman and Sepehr Kiani Ph.D. of Teradyne Connection Systems; I could not have completed this work without their help. Special thanks goes to Sepehr Kiani Ph.D. for guiding, aiding and urging me on during my tenure at TCS; everyone should have a supervisor as patient and understanding as Sepehr. I would also like to thank my colleagues Cathy Leighton, Micheline DeRosa, Robert Gustafson and Blair Weiss for their support throughout the project.

I would like to thank Prof. Samir Nayfeh for instructing, mentoring and carefully reading the manuscript; Prof. Alexander Slocum for pushing for better designs and insightful comments on the manuscript; Prof. Lionel Kimerling for patients and photonics insights; and Prof. Warren Seering for product design insights and assessing my progress.

Most of all, I would like to thank my parents and sister, Lonnie, Bonnie and Meredith, for their never ending love and support; without whom, none of this would have been possible.

Contents

Chapter 1

Introduction

The major contribution of this thesis is to present a comprehensive solution to the problem of inspection of fiber endfaces in optical backplane systems. The inspection problem is framed by laying out top-level functional requirements on defect detection and then developing secondary constraints and requirements on the inspection system. These include requirements such as maximum machine size, motion requirements, defect detection such as finding scratches on the fiber endface and imaging requirements such as Rayleigh resolution. The key components of the solution are optics, machine vision and mechanical design. The work resulted in development of an inspection system, *fiber optic ferrule inspection machine* (FOFIM), that performs automatic in-situ inspection of optical fiber endfaces. The subsequent chapters detail each component but first the need for inspection is motivated.

1.0.1 Fiber Optics Background

> An optical fiber is a dielectric waveguide that operates at optical frequencies... it confines electromagnetic energy in the form of light to within its surfaces and guides the light in a direction parallel to its axis [1].

Fibers typically consist of a core, cladding and a buffer as seen in Figure 1-1. The optical data mainly travels through the core while the difference in index of refraction between the core and cladding allows for total internal reflection, maintaining signal integrity by preventing light from leaving the core (scattering). The buffer adds mechanical strength to the cable and protects the glass from the various stresses and strains while being handled and weathering the environment. Typical core and cladding materials are

silica (SiO_2) or silicate, doped with fluoride or oxides such as B_2O_5, GeO_2 or P_2O_5.

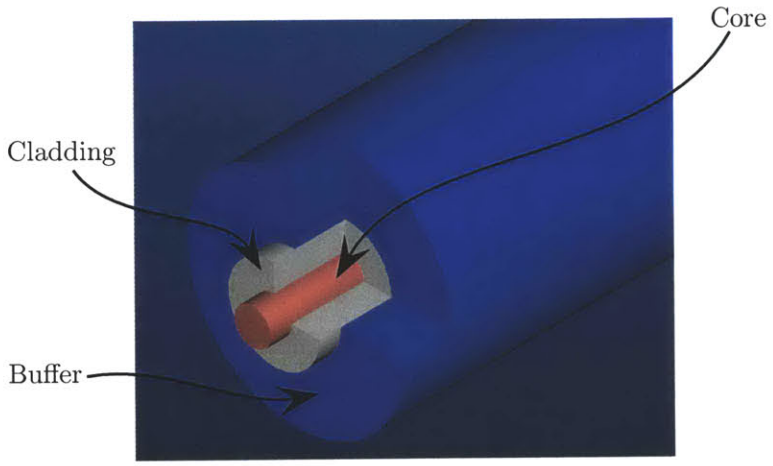

Figure 1-1: Fiber Detail

Single-mode fibers, as the name implies, sustain only *one* mode due to the small core size $\approx 9\mu$m. Having such a small core size makes optical interconnects, fiber splicing, and data launching much more difficult due to strict mechanical tolerances. An advantage is that bandwidths are on the order of terahertz with a light wavelength of λ =1550 nm.

Multimode fibers have much larger cores, typically 50 μm, and are able to carry *multiple* optical modes. Due to the larger core size; data launching, fiber splicing, and optical interconnects are more economical because the mechanical constraints are not as strict. These fibers may suffer from inter-modal dispersion and therefore have a lower bandwidth of 2000/500 MHz/km [1].

Million dollar optical routers utilize thousands of optical connections to obtain data transfer rates in the hundreds of GBits/s. In order to reliably do so, the endface of each fiber must be *defect free* [2], and therefore each endface must be inspected each time a connection is made.

There are many reasons why the fiber endface must be defect free, but the most obvious and important is to maintain optical signal integrity. Insertion loss (IL) and reflectance loss (RL) are typical tests to determine optical system performance. Insertion loss is the measure of optical power loss upon signal launch, thus ensuring a high signal to noise ratio for cables/connectors. Reflectance loss is a measure of the optical power reflected

back from a fiber cable system, low RL ensures minimal damage to the launching laser and/or a connector [3]. Current fiber optic connectors are capable of the performance listed in Table 1.1.

Fiber Type	Insertion Loss	Repeatability	Reflectance loss
Single Mode	0.30-0.5 dB	0.10 dB	-50 dB
Multi Mode	0.5-1.0 dB	0.25 dB	-60 dB

Table 1.1: Insertion Loss and Reflectance Loss Requirements

Automation improves production, test and inspection capabilities in many ways [4]:

- Increased System Bandwidth: Endface inspection time is reduced, as is the overall card-based machine down-time. There would be minimal connector disassembly on the daughter card or backplane because an inspection machine capable of in-situ inspection is much more dexterous than a human.
- More Repeatable and Quantitative Results: Machine capabilities are more deterministic than those of a human, lending more confidence in the accuracy of the results.
- Reduced Opportunity for Error: The less human involvement in such an inspection task, the less likelihood for error in data collection.
- Reduced User Involvement: This allows the operator to work on other important tasks as inspection proceeds creating a more productive work environment.
- Traceable Results: This allows for quick and accurate determination of defect characteristics with respect to time.

1.0.2 Currently Available Solutions

In comparison to copper interconnects, fiber optic interconnects have been notoriously difficult systems to maintain with the current set of available tools. There are many reasons for this:

- The available automated tools inspect a single ferrule only [5, 6, 7, 8, 9]. Their automation lies in defect detection (image processing), not in

acquiring the ferrule (positioning the camera, focusing and taking pictures). Ferrules on a daughter card or backplane must be inspected manually, as there currently are no solutions for these tasks. Manual inspection requires daughter card disassembly and easy access to the backplane connectors, which may not always be available. With each card-based machine holding thousands of ferrules, the down time for disassembly is unacceptable. There is a clear need for in-situ inspection.

- There has been relatively little research and development on optical interconnect maintenance as opposed to fiber optic component manufacturing and design.
- There are *technology barriers* that must be overcome in order to successfully design, manufacture, and sell such an automated machine in the current business market. For example, a typical servo axis costs typically $5,000 per axis and therefore a 3-axis inspection machine would be a viable solution only for *high-end* optical routers or super computers as this is a fraction of the machine's cost. Thus we must find or develop new technology to meet the market demand.
- There are diverse system connector configurations and standards, therefore it is difficult for a single design to work with all systems as the current installed base has a plethora of mechanical and electrical configurations.

Difficult maintenance of optical interconnects has been a key hindrance preventing designers from integrating them into datacom and computing applications, especially backplanes. System designers see this lack of support, and rarely design optical interconnects into the backplane. A quality inspection machine eliminates one of the key hindrances to adoption of optical interconnects, and attainment of high connection bandwidth.

1.1 Functional Requirements

The FOFIM is required to perform in-situ inspection of backplane connectors in large card-based machines such as routers and super computers. Card-based machines do not have a standard mechanical configuration; for example, routers form factors vary from large refrigerator sized units to small 600 x 600 mm boxes as seen in Figure 1-2. In general they have a backplane, which serves as an electrical or optical interconnect at the back

of the router between *daughter cards*. A daughter card is a module that plugs into the router backplane to perform specific tasks, for example:

- An ingress card receives incoming data
- An egress card sends outbound data
- A switch fabric card
  - performs IP address lookup
  - sends and receives datagram headers
  - calculates routing path dynamically

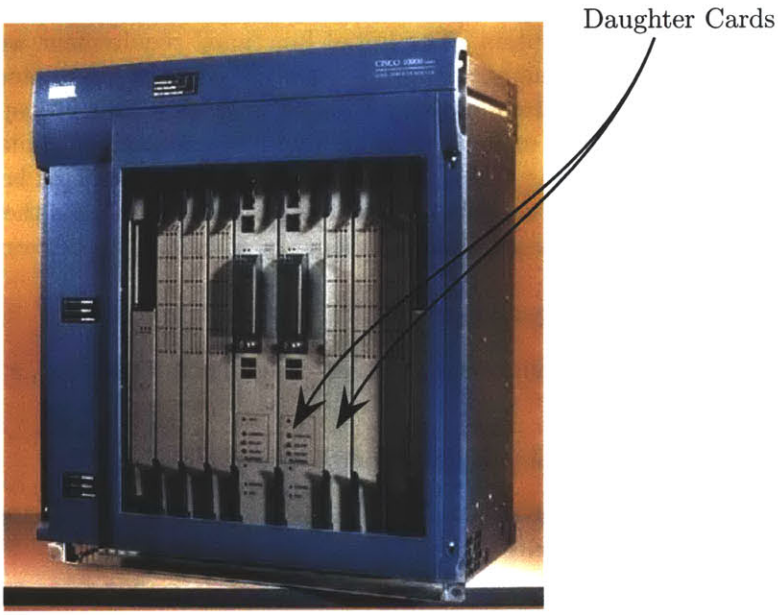

Figure 1-2: Router

The various daughter cards generate heat, and therefore a router's temperature can fluctuate from 18 to 70° C. To suppress this heat, fans are installed, thus we also have variable air flows and vibrations. These problems must be dealt with in our inspection machine design.

Their are broadly two methods to inspect backplane connectors, 1) remove the daughter card to gain access from the front, or 2) remove the connector from the backside of the router.

At first glance, the second method seems to be the easiest, but many of the currently installed routers have minimal backplane access and, even if there is backplane access, such a task is drastically more difficult to automate than the first method. There would be thousands of connectors to disassemble and load into the inspection machine. This would mostly likely be a manual process as a pick and place machine for this task would be prohibitively expensive. Next the connectors would have to be reassembled without incurring any damage, a rather tedious and formidable task. The first method is laid out in Section 1.2, and is convincingly more feasible than the second scenario.

Thus we decide to inspect the backplane connectors by removing the daughter card. Having to fit within the daughter card envelope has great impact upon the FOFIM design, but detailed discussion is deferred to the subsequent chapters. The initial functional requirement was given by interviews with many costumers, namely, "We need automated backplane inspection." Further probing revealed time constraints: inspection of a 12 fiber ferrule in under 2 minutes would be acceptable. Building a few prototypes, showing them to customers and getting feedback helped shape the functional requirements and prototype discussed in this thesis. For now it suffices to summarize the functional requirements as follows:

Mechanical Requirements

- The machine must fit within daughter card envelope, a 15x80x300 mm volume.
- The machine must provide 3-axis motion
  - Fiber-to-fiber, travel over a total range of 3.5 mm and minimum velocity 1 mm/s
  - Ferrule-to-ferrule, travel range up to 700 mm at a minimum velocity of 1 mm/s.
  - Focus, travel range up to 20 mm with a minimum velocity of 1 mm/s.

Imaging Requirements

- The machine must detect 1-2 μm defects:
  - scratches: placement, contrast, and width
  - particles, Oils, Chips and Pits: area, placement and contrast

Miscellaneous Requirements

- determine pass/fail
- user interface to generate reports
- quick inspection time, approximately 1-2 minutes for a 12 fiber MT ferrule
- salable at $5k-$10k
- non-destructive to fiber endface

1.2 Machine Usage: Preferred Embodiment

Figures 1-3 through 1-6 illustrate the intended FOFIM usage. A cart holds the FOFIM, motion-controller and image processing computer with a simple touch screen interface. This system could either be plugged into an outlet or powered by a battery for maximum mobility.

An inspection-card is stored in an empty slot within the router, or any other available storage space. The inspection-card is inexpensive and is designed specifically for each router to be inspected. When the user needs to install a new daughter card, each backplane connector needs to be inspected to ensure that the card will work properly. Thus the technician proceeds as follows:

1. The operator brings the inspection-cart to the router and removes the faulty card.
2. The operator removes the camera's protective cover.
3. The operator mounts the camera onto the inspection-card, as shown in Figure 1-3.

Figure 1-4 depicts the user loading the inspection-card into the router and connecting the inspection-cart controller to the camera. Next, the FOFIM begins to inspect each connector within the backplane. It is desirous to have inspection time be less than 2 minutes for a 12-fiber MT ferrule, and to provide a graphical user interface with live fiber images, the defects found and store all the results within a database. The database adds traceability, allowing retrieval of previous inspection results to compare with current results.

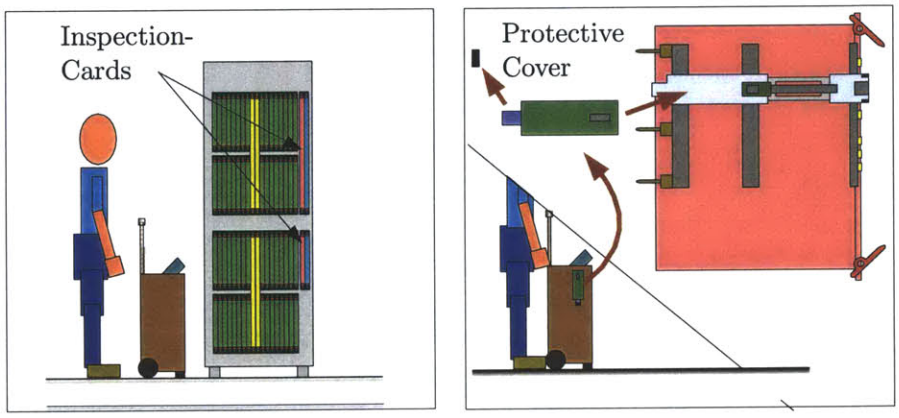

Figure 1-3: Inspection System Setup

Figure 1-6 shows the inspection-card being returned to its slot. The new daughter card is prepped by removing dust caps and is then installed into the vacant slot.

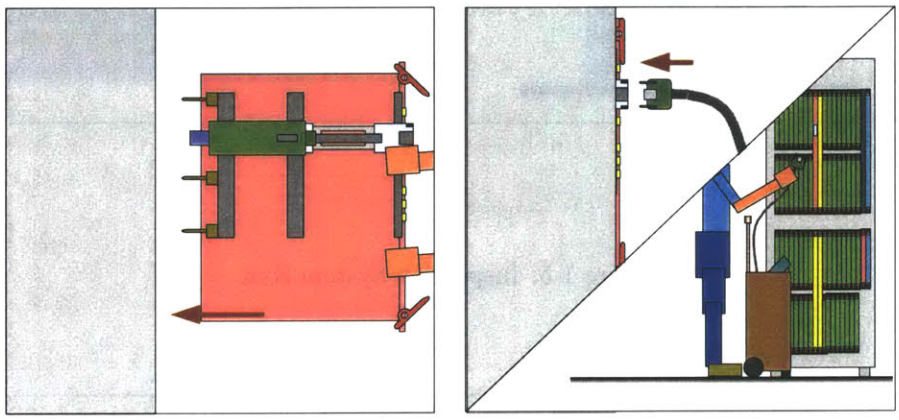

Figure 1-4: Inspection System Load

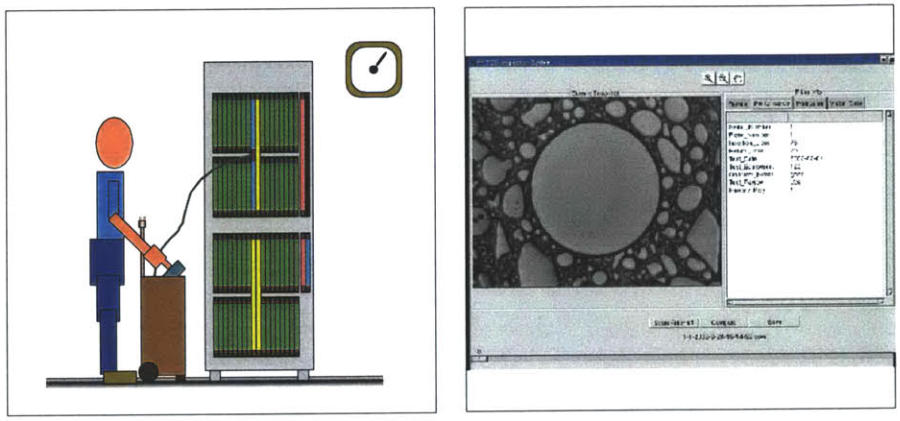

Figure 1-5: Inspection System Run

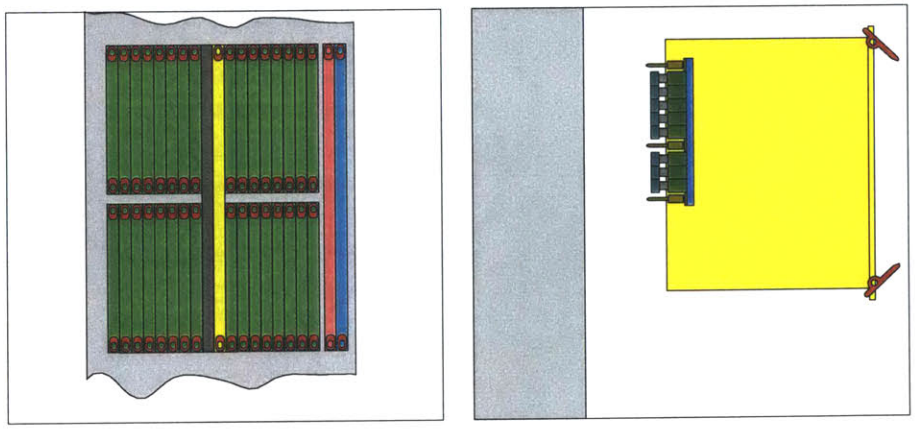

Figure 1-6: Inspection System Done

1.3 Solution Preview

The prototype design is shown in Figure 1-7 and a short summary of the various items that solve the problem follows:

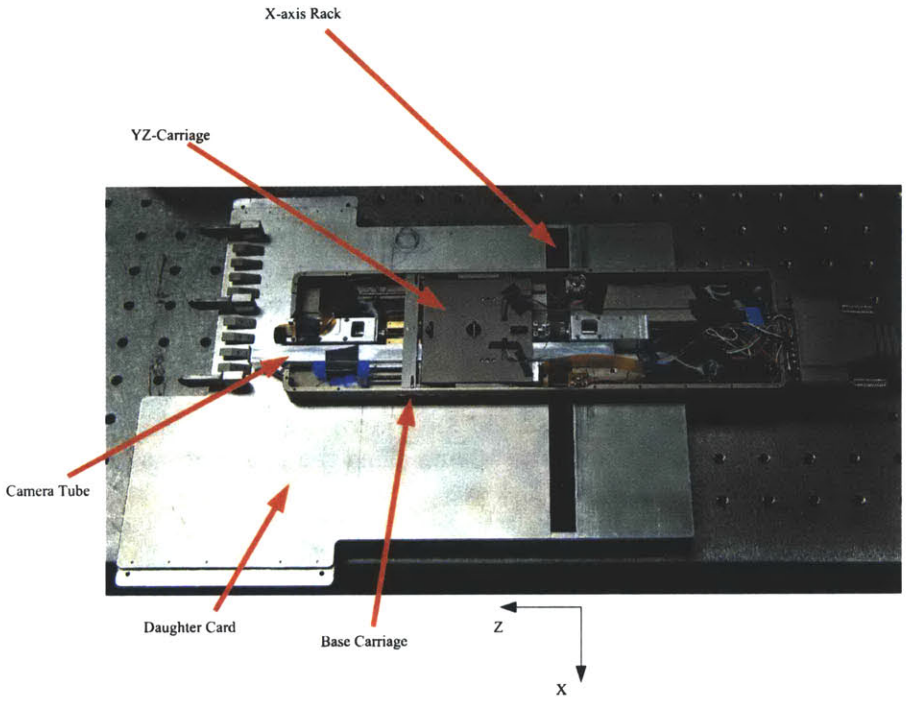

Figure 1-7: FOFIM prototype

- Optics: Through the use of computer automated design, an ultra long working distance 15X microscope objective was designed. Post-processing via inverse filtering achieves 1 μm Rayleigh resolution. The main challenge was to balance the trade-offs between Rayleigh resolution and the packaging constraints (small lens diameter and long working distance).

- Machine Vision: All available fiber intensity information is captured through high-dynamic-range and high-depth-of-field imaging. Edge finding, the Hough Transform and various morphological operators accurately detect the fiber endface, particles and scratches. The main

challenge was developing fiber and defect detection algorithms that are contrast and illumination invariant.

- Machine Design: Extensive use of an error-budget and lumped parameter dynamic modeling allowed us to design a 3-axis inspection machine with sub-micron resolution. The main challenge was to design a 3-axis machine within a small envelope and tight cost constraints.

1.4 Summary

To summarize, the major goal of this thesis is to lay out the framework for backplane fiber-optic connector inspection. We present solutions to the three major aspects of the problem: optics, machine vision and machine design. Strict functional requirements constrain the possible solution space for each of the three areas, and are summarized as:

- fit within a 15x80x300 mm envelope
- travel 700 mm, 3.5 mm, and 10 mm along the x, y, and z axes respectively
- inspect a 12-fiber ferrule in under 2 minutes
- detects, characterizes and catalogs 1 μm defects automatically
- run within a *live* router
- salable at \$5k-\$10k

Chapter 2

Fiber Optic Ferrule Imaging

2.1 Introduction

A fiber optic cable typically consists of a core, cladding and buffer, where the core and cladding are made of silicon glass differentiated by their indicies of refraction ensuring total internal reflection, as shown in Figure 2-1. Usually the buffer consists of plastic to prevent cable damage during handling.

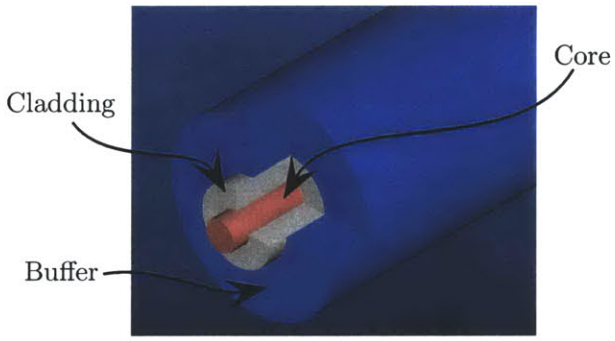

Figure 2-1: Fiber cable detail

Core diameter ranges from 9 μm for singlemode fibers to 62.5 μm for multimode fibers, and a typical cladding outer diameter is 125 μm. There are numerous optical connectors ranging from multi-fiber MTP[1] and MTRJ[2]

[1]Multiple terminations, push-pull latch; a monolithic ferrule housing multiple optical fibers utilizing a push-pull latch for insertion.

[2]MT ferrule, register jack latch; an MT ferrule with a telephone style latching mechanism.

connectors, capable of housing up to 72 fibers, to a single-fiber connector such as the LC[3] connector Figure 2-2. While there are 20 or 30 different specific fiber optic connectors, fundamentally they all can be classified as either a single fiber ceramic connector or a multi-fiber plastic connector. Both connector types can house either multi-mode or single-mode fibers. Each connector type has many applications such as, telecom/datacom, LANs[4]/CATV[5]/video, fiber to the home, premises distribution, gigabit applications (Ethernet, ATM[6], SONET[7], etc.), and our application the interconnect between PC cards and patch panels. Typical single-mode performance characteristics are less than 0.3 dB insertion loss (IL) and -55 dB average return loss (RL), while multi-mode performance characteristics are less than 0.5 dB insertion loss and -60 dB return loss.

2.2 Problem Statement

In this section we will discuss the optics problem statement, how the FOFIM's various functional requirements such as in-situ backplane inspection, imaging angle or flat polished ferrules, imaging ceramic and plastic ferrules, and imaging 1 μm defects, translate into hard constraints on the optical system: the Rayleigh resolution, dynamic range, depth of field, working distance, lens diameter and tube length.

2.2.1 Imaging Resolution

Small dimensions of the optical fiber core means that any defects such as scratches, dust-particles, oil, chipping and pitting may adversely effect the optical performance of fiber optic interconnects. Also, defect location and size are important parameters in quantifying their effects upon optical performance.

The impact of defects upon optical signal performance is difficult to quantify analytically and will require years of research to achieve a complete set of answers. Initial attempts at quantifying the effect defects have upon

[3]Lucent connector; small form factor connector made of plastic with an RJ-style latch (similar to a phone jack).

[4]Local Area Networks; a group of computers that share a common communications line

[5]Community Access Television

[6]Asynchronous transfer mode; a network technology capable of transmitting video, audio and computer data over the same network

[7]Synchronous optical network; ANSI's standard for connecting fiber optic transmission systems.

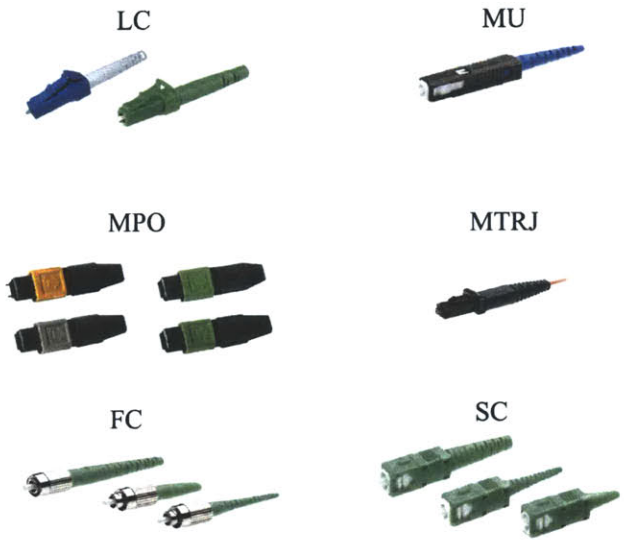

Figure 2-2: Various fiber connector types; LC = Lucent Connector, MU = Miniature Unit, MPO = Houses an MTP connector, Multiple-Terminations , Push-pull latch, MTRJ = Multiple-Terminations with RJ style jack, FC = Fiber Connector, and SC = Subscriber Connector

fiber performance are promising, Marcuse lays down the initial foundation for modeling single-mode fiber splices losses caused by misalignment between two fibers being joined, parameterizing longitudinal displacement, tilt and offset [10].

Currently, the TIA[8] has developed many fiber optic standards which cite general guidelines to the appearance of fiber end-faces but they are not designed for *permanent terminations* (i.e. connectorization or splicing) [11]. They are intended for the examination of "macro-type" defects and the user is invited to establish their own method to measure "micro-type" defects [12, 13, 14].

Recently a renewed effort has been started; Mahmood *et al* and Avram *et al* modeled the effect of scratches and digs upon back reflection or RL using wave scattering theory [15, 16]. As expected, their analysis shows a correlation between dig/scratch count and RL, but unfortunately they left model correlation with experimental data for future work. Their defect

[8]Telecommunications industry association; develops standards for communications and information technology products and services

model neglects defect depth, where scratches are parameterized by length and width while diameters parameterized pits, particles and chips. Scratch depth or dust particle height is expected to impact the cable's performance, hence defect depth should be accounted for in the models.

Recently iNEMI[9] started a project quantifying the effects of endface defects upon optical performance [17]. The overall goal is to define a set of endface inspection criteria to be used as an extension the existing to TIA and Telcordia specifications on connector performance. Various papers presented by iNEMI indicate that defect type, location, and size have drastically different effects upon the optical performance. As expected, defects closer to the fiber core more significantly impact optical performance.

A summary of the results follows [18, 19]:

- Scratches outside the fiber MFD (mode field diameter, slightly larger than core), have minimal impact on IL, RL and BER.
- 2 μm wide or smaller scratches within MFD have no impact on IL but can degrade RL. The amount of degradation depends on the size (width and depth) and the number of scratches crossing the fiber MFD.
- Particles on the core result in catastrophic failures while particles on the ferrule fail to show performance degradation.
- Critical particle parameters are distance from the core, size, type, hardness and thickness of the particle.
- Oil significantly decreases RL by up to 10-12 dB, but does affect IL, as it behaves like an index matching gel.

Based on these results, for a single-mode ceramic connector, the recommend inspection guidelines are as shown in Fig 2-3. The FOFIM must inspect fibers with the criteria put forth as an industry standard. The smallest defect, associated with the recommended inspection guideline, is 2 μm. As a conservative design, the FOFIM imaging system should be able to resolve 1 μm objects to accurately and repeatably detect 2 μm defects.

2.2.2 Dynamic Range

Multi-fiber connectors generally consist of a plastic (thermoset or thermoplastic) and glass resin mixture, which makes for an interesting fiber imaging

[9]International Electronics Manufacturing Initiative; they road map the needs of the global electronics industry providing standards and dissemination of efficient business practices

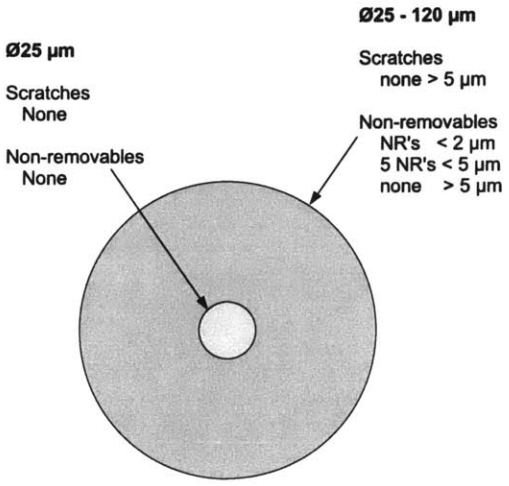

Figure 2-3: iNEMI fiber inspection guidelines

background (see Figure 2-4). Current off-the-shelf fiber inspection systems use a coaxial lighting schemes (see section (2.3.1)), which may induce a back reflection manifesting as a lit-core (Figure 2-5). The lit-core phenomenon depends on the fiber cable length and on how the other end of the cable is terminated.

From experimental data, the MT ferrule with an un-lit core image typically is a 6-stop scene (35 dB), while a lit-core typically has an 8-stop scene (48 dB). Also, as shown in Figures 2-6 and 2-7, the ceramic ferrule reflects light back toward the imager with coaxial lighting. With an un-lit core, the ceramic ferrule image can be captured in about 7-stops (42 dB) and with a lit-core 9-stops (54 dB). Thus, we must capture up to a 54 dB scene.

2.2.3 Depth of Field

Ceramic and plastic ferrules have either an 8° angled polish, known as an angled physical contact connectors (APC connectors) which reduces back reflection, or a flat polished connector (PC). The FOFIM is required to inspect both APC and PC connectors. Unless the APC connector is tilted 8° bringing the endface parallel to the object-plane, the optics require an 18 μm depth of field for the entire fiber to be in focus.

Also, some proprietary MT ferrules have fiber protrusion of up to 10 μm from the ferrule endface to ensure low insertion loss. It is desirable to capture the surrounding ferrule endface in focus too, in order to ensure that defects

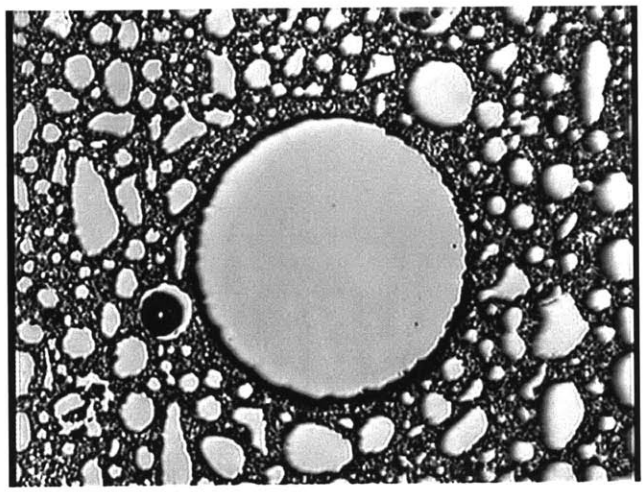

Figure 2-4: MT fiber endface image, Multimode

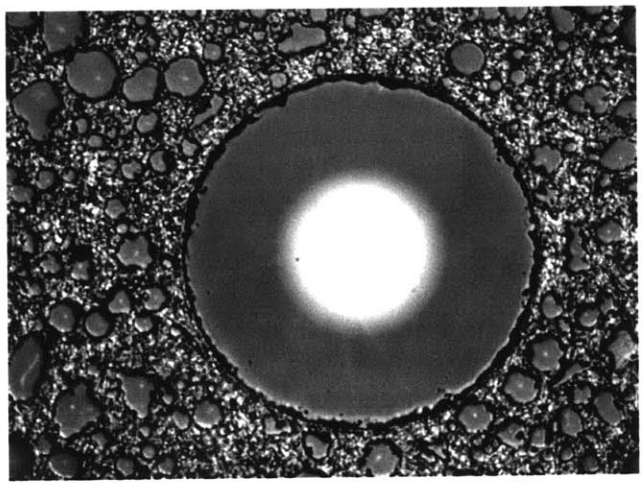

Figure 2-5: MT fiber endface lit core, Multimode

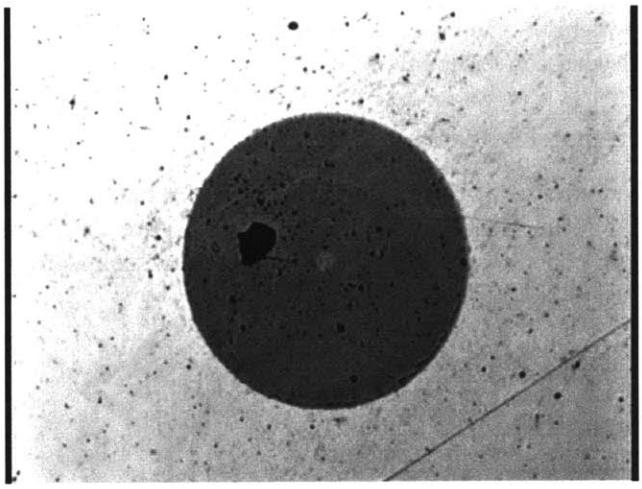

Figure 2-6: Ceramic fiber endface, Singlemode

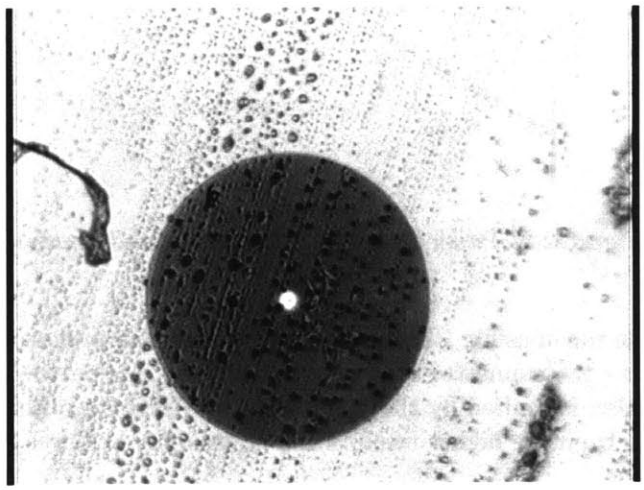

Figure 2-7: Ceramic fiber endface lit core, Singlemode

such as dust in the surrounding area may be found.

Typical microscope objectives with 10X to 20X magnification usually have depth of field on the order of 1 μm, it is difficult to achieve an 18 μm depth of field with conventional optics.

2.2.4 Working Distance

The FOFIM is required to inspect panel connectors which are recessed within a housing by 18 mm (Figure 2-8). As shown in Figure 2-9, there are three possible imaging conditions used to inspect the panel connectors depending on the location of the inspection optics:

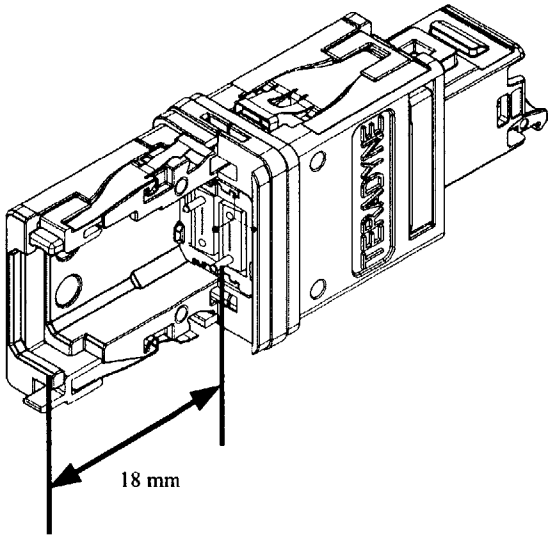

Figure 2-8: Panel connector, deeply recessed housing

1. Outside the housing: This allows larger optics and prevents them from touching the connector endface. Although in this particular case the resolution is limited by the panel connector shroud, other connectors benefit from the higher resolution a larger optic achieves.

2. Inside the recess just in front of the fiber endface. Most MT connectors have a guide pin protruding from the ferrule which aligns the connectors upon mating. This pin protrudes by 3 mm, so we should keep the optics slightly further away in order to prevent damage to the optics.

Also, the optics must be able to image each fiber, and therefore the optic diameter can be no larger than 5 mm in order to fit within the panel connector recess, and to image each fiber with the lens centered on the fiber.

3. Within the 3 mm envelope of the ferrule pin: The optic size would have to be reduced even more as the distance between the pin and the first fiber is 250 μm.

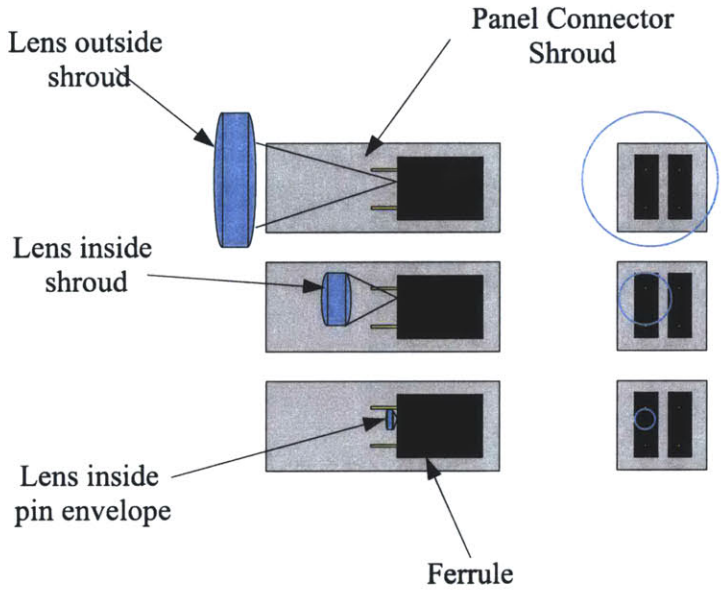

Figure 2-9: Imaging optics placement for panel connector inspection

The last imaging method, with the smallest lens very close to the ferrule, should have the highest resolution of the three imaging conditions. The lens could be damaged by the ferrule pin during a focus movement or it could come into contact with the ferrule endface possibly damaging the fibers, making manipulation quite difficult.

While imaging the panel connector, the first two optic systems have approximately the same numerical aperture (NA) and thus the same image resolution. But when inspecting other connectors without the recessed shroud, the large lens yields a much higher resolution and it is less likely to the hit the ferrule endface or the ferrule guide-pins. We choose to design

with a 20 mm working distance ensuring the highest resolution for all connectors and eliminating the possibility of lens damage as could occur when the lens is placed inside the shroud.

2.2.5 Maximum Lens Diameter

As shown in Figure 2-10, the lens diameter can be no larger than 12 mm in order for the optic to be placed on axis with each fiber in an MT connector[10] and to fit within the 15 mm daughter card pitch. We must also account for the lens mount size and the actuators. Therefore, for a practical implementation, we can not have an optic diameter larger than 10 mm.

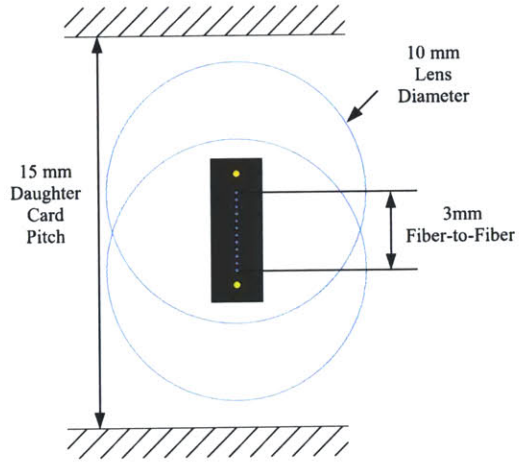

Figure 2-10: Daughter pitch constraint

2.2.6 Tube Length

As discussed in Chapter 4, the FOFIM's envelope can be no larger than 15x75x300 mm. The system's motors, actuators, connectors, cabling, and so on, along with the optics must fit within that envelope. A 200 mm tube length should leave adequate room for the supporting FOFIM components, yet provide good imaging properties.

[10]The maximum distance from the first fiber to the last fiber is 3 mm for MT ferrules.

2.2.7 Summary of Requirements

In summary, the fundamental functional requirements for our imaging device are: 1 μm minimum Rayleigh resolution, 20 mm minimum working distance, 10 mm maximum optic diameter, 20 μm depth of field, and 200 mm maximum tube length. Next we discuss currently available solutions to the imaging problem.

2.3 Currently Available Solutions

2.3.1 2D Microscopy

It is well known that microscopes provide an enlarged two-dimensional image. A common brightfield microscope setup is shown in Figure 2-11. The objective lens is focused on the object to be imaged, light reflects off/passes through the object and travels coaxially up through the lenses focusing onto the image plane.

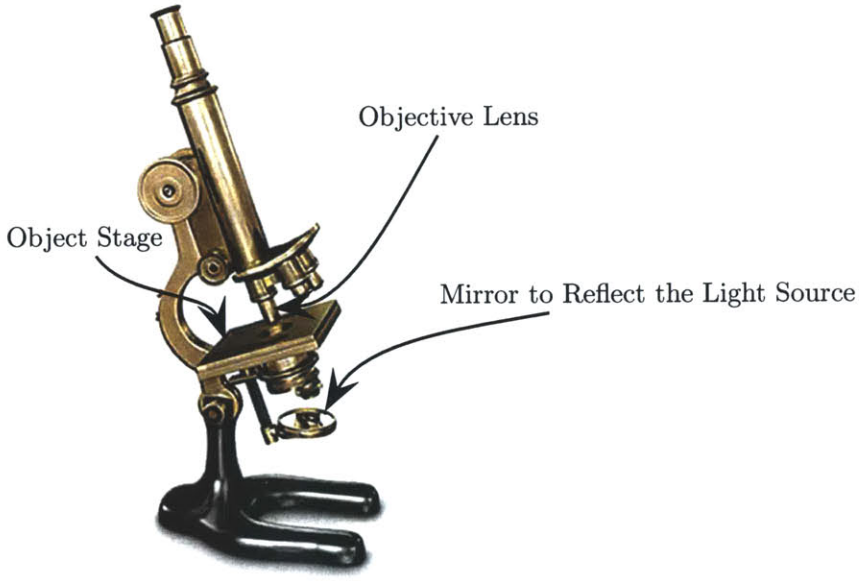

Figure 2-11: brightfield microscope[11]

[11]Printed here with the express written permission of the author Nikon Inc. [20]

A few "tricks" employed in 2D Microscopy aid in imaging different object types.

2.3.2 brightfield Illumination

Brightfield refers to a setup where the light source is injected coaxially into the imaging system, either via a beam splitter above the objective or through a condenser underneath the object (as shown in Figure 2-11). The light is then reflected off/passed through the object through lenses and onto the image plane, typically a human eye or a camera sensor. This is the familiar microscope setup often used in high-school science classes.

2.3.3 Dark-field Illumination

Dark-field (dark-ground) illumination occurs when the lighting is a hollow cone with numerical aperture greater than the objective [21, 22]. An example of coaxial dark-field lighting can be seen in Figure 2-12, the light travels axially down the lens tube and is reflected by a few mirrors directing the light toward the object at an oblique angle. Assuming the object is not perfectly flat, it will scatter light in different directions depending on surface orientation and its index of refraction. Thus some of the diffracted light passes back through the optics and onto the image plane.

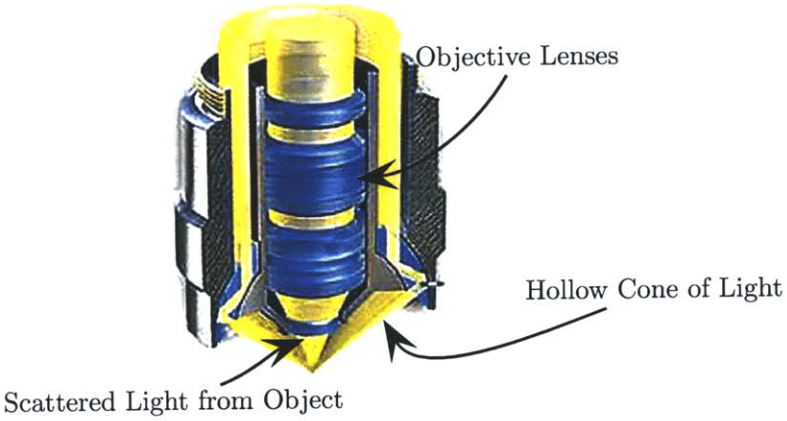

Figure 2-12: Dark-field objective[12]

[12]Printed here with the express written permission of the author Michael W. Davidson [23]

The advantage of dark-field illumination is that makes it easier to observe defects such as surface imperfections. For example, if we are trying to image a flat piece of glass with a single scratch, under brightfield illumination the scratch may be "drowned out" by the reflection of the rest of the glass being imaged. Under dark-field lighting, the only light passing into the optical system will be that scattered by the scratch.

2.3.4 Other Illumination Variants

- Julius Rheinberg developed an interesting illumination scheme, comprising a combination of brightfield and dark-field illumination, where the brightfield consists of one color and the dark-field of another. This produces interesting colorful images up to a moderate magnification (40X) [24].

- Apodization—The exit pupil shape and attenuation determine the amplitude point spread function (PSF) of a diffraction limited optic system [25][13]. For example, a system with a round pupil exhibits a diffraction-limited PSF in the shape of a sinc[14] function, as shown in Figure 2-13, where height represents attenuation.

  The image is the convolution of the PSF with the object, and therefore the side-lobes may have significant impact on the result. Apodization attempts to reduce the impact of the side-lobes via an attenuation mask at the exit pupil. A Gaussian attenuation mask is a rather popular method for this, but has the drawback of broadening the main-lobe along with decreasing the PSF height (effectively boosting low frequency response characteristics at the expense of the high frequency response). Also, inverse apodization boosts high frequency response at the expense of the low frequency response [26, 25].

- Phase Contrast: Frits Zernike developed a method to view "invisible" organisms. These organisms have varying indicies of refraction and thickness thus the optical path length of the light diffracted by them changes and accordingly so does the phase. The phase contrast microscope simply introduces another phase shift between the diffracted and the direct light such that constructive/destructive interference occurs, thus allowing the user to see the "invisible" phase object [27].

[13]The PSF is the optical equivalent of the impulse response, the image output of the optical system to a point-source input.

[14]sinc(x)= $\sin(x)/x$

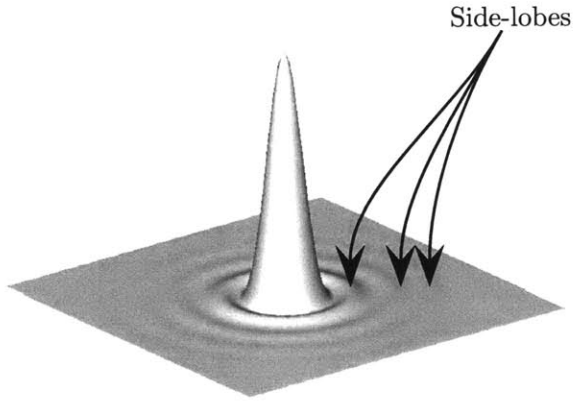

Figure 2-13: PSF of circular pupil

The curious reader is invited to read the literature for more information on the world of 2D microscopy [27].

2.3.5 3D Microscopy

Significant research has recently been done on 3D microscopy, as it gives much more information.

A brief overview follows:

- Interferometry: There are many different types of interferometers, but the preferred embodiment for fiber endface inspection is along the lines of the Michelson Interferometer, as it is simple in concept. Basically, a diffuse monochromatic light source is split into two paths via a beam splitter. One path goes to a reference mirror and the other path goes to the object to be inspected. The light reflects back down the paths and meets again at the beam splitter, where they form an interference pattern which is directly correlated with the difference in distance of the object and the reference mirror, as shown in Figure 2-14

- Holography: Dakoff *et al* developed digital interference holography where the interference pattern of an object is generated optically and

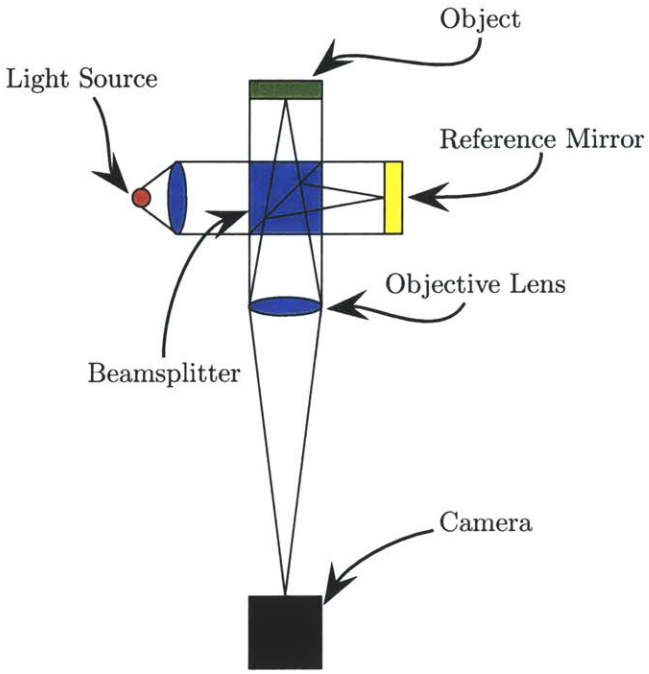

Figure 2-14: Michelson interferometer

digitally recorded using an CCD/CMOS imager. The holographic image field is numerically calculated and the process is repeated for a large number of varying wavelengths. It is the numerical superposition of the holographic image fields that produces the 3D measurements of the object [28].

- Contact Microscopy: This method basically involves dragging a stylus across the object while measuring height variations at known positions. This scanning method is a rather slow process, and because it requires physical contact with the object, damage to the fiber endface could occur.

Numerous other 3D Microscopy solutions exist but they are typically too expensive to be of use for the FOFIM.

2.3.6 Off the Shelf Solutions

Nikon, Zeiss, Leica, Olympus and several other optical design and manufacturing companies produce excellent objectives which can satisfy a 1 micron

resolution imaging condition. We must remember that the system must fit within the daughter card envelope, have 20 mm or greater working distance and relatively low cost.

A typical CCD/CMOS sensor has 5-10 μm pixel spacing[15], hence to image a 1 μm object we need between 10X and 20X transverse magnification from the objective. Searching through optical catalogs, we find objectives satisfying our requirements. However, all of the off-the-shelf objectives with this resolution, working distance and magnification have a minimum cost of $2,000, and a minimum diameter of 30 mm. A few reasons why these objectives are rather large and of high cost follow:

- They are highly optimized for chromatic aberration, typically either for the entire visible light range (500 nm to 750 nm) or deep ultraviolet (250 nm to 350 nm). Hence, they contain many lenses, usually 10 or more.
- They simply were not designed with the size constraints that we face.
- They have longer tube lengths on the order of 300 mm.

These microscope objectives exceed our cost and size functional requirements, hence they are not a satisfactory solution. After a wide search, we conclude no existing optics are capable of meeting all of the functional requirements. The only suitable solution is to design custom optics specific to this application.

2.4 Optical Design

After an exhaustive review of currently available solutions, it becomes clear that a custom designed objective is the best possible solution. The following section details a lens design which achieves the following capabilities:

- 15X magnification
- 20 mm working distance
- 200 mm tube length
- 0.22 object NA

[15]Recent technology has pushed pixel spacing near 2 μm, but the signal-to-noise also drops significantly and likewise the image quality.

- 1.4 μm diffraction limit
- Seidel aberrations significantly reduced below the diffraction limit

A rather simple "reversed telephoto" design consists of two doublets and two singlets [29], as shown in Figure 2-15. This design is chosen for the FOFIM optics and key design details are presented in the following paragraphs.

Figure 2-15: Final design

The lens design process often starts with a patent search to prevent the usual problem of reinventing the wheel. There are thousands of optical design patents readily available, the more recent and relevant ones are U.S. patent numbers 4521083, 6016226 and 6721094. These patents were designed for very specific use in the UV band or require numerous lenses. As shown in the next section, the functional requirements lead to a simple design not requiring very many lenses or ultra-tight tolerances.

If no patents are found that solve the imaging problem, we must resort to designing the system from scratch. A flowchart depicting this process is shown in Figure 2-16. First we layout the first-order design that satisfies all the functional requirements, it is typically an arrangement of component focal lengths and spacings providing the appropriate image. Next the first-order design is input into the optical design software and variables are set, for example, lens properties such as radii, spacings, and glass properties. An error function penalizing the current design for not meeting the user's performance criteria is generated and then the system is run through a minimization function to reduce the error on the error function. This process is repeated until the system is satisfactory. More details of this process are discussed later in the chapter but for now we give a little optics background information and discuss the first-order design.

2.4.1 First Order Design

As applies to all design processes, before any actual design work begins we must determine the system's functional requirements; determine which requirements have firm limits and those which can tolerate deviation. We must question the requirements so as to not over constrain the problem and to seek a physically realizable and practical solution [29].

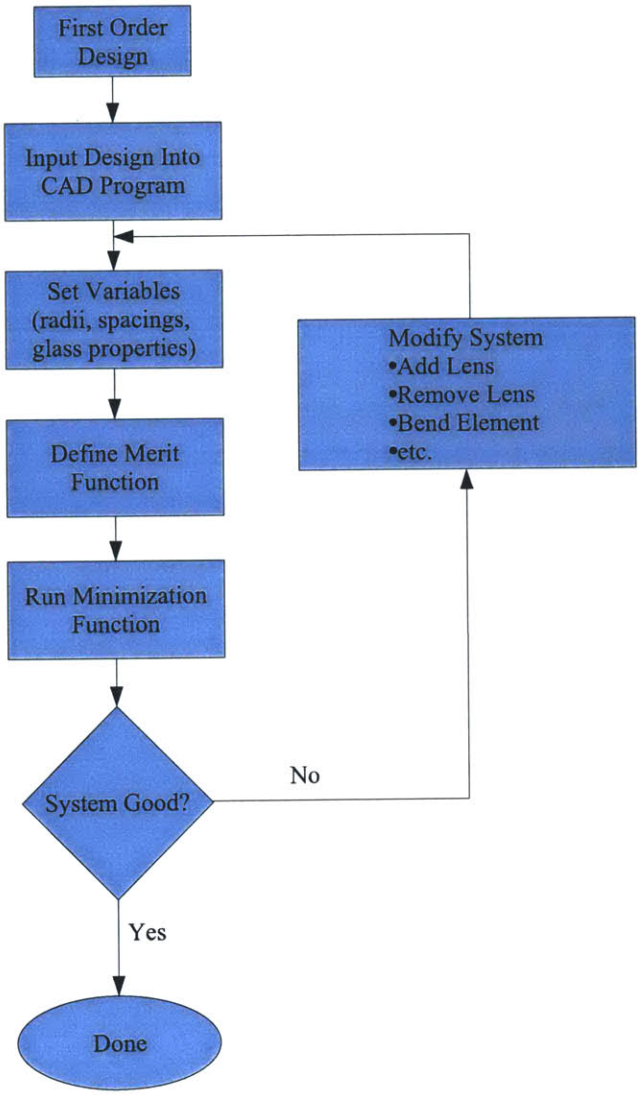

Figure 2-16: Optical Design Process

Recalling the aforementioned functional requirements in the order of decreasing importance:

- 10 mm maximum optic diameter
- 20 mm minimum working distance
- 1 μm minimum Rayleigh resolution
- 200 mm maximum tube length
- 5-10 μm depth of field

The lens diameter and working distance arrive from strict physical constraints for the FOFIM. We cannot exceed these constraints or the system simply will not fit within the card slot. Soon we will see how these requirements impact the system design. The resolution requirement is not as firm a requirement, but the 1 μm resolution is desired at the expense of the tube length and depth of field.

Small Diameter vs. High Resolution:

As the accepted practice, Rayleigh's resolution criterion,

$$\text{resolution} = \frac{0.61\lambda}{\text{NA}} \tag{2.1}$$

shall be used to determine the system's optical resolution. The parameter λ is the working optical wavelength and NA is the numerical aperture of the optical system. As a matter of physics, the image of a diffraction limited optical system is always blurred and of reduced contrast. Better optics induce less blurring and less reduction of contrast. For example, a simple point source will be imaged as a circle, where its intensity is brighter in the center and gradually decays as does a sinc[16] function. The diameter and intensity distribution are determined by the system's optical properties.

Rayleigh resolution is defined as the minimum distance between two point sources where the two sources can still be resolved in the image. The amount of blurring and reduction of contrast ultimately determines the system Rayleigh resolution.

What does this mean in terms of detecting fiber endface defects? In practice we are not concerned about mislabeling a 1 μm particle as a 2 μm

[16] sinc(x)= $\sin(x)/x$

particle which could easily happen due to image blurring. Also we are not concerned about detecting two closely spaced 1 μm particles as separate particles; we would be satisfied labeling it as one larger particle. So, if the optics are designed to meet the 1 μm Rayleigh resolution, we should be able to detect defects smaller than 1 μm, since we are not concerned with accurate signal reconstruction.

The definition of NA is depicted in Figure 2-17, where NA= $n \sin\theta$, n is the index of refraction of the medium through which the light travels as it approaches the lens, θ is the angle of light that is accepted by the lens.

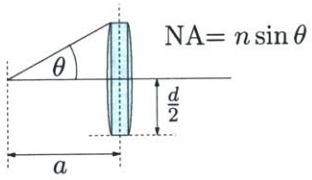

Figure 2-17: NA, numerical aperture definition

Trigonometry immediately shows that the NA is related to working distance, a, and half diameter, $d/2$.

$$NA = n \sin\theta = n \frac{d/2}{\sqrt{a^2 + \left(\frac{d}{2}\right)^2}} \tag{2.2}$$

and so resolution is found as

$$\text{resolution} = \frac{1.22\lambda}{nd} \sqrt{a^2 + \left(\frac{d}{2}\right)^2} \tag{2.3}$$

When $a >> d/2$ we obtain the simple relationship

$$\text{resolution} = a \frac{1.22\lambda}{nd} \tag{2.4}$$

Clearly the Rayleigh resolution improves (smaller and smaller objects become visible) as lens diameter increases.

Earlier technical considerations established a 20 mm minimum working distance and 15 mm daughter card pitch. Now we need to maximize the lens diameter to minimize the resolution limit. Thus daughter card pitch directly influences the system's Rayleigh resolution; it dictates the maximum optic size which is less than 10 mm in diameter allowing enough room to hold the

lenses and move it around for viewing the various fibers within the 15 mm envelope.

Minimization of the working wavelength λ also improves the resolution limit (see Eq. 2.1). As an example, with blue lighting ($\lambda = 470$ nm) and 10 mm lens diameter, we can nominally resolve two point sources separated by 1.2 μm. While it is possible to design optics with lighting at UV wavelengths (approx. 300 nm), these systems are typically much more expensive as they require exotic glass and the image sensors are a bit more expensive too. While blue lighting does not give quite the desired resolution we will discuss how to resolve past the Rayleigh resolution later in the chapter.

Magnifications vs. Tube Length:

Figure 2-18 depicts a singlet with focal length f, working distance a and tube length b. Working distance is the distance between the object and the lens, and tube length roughly is the distance between the lens and the image plane. These loose definitions are approximate but will suffice for this discussion.

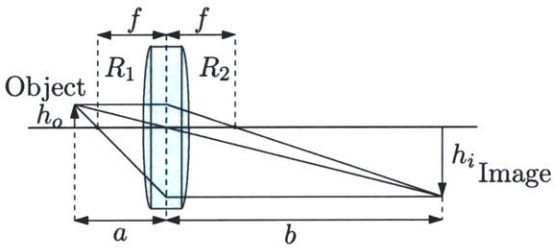

Figure 2-18: Singlet imaging condition

The transverse magnification T_{trans}, is defined as the ratio between image and object heights, i.e. $T_{trans} = h_o/h_i$. With a little analysis, using the simple lens maker formula

$$\frac{1}{f} = \frac{1}{a} + \frac{1}{b} \tag{2.5}$$

and some simple paraxial ray-tracing rules:

- A ray parallel to the optical axis on the object side passes through the focal point on the image side
- A ray passing through the focal point on the object side runs parallel to the optical axis on the image side.
- A ray aimed through the center of the lens is passed straight through.

one can derive

$$T_{trans} = \frac{h_o}{h_i} = \frac{f}{a - f} \tag{2.6}$$

and applying Equation (2.5) we get

$$T_{trans} = \frac{h_o}{h_i} = \frac{-b}{a} \tag{2.7}$$

Thus, for our system, with $a = 20$ mm and T_{trans} ranging from 10X to 20X[17], the tube length range is 200 to 400 mm. This brings us close to the desired requirements, but we need to minimize the tube length if possible. Our task is to find an optimum point where we can obtain the desired working distance along with an appropriate tube length.

Several techniques are available to effectively shorten the tube length with minimal impact upon the other system properties. The most common introduce mirrors or prisms to fold the optical path back and forth from the object to the image. Technically the effective tube length remains the same, but the distance from the back lens to the imaging sensor is shortened because the path is folded. While this is a viable solution, it is not quite suitable for our application as it widens the camera system, requiring very precise mirror/prism alignment. Moreover these mirrors and prisms are fairly expensive.

Another way to slightly skirt this working distance vs. tube length issue is by adding more lenses. A lens's basic function is to bend light, thus the more lenses the easier it is to bend the light. Figure 2-19 depicts two systems with equal transverse magnification, the main differences being the number of lenses and tube length. By shortening the focal length of the positive singlet and placing a negative lens behind it we are able to achieve the same transverse magnification while shortening the tube length.

Applying Eq. (2.5) in a cascaded fashion allows quick modeling of multi-element systems. Also using a spreadsheet program, we can quickly setup our optic system and see how system parameters change with variables. For example, for the two lens example (see Figure 2-20) we desire a 15X magnification with 20 mm working distance. Thus in our spreadsheet as shown in Table 2.1 we have $a_1 = 20$ mm.

The application of the lens maker formula to our first order design is as shown in Figure 2-21. Since we are using a "reversed telephoto" design we definitely want b_1 to be positive (i.e. to the right of the lens). Therefore,

[17]This assumes 5-10 μm pixel pitch on the image sensor for 1 pixel = 0.5 μm

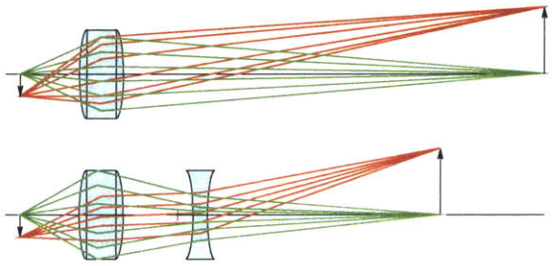

Figure 2-19: Singlet vs. doublet; same magnification different tube lengths

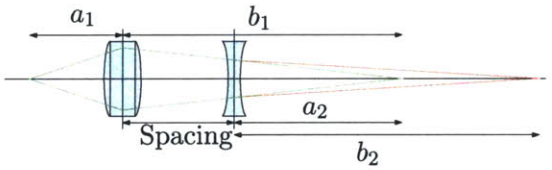

Figure 2-20: Two element system

by Eq. (2.5) our focal length should be slightly smaller than the a_1 so we set $f_1 = 16$ mm. Applying Eqs. (2.5) and (2.6) we obtain $b_1 = 80$ and $T_{trans_1} = -4$.

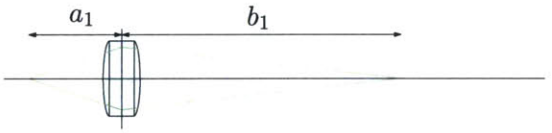

Figure 2-21: First lens tracing

Again the lens maker formula is applied to the subsequent lens, as shown in Figure 2-22. The lens spacing is arbitrarily set to 50 mm, as computations are performed via spreadsheet we can easily change this later to observe its effects. Now a_2, the distance between the object seen by the second lens to the second lens, is simply calculated by subtracting b_1 from the lens spacing, 50 mm − 80 mm = −30 mm. Also since the total system magnification is simply the multiplication of each lens' magnification, we find $T_{\text{trans}_2} = 3.75$. Applying Eqs. (2.6) and (2.5) we find $b_2 = 112.5$ mm and $f_2 = -40.9091$ mm.

This example clearly shows how two lenses effectively shorten tube length from 300 mm to 112.5 mm. For example, it is quite simple to demonstrate that the wider we space the two lenses, the shorter the tube length becomes. Also, we can easily determine the required focal lengths to make a 10X or

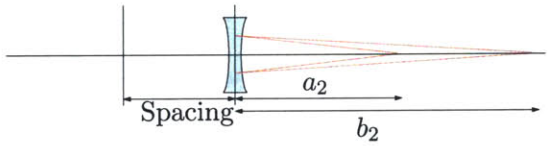

Figure 2-22: First lens tracing

Lens	a	b	f	T_{trans}	Spacing
1	20 mm	80 mm	16 mm	-4X	50 mm
2	-30 mm	112.5 mm	-40.9091 mm	3.75X	
			total mag	-15X	

Table 2.1: First order spreadsheet calculation

20X objective.

We need to be careful with this reversed telephoto design for a few reasons: One may notice that the NA of the singlet system is slightly higher than that of the doublet, thus the system resolution is slightly decreased in the doublet case. For extremely short tube lengths this setup requires a significant amount of "optical work," bending of light at each lens which easily results in large aberrations[18].

In practice, a good objective design certainly needs more than one lens to correct for the various aberrations (spherical, astigmatism, chromatic, etc.), as long as we are aware of this problem and try not to go overboard with shortening the tube length we should be fine.

Now that we have a decent back-of-the-envelope system, we can move to a optical design software program to check the details.

2.4.2 Computer Aided Design

Optical computer-aided-design software quickly allows us to investigate many design permutations, giving freedom to explore many designs, of which hopefully one solves the imaging problem. Such computer programs are simply optimization algorithms minimizing a user defined *merit function* operating on the user's design. It is not an automated process; the minimization of a non-linear multi-variable system allows many solutions and without applying some intuition it becomes quite difficult to find a satisfactory solution.

[18] "...deep curvatures and large angles of incidence and obliquity...lead to unusually large amounts of secondary and tertiary aberrations" [30]

Blind application of the minimization algorithm results in finding a local minimum that is nowhere near the global minimum. With experience, a little insight as to how to define an appropriate merit function and how to move the optimization routine out of the local minimum, a good first order optical design, and a little luck we should be able to find a decent solution.

A simplified overview of a CAD process follows along the lines of:

1. input first order lens design
2. define system variables to be optimized (radii, thickness, indicies of refraction)
3. define optimization merit function
4. run minimization algorithm on the merit function with the defined system variables
5. if the system is not satisfactory go to step 2 and redefine some system variables and/or the merit function and repeat the steps until the system meets the desired performance.

Inputting the first-order design into the software is a matter of inputting lens spacings, lens radii and glass properties into a spreadsheet. From the first order design, we know the desired lens power (or inversely their focal lengths, power $= 1/f$) and the lens placements, i.e., 20 mm working distance, and the 50 mm lens separation. To determine appropriate lens radii, we return to the basics; Eq. (2.8) demonstrates the paraxial approximation between lens radii, index of refraction and focal length. It is clear that many different combinations of radii and indicies of refraction give the same focal length f, so a simple method to determine radii is to set them to equal in magnitude but of opposite sign and to assume glass index of BK7 as it is ubiquitous.

$$\frac{1}{f} = (n-1)\left(\frac{1}{R_1} - \frac{1}{R_2}\right) \tag{2.8}$$

The radii R_1 and R_2 are shown in Figure 2-18.

Applying Equation (2.8), the radii are solved for as as shown in table 2.2.

The next step is to define an optimization merit function. This optimization is largely an art and is perhaps the most important task as it determines how the design will progress. The optimization merit function, also known as an error function, is based on the premise that our desired optical quality and capability can be quantified into a single number. Typically this consists of a combination of the following items:

Surface	Radius [mm]	Thickness [mm]	Glass
0	0	20	AIR
1	16.231052	0	BK7
2	-16.231052	50	AIR
3	-31.564034	0	BK7
4	31.564034	94.793669	AIR

Table 2.2: System detail input: 15X transverse magnification at $\lambda = 470$ nm

- Seidel Aberrations: These refer to aberrations that occur in monochromatic light due to the paraxial approximation inaccuracies, namely $\sin\theta \neq \theta$. The main aberrations are spherical, coma, astigmatism, field curvature, and distortion. The curious reader will find [31] to be a good introductory read on the Seidel aberrations.

- Modulation Transfer Function (MTF): This is a plot of system contrast with respect to input frequency, the optical analog of the Bode plot from systems theory. Basically, an object containing frequency swept sinusoids (see Figure 2-23) is input into the optic and the contrast is measured for each frequency. The MTF from our final system design is shown in Figure 2-23. It shows the typical output from an incoherently-lit diffraction-free optic, contrast decreases almost linearly as input frequency increases for the desired wavelengths (454-485 nm). This shows that the optical system will have trouble imaging frequencies above 715 cycles/mm at the object plane, approximately 1.4 μm Rayleigh resolution on the object[19].

- Point Spread Function (PSF): This is the illumination distribution of a point source's image, effectively an optical impulse response. Figure 2-24 shows the PSF of the final design. The central peak is near unity and decays rather quickly, both desirous traits. This shows the diffraction effects which slightly blur and reduce the contrast of all images, as the image is simply the convolution of the object with the PSF. Off-axis points behave quite similarly to on-axis points thus creating a uniform response across the field of view.

- Spot Diagram: This is a plot of rays from many wavelengths traced from various points within the field of view to a spot on the image. This diagram allows us to easily see the various Seidel aberrations and

[19]Rayleigh resolution diffraction limit corresponds to about 9% on the MTF curve.

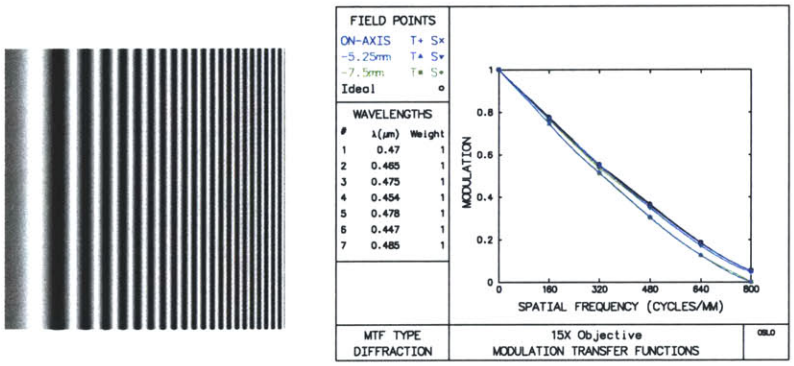

(a) Swept Sine Input

(b) MTF Plot

Figure 2-23: MTF plot and sine sweep

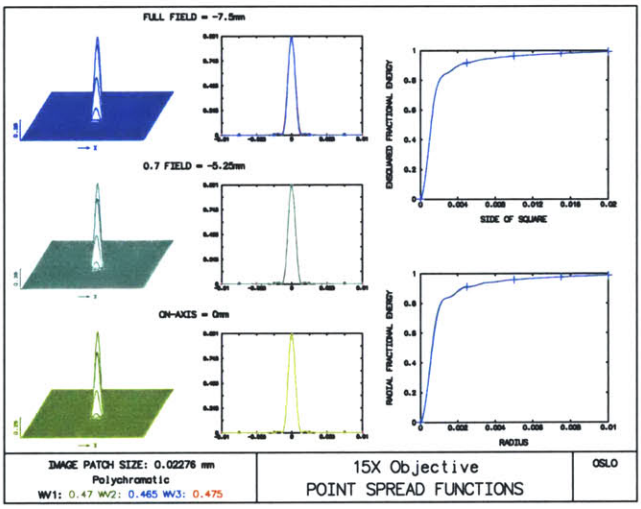

Figure 2-24: Point spread function

chromatic aberrations. An example from the final design can be seen in Figure 2-25. It shows slight astigmatism in the off-axis points but since all rays are well within the diffraction limit, the circle surrounding each field point, we see diffraction effects rather than chromatic or Seidel aberrations.

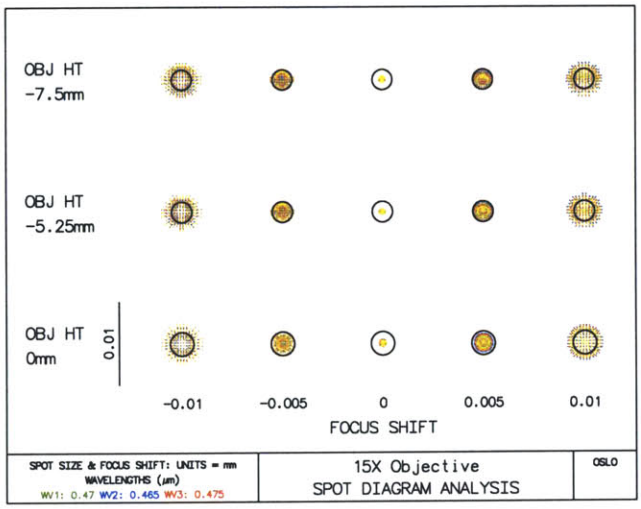

Figure 2-25: Spot diagram

- Optical Path Difference (OPD): This is a measure of the departure of the actual wavefront from an ideal spherical wavefront [29]. In other words, light traveling from a single point on-axis and off-axis should have the same optical path lengths resulting in no wavefront errors. A system with OPD less than $1/4$-wavelength is known as diffraction limited, because diffraction effects dominate the system output as opposed to the Seidel aberrations. A wavefront plot of the final design can be seen in Figure 2-26, which shows that all field points have OPD $< 0.06\lambda$, which is quite good.

- Departure from physical constraints: We can specify a desired system magnification, tube length, working distance, basically any physical constraint and have the departure from the desired level be part of the error function.

After a few optimization iterations on the first order system (shown in Table 2.2), with the various error functions it becomes apparent that we

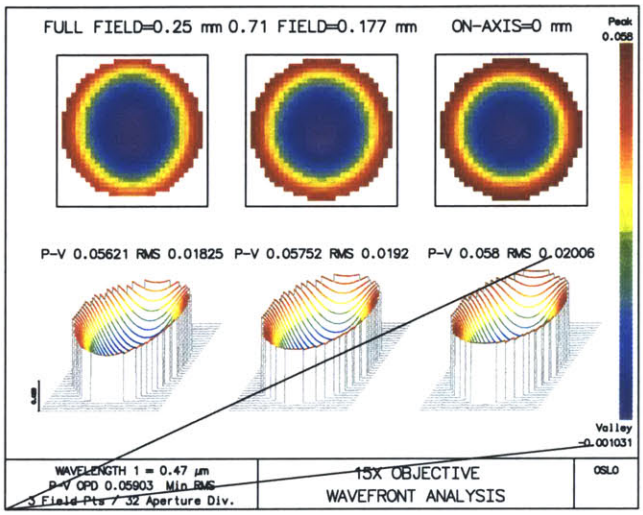

Figure 2-26: Optical path difference

are rather far from a solution. An abbreviation of techniques employed by Smith [29] to improve the convergence to the desired solution are as follows:

- Bend the optical elements, i.e., hold fixed the optical power while changing the lens shape.
- Try to remove "weak" optical elements
- Try to split a "strong" optical element into two or more "weaker" elements.
- Add an element.
- Remove an element.
- Try reversing elements to "jar" the optimization out of the local minima.
- Change optimization merit function drastically for a few iterations and then go back to the original merit function.
- Hold some variables constant for a few iterations and then allow them to vary.

After many iterations and experiments with the various tips listed above, a good solution was found, as shown in Figure 2-27. This consists of two doublets and two singlets, detailed specs are shown in Table 2.3. One should keep in mind that the glass used is specific to the manufacturer, see Appendix A.0.2 for detailed glass information. The previous system results presented on MTF, PSF, spot diagram and OPD indicate that the system will perform very well, nearly diffraction limited with 1.4 μm Rayleigh resolution.

Figure 2-27: Optical design solution

Surface	Radius	Thickness	Glass
Object	0	20.0	Air
1	-319.761	2.0	LAF6
2	-10.16	2.0	K20
3	-20.193	4.664026	Air
4	28.6	2.0	K20
5	-12.014	2.0	ZF13
6	-202.66	22.949037	Air
7	18.155	6.87	QF8
8	-27.48	6.890578	Air
9	-11.172	2.175	K20
Image	12.446	148.452244	Air

Table 2.3: System design table

Illumination

Experimentation with the bench top testbed, (as detailed in Chapter 4), with a few different lighting schemes shows dark-field illumination may be an appropriate solution to image small defects upon the fiber endface. Unfortunately, dark-field illumination requires a significant level of illumination and packaging constraints make it difficult to practically implement. Thus coaxial illumination appears to be the only practical solution.

Implementing coaxial illumination is also not trivial as back reflections can wreak havoc on the final image. One must be careful when selecting optical coatings and lens radii to reduce the amount of reflections in the

optical system. Discussions with a few optical design experts, Warren Smith and Tom Hubin, provided some practical design tips:

- If possible, locate the beam splitter in collimated space to reduce astigmatism for plate beam splitters or spherical and chromatic aberrations for cube beam splitters.
- Make sure to use anti-reflective coatings on all surfaces of the beam splitter to reduce ghosting affects.
- Use flocking paper, or matte black paint to absorb stray light.
- If possible, the image sensor should receive the reflected light from the beam splitter as a first surface reflection and the light should be transmitted through the splitter.
- Locate the splitter as far as possible from the image sensor.
- The light source should pass through all optics, tubes, apertures without hitting anything that might scatter light toward the imager. Use baffles to counteract this if required.
- Include the beam splitter in your optical lens design to account for the aberrations that it introduces.

The system design utilized a cube-beam splitter located directly behind the last lens element. Upon implementation, the image contrast was greatly reduced to the point where no practical image could be formed. Upon close inspection, we found that the beam splitter mount reflected light back toward the imager, reducing the system contrast. The cube beam splitter and mount were switched with a plate-beam splitter and a different mount that did not scatter the incoming lighting. This greatly alleviated the scattering problem and the system produced significantly better images, which are adequate for this optical system.

Design for Manufacturing: Error Budget

With CAD software it is fairly easy to simulate the effects of manufacturing tolerances and mechanical positioning of each lens. Speaking with a few manufacturers to determine manufacturing capabilities and the associated costs greatly aids in design for manufacture. For example a typical manufacturer may have a spec sheet as found in Table 2.4.

Applying the appropriate quality to the lens design by carefully specifying tolerances and appropriate statistical distributions on all parameters; radius, power fringes, irregularity fringes, thickness, indicies of refraction, decentration and tilt, we can performing a Monte-Carlo simulation to determine how quality affects system performance.

Also, we can reduce the overall system sensitivity to each of the tolerances and to spread the sensitivity evenly among the components by simultaneously optimizing all the systems created from the Monte-Carlo simulation. This allows us to "loosen" tolerances on each component, effectively making them easier and less expensive to manufacture and assemble.

Attribute	Commercial Quality	Precision Quality	MFG Limits
Glass Quality (n_d)	0.001	0.0005	Melt controlled
Diameter (mm)	+0.00/-0.10	+0.000/-.025	+0.000/-0.010
Radius (mm)	0.2%	0.1%	0.025%
Power SAG(fringes)	10	5	1
Irregularity (fringes)	2	0.5	0.1
Tilt (arc, min)	3	1	0.5
Decentration (mm)	0.050	0.010	0.002
Scratch-Dig	80-50	60-40	10-5

Table 2.4: Typical tolerance specification sheet

This method quickly helped move the system tolerances from the *manufacturing limits* down to *precision quality* greatly reducing costs. Detailed Drawings can be found in the Appendix A.

2.4.3 Depth of field and Dynamic Range

Depth of field (DOF) is calculated as

$$\text{DOF} = \frac{b}{2\text{NA} \times T_{\text{trans}}} \tag{2.9}$$

where b is the acceptable blur size at the image-plane, typically the CCD/CMOS pixel size, and NA is the object numerical aperture. For this system we have NA = 0.22, $b = 7$ μm and $T_{\text{trans}} = 15\text{X}$, giving DOF = 1.1 μm. This does not meet the 20 μm functional requirement; section 3.3.2 details how the DOF is extended via digital image-processing.

The imaging device limits the system's dynamic range, which in this case is approximately 40 dB from the manufacturers specification sheet. Extension of dynamic range via image-processing is also deferred to Chapter 3.

2.4.4 Verification

Examples of images taken with the design optics can be seen in Figs 2-28(a), 2-29(a), and 2-30(a). Beside each is an image of the same fiber taken with a higher resolution objective, 0.96 μm resolution. The FOFIM's images are slightly blurred, owing to the lower 1.4 μm resolution as expected.

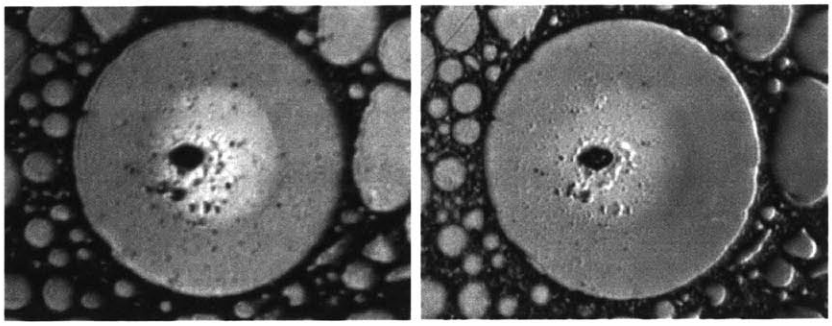

(a) Image by Designed Objective (b) Image by Objective with 0.3 NA

Figure 2-28: MT fiber 1 image with designed optics

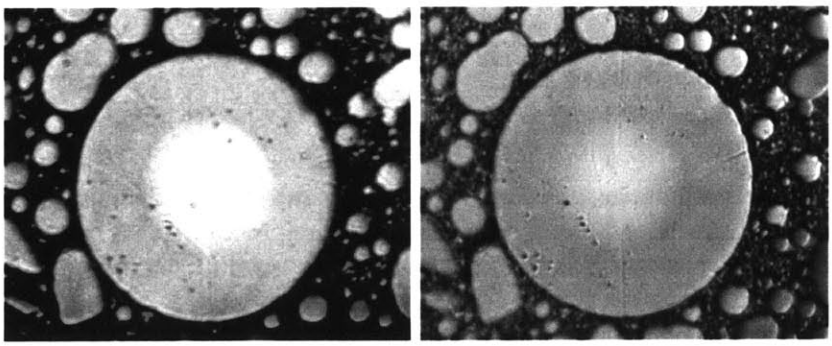

(a) Image by Designed Objective (b) Image by Objective with 0.3 NA

Figure 2-29: MT fiber 2 image with designed optics

Due to limited resources, we are unable to directly measure the system MTF and PSF, but it can be argued that we can compare the general results with the different sets of images from each objective. Images from the 0.3 NA objective achieves a higher contrast and appear "sharper," due to the higher resolution. This is roughly the performance we are looking for from the portable FOFIM. Fortunately, there are a few methods for reducing the

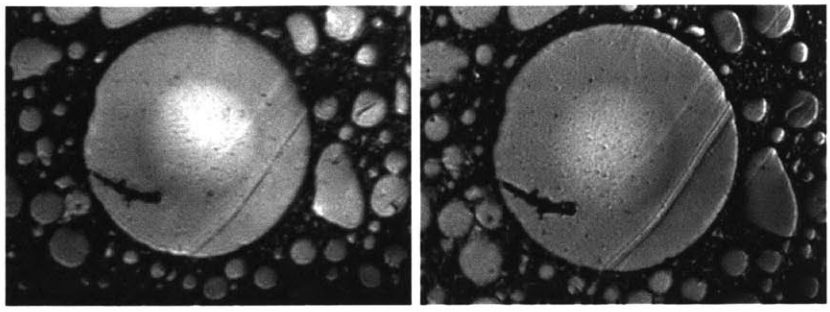

(a) Image by Designed Objective (b) Image by Objective with 0.3 NA

Figure 2-30: MT fiber 3 image with designed optics

diffraction effects as discussed in the next section.

2.4.5 Deconvolution

Optics are typically modeled as linear and shift-invariant, the recorded image I is found as

$$I = P \otimes O + N \tag{2.10}$$

or in the Fourier domain,

$$\hat{I} = \hat{O} \times \hat{P} + \hat{N} \tag{2.11}$$

where $\hat{}$ denotes Fourier transform, O is the 2D object being imaged, P is the PSF, N is noise introduced by the image capture process, and $\otimes$ denotes the convolution operator [32]. A diagrammatic portrayal of the image capture process can be seen in Figure 2-31.

Image deconvolution's goal is to reconstruct O, given I and P. If we simply neglect the noise, it appears that we can reconstruct the original image as $\hat{O} = \hat{P}^{-1}\hat{I}$. This computation is very fast as it only requires an FFT and division, but noise wreaks havoc upon high frequency components [33, 34]. Due to the system noise, the image inversion problem is ill-posed, i.e., a unique and stable solution may not exist.

A quick example of typical deconvolution filtering capabilities is shown by a simulated frequency response of the designed optics. Figure 2-32(a) shows that the optical system resolution is about 715 cycles/mm[20] and upon

[20]Rayleigh resolution corresponds to 9% contrast on the MTF curve.

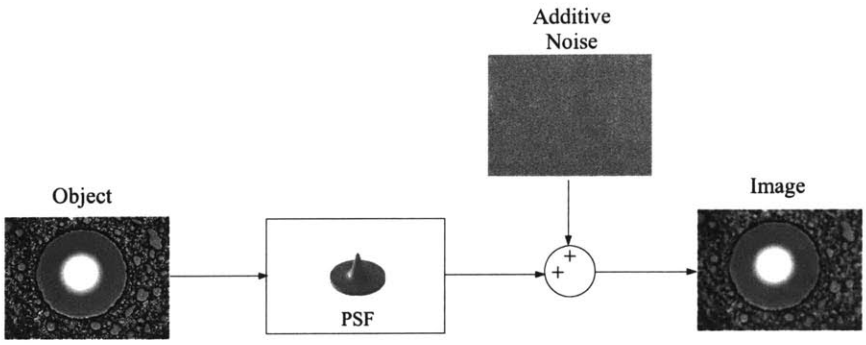

Figure 2-31: Imaging system

deconvolution via Weiner filter we achieve approximately 900 cycles/mm (Figure 2-32(b)). One should note that noise reduction would slightly improve the deconvolution results. A short survey of the many different approaches to solving the image inversion problem follows:

- Linear Regularization Methods: Ivanov and Tikhonov first proposed regularization methods to reduce the set of solutions to one optimal solution, differences in the definition of optimality have created many distinct methods [35, 36]. The basic premise is to use the physics of the problem to obtain an optimal solution while minimizing $\|I - P \otimes O\|^2$. Typical physical constraints used to regularize the problem are bounds on system noise or bounds on the energy of O, the smoothness of the object. A few regularization methods follow:

  - Tikhonov introduced a high pass filter H and regularization parameter λ to minimize $\|I - P \otimes O\| + \lambda \|H \otimes O\|$, where the second term is an image smoothness weighting function [36]. The reconstructed image in the frequency domain is then:

$$\hat{O}_{\text{est}} = \frac{\hat{P}^* \hat{I}}{\hat{P}^* \hat{P} + \lambda |\hat{H}|^2} = \hat{W} \frac{\hat{I}}{\hat{P}} \tag{2.12}$$

    P^* denotes the complex conjugate of P, and W is known as the window function, the window function is different for the various definitions of optimality.

  - The Weiner filter, assumes O and N have Normal distributions with zero mean and variance, σ_O and σ_N respectively, giving the

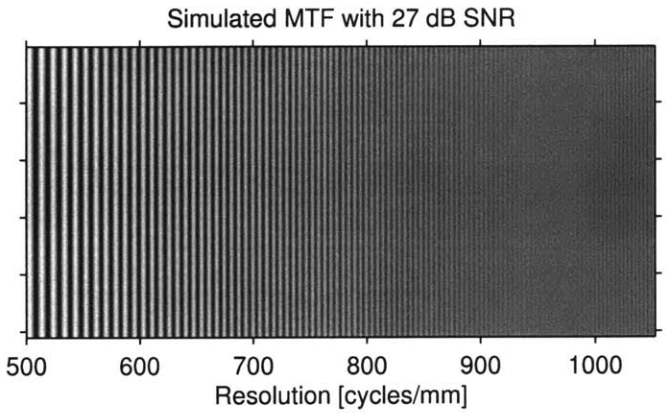

(a) Simulated MTF with 27 dB SNR (RMS)

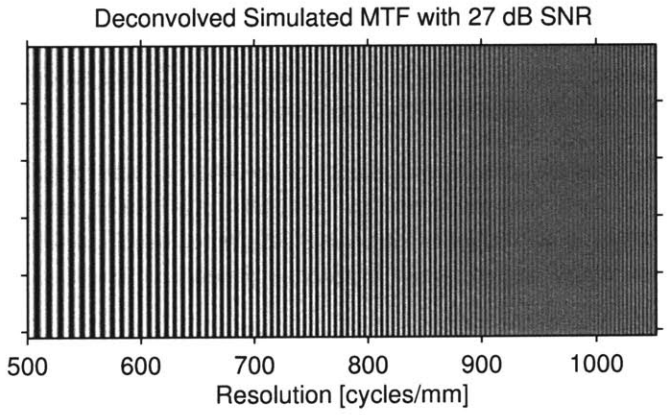

(b) Simulated MTF with 27 dB SNR (RMS) Deconvolved

Figure 2-32: Simulated MTF

Fourier filter as:

$$\hat{O} = \frac{\hat{P}^* \hat{I}}{\hat{P}^* \hat{P} + \sigma_N^2 / \sigma_O^2} \tag{2.13}$$

The result is optimal in minimization of the mean-square-error between the estimate and true images, and reduces to the ideal inverse filter in the absence of noise.

- Maximum-likelihood methods regularize the problem by maximizing the probability of obtaining the observed image [32]. For example the probability of obtaining the image I given the object O with Gaussian noise is

$$p(I|O) = \frac{1}{\sqrt{2}\pi\sigma_n} e^{-\frac{(I - P \otimes O)^2}{2\sigma_n^2}} \tag{2.14}$$

which leads to the minimization of

$$\frac{\|I - P \otimes O\|^2}{2\sigma_n^2} \tag{2.15}$$

which is usually solved in an iterative fashion [32]. The ML methods allow for constraints such as system bandwidth, the result must be positive, and the object must belong to a given spatial domain. Recently there has been some interest in the Viterbi algorithm, a well known ML method [37, 38], which in practice performs the deconvolution sub-optimally in order to keep a reasonable computation time.

- MEM (Maximum Entropy Methods) initially presented by Jaynes, solves for the image with maximum entropy (the smoothest solution), "when we make inferences based on incomplete information, we should draw them from that probability distribution that has the maximum entropy permitted by the information we do have [39]." It it is quite difficult to find the optimal regularizing parameter to accurately reconstruct both high and low frequencies [40].

Fourier based methods are computationally quick compared to the iterative ML and MEM methods, but as always there are trade-offs. The iterative methods initially have been shown to converge, but upon further iterations tend to diverge [32]. Fourier methods also have problems: the

Gibbs phenomenon (local oscillations about singularities), finding an optimal λ is non-trivial, and the trade-off between resolution and noise. As a result the final result is band-limited.

An interesting technique called Wavelet-Vaguelette Decomposition attempts to capitalize on the speed of Fourier methods without having to trade-off between noise and resolution. It estimates the inverted image as

$$F = P^{-1} \otimes I + P^{-1} \otimes N \tag{2.16}$$

where $\hat{P}^{-1} = 1/\hat{P}$, and is followed by the well-known denoising via thresholding wavelet coefficients [41, 42]. In practice, it is a non-trivial task to select the appropriate wavelet transform and optimal threshold, but there has been significant progress in the recent years [43, 44, 45].

Deconvolved Fiber Images

After experimenting with a few of the different convolution methods we found that deconvolution via the Weiner filter effectively boosts the system resolution from 1.4 μm to 1.1 μm as shown in the MTF plots in Figures 2-32(a) and 2-32(b). This resolution is satisfactory for the FOFIM system. While other methods do provide slightly "better" results, their computation time can be rather large. In order to reduce the overall system cost, we selected the Weiner filter since it provides adequate resolution and reduces the computational requirements.

For the images presented earlier in the chapter, deconvolution gives the results shown in Figures 2-33, 2-34 and 2-35. There is a clear improvement, the contrast is increased and the singularities are "sharper." The spectral response "before" and "after" deconvolution are shown in Figure 2-36. The higher frequencies are more attenuated in the original power spectrum, proving that deconvolution restores some of the original high-frequency data.

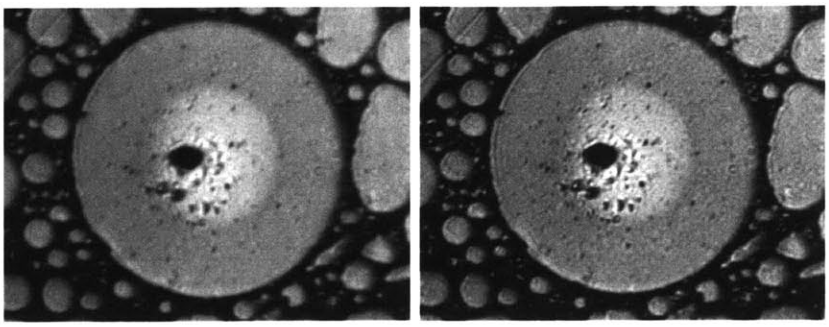

(a) Original Image (b) Deconvolved Image

Figure 2-33: Fiber 1 deconvolved

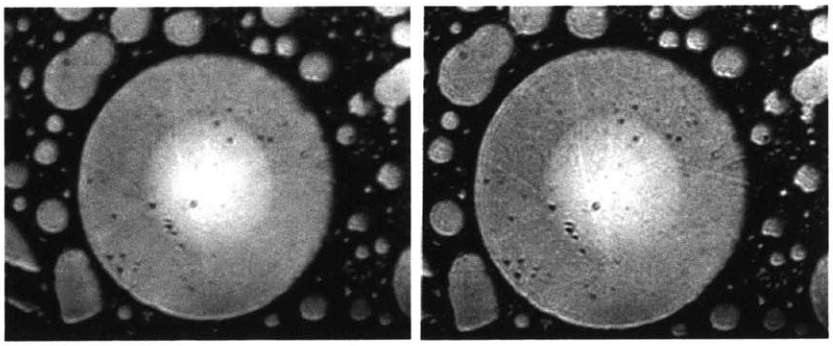

(a) Original Image (b) Deconvolved Image

Figure 2-34: Fiber 2 deconvolved

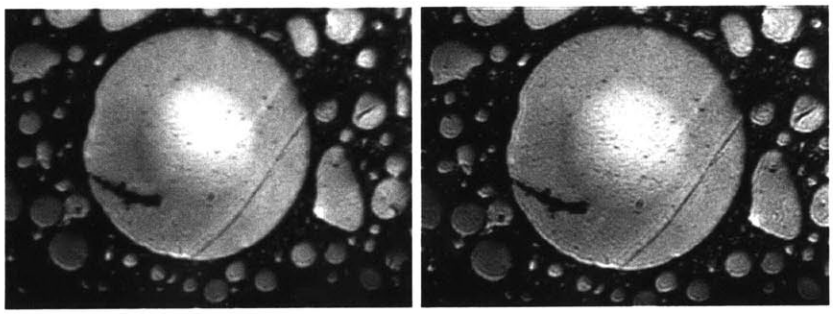

(a) Original Image (b) Deconvolved Image

Figure 2-35: Fiber 3 deconvolved

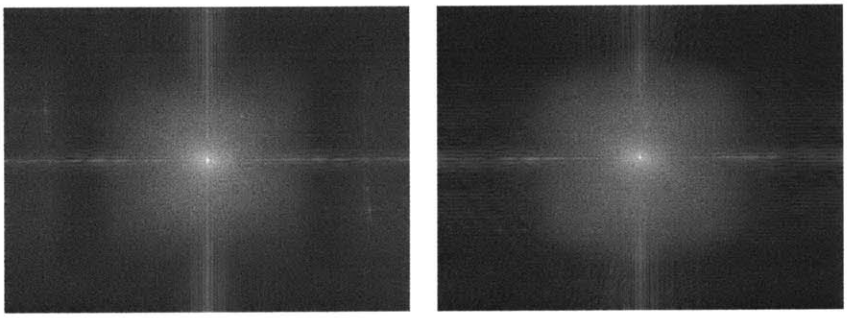

(a) Original Image Power Spectrum (b) Deconvolved Image Power Spectrum

Figure 2-36: Fiber 3 power spectrum

2.5 Summary and Future Work

In summary, after searching traditional optic vendors and a deep literature survey it was found that the best imaging solution was to design and manufacture a custom objective. The designed objective gives 15X magnification with 0.2 NA and is optimized for 470 nm light, thus giving 1.4 μm object Rayleigh resolution. Using deconvolution methods, optical system resolution performance is increased to 1.1 μm, well within the 1-2 μm requirement given by iNEMI. Chapter 3 includes a discussion of dynamic-range and depth of field improvements. Otherwise, the optic successfully meets all functional requirements.

Future work could be on reducing the number of lenses and position tolerances on each lens. Also implementation of a better deconvolution method without increasing the computational cost would be an asset.

Chapter 3

Machine Vision

3.1 Introduction

Detecting endface defects inherently assumes that inspection images contain all information need to detect all relevant defects: the inspection image has minimal noise (the defect SNR is high), appropriate illumination, is completely focused throughout the field-of-view, and without under or over exposure. Also the fiber must be detected before it can be inspected, which is a non-trivial task for some ferrules. Most of these problems have been thoroughly discussed in the literature and a short review is provided for each, but first the machine vision functional requirements are discussed.

3.2 Machine Vision Requirements

As discussed in Chapter 2, any defects such as scratches, dust-particles, oil, chips and pits may adversely affect the optical performance. It is quite difficult to analytically determine the impact defects may have, but recently iNEMI started an initiative to empirically quantify optical performance degradation due to defects [17, 19, 18].

Based on early findings, they propose inspection guidelines as shown in Figure 3-1. No scratches or non-removables (chips and pits) are allowed within the core. In the cladding, scratches with width less than 5 μm and non-removables smaller than 2 μm in diameter are acceptable. Also up to five 5 μm diameter particles are allowed but none larger than 5 μm.

These guidelines suggest that any removable defect such as oil and dust be removed and are not allowed. Also, they neglect to discuss the contrast of the particle, for example if we have two scratches, one wide and barely visible

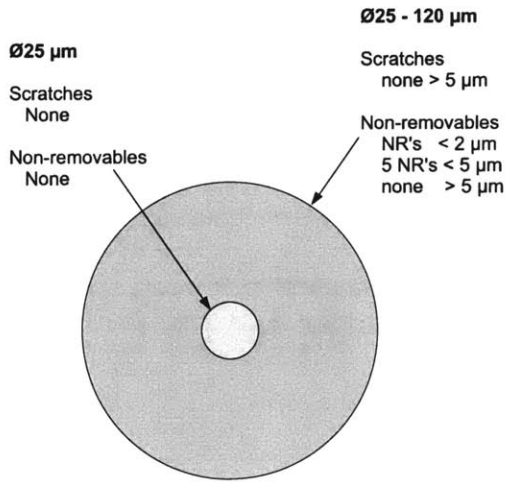

Figure 3-1: iNEMI fiber inspection guidelines

and one fine and dark, from experience we know that the dark but narrow scratch degrades optical performance much more than the faint and wide scratch. The faint and wide scratch may not effect the fiber performance at all.

They also neglect to determine the lower limit on defect size to be detected, for example are $\frac{1}{5}\,\mu$m wide scratches acceptable? According to their no-defect rule in the core, it is not, but in practice it is nearly impossible for an area scan imaging device with air spacing to resolve past $\frac{1}{2}\,\mu$m (see Chapter 2 for Rayleigh resolution limits), and the equipment with which they are inspecting has typical Rayleigh resolution down to 1 μm.

We propose that all defects whose characteristic length of 1 μm or larger need to be detected. That is, scratches of 1 μm width, dust-particles, oil, chips and pits with major diameter 1 μm and larger must detected to ensure that an accurate and repeatable pass or fail decision can be rendered.

3.3 Enhanced Imaging

3.3.1 High Dynamic Range Images

Lit-cores and ceramic ferrules require high dynamic range imaging, well beyond the sensor's capability; thus, it is quite difficult to reliably detect all defects upon the ferrule endface within a single image. Typically a sensor

can capture the entire dynamic range with large quantization errors or image with small dynamic range and minimal quantization errors as it is a finite digital process [46]. The elegant solution of fusing multiple images of any scene at different exposures has been discussed in the literature [47, 48, 49, 50, 51].

Debevec *et al* [48] and Mann *et al* [50] have proposed methods recovering the image sensor's response function from images of the same scene with differing exposure values. The response function is then inverted to accurately fuse the images into a single high-dynamic range (HDR) image whose pixel values are a direct function of the true radiance of the scene. These methods are rather simple but are computationally demanding.

Grossberg shows that, without loss of information, all data within each image can be combined by a simple summation [46]. This is the simplest method to capture HDR images, and is the least computationally demanding algorithm. Example exposure sequences and the resulting summation image are shown in Figures 3-2 and 3-3. The top images are the images at different exposures and are summed to give the larger image.

The HDR images do appear "flat" or of low contrast, this is due to limited dynamic range of current print media and image displays. Many techniques have been presented to overcome this issue, compressing HDR data to low dynamic range media to still have meaningful results [52, 53], but fortunately the defect detection algorithms deal directly with the numbers and are not of limited dynamic range. HDR imaging effectively gives nearly unlimited dynamic range while minimizing quantization defects.

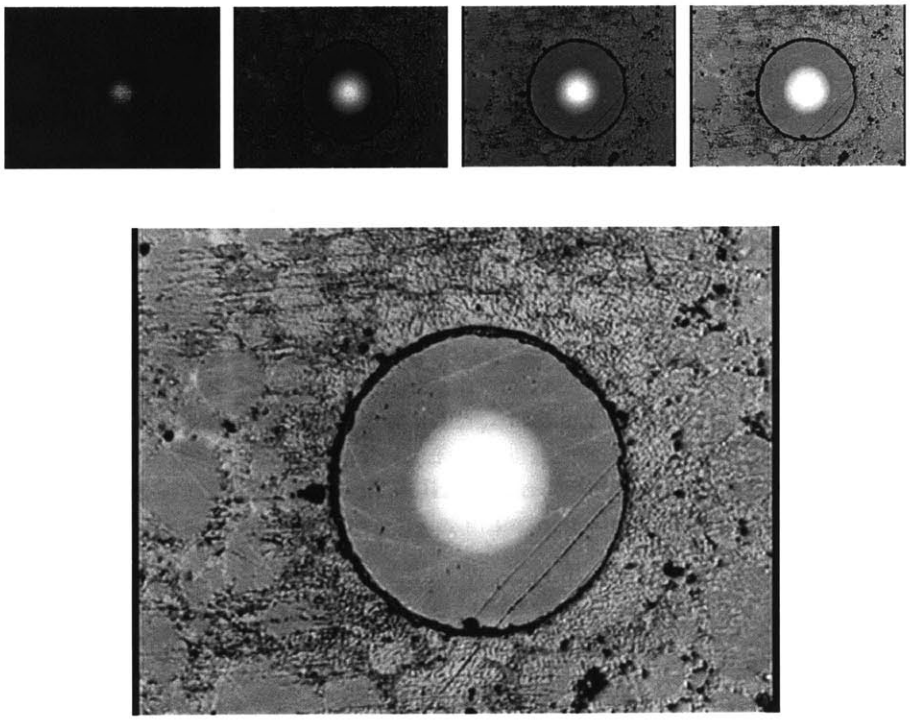

Figure 3-2: HDR MT fiber image

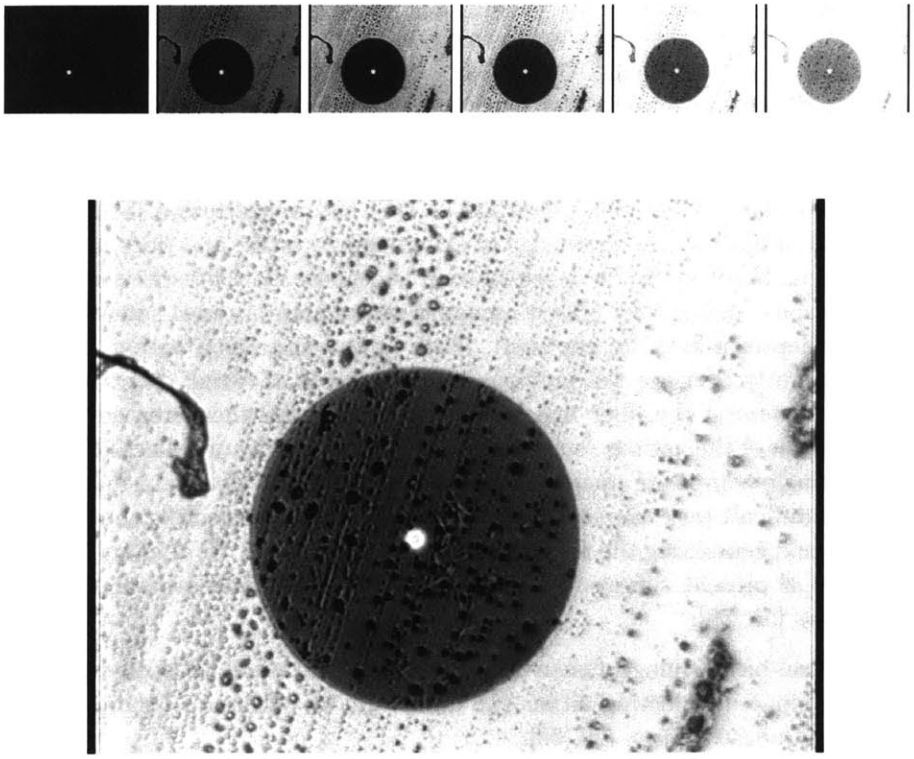

Figure 3-3: HDR ceramic ferrule fiber image

3.3.2 Extended Depth-of-Field Images

As previously discussed, depth-of-field (DOF) is calculated as

$$\text{DOF} = \frac{b}{2\text{NA} \times T_{\text{trans}}} \tag{3.1}$$

where b is the acceptable blur size at the image-plane, typically the CCD or CMOS pixel size, and NA is the object numerical aperture. The designed lens has NA = 0.22, b = 7 μm and T_{trans} = 15X, giving DOF = 1.1 μm. Shallow DOF is rather common in microscopy as greater magnification and NA result in a decrease in DOF. In our case the MT ferrules with protruding fibers and APCs require DOF up to 20 μm, which can not be captured within one image.

Many solutions have been presented to create high-depth-of-field (HDOF) images, deconvolution [54], phase masks [55], and image fusion [56]. Image fusion does not require knowledge of the imaging system and does not need any special hardware as do deconvolution and phase masks respectively [57]. It is a robust method for HDOF imaging where many images spanning the desired depth-of-field are captured. Each image contains a region of focus which slightly overlaps the previous image's region of focus, effectively *optically sectioning* the fiber image. HDOF images are then created by the aggregation of the various focused regions from the array of collected images into a single composite image where the entire field-of-view is in focus.

The difficult task in creating the composite image is selecting the focused regions and combining the results in an accurate manner. Li *et al* and Valdecasas *et al* present surveys of the various approaches and are summarized as follows [56, 58]:

- Pixel-based image fusion is where the same pixel in each image is compared, selecting either the maximum or minimum brightness for the focused image [59, 60].
- Neighbor-based image fusion is where the entropy or variance of a pixel neighborhood is compared in each image to select the "focused" pixel from the stack of images [61].
- Multiscale-based image fusion, essentially an extension to the neighbor-based image fusion, is where the neighborhood regions change size and the selection is usually based on the neighborhood with highest frequency content [47, 56]. For example, the discrete wavelet transform (DWT) is computed on each image in the focus stack. DWT coefficients are selected from each image via maximum absolute value [57],

and the fused image is computed from the inverse DWT from the selected DWT coefficients [62].

Experimentation with the various fusion methods quickly showed which algorithms work best for the FOFIM imaging system. Pixel-based image fusion inaccurately selected focused pixels because defocused fiber images turn either much darker or brighter than the focused image, as shown in Figure 3-4. Wavelet based multiresolution image fusion was fairly accurate at reconstructing a focused image. The wavelet method did show some fusion artifacts, for example Figure 3-5 shows an abrupt tonal discontinuity on the left side of the fiber. We took the general idea of the wavelet based method and slightly modified it to reduce reconstruction artifacts as discussed below.

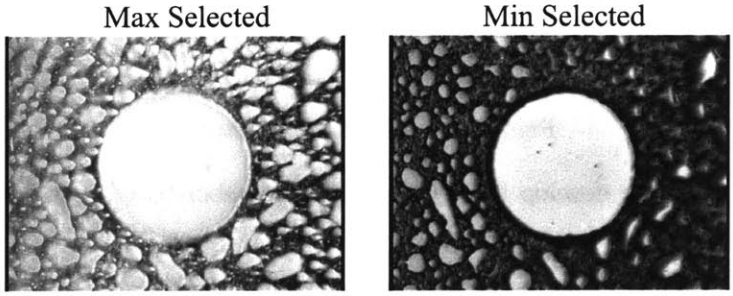

Figure 3-4: Pixel based focus selection

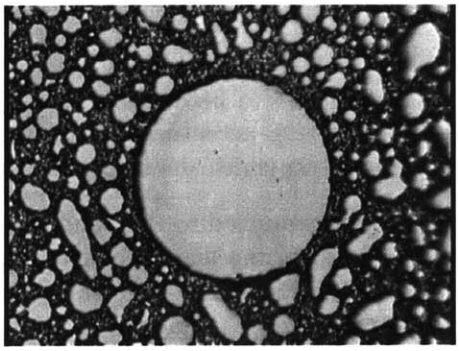

Figure 3-5: Multiresolution based focus selection using wavelets

It is well known that an "in focus" image has more singularities, sharp edges or points within the image, and therefore contain much higher frequency content than does a defocused image [63]. Flat surfaces are being

inspected, thus large regions of the image should be in focus at one time and these regions should be localized. For example an angled fiber endface will have focused regions that sweep across the ferrule endface as we proceed through the focus stack, see Figure 3-6.

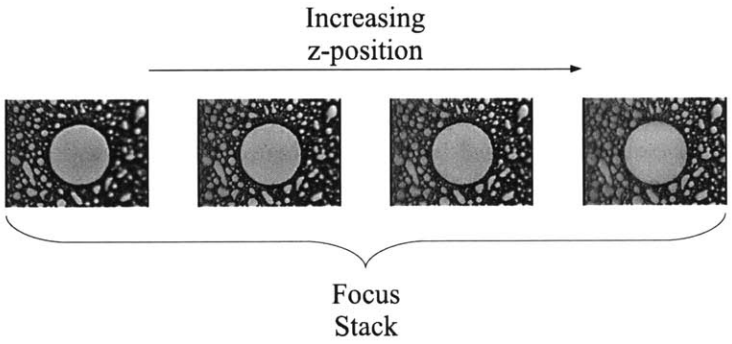

Figure 3-6: HDOF image stack

We therefore develop a FIFOM HDOF neighbor-based algorithm proceeds as follows:

1. Two images from the focus stack are selected, labeled as images A and B.

2. A low pass filter is applied to each of A and B, giving A_L and B_L respectively. This step removes spurious high-frequency content from noise.

3. A high-pass filter is applied to each of A_L and B_L giving A_{LH} and B_{LH} respectively. This step accentuates the high-frequency content (fiber edge, and defects) on which the inspection machine is focusing.

4. A second low-pass filter is applied to A_{LH} and B_{LH} giving A_{LHL} and B_{LHL} respectively. Most of the high-frequency items accentuated in the previous step are highly localized, typically 3-4 pixels wide. Low-pass filtering spreads the high-frequency results over larger regions which are used for selection.

5. A_{LHL} and B_{LHL} are subtracted to create the selection mask, $M = A_{LHL} - B_{LHL}$, where positive values select pixels from image A for better focus and negative values select pixels from image B for better focus.

This process is repeated for each image in the focus stack until the final focused image is created. A diagram of this algorithm is shown in Figure 3-7.

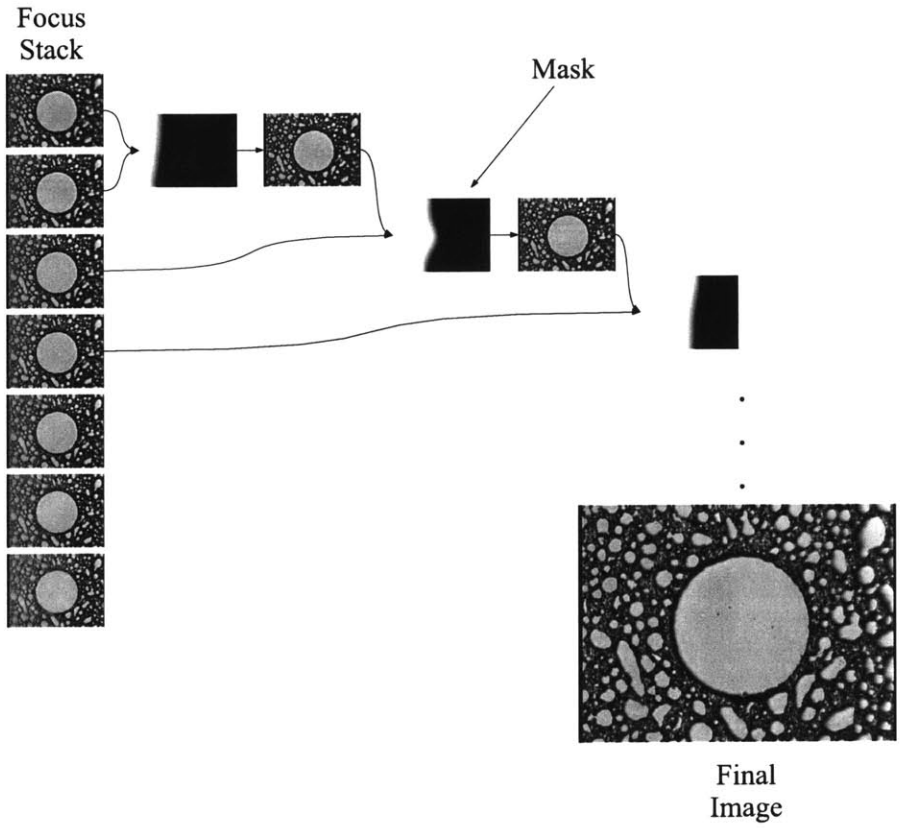

Figure 3-7: HDOF image capture

Processing a few hundred pictures shows this method to be quite robust and repeatable. Also, it is very fast as lends itself very well to multiscale methods. That is, the mask can be computed from scaled-down images to reduce computation time as we are searching for large areas being in focus. In the end, the proposed HDOF algorithm effectively gives unlimited depth-of-field, easily allowing the FOFIM to inspect APCs.

3.4 Fiber Detection

In order to detect defects on the fiber endface we must first find the fiber within the image and the boundary between the fiber-cladding and ferrule. Also, finding the fiber within the image allows for the inspection machine to recenter the system such that the each fiber being inspected is at the center of the field of view, this effectively extends the mechanical repeatability of each axis of motion, a more detailed discussion is found in Chapter 4. As previously discussed, many variables make this task difficult; fiber diameter tolerances, lit and unlit cores, and occluding defects such as scratches, oils and dust, as shown in Figure 3-8.

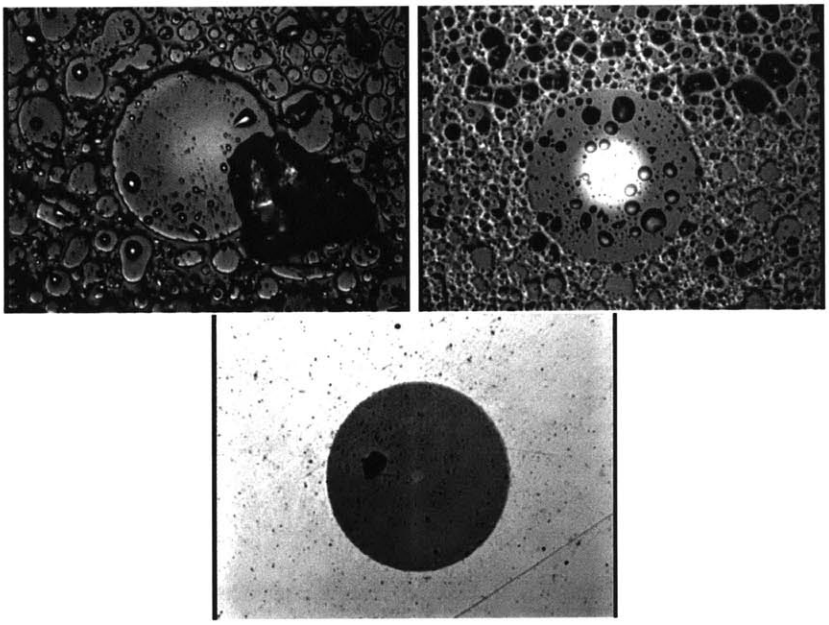

Figure 3-8: Fiber images with occluding dust and oil contamination

Many object recognition algorithms have been proposed, of which the majority are based on template matching. Template matching attempts to detect a known template image t of size $n \times n$ within an image f of size $N \times N$ via a measure of match. Many different measures of match have been proposed, a few of which are;

- Normalized Cross-Correlation. Pearson's normalized cross-correlation coefficient, r, is widely used for feature detection, where

$$r = \frac{\sum_{x,y} \left[f(x,y) - \bar{f}_{u,v}\right] \left[t(x-u, y-v) - \bar{t}\right]}{\sqrt{\sum_{x,y} \left[f(x,y) - \bar{f}_{u,v}\right]^2 \sum_{x,y} [t(x-u, y-v) - \bar{t}]^2}} \tag{3.2}$$

f is the image and the sum is over (x,y) under the window containing the template t at position u, v. $\bar{t}$ is the mean of the template and $\bar{f}_{u,v}$ is the mean of $f(x,y)$ under the window of the feature. A perfect match yields $r = 1$ and if the image and template are completely uncorrelated r=0.

Problems with normalized cross-correlation have previously been published [64, 65, 66], and are summarized as: (1) It is computationally demanding, although Lewis provided a significant speed up with minimal loss in accuracy [67]. (2) It is highly sensitive to image distortion such as vignetting, skewing or pincushon. This does not pose a difficult problem for the FOFIM as optical tests show negligible image distortion. (3) r may be unaffected by occlusions [64], which is actually very helpful to detect fibers with significant defects, as the template image may not exactly match the fiber in the image.

- Variance of Difference or Root Mean Square Intensity Difference Measures: There are many different intensity-difference measures which calculate pixel intensity differences between the template and image [68]. For example, the root mean square distance metric is typically found as

$$d_{rms} = \sqrt{\frac{1}{n} \sum_{A} (f_{ij} - t_{ij})^2} \tag{3.3}$$

and the variance of difference is found as

$$d_{vod} = \frac{n \sum_{A} (f_{ij} - t_{ij})^2 - \left[\sum_{A} (f_{ij} - g_{ij})\right]^2}{n^2} \tag{3.4}$$

The minimum of d_{rms} or d_{vod} corresponds to the position with the best match between the template and image. In practice, intensity difference measures are computationally quick, but are highly sensitive

to sensor noise, image intensity changes and image contrast changes.

- Sequential Similarity Detection Algorithms (SSDAs): SSDAs recognize that cross correlation and intensity difference methods perform an exhaustive search which is computationally expensive. SSDAs compute the measure of match in random order across the image while a running error measurement is used as a Monte Carlo estimate to determine if the last match location is near the maximum of the measure of match [69, 67].

  Problems with SSDAs are that they inherit all the drawbacks of the match measurement calculation (normalized cross-correlation, RMS intensity difference, etc), and they are not guaranteed to find the global maximum because it is not an exhaustive search. Also determination of the optimal threshold from the Monte Carlo estimate is non-trivial [67].

- Hough Transform. The Hough Transform (HT) is a standard image processing technique used to find various shapes within an image. Bennet *et al* have shown an efficient implementation for detecting ellipses which is well suited for finding the fiber endface within an image [70]. Detailed discussion of the HT is discussed later in Section 3.5.2, but for now, its major drawback is its significant computation time.

- Integrodifferential Operators: Daugman introduced an integrodifferential operator for detecting a human iris [71]:

$$\max_{(r,x_o,y_o)} \left| G_\sigma(r) * \frac{\partial}{\partial r} \oint_{r,x_o,y_o} \frac{I(x,y)}{2\pi} d\theta \right| \tag{3.5}$$

  The operator simply transforms the image I from Cartesian to polar coordinates where $x = r\cos\theta$ and $y = r\sin\theta$ and integrates about θ to give a radial image. The maximum radial derivative corresponds to the best fit circle. A Gaussian filter G is used to smooth the data to reduce spurious results from noise.

  In practice this "circle detector" is computationally expensive as many radii and integrodifferential centers (x_o, y_o) have to be computed. Also this does not work well for ellipses or circles with large defects upon the edge.

In detection of fiber position and the edge between the fiber-cladding and ferrule, it was found that template matching algorithms work well at finding the general location of the fiber even with significant defects such

as dust or scratches; the problem lies in detection of the fiber cladding and ferrule boundary. Template matching algorithms, as the name implies, only match a template to an image, they do not explicitly find the boundary between the fiber-cladding and ferrule. Due to variances between the fiber and template images, template matching is only practical for finding the general location of the fiber.

3.4.1 Solution

We present a fiber detection algorithm based on template matching algorithms and extend it through morphological operators and the Hough Transform to detect the boundary between the fiber-cladding and ferrule. It proceeds as follows:

1. The image f is scaled down to reduce computational requirements, then Lewis's normalized cross correlation between the template t and image f quickly finds the general location of the fiber. As shown in Figure 3-9, the point corresponding to maximum correlation between t and f is found near the center of r. Even though the fiber image does not quite match the template, especially with the dust and oil defects, normalized cross correlation detects fiber position to within $\pm$ 10 pixels (6.25 μm for the FOFIM Optics).

   In the absence of a fiber, the normalized cross correlation produces low r values everywhere, thus giving a clear indication that no fiber is within the image. The algorithm returns an error message alerting the system to the problem.

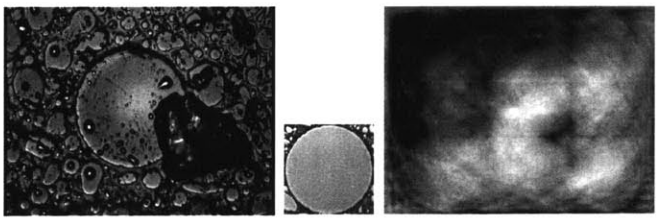

(a) f (b) t (c) r

Figure 3-9: Correlation results

2. The (x,y) position where r is maximum corresponds to the best matching region between f and t. The image is cropped to this best matching

region to reduce computational requirements for the fiber-cladding and ferrule edge detection (the next step), as shown in Figure 3-10.

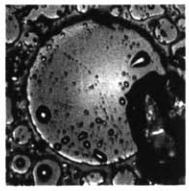

Figure 3-10: Cropped image

3. The cropped image is morphologically opened, which detects the boundary between the fiber and ferrule by preserving fiber regions while eliminating the smaller defects and ferrule region.

   Morphological operations are used to detect forms within an image by detecting boundaries [72, 73] and morphological opening is an erosion followed by a dilation using the same structuring element for both operations. Symbolically:

$$(A \ominus B) \oplus B \tag{3.6}$$

   Where A is the image to be operated on and B is the structuring element determining pixel *connectivity*. The symbol $\oplus$ denotes dilation defined as:

$$A \oplus B = \{x : \hat{B}_x \cap A \neq 0\} \tag{3.7}$$

   and morphological erosion, denoted by the symbol $\ominus$, is defined as:

$$A \ominus B = \{x : B_x \subseteq A\} \tag{3.8}$$

   Where B_x denotes the translation of B by x, $B_x = \{c : c = a + x, \text{for } a \in A\}$, and $\hat{B}$ denotes the reflection of B, $\hat{B} = \{x : x = -b, \text{for } b \in B\}$.

   4-way connectivity refers to the pixel's four closest neighbors and 8-way connectivity refers to the pixel's eight nearest neighbors (Figure 3-11). Any arbitrary structuring element is possible, but as they grow, so do computational requirements.

   For example, Figure 3-12 shows erosion and dilation results (the dashed rectangle) when B is a disc shape and A is a rectangle. The dilation

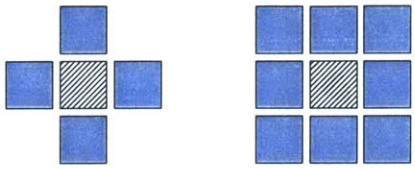

Figure 3-11: Morphological structuring elements

and erosion operations are very similar to a convolution mask [74, 75].

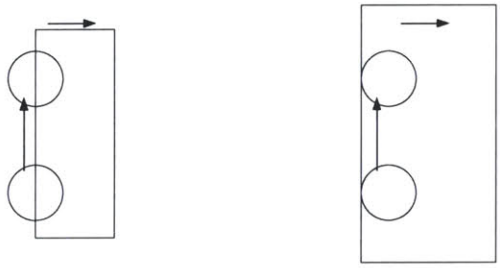

(a) $A \oplus B$ (b) $A \ominus B$

Figure 3-12: Morphological erosion

Results of the grey-level morphological opening of the cropped fiber region are shown in Figure 3-13.

4. The morphologically opened image is then passed through an auto-threshold algorithm to differentiate the region enclosed by the fiber and the ferrule. While there have been many different auto-thresholding methods suggested [76, 77], we use the "Isodata" method presented by Ridler and Calvard [78]. The Isodata auto-thresholding assumes that the greyscale image is distributed as a bi-modal Gaussian, and iteratively calculates the threshold value to separate the two Gaussian modes.

   This algorithm works very well for most fiber images as the average fiber grey-value is different than the average ferrule grey-value. The auto-threshold easily selects the lighter regions which correspond to the fiber and also the glass in the ferrule epoxy matrix, as shown in

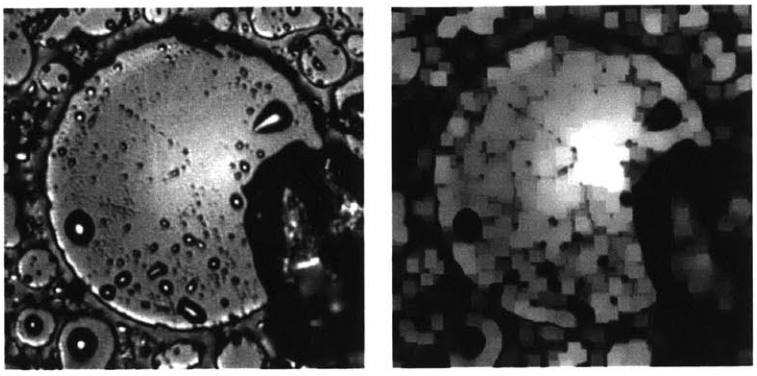

(a) Fiber Image (b) Morphologically Opened Image

Figure 3-13: Opening of fiber image

Figure 3-14.

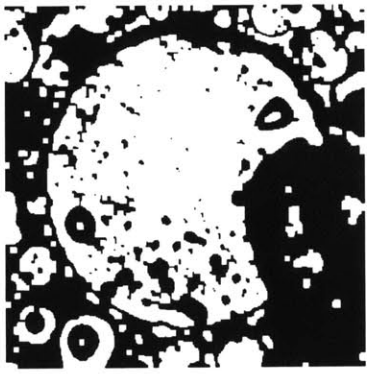

Figure 3-14: Auto-threshold image

5. The fiber endface is definitely the region with largest area, this will always be the case unless the fiber is not in the image or significant defects block the fiber. As previously discussed, the normalized cross correlation flags images without a fiber. For the second case, nominal fiber dimensions are known, thus nominal fiber area is known. If significant defects are present then the total area calculated is drastically reduced and raises a flag that the fiber is too dirty to be reliably inspected. Otherwise the fiber-cladding area is then detected as the region with the largest area, and is cropped to select only that region,

as illustrated by Figure 3-15.

Figure 3-15: Fiber cladding mask

6. Next a Hough Transform is used to interpolate the fiber edge. The defect in the lower right corner of Figure 3-15 drastically affects the fiber cladding mask. The best fit ellipse computed via HT is used to interpolate the fiber edge, as shown in Figure 3-13(a). The Hough Transform is a well known feature detection tool, and detailed discussion is deferred to section 3.5.2 [79, 80].

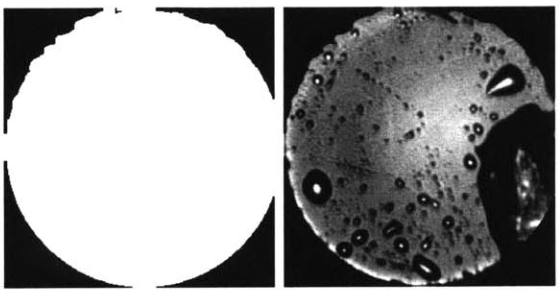

(a) Fiber Mask from HT (b) Masked Fiber

Figure 3-16: Fiber cladding mask after Hough Transform

Now that we have found the fiber, we begin the defect detection routines.

3.5 Defect Detection

Repeatable and robust defect detection is difficult due to many variables: varying intensities across the fiber endface (some fiber endfaces may have curvature causing an intensity gradient), variances in intensities between

different fiber connectors, lit-cores, system noise, and uneven illumination from the inspection system. Many different algorithms have been proposed to overcome these problems to detect defects. A short survey of general defect detection algorithms follows:

- Thresholding: A naive algorithm assumes defects have greater or lesser intensities than the "good surface" which has uniform intensity, and a threshold value is then selected such that all pixels above or below correspond to a defect.

  More advanced dynamic and adaptive thresholding techniques have been developed to account for gradual changes in the "good surface's" intensity or varying noise levels. Other methods rely on statistical models of the images to select the threshold value [76, 77, 78]

- Filtering: A simple approach attempts to increase the defects contrast while minimizing the image content of the texture being inspected. The premise is that the "good surface" is well known and so is its frequency content. Defects should have intensities that are random and quickly changing. Filtering attempts to select only the random quickly changing frequency content generated by the defects [81, 82, 83, 84].

- Morphological Operations: As previously discussed, morphological operations attempt to determine structure and shape of an image through transformations with a user-defined structuring element. Various morphological operations have be used to detect defects [82, 85].

- Fourier and Wavelet analysis: As in the filtering methods, Fourier and wavelet methods assume that we are inspecting a known image structure, i.e., that we know the typical frequency content of a "clean" image and that defects are detected as anything that disrupts the known frequency content [86].

- Active Appearance Models: Active appearance models use principle component analysis to model 2D shapes with a small number of parameters. These models are trained on a set of known "good" images and then are applied to inspection images to detect the various components of the image [87].

These are just a few of the methods currently being discussed, the reader is invited to read any image processing hand book or machine vision and image processing journals. No single algorithm is capable of detecting all

defects, as each algorithm has its trade-offs. It is left to the user to experiment with many different algorithms, perhaps modifying and extending them to suit the problem.

3.5.1 Particle Detection

We now present a simple particle detection algorithm using an edge detection filter followed by two enhancement rules.

1. Edge Detection: There are many edge detection filters, the most well known were proposed by Canny, Sobel, and Prewitt. The general approach is the image is smoothed with a Gaussian filter, reducing spurious high-frequency content, imager noise and quantization effects [84] (Figure 3-17(b)). A derivative filter computes the gradient magnitude (Figure 3-17(c)) and non-maximal suppression determines edge location with sub-pixel accuracy via interpolation as shown in Figure 3-17(d). Hysteretic thresholding then selects all edge pixels above threshold T_1 and their connected edge neighbors with pixel value above threshold value T_2 as shown in Figure 3-17(e).

   Passing simulated fiber images with known defects through the edge detection routine easily allows us to iteratively determine the appropriate blurring and threshold levels that give 1 μm defect detection. It also allows us to see output sensitivity to noise.

   At this point we have detected all defects upon the fiber endface, we must now determine if the fiber passes or fails by quantifying the them, determining their area, location and contrast. It is desirous to determine the defect area as accurately as possible. As shown in Figure 3-17(e) edge detection simply finds the border of the defect, thus there will only be a ring around it. Filling in the ring accurately determines the defect size and area. A few fill tests are computed to accurately determine defect area:

   - Defect Fill Test 1: Each defect is passed through what is known as a reconstruction operator which fills in bounded regions (i.e. a ring is filled to become a circle). Repeated application of the morphological dilation operator upon the negative of the edge image performs this operation very quickly. Sometimes the shape is not fully closed, (e.g., a U-shape instead of a circle): To combat this, the two ends are extrapolated to see if they intersect within a few pixels and then the shape is filled. Figure 3-18(b) shows

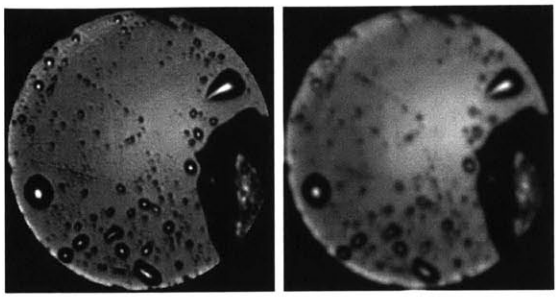

(a) Fiber Image (b) Blurred Image

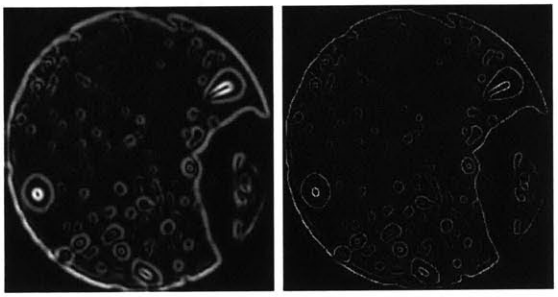

(c) Gradient Magnitude (d) Non Max Suppression

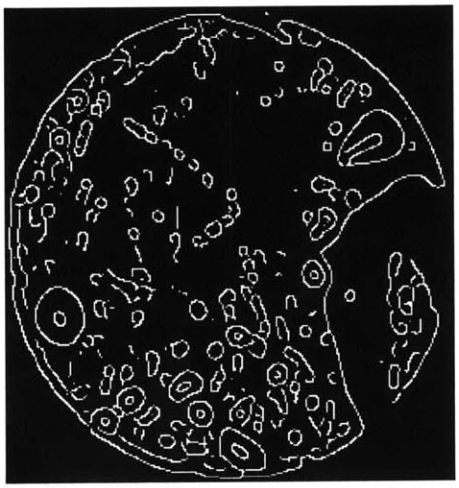

(e) Hysteretic Threshold

Figure 3-17: Edge detection

an example with the defects filled by this method, there are still quite a few defects left that need to be filled in.

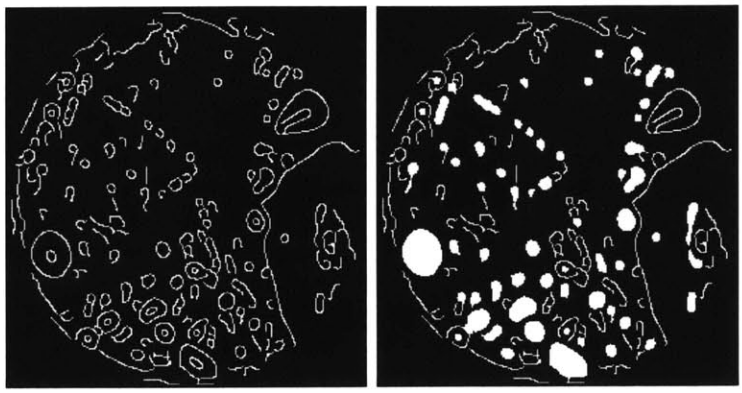

(a) Before Defect Fill Test 1 (b) After Defect Fill Test 1

Figure 3-18: Defect fill test

- Defect Fill Test 2: The contrast ratio of each defect not filled by the previous test is computed. If there is a large disparity in intensity between the defect and its surroundings (high contrast), the area is thresholded with the average defect intensity as the threshold value. The threshold area is morphologically reconstructed using the defect edge as a marker to detect the entire defect area. Figure 3-19(b) shows that this second test is able to effectively fill in the interior of most of the defects.

For the rest of the defects, we use the industry standard of using the smallest circle enclosing the entire defect as the defect area. the rest of the defects either are not fillable (scratches), or are of such low contrast that they pose no threat to fiber cable performance.

3.5.2 Scratch Detection

The Hough Transform [80] is an effective statistical method for object detection even in the presence of significant noise and object occlusion. A drawback is that the transformed parameter space grows rapidly along with computation time and as accuracy requirements increase [88]. Fortunately, fiber endface inspection only requires scratch slope detection to within $\pm 1°$, computing the HT of a 640 X 480 image is fairly easy for today's PC's.

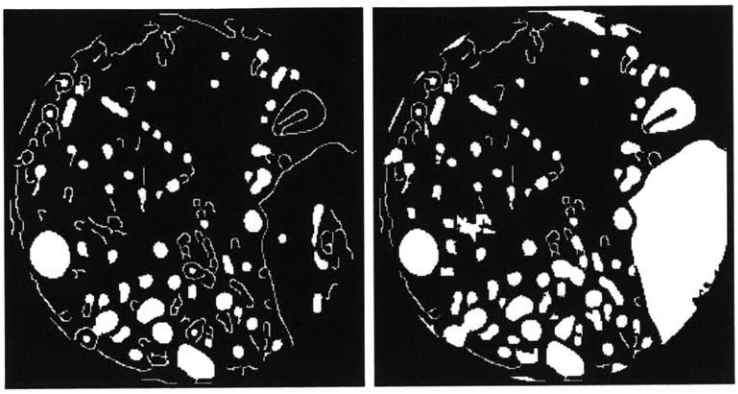

(a) After Defect Fill Test 1 (b) After Defect Fill Test 2

Figure 3-19: Defect fill test 2

Hough Transform Algorithm

The general approach is to compute the Hough Transform (HT) of the binary image G, and search through HT(G) for statistically improbable maxima. The final step inverts $\text{HT}(G)_{\text{maxima}}$ to find the lines in the original image G.

The HT line detection algorithm developed by Duda and Hart [79] was implemented. Duda and Hart show that a straight line can be parameterized by the angle θ of its normal and its algebraic distance ρ from the origin, as shown in Figure 3-20. This convenience avoids the complication of an infinite slope in the standard slope-intercept notation $y = mx + b$.

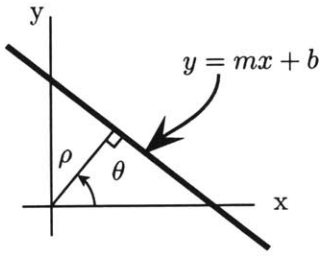

Figure 3-20: (θ,ρ) parameterization

Properties of this transformation can be summarized as:

- a point in the image plane maps to a sinusoid in the Hough plane

- a point in the Hough plane maps to a straight line in the image plane
- points from a straight line in the image plane map to sinusoids through a common point in the Hough plane
- points on the same sinusoid in the Hough plane map to lines through the same point in the image plane

We proceed as follows: Given the discrete binary image G, each image point (x_i,y_i) in G maps to a sinusoidal curve via Equation 3.9. We have an accumulator matrix A where rows specify the discretized increment angles of θ and columns specify the accumulation of the calculated ρ's.

$$\rho = x_i \cos\theta + y_i \sin\theta \tag{3.9}$$

Given the image points (x_i,y_i), we sweep θ through 0 to π, while accumulating ρ. For uniformly distributed points, each point in the accumulator should have a Poisson distribution count with mean proportional to line length . Storkey admits that this is not strictly correct due to the interdependence of accumulators at different angles, but in practice holds very well [89]. Thus if we have *a priori* information of our point distribution, lines can accurately be detected by inspecting the accumulator count and comparing with the probability associated with that point.

Hough Transform inversion requires finding the statistically improbable points in HT(G). Their location in the (θ,ρ) plane parameterizes the line in the image space as shown in Figure 3-20.

An example binary image, its Hough Transform and Inverse Hough Transform can be seen in Figure 3-21. Despite the high level of noise in the image it is clear that there are five distinct lines in the image. One can easily see the five corresponding bright spots in the accumulator even though it is not normalized. The HT itself is very simple to implement. The more interesting parts of the problem are generating an ideal binary image from an 8-bit greyscale image and finding the local maxima of HT(G).

Binary Image Generation

How do we accurately convert the greyscale image from a typical inspection camera to a binary image while retaining all scratch information? The first thought that comes to mind is edge detection followed by a threshold. System variability, lighting, defocus, CCD noise, etc., makes it very difficult to detect scratches with high repeatability using a derivative filter

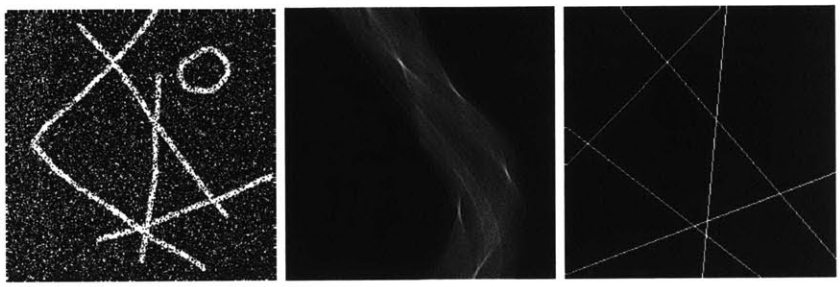

Binary Image G $\quad$ HT(G) $\quad$ HT^{-1}(HT(G))

Figure 3-21: Binary image, Hough Transform and inverse HT

and thresholding, as the derivative filter is highly sensitive to the mentioned variabilities.

Also, edge detectors output two responses to a scratch as there are two discontinuities per scratch, hence there will be two closely spaced points in (θ,ρ) space. We would like to avoid this if possible, as most scratches on fiber endfaces tend to be parallel, i.e. scratches created by dragging the ferrule along a rough object, and it can be difficult to determine which edge belongs to which scratch. An example of a Canny [84] edge detection output can be seen in Figure 3-22.

Kovesi has written some very interesting papers on implementation of phase congruency algorithms [83]. Phase congruency assumes that objects tend to have uniform phase; that is, they are highly ordered in the Fourier Domain. For example, all of the Fourier components of a square wave are in phase, thus detection of the areas with congruent phase equates to detecting an object. The result is a dimensionless number ranging from 0 to 1 that provides an absolute measure of significance of the object. This allows for much simpler threshold selection.

There are a few drawbacks to the phase congruency algorithm, mainly that calculation of the phase congruency is ill conditioned if there are few frequency components or if the all Fourier components are very small, and the phase congruency algorithm is highly sensitive to noise. An example of the phase congruency detector output can be seen in Figure 3-23. It shows that image noise is quite low and is not detrimental to the phase congruency detector output and that fairly faint scratches are detectable.

It is interesting to compare the results from the edge detector and phase congruency detector. The phase congruency detector places a single mark directly on top of the scratch, while the edge detector places two marks

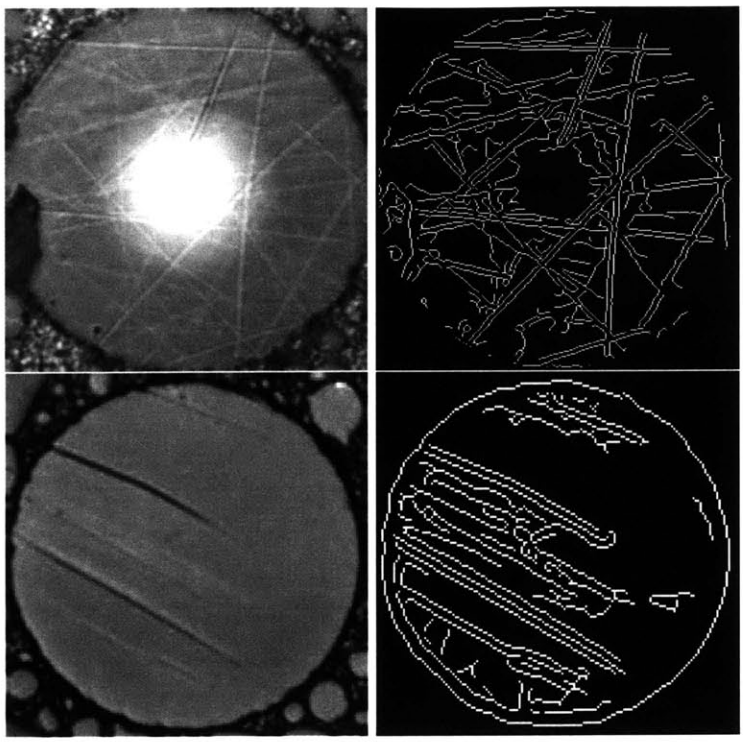

Figure 3-22: Greyscale image and Canny edge detector

slightly displaced from the two edges of the scratch, a side-effect of the blurring process that most edge detectors implement. Also, since the phase congruency detector output is an absolute measure of significance, it is much easier to automatically threshold. For the edge detector, low contrast objects require careful threshold selection in order to minimize the noise in the resulting binary image.

Edge detectors such as Canny [84], Sobel, Marr and Hilbreth [90] are computationally quick. The phase congruency detector is much more complicated because the phase must be measured in each possible direction to ensure accurate corner detection [83], thus computation time is much longer. For the inspection system, accurate and repeatable results are desired, so Kovesi's phase congruency algorithm [91] was used despite its lengthy computation time.

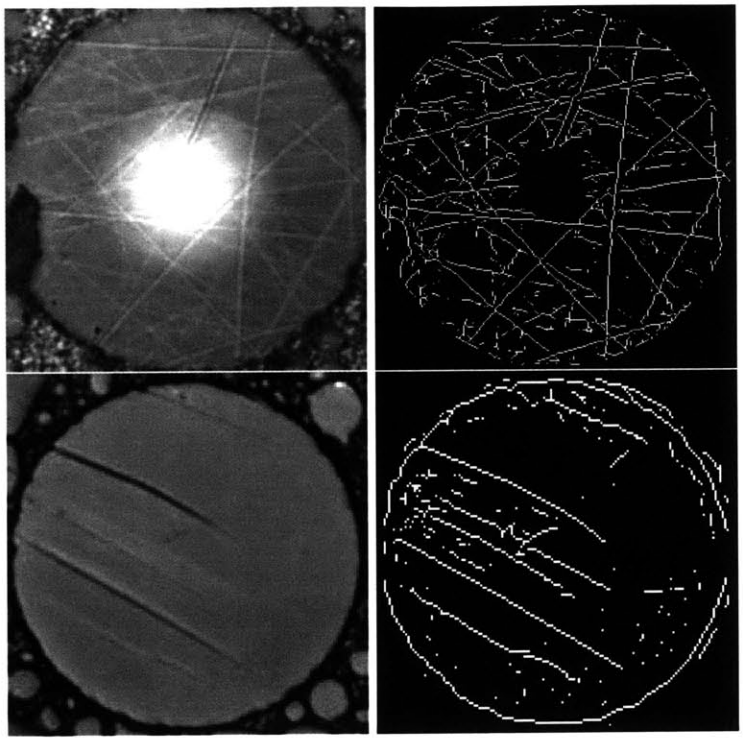

Figure 3-23: Greyscale image and phase congruency detector

Finding Local Maxima

Longer scratches accumulate more "votes" in the accumulator than shorter scratches. Searching for the maxima of $\mathrm{HT}(G)$ without proper normalization will result failure to detect shorter scratches. As a result, we must compute the probability at each point in the transformed image.

Let us assume we can obtain an ideal binary image G_i with uniform noise. An ideal binary image contains data for all scratches to be detected. Accumulator probability A_p is simply the appropriately scaled HT of a pure white image of same dimension as G_i.

$$A_p = \mathrm{HT}(W) \times \frac{\max[\mathrm{HT}(n)]}{\max[\mathrm{HT}(W)]} \tag{3.10}$$

where W is a white image with same dimensions as G_i, n is an image of

uniform noise without scratches whose total white pixel sum is equal to that of G_i's. To normalize $\mathrm{HT}(G_i)$, we subtract the image inversion[1] of A_p from $\mathrm{HT}(G_i)$ to obtain

$$N = \mathrm{HT}(G_i) - A_p^{-1} \tag{3.11}$$

Where N is our normalized $\mathrm{HT}(G_i)$. We can now search the surface N for its maxima. There are a few methods for doing this:

- Thresholding: Thresholding N works fairly well as can be seen in Figure 3-24. The maxima is found for each area segmented by the threshold operation. If two peaks are very close, the threshold will probably not segment the two peaks, resulting in only finding a single line when we should find two lines.

- Differentiation and solving for zero crossings: There are inherent discontinuities in the HT image because it is based upon the summation of sinusoidal curves. Consequently, many zero crossings are obtained that don't correspond to peaks in N. An example of a HT that has been differentiated can be seen in Figures 3-24 and 3-25. It is clear that it is much more difficult to determine which zero crossings correspond to the maxima of N.

- Watershed: This is a technique for finding local maxima and minima. It models a greyscale image as a topographic map where intensity is linearly proportional to elevation. Watershed lines and catchment basins (local minima) are found by determining where water would flow over such a topographic map. To find the local maxima, simply invert the image and apply the watershed algorithm. Vincent and Soille present an efficient algorithm which can be found within the MATLAB image processing toolbox [92]. An example of scratches detected by the watershed algorithm is shown in Figure 3-24.

Finding the zero-crossings of the derivative of the HT is not robust, so it is does not work well for this system. Thresholding is robust and is very fast while the watershed method appears to be very good at finding local maxima, especially those with nearby neighbors. The main problem with the watershed algorithm is that it finds maxima that are not statistically significant, which is clearly not desirable.

[1] $X^{-1} = \max(X) - X$, for image inversion.

We implement a threshold plus watershed algorithm to robustly detect the appropriate local maxima. That is, threshold the HT so that watershed is only calculated on statistically improbable points. As one can see in Figure 3-25, the threshold plus watershed procedure detects the 6 scratches correctly whereas the threshold only finds 5. The watershed operation allows for detection of closely spaced local maxima. For the inspection system, accuracy and repeatability are the most desirable traits, thus threshold plus watershed was selected even though it is somewhat slower than simply thresholding.

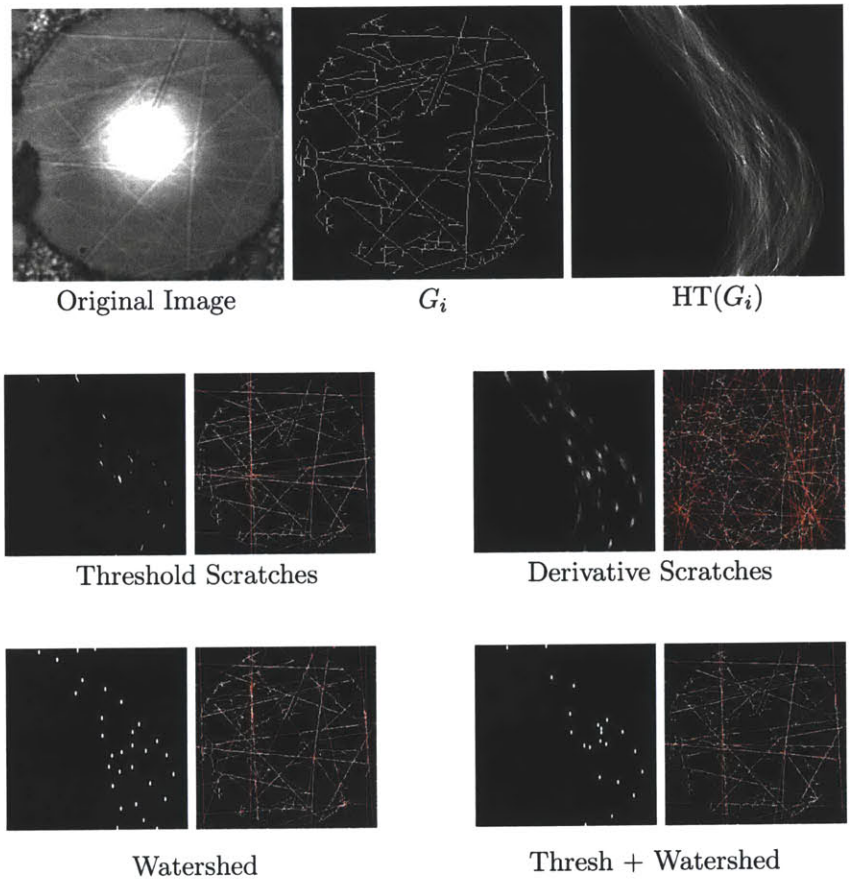

Figure 3-24: Maxima of HT via thresholding, derivative, and watershed, and their respective scratch maps

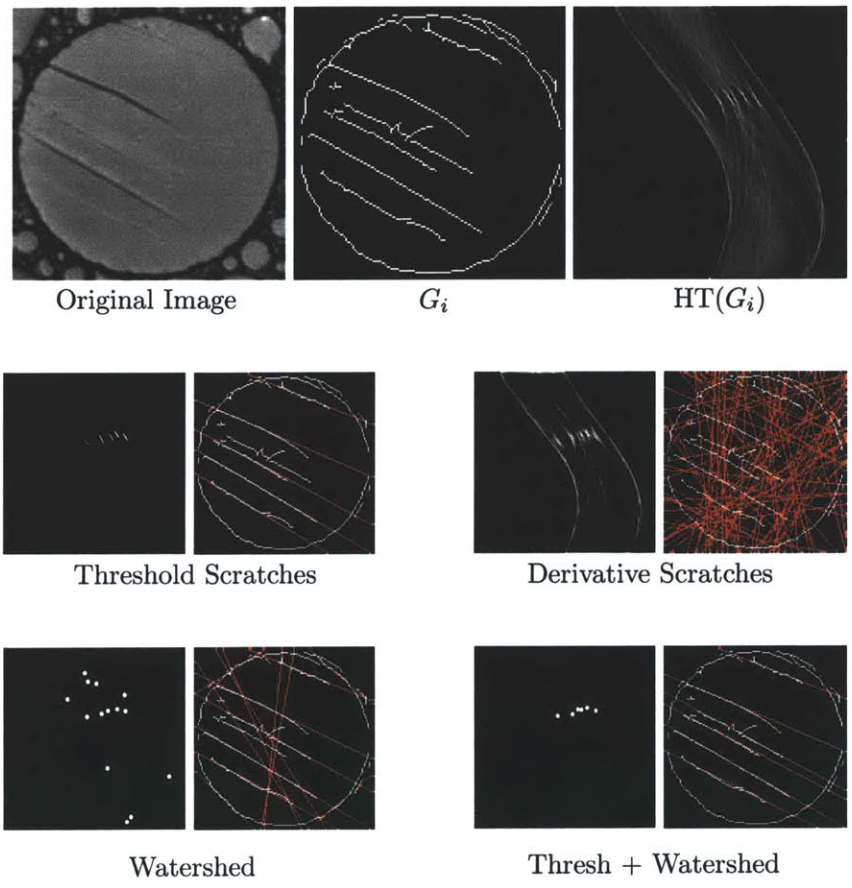

Figure 3-25: Maxima of HT via thresholding, derivative, watershed, and thresholding + watershed and their respective scratch maps

3.6 Summary and Future Work

We've presented a few methods to accurately and repeatably detect defects upon the fiber endface. A simple method providing virtually limitless HDR images was shown to be quick and robust, and for future work it may be desirous to implement a compression algorithm to display the information on low dynamic range media such as print and computer display for better user interaction.

HDOF imaging extends the inherent 1 μm depth-of-field limit to inspect well beyond 20 μm needed for angle polished connectors. For future work we could implement a better wavelet thresholding algorithm to reduce fusion artifacts.

Through capturing HDR and HDOF images all information needed to detect all defects is available. To detect the defects, the fiber endface must first be found. A quick and robust algorithm was presented for detecting the fiber-cladding and ferrule interface by combining the best attributes of template matching, morphological operators and the Hough Transform.

Endface defects are quickly detected via an edge filter and application of morphological operators. For scratch detection it was found that the HT is a robust method for detection of objects within binary images. Its implementation is straightforward, but can be rather slow for large images. Fortunately, we are only computing upon 640 X 480 pixel images and it only requires $\pm 1^\circ$ angular resolution. More interesting are the pre- and post-processing of the images; that is, generating the binary image G_i from the HDR image and searching for local maxima within the HT.

We found that despite its computational complexity, phase congruency is a highly accurate and repeatable algorithm for generating G_i for our fiber images. It is not without its flaws (especially high sensitivity to noise) but the HDR images effectively reduce the system noise via averaging across multiple exposures. Thus, in practice this is only a problem for the faintest scratches, which are not likely to degrade fiber optic cable performance. Local maxima searching within the HT was implemented as a combination of thresholding plus a watershed operation. Thresholding ensures only those points of low probability are searched and the watershed algorithm finds multiple local maxima that are near each other.

For future work, an algorithm that measures other parameters such as thickness and the beginning and ending points of the lines is needed, as the HT only measures the line's (θ,ρ) parameters. Perhaps use of the phase output from the phase congruency algorithm in conjunction with an edge detector could be put to good use here.

Chapter 4

Machine Design

4.1 Introduction

A bench-top inspection test bed was developed for experimentation and evaluation of with many different actuator and feedback techniques before any design work began on the portable inspection system. This test bed was key in developing a practical FOFIM for in-situ inspection as any new actuator or control idea could be quickly implemented and evaluated. It provided us experience running a FOFIM, and we could quickly find any faults and spot the *must haves* and *would likes.*

The bench-top system shown in Figure 4-1, has three linear axes driven by stepper-motors and leadscrews to provide Cartesian positioning of the ferrule to be inspected. The $\hat{x}$ and $\hat{y}$ axes are co-planar to the ferrule end-face and point along fiber-to-fiber motions and ferrule-to-ferrule motions depending on the ferrule orientation. The $\hat{z}$ axis runs co-linearly with the fiber, pointing along the focus direction. Through experimental verification via repeatability and resolution tests described later in the chapter the test bed performance capabilities are as follows:

- repeatability = $\pm 25 \mu$m
- resolution = 5 ± 20 μm
- backlash = 100 μm

The camera, objective and lighting are mounted upon a second independent z axis to experiment with different focus actuators (shape memory alloys, voice coil and stepper-motors) and feedback sensors (photodiode and

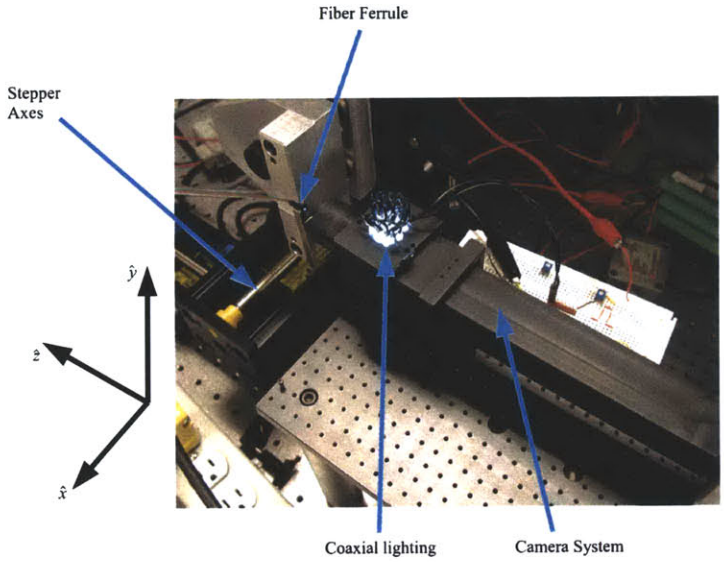

Figure 4-1: Bench-top test bed

magnetic field sensors). Despite its limited performance, it is sufficiently adequate for automated ferrule inspection.

An initial prototype FOFIM for in-situ backplane-inspection was developed, as shown in the photograph in Figure 4-2. This first prototype served as a test bed for bearing experimentation on the three axes. The z-axis preload-gib/camera-tube bearing and the x-axis vee-wheel/rail-bearing system carried over to the second prototype design.
The second prototype FOFIM development, design and verification tests are detailed in this chapter. Design details are included for bearings, dynamic models, and error budgets as well as experimental verification. Key functional requirements are considered in the next section.

4.2 Mechanical Functional Requirements

4.2.1 Physical Envelope Requirements

A simple diagram of a large card-based system such as a network router or super-computer can be seen in Figure 4-3. There is no current standard on daughter-card size or router size. The FOFIM must be quite compact to fit within all possible daughter-card slots, thus the total inspection machine

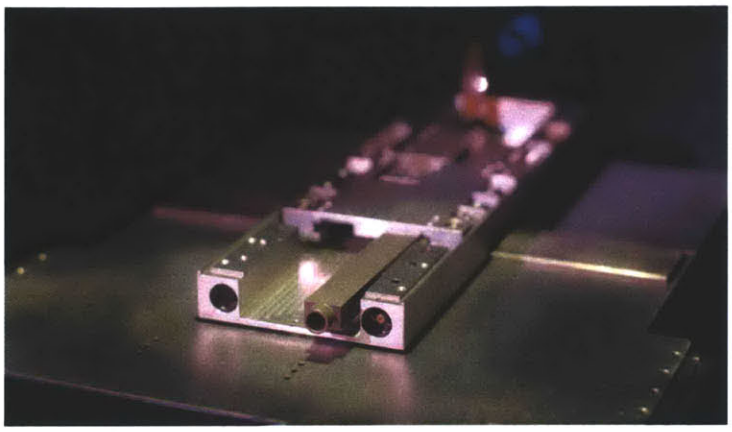

Figure 4-2: First prototype

thickness should be no larger than 15 mm in order to be placed in the narrow daughter-card slots.

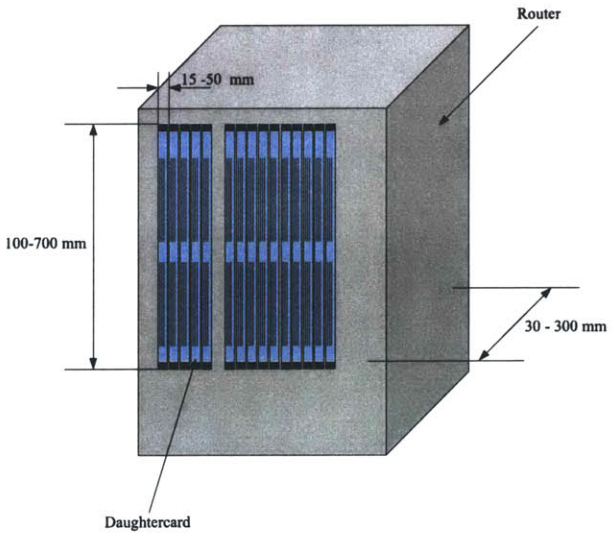

Figure 4-3: Router daughter card envelope

FOFIM width should be as narrow as possible in order for it to inspect connectors near the top and bottom of the daughter-card slot within the backplane as indicated by Figure 4-4. After some discussion with potential

customers, it was determined that a 40 mm gap on the top and bottom of the daughter-card is acceptable and therefore the FOFIM width should be no larger than 80 mm.

FOFIM length in the $\hat{z}$ direction should also be minimized in order to maintain portability, but this axis has the most leeway as the FOFIM can protrude outside the front of the card cage. Most users would not object to a 300 mm length along $\hat{z}$, thus the entire FOFIM should fit within a 15x80x300 mm envelope to inspect most fibers in most systems.

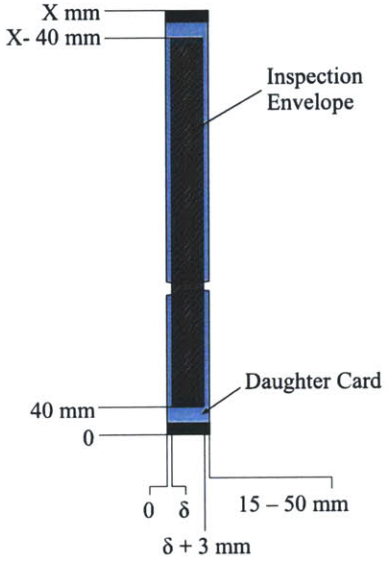

Figure 4-4: FOFIM inspection envelope

System Requirement	Value	Units
Physical Envelope	15 x 80 x 300	mm
X-axis Travel Range	700	mm
X-axis Resolution	5	μm
X-axis Repeatability	20	μm
X-axis Settling Time	0.05	second
X-axis Minimum Velocity	1	mm/second
Y-axis Travel Range	3.5	mm
Y-axis Resolution	5	μm
Y-axis Repeatability	20	μm
Y-axis Settling Time	0.05	second
Y-axis Minimum Velocity	1	mm/second
Z-axis Travel Range	24	mm
Z-axis Resolution	0.5	μm
Z-axis Repeatability	25	μm
Z-axis Settling Time	0.05	second
Z-axis Minimum Velocity	1	mm/second

Table 4.1: Mechanical Performance Requirements

4.2.2 Performance Requirements

Table 4.1 summarizes the mechanical performance requirements for the FOFIM, and detailed discussion of each requirement follows.

Range

- As shown in Figure 4-3, the FOFIM must traverse up to 700 mm along $\hat{x}$ in order to inspect all connectors along the length of the backplane.

- Figure 4-5 shows a typical angled end-face MT connector with width by height of 2.5 x 6.4 mm. The two large holes at the opposite ends are for alignment guide pins between mated ferrules. Their distance is typically 4.6 mm. The 12 holes between the alignment holes position the optical fibers and are spaced 250 μm apart, thus the inspection machine must travel at least 3.5 mm in the $\hat{y}$ direction to account for connector location tolerances. There are also standard arrangements for up to 72 fiber MT connectors. See the MT connector specification [93] for further details.

- Ferrule lengths have a manufacturing tolerance range of about 1-2 mm along the axial direction. Also, some connectors have a protective shroud that must be retracted by pressing back the shroud face roughly 6 mm, thus the inspection machine travel along the $\hat{z}$ must be on the order of 10 mm.

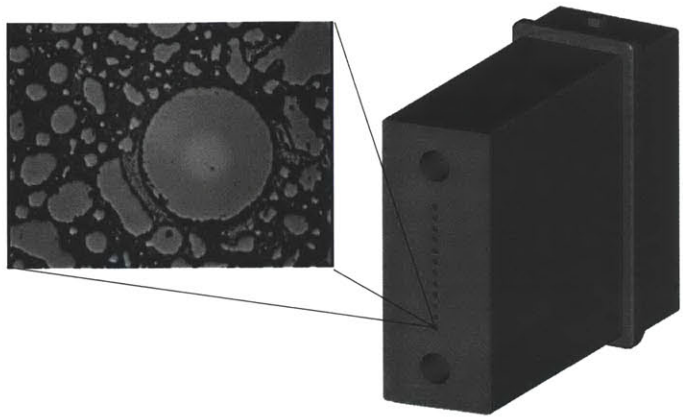

Figure 4-5: Fiber endface on an MT ferrule

Velocity/Bandwidth

From the bench-top system experiments we found a 1-minute inspection time is quite feasible for a 12-fiber ferrule. Assuming that the first fiber is within the FOV of the optics, the inspection time line is as follows:

- center the system (2 second)
- take HDR+HDOF Image (1 second)
- traverse to next fiber (1 second)
- repeat the previous steps until all 12 fibers are inspected

Collection of the 12 images takes a total run-time of 48 seconds, leaving 12 seconds for ferrule-to-ferrule motion, which is more than adequate on the bench-top system.

Fiber-to-Fiber range is nominally 250 μm and typical ferrule-to-ferrule distances range from 3 mm to 700 mm. Moving 700 mm in under 12 seconds may be unrealistic but the fiber-to-fiber motion only requires 0.25 mm/sec velocity. The x axis and y axis have 1 mm/sec velocities as design practicalities.

Capturing HDOF images of an 8° angled endface fiber requires the focus axis to travel approximately 0.020 mm, thus a 1 mm/sec velocity capability for the focus axis is adequate.

In practice the actuator should be as stiff (dynamically and statically) as possible, ensuring suppression of external disturbances, quick settling time,

and greatly simplified controller design. Achieving the desired inspection time line requires each axis to have settling time $4\tau = 0.05$ seconds. In terms of bandwidth, if we have damping $\zeta = 0.8$ then $\omega_n = 1/\zeta\tau = 100$ rad/s or $f_n = 16$ Hz.

Accuracy, Repeatability and Resolution

Nominal ferrule position and orientation can vary as $\delta_{x,y,z} = \pm 300$ μm and $\delta_{\theta_x,\theta_y,\theta_z} = \pm 0.7°$. Starting the FOFIM perfectly aligned to the first fiber, and then traversing to the next fiber position without external feedback proved too inaccurate. On the bench-top inspection system, due to the lack of positional accuracy, ferrule tolerances and the stepper-motor slip. The inaccuracy was resolved by image processing the live video which provided an accurate end-point feedback independent of the stepper-motor count. The effective accuracy was improved greatly.

The control-system consists of two parts: (1) a host-computer capturing and analyzing live video and generating trajectories for camera positioning, and (2) a microcontroller (μC) in Figure 4-6, that takes a desired position as input and performs lead-lag motion control upon the three position axes, with feedback from quadrature encoders mounted on each motor.

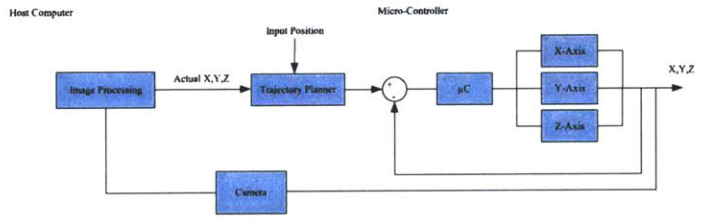

Figure 4-6: Motion control block diagram

The control system operation is as follows:

- The host computer sends to the μC a position of the fiber it wants to inspect.
- The μC then moves each axis to the desired location to within each axis's repeatability and accuracy limits.
- The host computer then captures images of the fiber from which it computes incremental displacements which bring the camera on center with the fiber; see Section 3.4 for image processing details.

- The host computer sends the incremental displacements to the μC which in turn repositions the camera system on center with the fiber.
- The host computer then collects images of the fiber endface for inspection.

This method effectively allows each axis to have relatively low repeatability performance. Each time the system moves a short distance (250 μm) to a new fiber, the system uses the live video feed to re-center upon the fiber. Upon re-centering the system, the accumulated error motions are effectively zeroed, and do not have a great impact on the inspection performance. The machine requires high resolution to re-center the sensor/optics on each fiber.

For this control-scheme to work well, the fiber must be within the image for incremental re-centering displacements to be calculated. The camera's field of view (FOV) dictates the repeatability requirements for each axis. A diagram of an off-center fiber is shown in Figure 4-7. Fiber diameter at the image plane is approximately 270 pixels (125 μm diameter $\times$ 15X mag / 7 μm pixel size), we have a 640x480 pixel sensor, so the maximum acceptable fiber offset while retaining the entire fiber within the FOV is 210 pixels (40 μm).

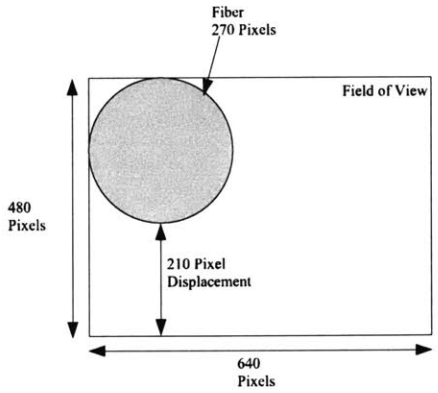

Figure 4-7: Fiber in field of view

To ensure that the camera position will have a FOV encompassing the fiber, the x axis and y axis repeatabilitys should be below $\pm$20 μm. Optics generally have a *sweet-spot* providing the best image due to aberrations and lighting issues, usually located on the optical axis, thus the fiber should be centered to within $\pm$10 μm. Accordingly, the x axis and y axis resolution should be at least 5 μm to achieve the centering tolerance.

Z-axis motion requirements can be determined from how the FOFIM system is focused. An analog circuit computes a focus value from the live video. To provide auto focus, the z axis sweeps through its movements in small increments while measuring focus values. Once the best focus value is found, the system holds to that position. With the 1-second time constraint on finding focus, assuming the focus at velocity 1 mm/s, then the fiber endface and the optical focal plane must be within 1 mm of each other. On the conservative side, the z-axis repeatability must be within ± 0.25 μm to meet focus time constraints. From the optical design we know that the depth of field is on the order of 1 μm, z-axis resolution must therefore be at most half of that, or 0.5 μm.

Since we have end-point fiber-position feedback for all axes, the effective system accuracy is nearly equal to the repeatability. The control-scheme implementation allows axes design with "sloppier" repeatability and accuracy, but we must still maintain high local resolution. The x axis and y axis need 5 μm resolution with ± 20 μm repeatability, while the z axis needs at least 0.5 μm resolution and ± 25 μm repeatability.

4.3 Conceptual Design

Decision matrices identify possible design solutions. For example, the actuator decision matrix, shown in Table 4.2, compares Nitinol, DC motors, stepper motors and voice coils with criteria such as cost, robustness and packaging size. DC motors are the most suitable actuator owing mainly to its high efficiency and compactness.

A decision matrix for bearing selection between rolling element bearings, sliding contact bearings, and flexures is shown in Table 4.3. Sliding contact bearings are found to be the most appropriate choice bearings for the inspection machine mainly due to small packaging capabilities and low cost.

A decision matrix serving as a comparison between leadscrew, wire drive, rack and pinion, harmonic drive, belt drive, and worm and rack drive mechanisms is shown in Table 4.4. Leadscrews were found to be a good choice based on packaging constraints and resolution requirements.

Through decision matrices, it was found that leadscrews driven by DC motors and motion via sliding contact bearings are appropriate ingredients for a successful FOFIM design. With these components in mind a thorough search through catalogs followed. It was found that very few off-the-shelf components would fit within the envelope constraint. For example, the nut

on small leadscrews are typically 20 mm in diameter, violating the 15 mm height requirement. Also most linear bearings have carriage height near the 15 mm height constraint, rendering them unusable for the FOFIM.

The entire FOFIM must fit within the *working envelope* as shown in Figure 4-8. The camera tube houses the optics and provides vision to inspect each optical connector. We immediately see that the daughter card should provide a great bearing for $\hat{x}$ motion. It is certain that a right angle drive such as rack and pinion, friction drive, or miter gear would easily allow a larger sized motor to fit within the working envelope.

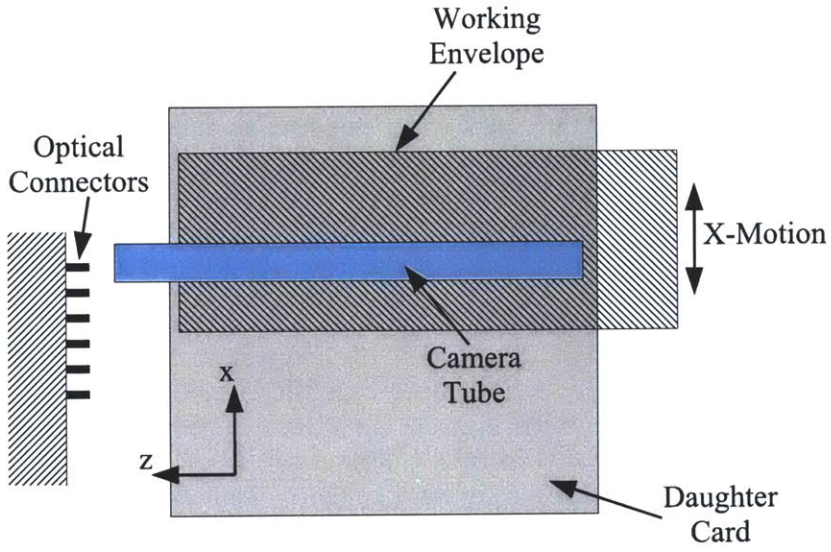

Figure 4-8: Machine design space for x axis

For y-axis motions, 3.5 mm fiber-to-fiber motions, we have a very tight working envelope constraint as shown in Figure 4-9. A direct driven leadscrew would certainly not fit but the idea of a cam drive or wedge drive would easily allow a properly sized motor to fit and provide robust actuation.

The z-axis focus motion is less demanding as shown in Figure 4-10. A simple leadscrew drive may suffice as the motor can be easily mounted coaxially with the camera.

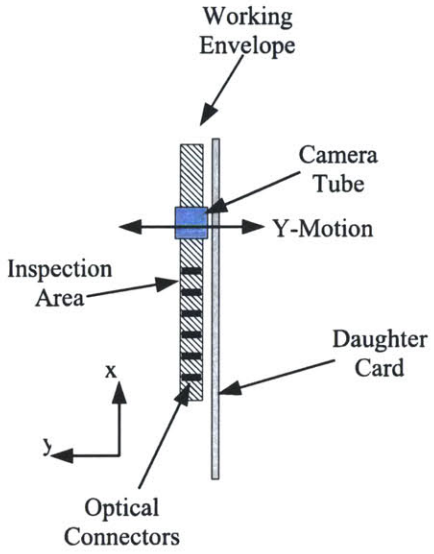

Figure 4-9: Machine design space for y axis

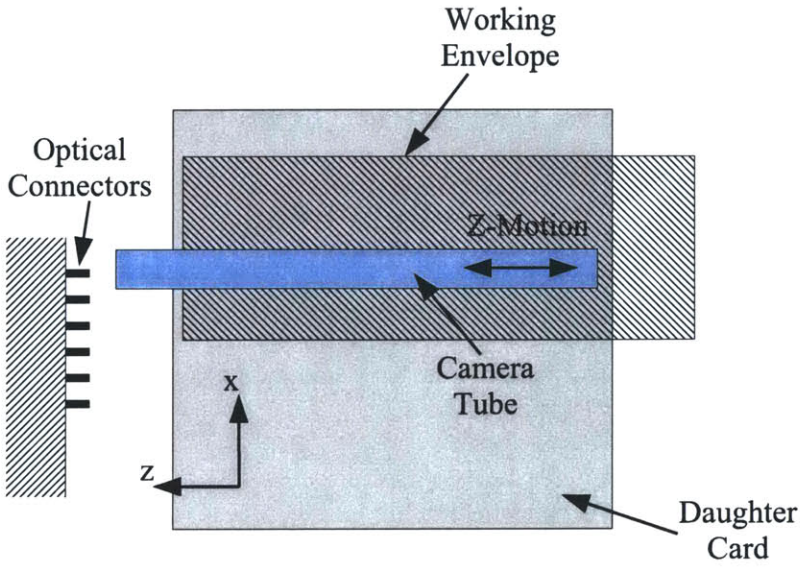

Figure 4-10: Machine design space for z axis

Table 4.2: Actuator decision matrix

Item #	Design Requirements & Tradeoffs	Weight 1-3=Low 4-6=Med	Design Goal	Rating Criteria			Nitenol			DC Motor			Stepper Motor			Piezo Motor			Voice Coil		
				1 Point	2 Points	3 Points	Weighted Score	Score	Actuals	Weighted Score	Score	Actuals	Weighted Score	Score	Actuals	Weighted Score	Score	Actuals	Weighted Score	Score	Actuals
1	# of components (reliability)	1	relative	Worst	Average	Best	3	3	Best	2	2	Average	2	2	Average	2	2	Average	3	3	Best
2	Cost of manufacture (Labor)	7	relative	Worst	Average	Best	21	3	Best	14	2	Average	14	2	Average	7	1	Worst	21	3	Best
3	Risk (confidence/experience)	5	Low	High	Average	Low	5	1	High	15	3	Low	15	3	Low	10	2	Average	15	3	Low
4	Addresses 8 degree problem?	2	Yes	No		Yes	2	1	No	2	1	No	2	1	No	2	1	No	2	1	No
6	Patent Infringement	3	No	Yes		No	3	1	Yes	3	1	Yes	3	1	Yes	3	1	Yes	3	1	Yes
7	Meets DC package requirements	8	Yes	No		Yes	24	3	Yes	24	3	Yes	16	2	0	16	2	0	16	2	0
8	Achieve required resolution	8	Yes	No		Yes	8	1	No	24	3	Yes	24	3	Yes	24	3	Yes	24	3	Yes
9	Number of axises required	3	Low	High	Average	Low	6	2	Average	6	2	Average	6	2	Average	6	2	Average	6	2	Average
10	Package robustness	5	High	Low	Average	High	5	1	Low	15	3	High	15	3	High	10	2	Average	15	3	High
11	Scales easily to larger ferrules	4	Yes	No		Yes	8	2	0	12	3	Yes	12	3	Yes	12	3	Yes	12	3	Yes
12	Feasibility	9	relative	Worst	Average	High	9	1	Worst	27	3	High	27	3	High	9	1	Worst	18	2	Average
13	Cost of Control	7	High	Low	Average	High	7	1	Low	21	3	High	21	3	High	14	2	Average	14	2	Average
14							0	1	0	0	1	0	0	1	0	0	1	0	0	1	0
15							0	1	0	0	1	0	0	1	0	0	1	0	0	1	0
16							0	1	0	0	1	0	0	1	0	0	1	0	0	1	0
17							0	1	0	0	1	0	0	1	0	0	1	0	0	1	0
18							0	1	0	0	1	0	0	1	0	0	1	0	0	1	0
19							0	1	0	0	1	0	0	1	0	0	1	0	0	1	0
20							0	1	0	0	1	0	0	1	0	0	1	0	0	1	0
	Total Score						101			165			157			115			149		

Table 4.3: Bearing decision matrix

Item #	Design Requirements & Tradeoffs	Weight 1-3=Low 4-6=Med	Design Goal	Rating Criteria			Flexure			Rolling Element			Sliding Contact		
				1 Point	2 Points	3 Points	Weighted Score	Score	Actuals	Weighted Score	Score	Actuals	Weighted Score	Score	Actuals
1	# of components (reliability)	1	relative	Worst	Average	Best	3	3	Best	1	1	Worst	2	2	Average
2	Cost of manufacture (Labor)	7	relative	Worst	Average	Best	21	3	Best	7	1	Worst	14	2	Average
3	Risk (confidence/experience)	5	Low	High	Avg	Low	5	1	High	10	2	Avg	10	2	Avg
4	Addresses 8 degree problem?	2	Yes	No		Yes	2	1	No	2	1	No	2	1	No
6	Patent Infringement	3	No	Yes		No	3	1	Yes	3	1	Yes	3	1	Yes
7	Meets DC package requirements	8	Yes	No		Yes	8	1	No	8	1	No	24	3	Yes
8	Achieve required resolution	8	Yes	No		Yes	24	3	Yes	16	2	0	8	1	No
9	Number of axises required	3	Low	High	Avg	Low	3	1	High	3	1	High	3	1	High
10	Package robustness	5	High	Low	Avg	High	10	2	Avg	5	1	Low	15	3	High
11	Scales easily to larger ferrules	4	Yes	No		Yes	4	1	No	8	2	0	12	3	Yes
12	Feasibility	9	relative	Worst	Average	High	18	2	Average	18	2	Average	27	3	High
13	Cost of Control	7	High	Low	Avg	High	7	1	Low	7	1	Low	7	1	Low
14							0	1	0	0	1	0	0	1	0
15							0	1	0	0	1	0	0	1	0
16							0	1	0	0	1	0	0	1	0
17							0	1	0	0	1	0	0	1	0
18							0	1	0	0	1	0	0	1	0
19							0	1	0	0	1	0	0	1	0
20							0	1	0	0	1	0	0	1	0
	Total Score						108			88			127		

Table 4.4: Actuator drive decision matrix

Design Requirements & Tradeoffs		Weight 1-3=Low 4-6=Med	Design Goal	Rating Criteria			Lead Screw			Wire Drive			Rack + Pinion			Harmonic			Belt/Tape			Worm + Rack		
				1 Point	2 Points	3 Points	Weighted Score	Score	Actuals	Weighted Score	Score	Actuals	Weighted Score	Score	Actuals	Weighted Score	Score	Actuals	Weighted Score	Score	Actuals	Weighted Score	Score	Actuals
Item #																								
1	# of components (reliability)	1	relative	Worst	Average	Best	3	3	Best	2	2	Average	2	2	Average	3	3	Best	2	2	Average	2	2	Average
2	Cost of manufacture (Labor)	7	relative	Worst	Average	Best	21	3	Best	21	3	Best	7	1	Worst	7	1	Worst	14	2	Average	7	1	Worst
3	Risk (confidence/experience)	5	Low	High	Avg	Low	15	3	Low	10	2	Avg	5	1	High	5	1	High	10	2	Avg	10	2	Avg
4	Addresses 8 degree problem?	2	Yes	No		Yes	2	1	No	2	1	No	2	1	No	2	1	No	2	1	No	2	1	No
6	Patent Infringement	3	No	Yes		No	3	1	Yes	3	1	Yes	3	1	Yes	3	1	Yes	3	1	Yes	3	1	Yes
7	Meets DC package requirements	8	Yes	No		Yes	24	3	Yes	24	3	Yes	8	1	No	8	1	No	16	2	0	8	1	No
8	Achieve required resolution	8	Yes	No		Yes	24	3	Yes	24	3	Yes	8	1	No	24	3	Yes	16	2	0	8	1	No
9	Number of axises required	3	Low	High	Avg	Low	3	1	High	3	1	High	3	1	High	3	1	High	3	1	High	3	1	High
10	Package robustness	5	High	Low	Avg	High	15	3	High	5	1	Low	10	2	Avg	15	3	High	10	2	Avg	10	2	Avg
11	Scales easily to larger ferrules	4	Yes	No		Yes	12	3	Yes	12	3	Yes	12	3	Yes	12	3	Yes	12	3	Yes	12	3	Yes
12	Feasibility	9	relative	Worst	Average	High	9	1	Worst	9	1	Worst	9	1	Worst	9	1	Worst	9	1	Worst	9	1	Worst
13	Cost of Control	7	High	Low	Avg	High	7	1	Low	7	1	Low	7	1	Low	7	1	Low	7	1	Low	7	1	Low
14							0	1	0	0	1	0	0	1	0	0	1	0	0	1	0	0	1	0
15							0	1	0	0	1	0	0	1	0	0	1	0	0	1	0	0	1	0
16							0	1	0	0	1	0	0	1	0	0	1	0	0	1	0	0	1	0
17							0	1	0	0	1	0	0	1	0	0	1	0	0	1	0	0	1	0
18							0	1	0	0	1	0	0	1	0	0	1	0	0	1	0	0	1	0
19							0	1	0	0	1	0	0	1	0	0	1	0	0	1	0	0	1	0
20							0	1	0	0	1	0	0	1	0	0	1	0	0	1	0	0	1	0
	Total Score						138			122			76			98			104			81		

4.4 Machine Design Solution

The second prototype FOFIM is shown in Fig 4-11. It is compact, 75 x 15 x 280 mm in volume, with three axes of motion. The base carriage travels along the x-axis rack for ferrule-to-ferrule motion. In this case, range is limited by daughter-card height. The yz carriage carries the camera tube along $\hat{y}$ for a total range of 3.5 mm for fiber-to-fiber movement and $\hat{z}$ for total range of 24 mm for focusing. As seen in Table 4.5, the final machine has good performance, beyond those dictated by the functional requirements.

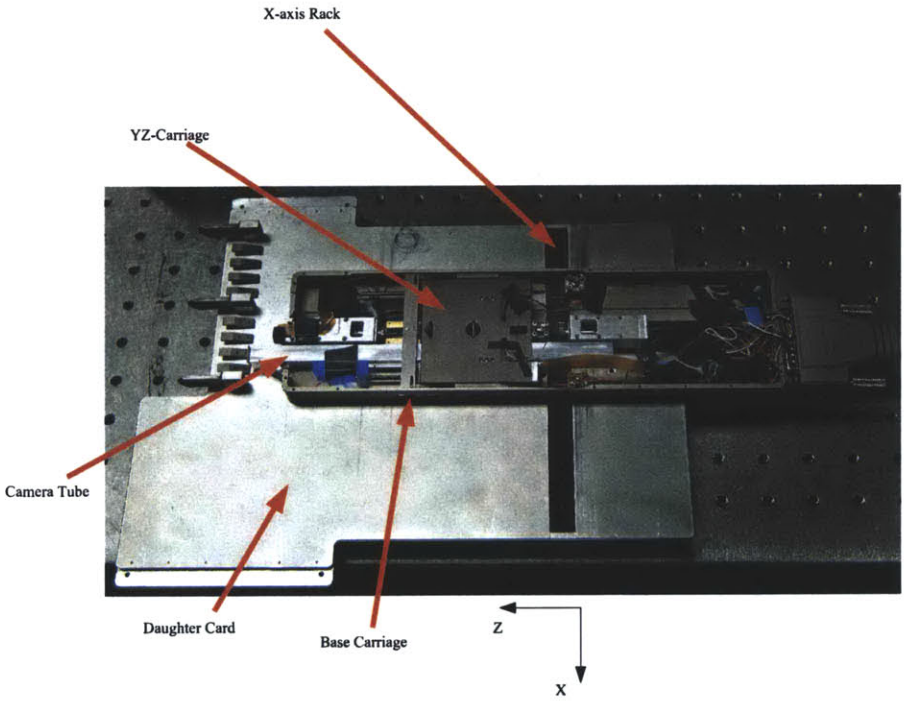

Figure 4-11: FOFIM prototype

Axis	Settling Time	Resolution	Repeatability	Range
X axis	0.05 second	0.128 ± 4 μm	± 8 μm	NA
Y axis	0.03 second	0.003 ± 4 μm	± 15 μm	3.5 mm
Z axis	0.03 second	0.0076 ± 10 μm	± 10 μm	24 mm

Table 4.5: Final system performance

We will now examine the design of each axis in detail.

4.4.1 X Axis

The x axis provides ferrule-to-ferrule motion on the order of 700 mm travel at a minimum velocity of 1 mm/s. A resolution of 5 μm and repeatability of ± 25 μm are needed to place the fiber within the center of optical field of view accurately and repeatably. Figure 4-12 depicts a general overview of the x axis; a DC motor rotates a pinion that engages a rack that also serves as the linear bearing.

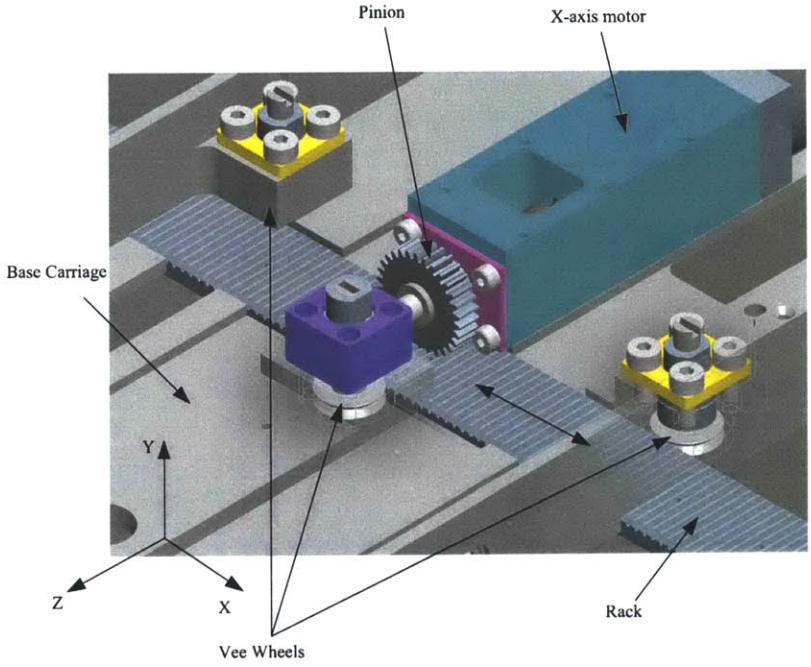

Figure 4-12: X axis

Kinematics

Figure 4-13 shows an exploded view of the x-axis motor assembly. At the heart of the system is the hard-mount coupling that also acts as an axle transferring torque from the motor directly to the pinion. The pinion is attached to the coupling via a flat on the coupling and setscrew on the

pinion. For short term prototype usage, tight tolerances on the motor-housing alleviates the need for a flexible coupling, allowing for a much shorter assembly along the z axis. The gearbox has 120 μm radial play and the motor housing locational tolerance is to within 50 μm, well below the gearbox radial play and thus it should not bear any radial load. This suffices for a low cost prototype design, but for long-term usability a flexible coupling is much more practical to maintain precision.

To fit within this envelope a custom flexible coupling is needed. For example, an electroform coupling is a feasible design, but low quantity production is cost prohibitive whereas higher quantity production on the order of hundreds it is quite economical. The motor is connected to the coupling via a flat on the motor-shaft and setscrew in the coupling. The coupling is held in the motor-housing by a set of single row angular-contact bearings in the back-to-back configuration ensuring high moment stiffness on the cantilevered pinion. It is desirous to have a double row angular contact bearing as they are more compact and are self-preloaded but we could not find any double row bearings in this small size. A screw threaded into the end of the coupling allows for careful preload setting on the angular-contact bearings. The outer-races are held in the motor housing by the outer-race retainer.

The primary bearings that constrain the x-axis to move along the rack is formed by the vee wheels. As shown in Figure 4-14, each vee wheel is mounted in a set of angular contact bearings in the back-to-back configuration ensuring high moment stiffness. The preload nut preloads the inner-races of the bearings onto the vee wheel. The bearing housing attaches the entire assembly to the base-carriage. The three vee wheels provide 5 constraints for quasi-kinematic motion, as shown in Figure 4-15. The center vee wheel is hand set along the z axis to preload against the rack, the combination of the stiffness of the base-carriage cantilever (discussed below), vee wheel shaft and angular contact bearings serve as the preload mechanism. This works fairly well for prototyping purposes but to maintain accuracy this vee wheel will be spring loaded against the rack to maintain better precision.

On the final machine, stiffness about the axis of motion was found to be rather low as the base-carriage would bounce up and down at every tooth engagement. This vee-wheel bearing scheme was born from the first prototype that was drastically lighter and the vee-wheel mounts were much stiffer, thus the overall stiffness was much higher and the axis performed very well. The second prototype's base-carriage has thinner walls to fit within our envelope constraint and a few cutouts allow the z-axis motors to fit within the system. As shown in Figure 4-16, the center vee wheel is effectively

Figure 4-13: X-axis motor assembly

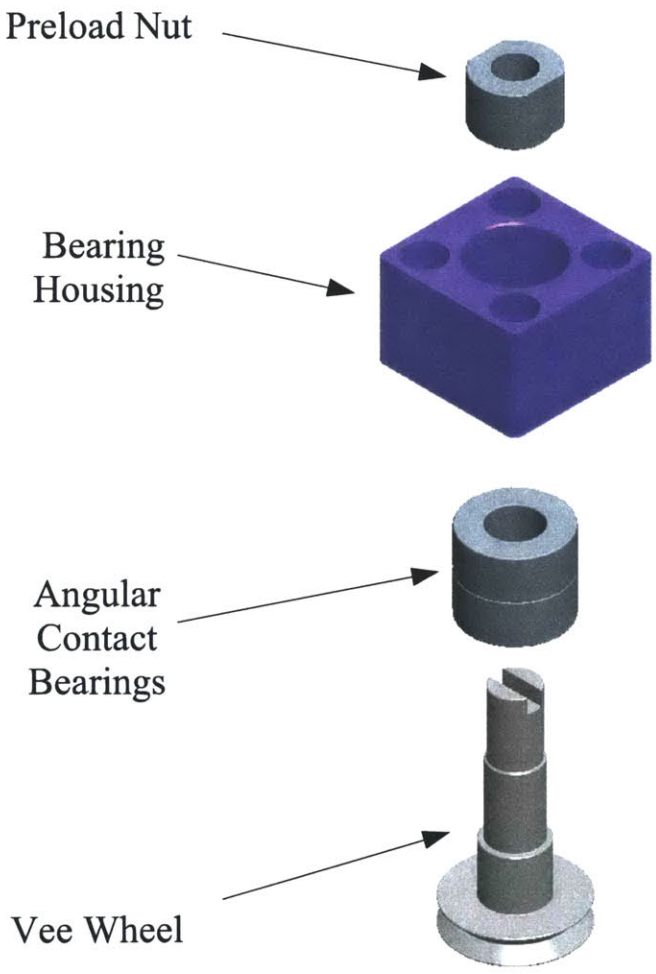

Figure 4-14: X-axis vee-wheel assembly

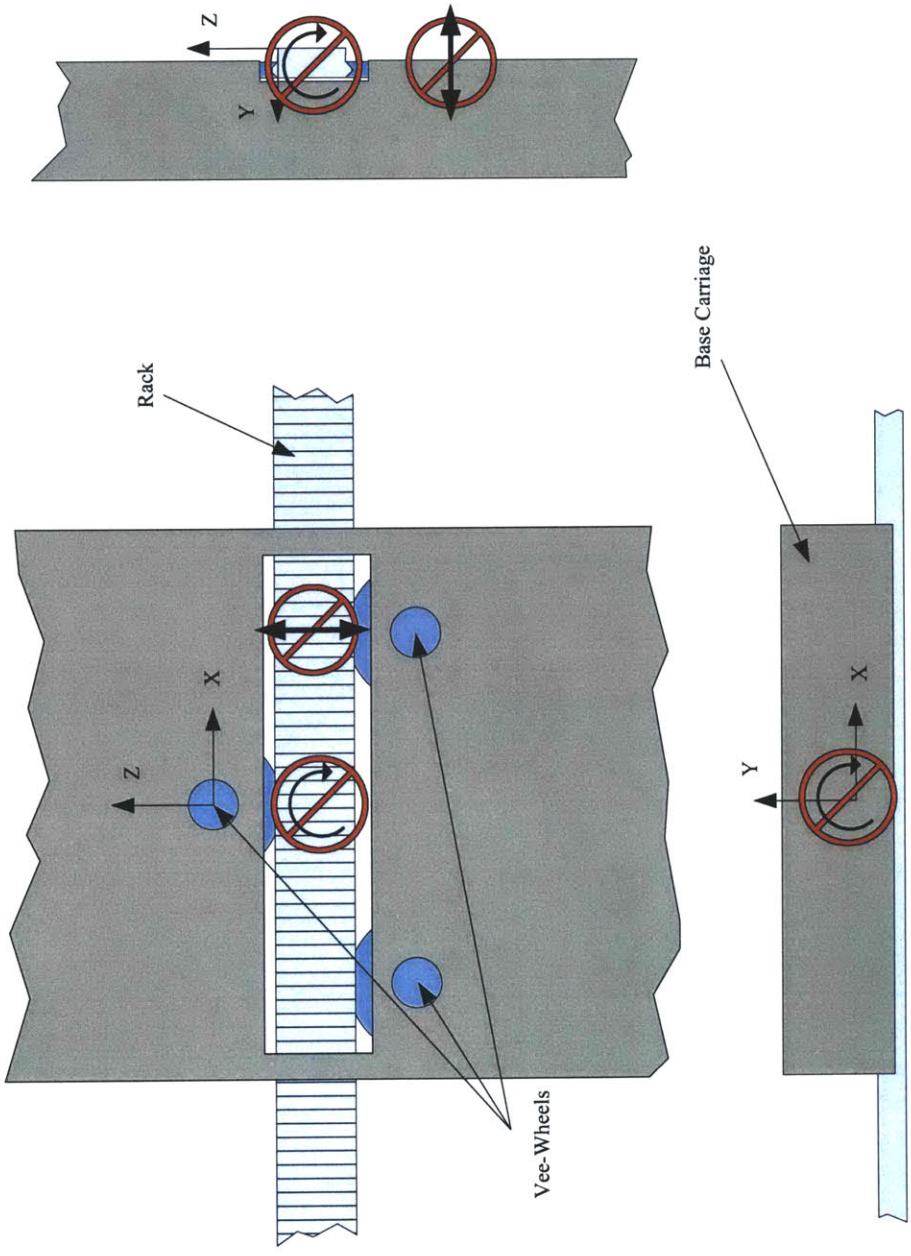

Figure 4-15: X-axis constraints

mounted on a cantilever beam of very low stiffness, which manifests in the bobbing motion. A simple solution was to glue Teflon pads on the bottom of the base-carriage on the cantilevered part and underneath the stiff side walls of the base-carriage. In this arrangement the vee wheel's simply preload the base-carriage against the daughter-card and the Teflon pads constrain rotation about the x axis as shown in Figure 4-17.

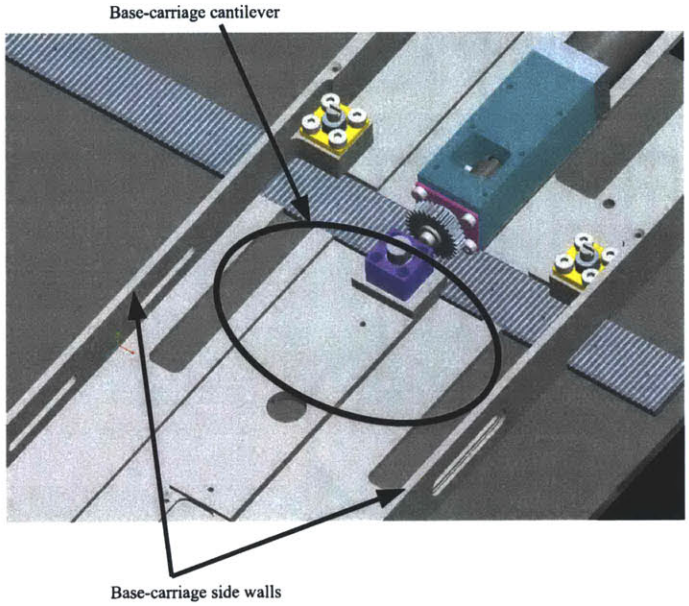

Figure 4-16: X-axis base-carriage cantilever

Dynamic Model

A block diagram of the x-axis dynamic model is shown in Figure 4-18. T_1 is the input torque from the DC motor, J_1 is the effective inertia of the motor and gearbox = 5.03E-3 kg·m^2, k is the effective stiffness of the leadscrew = 21.7 N·m/rad, J_2 is the effective inertia of the pinion and the entire inspection system = 1.4E-5 kg·m^2, θ_1 and θ_2 are the angular rotations of each end of the motor-coupling. The system transfer function can be seen in Equation (4.1),

$$\frac{\theta_1}{T_1} = \frac{s^2 J_2 + k}{s^2[s^2 J_1 J_2 + k(J_1 + J_2)]} \tag{4.1}$$

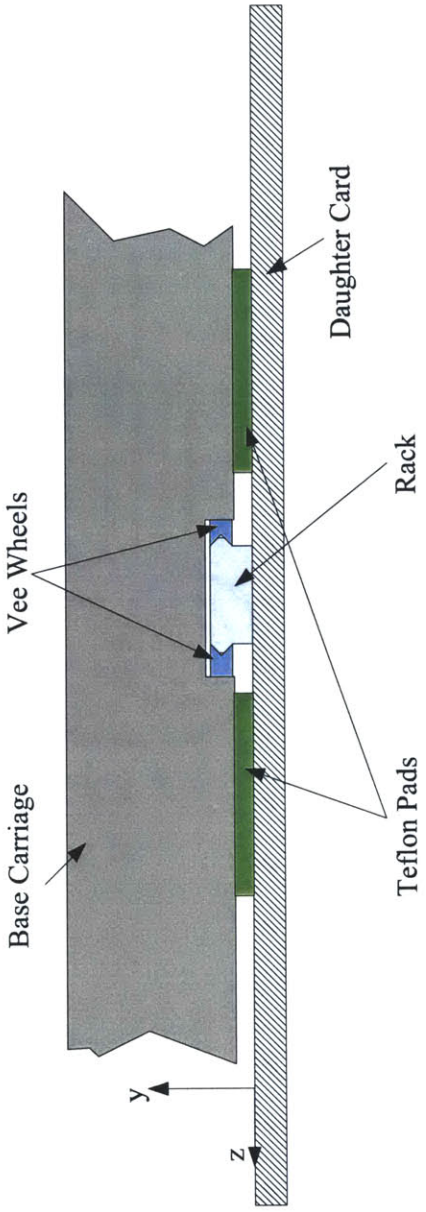

Figure 4-17: Teflon Pad Backing on x axis

Accordingly the system resonance is approximately 32.6 kHz which should easily meet the x-axis settling time requirement. Experimental verification of the system dynamics will be discussed later in Section 4.6.

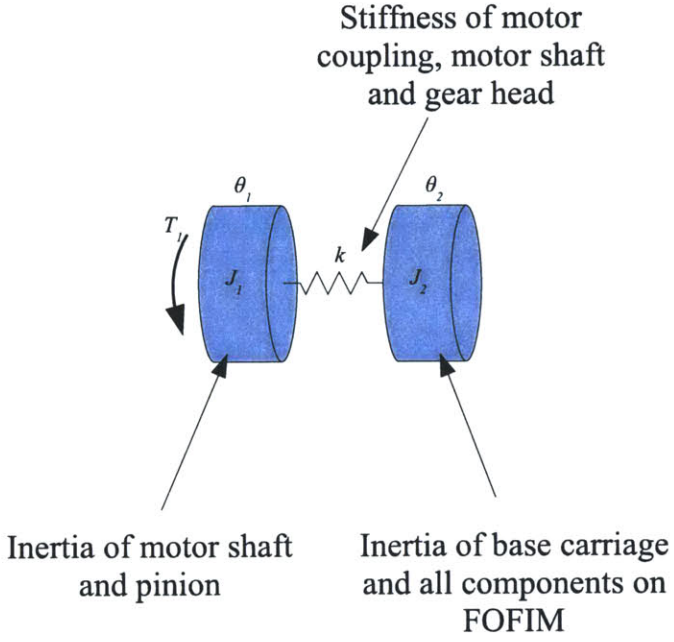

Figure 4-18: X-axis dynamic model

Actuator

The pinion is driven by a brushed DC motor rated at 3 Watts with a 275:1 gear-head reduction providing a maximum continuous torque of 0.30 Nm. This is more than adequate to drive the x axis with the system oriented in any fashion including the effects of gravity. The combination of the gear-head, 1024 count/turn quadrature encoder and the 12 mm pitch-diameter on the pinion gives 0.134 μm/count theoretical resolution, which is more than adequate for the 5 μm resolution requirement. Theoretical repeatability will be discussed later in the error budget section.

4.4.2 Y Axis

The y axis provides fiber-to-fiber motion for a total of 3.5 mm range of travel at a minimum velocity of 1 mm/second 5 μm resolution and ± 20 μm repeatability are needed to place the fiber within the center of optics' field of view accurately and repeatably. Figure 4-19 depicts a general overview of the y axis.

Kinematics

The y axis is actuated by a brushed DC motor directly coupled to a leadscrew and nut. In an attempt to make the system as compact as possible, the motor coupling was integrated directly into the leadscrew, effectively making a hard-mount coupling. Again, for short term low-cost prototype usage, tight tolerances on the motor mount and high load capability on the motor shaft alleviate the need for a flexible motor coupling. Long term product feasibility requires a flexible coupling. The leadscrew rotates within a set of angular contact bearings in the back-to-back configuration; the appropriate inner race preload is applied by the nut and preload spacer. The outer bearing races are held into the motor mount via the outer-race preload part, as shown in Figure 4-20.

Bronze preload gibs constrain nut rotation, θ_z, as the nut travels back and forth along $\hat{z}$. Clearly θ_y and θ_z are also constrained via the leadscrew and gib. The y-axis nut wing is attached to the nut which drives the ramps via the drive pin, where the pin is preloaded against the nut-wing by an integrated flexure, reducing system backlash. The ramps are preloaded against the side of the base-carriage by the preload flexures and are carefully set by a small screw, as shown in Figure 4-21. The bronze preload gibs also constrain the nut wing from shimming side to side thus preventing the ramps from shimming.

The yz carriage rides upon the ramps via the rollers, as shown in Figure 4-22. The y-axis ballguides provide three constraints as shown in Figure 4-23. The ballguide riding in the vee constrains translation in $\hat{x}$ and $\hat{z}$, while the combination of the two ballguides constrains rotation about the y axis. The two remaining rotational constraints are provided by the y-axis rollers riding on the y-axis Ramps. The side-view shows the θ_x constraint while there is one ramp on each side of the yz carriage constraining θ_z rotation. One may object to the 4 rollers as being over-constrained, but when the camera tube is fully extended, four rollers are far more stable than the kinematic arrangement of three rollers because it would be fairly easy to

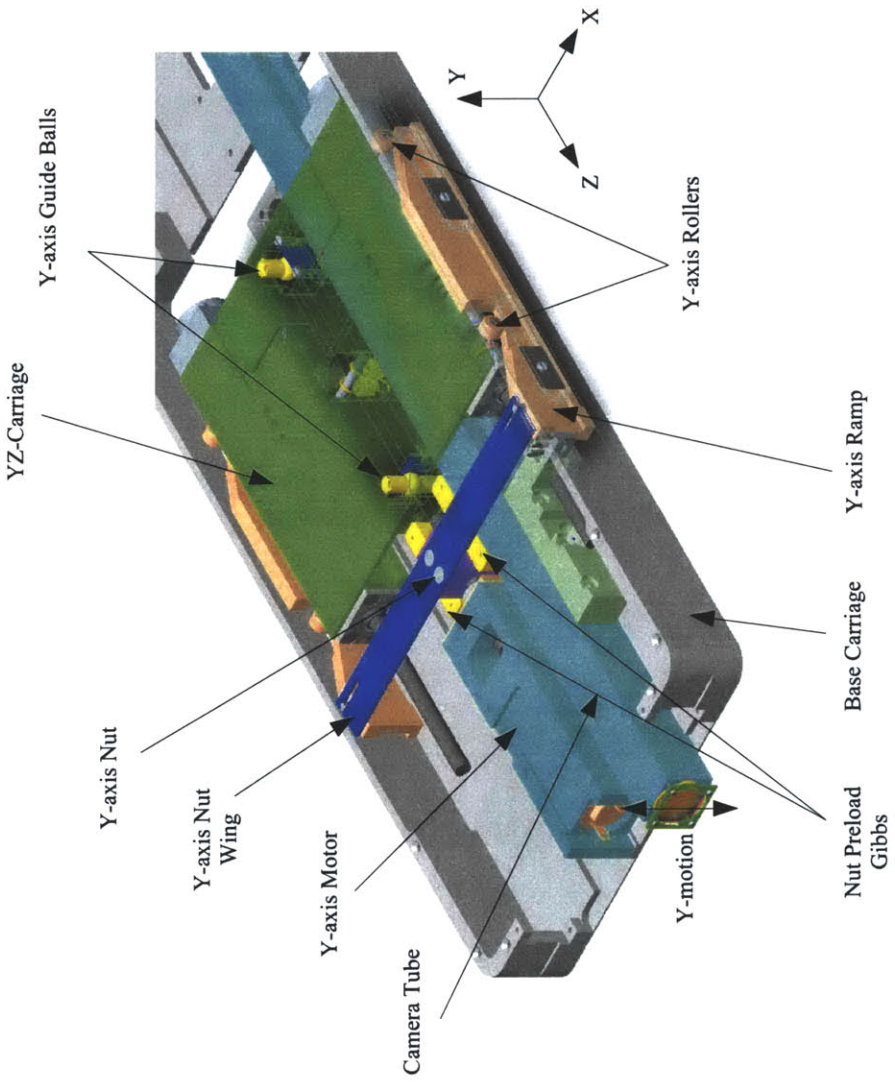

Figure 4-19: Y-axis assembly

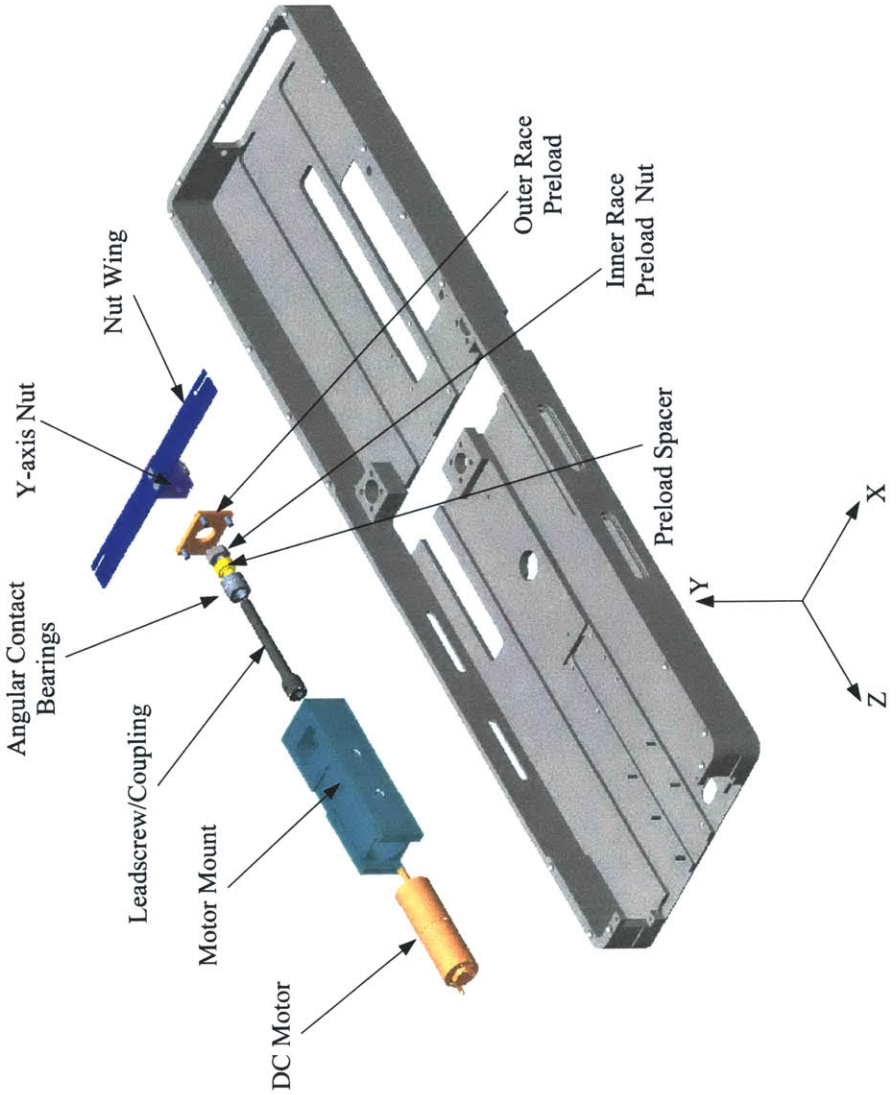

Figure 4-20: Y-axis motor, nut and leadscrew assembly

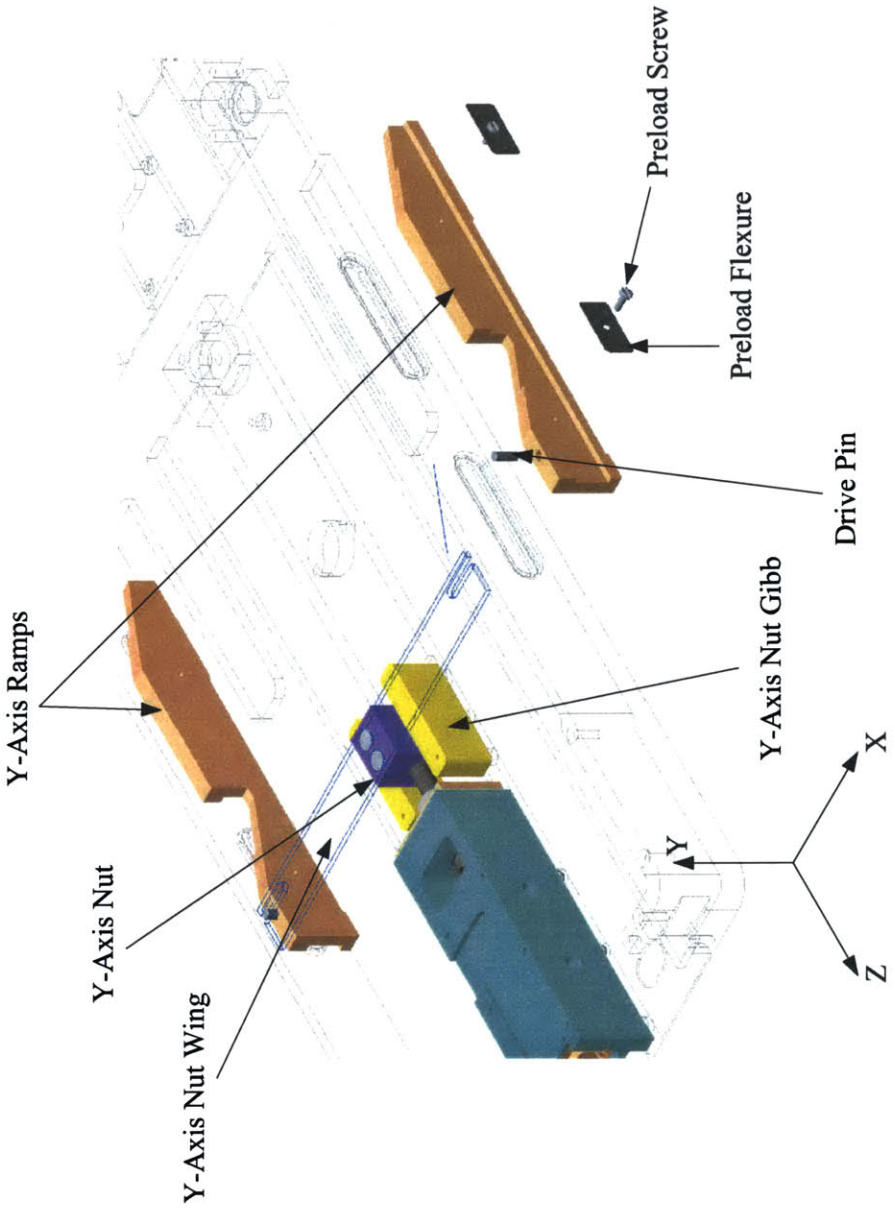

Figure 4-21: Y-axis ramps assembly

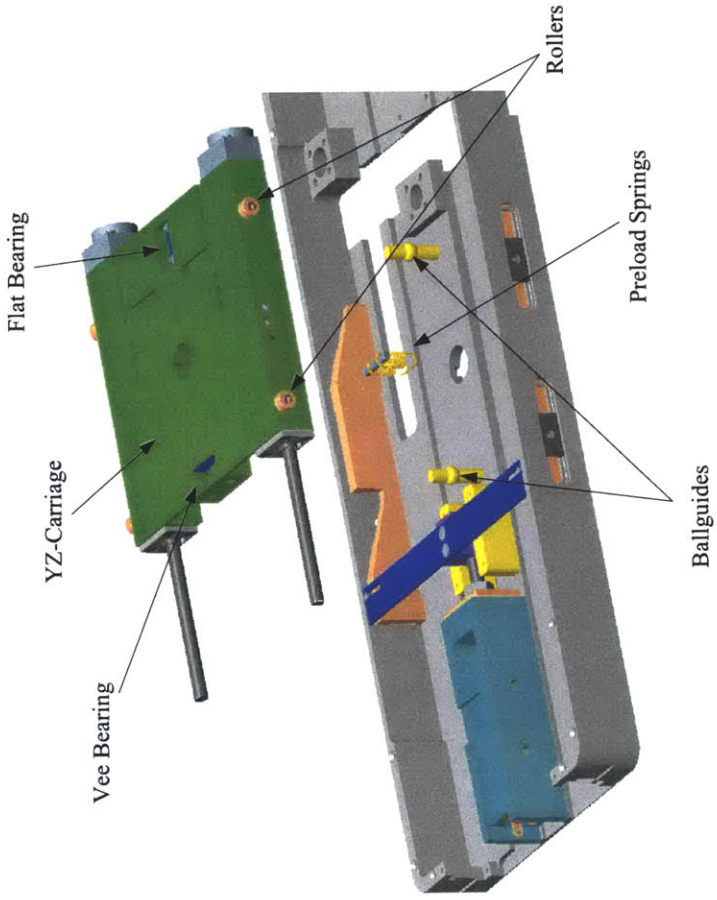

Figure 4-22: Y-axis yz carriage

unload the rollers if the camera tube is bumped.

The pins on which the y-axis rollers roll are designed to be a little "soft" in order to elastically average the load across the 4-rollers. The effective stiffness of combination of the four pins is $k_{\text{pins}} = 1.39\text{E}5$ N/m. A spring at the center of the yz carriage provides a minimum of 13 N preload onto the ramps. Thus the total deflection of the rollers is 93 μm.

As these ramps were manufactured by using an electro-discharge machining (EDM) the surface form errors is ± 10 μm, leaving all 4 rollers in contact, providing an elastically averaged system.

Due to the constraints provided by the ballguides, as the y-axis ramps are driven back and forth by the lead-screw and nut along $\hat{z}$, the yz carriage travels up and down in the $\hat{y}$ direction.

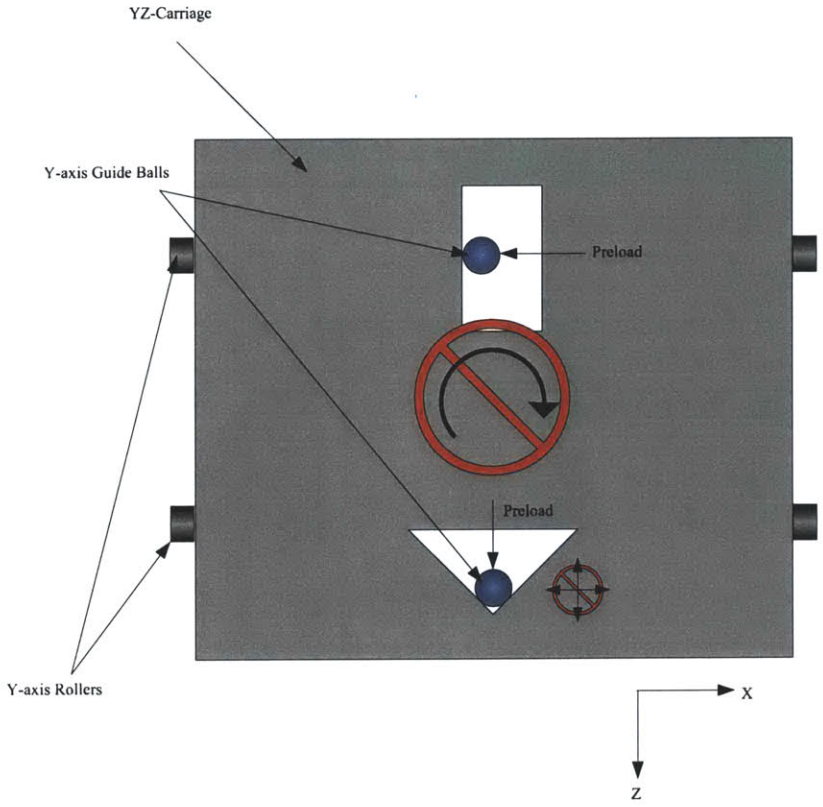

(a) Y-axis Top View

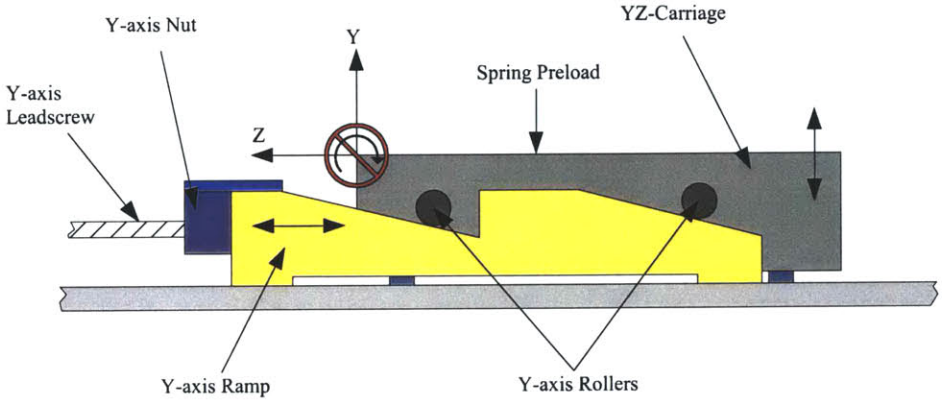

(b) Y-axis Side View

Figure 4-23: Y axis

Dynamic Model

The dynamic model for the y axis is sketched in Figure 4-24, where:

F_1	=	effective force of the DC motor
z_1	=	effective motor shaft position
z_2	=	effective nut position
y_1	=	yz-carriage position
k_1	=	effective leadscrew, motor coupling, and motor shaft stiffness
k_2	=	effective stiffness of the y-axis rollers
k_3	=	stiffness of the preload spring
m_1	=	effective mass of the leadscrew, gear-box and motor-shaft
m_2	=	effective mass of the y-axis ramps and nut
m_3	=	effective mass of the yz carriage and camera tube

The mechanical advantage of the ramps is modeled as a pulley system where the output is simply the input from z_2 multiplied by $c = \tan(20°)$. The state equations are

$$\begin{pmatrix} \dot{z}_1 \\ \ddot{z}_1 \\ \dot{z}_2 \\ \ddot{z}_2 \\ \dot{y}_1 \\ \ddot{y}_1 \end{pmatrix} = \begin{bmatrix} 0 & 1 & 0 & 0 & 0 & 0 \\ \frac{-k_1}{m_1} & 0 & \frac{k_1}{m_1} & 0 & 0 & 0 \\ 0 & 0 & 0 & 1 & 0 & 0 \\ \frac{-k_1}{m_1} & 0 & \frac{k_1+k_2c}{m_2} & 0 & \frac{k_2}{m_2} & 0 \\ 0 & 0 & 0 & 0 & 0 & 1 \\ 0 & 0 & \frac{k_2c}{m_2} & 0 & \frac{-(k_2+k_3)}{m_2} & 0 \end{bmatrix} \begin{pmatrix} z_1 \\ \dot{z}_1 \\ z_2 \\ \dot{z}_2 \\ y_1 \\ \dot{y}_1 \end{pmatrix} + \begin{pmatrix} \frac{1}{m_1} \\ 0 \\ 0 \\ 0 \\ 0 \\ 0 \end{pmatrix} F_1 \tag{4.2}$$

The system masses m_2 and m_3 were measured using a scale and m_1 was calculated based on the lead of the leadscrew and rotational inertia of the drive train where $m_1 = 0.038$ kg, $m_2 = 0.012$ kg and $m_3 = 0.090$ kg. The effective stiffnesses k_1 and k_2 were based on material properties and k_3 was determined from the product specification sheet where k_1 = 4.3E7 N/m, k_2 =1.39E5 N/m and k_3 = 1300 N/m.

Plugging in the parameter values shows that the system dynamics are dominated by the mass of the yz carriage and the stiffness of the roller pins, and the resonance occurs at approximately 250 Hz. The effective dynamic stiffness of this axis will be discussed in section 4.6.2.

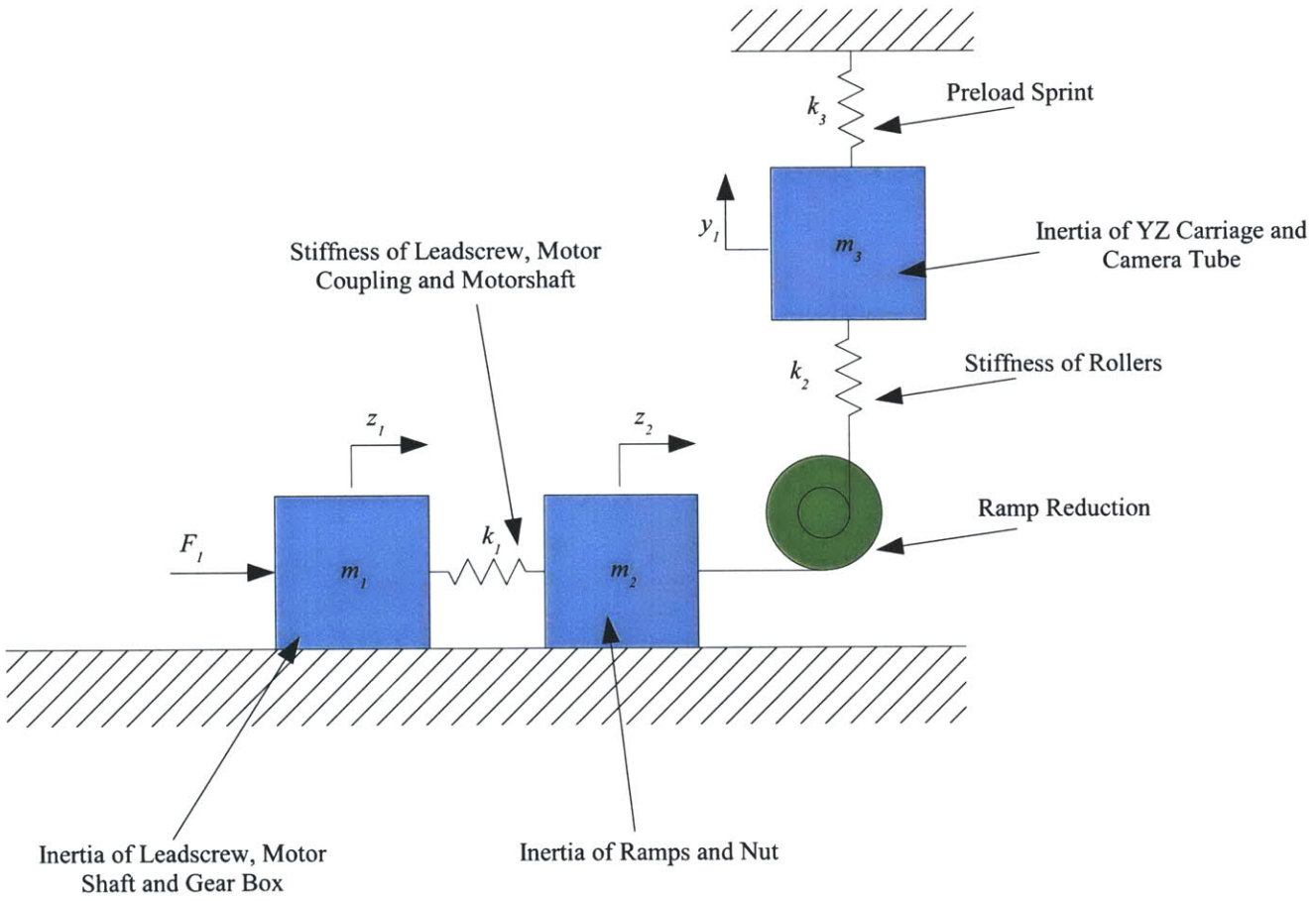

Figure 4-24: Y-axis dynamic model

Actuator

The y axis is driven by a 0.75 Watt brushed DC motor with 256:1 gear-head and 0.150 Nm maximum continuous torque output. The gear-head is coupled to a 3 mm leadscrew with 0.5 mm lead, driving the y-axis ramps back and forth along $\hat{z}$. With a 1024 $\frac{\text{count}}{\text{turn}}$ quadrature encoder, we have a theoretical 0.003 $\frac{\mu\text{m}}{\text{count}}$ resolution for yz carriage positioning. Theoretical y-axis repeatability capabilities will be discussed later in the error budget.

4.4.3 Z Axis

The z axis provides the focusing motion for the optics and secondary function of opening shuttered connectors. As previously stated, focusing requires at least 0.5 μm resolution with ± 25 μm repeatability and 16 Hz bandwidth. The z axis, seen in Figure 4-25, consists of a linear bearing actuated by a leadscrew and nut. One may notice the symmetry of the yz carriage and the second leadscrew. This is intended to actuate a cleaning system that will be designed in future work and is beyond the scope of this thesis.

Kinematics

As shown in Figure 4-26, tight tolerances on the motor and bearing mounts within the yz carriage along with a motor shaft capable of high moment loads, alleviate the need for a flexible coupling. For short term prototype usage the hard-mount coupling allows for a much shorter design. The leadscrew is mounted in a set of angular-contact bearings in the back-to-back configuration to ensure high moment stiffness. A preload nut and preload spacer allow for careful bearing preload setting, while the bearing retainer holds the leadscrew/bearing assembly within the yz carriage.

The linear bearing on the camera tube is in quasi-kinematic constraint. Bearing pads and preload gib seen in the *Top* view of Figure 4-27 provide two constraints: rotation about the y axis (θ_y) and translation in $\hat{x}$. Similarly, as shown in the *Right* view of Figure 4-27, there is a second set of bearing pads and preload gib that constrain θ_x and $\hat{y}$ motions. In the *Front* view of Figure 4-27 the combination of the two bearings sets provide the final θ_z constraint.

The bearing pads are integrated into the yz carriage, an aluminum piece with Teflon hard-coat anodization. The preload bearing pads are made of bronze and a Buna-N O-ring sandwiched between the bronze gib and the yz carriage provides the gib preload, as shown in Figure 4-28.

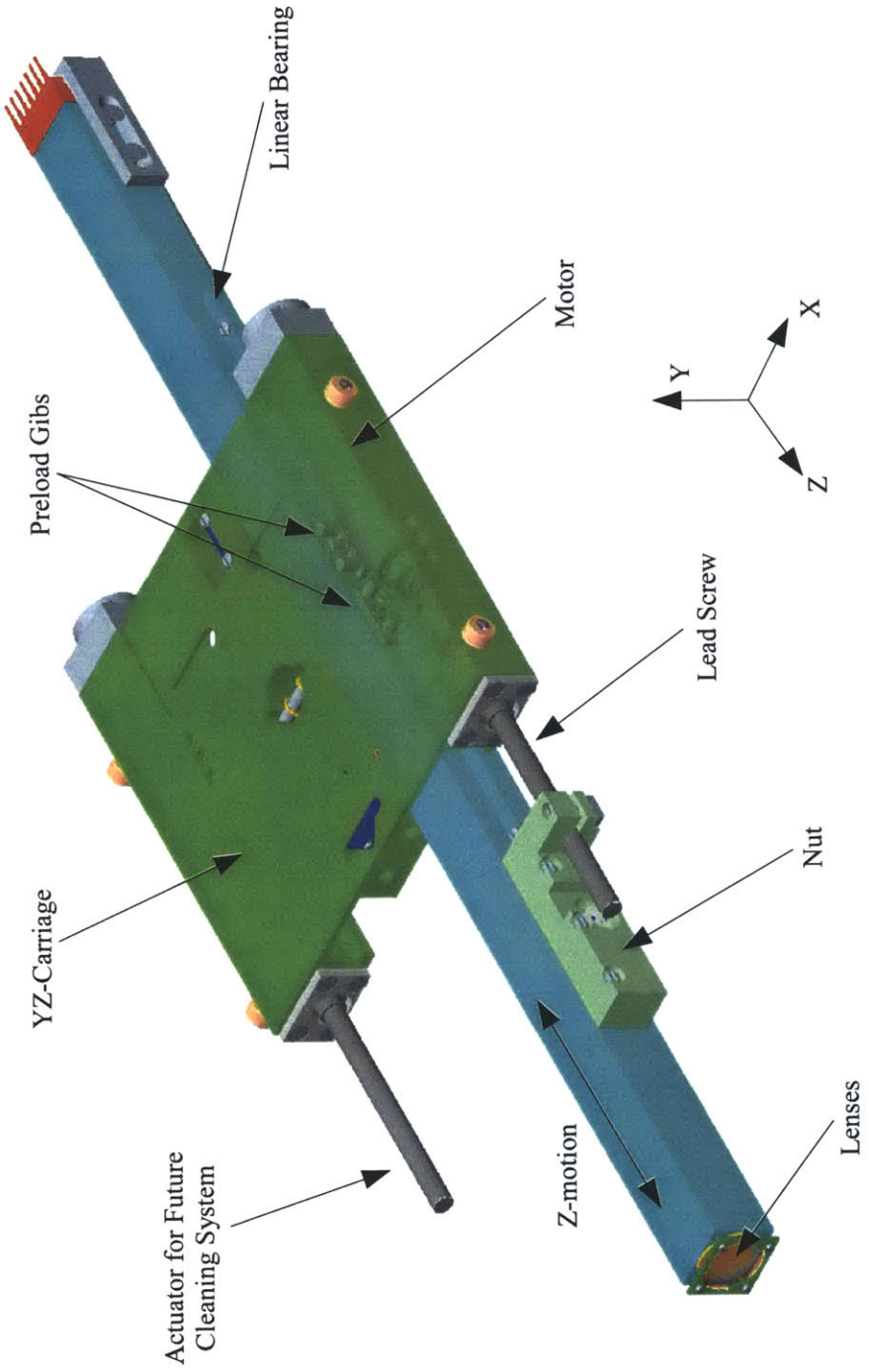

Figure 4-25: Z-axis assembly

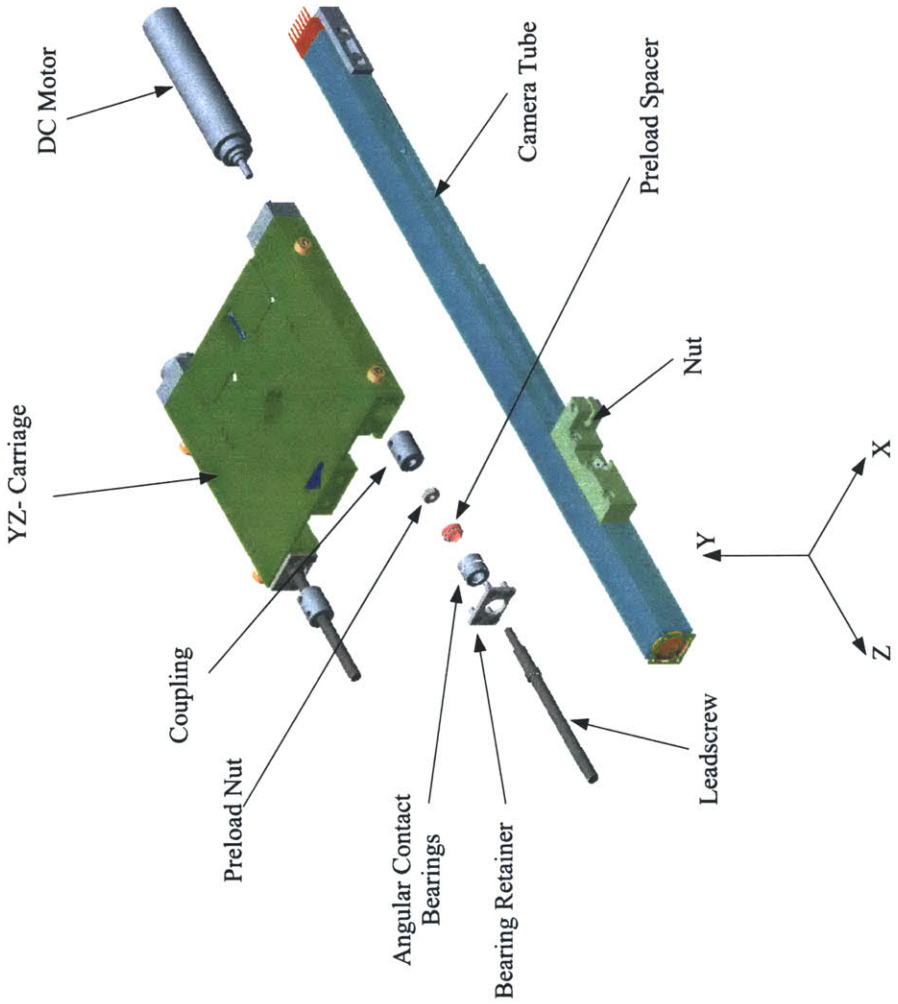

Figure 4-26: Z-axis motor assembly

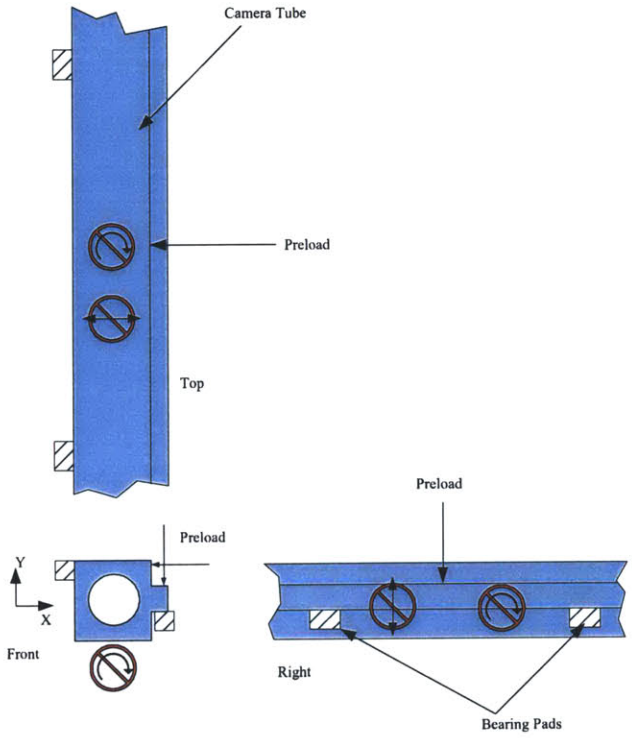

Figure 4-27: Z-axis constraints

Dynamic Model

Modeling the dynamics of the z axis is straight forward as shown in Figure 4-29. We have an effective input force F from the motor gear-head, the effective inertia comprised of the motor shaft, gear-head drive train and lead screw are modeled in $m_1 = 1.69$ Kg. The compliance between the driving mass and the camera tube mass is modeled as the series combination of leadscrew torsional and compressive stiffness and the nut stiffness. The leadscrew torsional stiffness is derived from the material shear modulus G = 80 GPa, shaft polar moment of inertia I_p and length L. Torsional stiffness is $k_t = GI_p/L = 12.4$ Nm/rad and is divided by $(l/(2\pi))^2$ to convert the stiffness from rotational to translational. l is the lead of the leadscrew (0.5 mm/rev.) which gives the effective linear stiffness of the leadscrew as 1.95E9 N/m. The compressive stiffness of the screw is $k_c = EA/L$ where E is the modulus of elasticity and A is the cross-sectional area. k_c is found

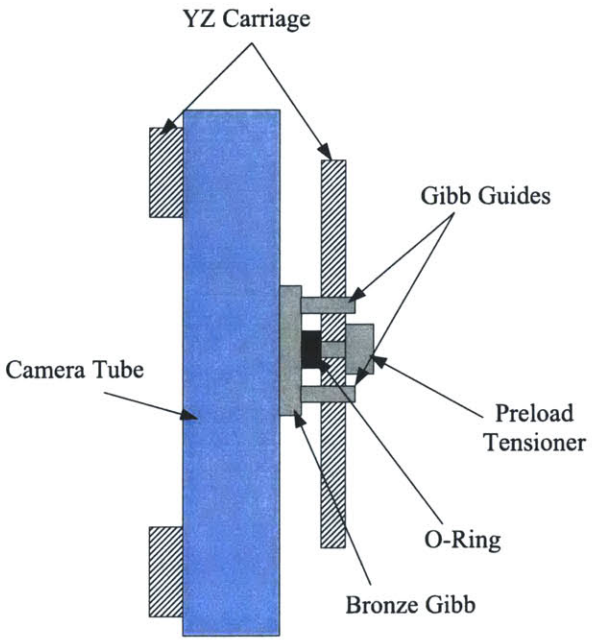

Figure 4-28: Z-axis gib design

to be 2.88E7 N/m. The effective stiffness of the nut is found using the Euler bending beam equation, and gives k_b = 1.21E6 N/m, which gives the effective linear stiffness as k = 1.16E6 N/m. The camera tube and nut are modeled as a single mass m_2 = 0.09 Kg. Subsequently, the system transfer function, Equation 4.3, shows that the z-axis bandwidth is ω_n = 586 Hz.

$$\frac{z_2}{z_1} = \frac{k}{s^2[s^2 m_1 m_2 + k(m_1 + m_2)]} \tag{4.3}$$

We have a 0.75 Watt motor driving the axis with 64:1 gear-ratio and 1024 count-per-turn quadrature encoder. Also, the lead on the leadscrew is 0.5 mm/rev., thus giving a theoretical axis resolution of 0.0076 μm/count.

4.5 Error Budget

The structural loop, Figure 4-30, starts with the first coordinate system (CS1) at the front of the lens system, and travels through each motion axis, Z, Y and X, respectively, and then back to the ferrule location for a total of 6

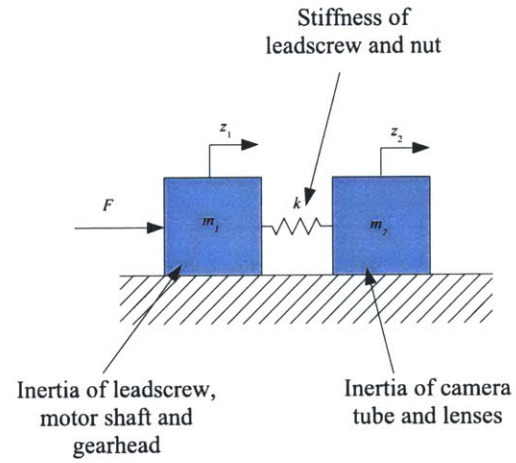

Figure 4-29: Z-axis lumped parameter dynamic model

coordinate systems. The 6 transformations between the coordinate systems comprise the error budget, all with linear transformations.

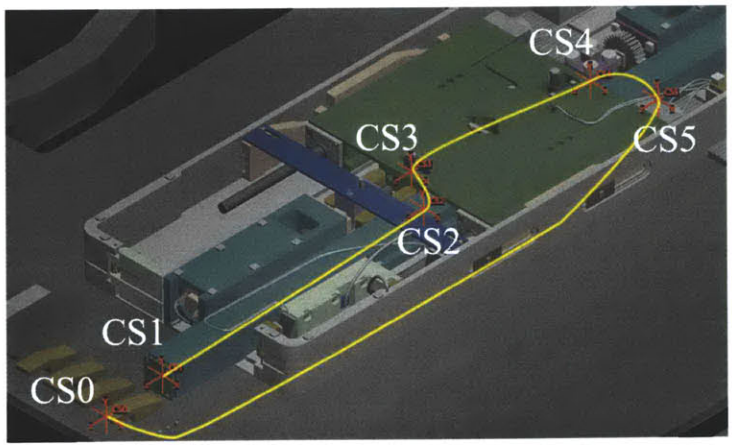

Figure 4-30: Structural loop

As previously discussed, we have 5 sensitive directions, three Cartesian and two rotational. The lenses must be positioned coaxially with the imaged fiber (± 20 μm repeatability along x axis and y axis), and focus requires ± 25 μm repeatability along the z axis. Rotation about the x axis and y axis are also sensitive as these determine how parallel we are able to place the

optic with respect to the ferrule endface. Rotation about the z axis is not sensitive as our optic is symmetric about the z axis, the image is independent of θ_z rotation. HDOF imaging requires the lenses to be parallel with the fiber endface with in at most $\pm 2°$.

4.5.1 CS1-CS2

The error budget for the transformation between CS1 and CS2, from the lens tip to the yz carriage, is computed to analyze the z-axis error motion performance, shown in Figure 4-31. The red vector corresponds to the nominal displacement between the two coordinate systems. X and Y systematic error motions are generated from camera tube and yz-carriage bearing pad locational tolerances, typically ± 200 μm. X and Y random error motions stem from the peak-to-valley error on the z-axis bearing rail (the camera tube). Because both the camera tube and yz carriage are designed to be CNC machined, we should expect the peak-to-valley error to be on the order of 5 microns. Z systematic and random error motions are due to systematic and random variations of the leadscrew and nut interface. Table 4.6 summarizes the error results, while Tables 4.7 and 4.8 provide detailed calculations.

Axes	Actual Dims.	Random errors	Systematic Errors	Units
X	**-5.0000**	**0.0050**	**0.2000**	**mm**
Y	**-1.0000**	**0.0050**	**0.2000**	**mm**
Z	**-98.2371**	**0.0100**	**0.2000**	**mm**
θ_x	**0.0000**	**0.0001**	**0.0038**	**rad**
θ_y	**0.0000**	**0.0001**	**0.0038**	**rad**
θ_z	**0.0000**	**0.0002**	**0.0058**	**rad**

Table 4.6: Camera tube to y-carriage error budget

As expected, the extended camera tube produces significant Abbe error motions in the reference coordinate system, see Table 4.9. Seemingly negligible rotations, θ_x and θ_y, are amplified by the long camera tube, giving up to ± 15 μm lens-tip random error motion as the z axis travels, just within the required ± 25 μm.

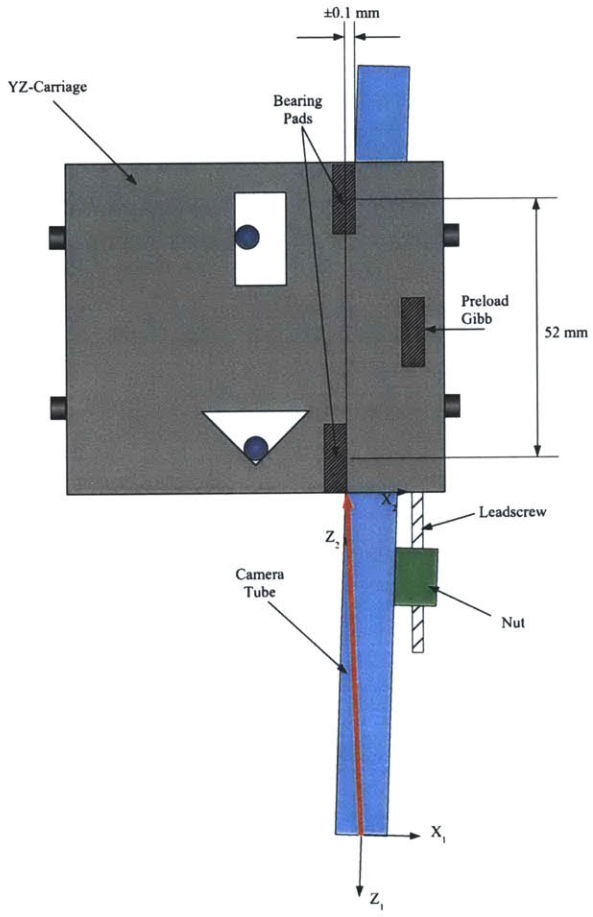

Figure 4-31: Camera tube to y-carriage

Error Motion	Description	Value	units	total
$X_{systematic}$	Camera Tube Tolerance Bearing Pad Tolerance	**1.00E-01** **1.00E-01**	mm mm	**2.00E-01**
X_{random}	Camera Tube Peak-to-Valley Error	**5.00E-03**	mm	**5.00E-03**
$Y_{systematic}$	Camera Tube Tolerance Bearing Pad Tolerance	**1.00E-01** **1.00E-01**	mm mm	**2.00E-01**
Y_{random}	Camera Tube Peak-to-Valley Error	**5.00E-03**	mm	**5.00E-03**
$Z_{systematic}$	Leadscrew Errors	**2.00E-01**	mm	**2.00E-01**
Z_{random}	Random Leadscrew Errors	**1.00E-02**	mm	**1.00E-02**

Table 4.7: CS1-CS2 Error Derivation; Cartesian

Error Motion	Description	Value	units	total
$\theta_{x_{\text{systematic}}}$	Camera Tube Tolerance	**1.00E-01**	mm	**3.85E-03**
	Bearing Pad Tolerance	**1.00E-01**	mm	
	Bearing Pad Spacing	**5.20E+01**	mm	
	t1	**3.85E-03**	rad	
$\theta_{x_{\text{random}}}$	Camera Tube Peak-To-Valley	**5.00E-03**	mm	**9.62E-05**
	Bearing Pad Spacing	**5.20E+01**	mm	
	t1	**9.62E-05**	rad	
$\theta_{y_{\text{systematic}}}$	Camera Tube Tolerance	**1.00E-01**	mm	**3.85E-03**
	Bearing Pad Tolerance	**1.00E-01**	mm	
	Bearing Pad Spacing	**5.20E+01**	mm	
	t1	**3.85E-03**	rad	
$\theta_{x_{\text{random}}}$	Camera Tube Peak-To-Valley	**5.00E-03**	mm	**9.62E-05**
	Bearing Pad Spacing	**5.20E+01**	mm	
	t1	**9.62E-05**	rad	
$\theta_{z_{\text{systematic}}}$	Camera Tube Tolerance	**2.00E-01**	mm	**5.77E-03**
	Bearing Pad Tolerance	**1.00E-01**	mm	
	Bearing Pad Spacing	**5.20E+01**	mm	
	t1	**5.77E-03**	rad	
$\theta_{z_{\text{random}}}$	Camera Tube Peak-To-Valley	**1.00E-02**	mm	**1.92E-04**
	Bearing Pad Spacing	**5.20E+01**	mm	
	t1	**1.92E-04**	rad	

Table 4.8: CS1-CS2 Error Derivation; Angular

Sum Random Errors For Z-axis Motion in the Reference CS	
δX	**0.0146**
δY	**0.0120**
δZ	**0.0165**
ϵX (rad)	**0.0001**
ϵY (rad)	**0.0001**
ϵZ (rad)	**0.0002**

Table 4.9: Sum random errors for z axis

4.5.2 CS2-CS3

Figure 4-32 depicts the coordinate transformation between CS2 and CS3, detailing the y-axis motions between the yz carriage and the front ballguide. As previously discussed, a leadscrew and nut drive the ramps back and forth along $\hat{z}$, and due to bearing constraints the yz carriage subsequently travels up and down along $\hat{y}$. The guideballs provide a rotational and two translational constraints and the combination of the spring preload and the moving ramps preloads the yz carriage against the guideballs.

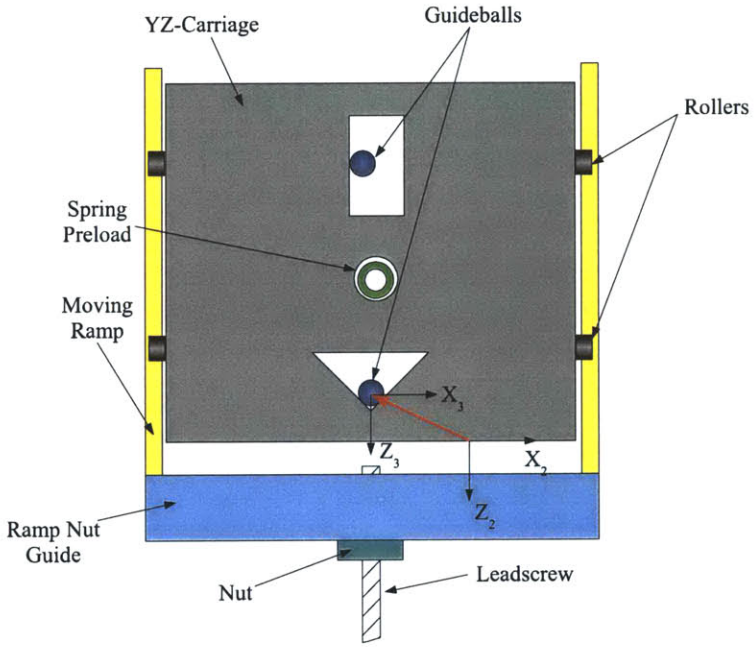

Figure 4-32: YZ-carriage error budget

Figure 4-33 shows how manufacturing tolerances on the ballguide diameter, vee angle, and vee location determine $X_{systematic}$, $Z_{systematic}$, and $\theta_{y_{systematic}}$ error motions. Assuming that the ballguides are in point contact with the vee-and-flat, X_{random}, Z_{random}, and $\theta_{y_{random}}$ error motions are dictated by the vee-and-flat's surface roughness.

Figure 4-34 shows $Y_{systematic}$ and $\theta_{x_{systematic}}$ error motions are caused by the locational tolerance on the yz-carriage roller mount, roller roundness errors, ramp form errors, and base-carriage form errors. The respective

random error motions are due to the combination of roller roundness errors, ramp peak-to-valley errors, and ramp to base-carriage peak-to-valley errors.

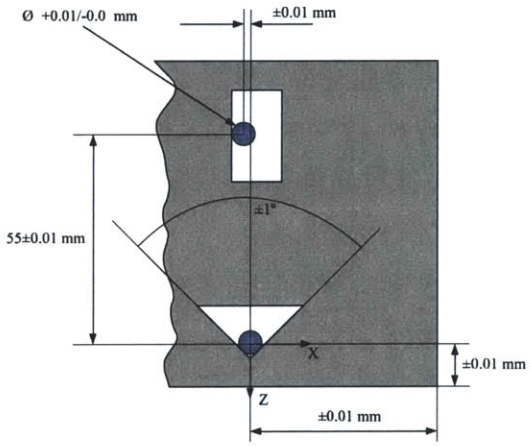

Figure 4-33: Y-carriage vee to ballguide rotational tolerance errors

$\theta_{z_{\text{systematic}}}$ error motions are also comprised of locational tolerance of the yz-carriage roller mount, roller roundness errors, ramp form errors and base-carriage form errors in addition to the ramp nut guide angular error. The $\theta_{z_{\text{random}}}$ error motions occur due to roller roundness errors, ramp peak-to-valley errors, base-carriage peak-to-valley errors and the nut and leadscrew straightness errors.

Table 4.10 shows the displacement vector between CS2 and CS3 along with the corresponding systematic and random error motions. Detailed calculations are provided in Tables 4.11, 4.12, 4.13 and 4.14.

Axes	Actual Dims.	Random errors	Systematic Errors	Units
X	**-8.0000**	**0.0050**	**0.0950**	**mm**
Y	**5.5386**	**0.0200**	**0.0800**	**mm**
Z	**-3.7000**	**0.0050**	**0.0950**	**mm**
θ_x	**0.0000**	**0.0001**	**0.0027**	**rad**
θ_y	**0.0000**	**0.0001**	**0.0017**	**rad**
θ_z	**0.0000**	**0.0002**	**0.0019**	**rad**

Table 4.10: Camera tube to yz-carriage error budget

Resultant error motions at the lens-tip can be seen in Table 4.15. Again, we have significant Abbe error motions due to the small rotations at CS3, but during a y traversal the system should stay fairly well centered. As

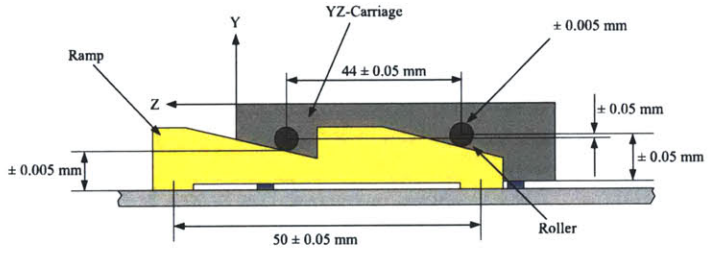

(a) Y-axis Side View

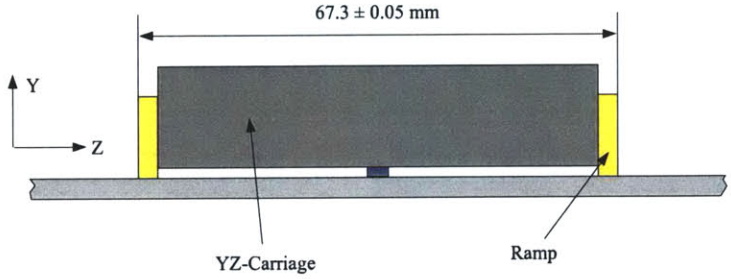

(b) Y-axis Front View

Figure 4-34: Y-carriage roller and ramp tolerances

expected we see ± 15 μm random motions along $\hat{x}$, and a slight defocus of ± 10 μm, which are both within the functional requirements.

Error Motion	Description	Value	units	total
$X_{systematic}$	Vee Locational Tolerance	**0.0500**	mm	**0.0950**
	Guideball Diametral Tolerance	**0.0100**	mm	
	Vee Angle Tolerance	**0.0350**	mm	
X_{random}	Vee and Flat Surface Roughness	**0.0050**	mm	**0.0050**
$Y_{systematic}$	Wheel Mount Location Tolerance	**0.0500**	mm	**0.0800**
	Roller Roundness	**0.0100**	mm	
	Ramp Form Errors	**0.0100**	mm	
	Base-Carriage Thickness Tolerance	**0.0100**	mm	
Y_{random}	Roller Wheel ID	**0.0050**	mm	**0.0200**
	Roller Wheel OD	**0.0050**	mm	
	Ramp Peak-to-Valley	**0.0050**	mm	
	Base-Carriage Peak-to-Valley	**0.0050**	mm	
$Z_{systematic}$	Vee Locational Tolerance	**0.0500**	mm	**0.0950**
	Guideball Diametral Tolerance	**0.0100**	mm	
	Vee Angle Tolerance	**0.0350**	mm	
Z_{random}	Vee and Flat Surface Roughness	**0.0050**	mm	**0.0050**

Table 4.11: CS2-CS3 Error Derivation; Cartesian

Error Motion	Description	Value	units	total
$\theta_{x_{\text{systematic}}}$	Roller locational Tolerance	**5.00E-02**	mm	**2.70E-03**
	Roller Roundness Errors	**5.00E-02**	mm	
	Ramp Form Errors	**1.00E-02**	mm	
	Roller Spacing	**4.40E+01**	mm	
	t1	**2.50E-03**	rad	
	Base Carriage Form Errors	**1.00E-02**	mm	
	Ramp Bearing Pad Spacing	**5.00E+01**	mm	
	t2	**2.00E-04**	rad	
$\theta_{x_{\text{random}}}$	Roller Wheel ID	**1.00E-03**	mm	**6.55E-05**
	Roller Wheel OD	**1.00E-03**	mm	
	Roller Spacing	**4.40E+01**	mm	
	t1	**4.55E-05**	rad	
	Base Carriage Peak-to-Valley Errors	**1.00E-03**	mm	
	Ramp Bearing Pad Spacing	**5.00E+01**	mm	
	t2	**2.00E-05**	rad	

Table 4.12: CS2-CS3 Error Derivation; Angular θ_x

Error Motion	Description	Value	units	total
$\theta_{y_{\text{systematic}}}$	Vee Locational Tolerance	**5.00E-02**	mm	**1.73E-03**
	Guideball Diametral Tolerance	**1.00E-02**	mm	
	Vee Angle Tolerance	**3.50E-02**	mm	
	Guideball Spacing	**5.50E+01**	mm	
	t1	**1.73E-03**	rad	
$\theta_{y_{\text{random}}}$	Vee and Flat Surface Roughness	**5.00E-03**	mm	**9.09E-05**
	Guideball Spacing	**5.50E+01**	mm	
	t1	**9.09E-05**	rad	

Table 4.13: CS2-CS3 Error Derivation; Angular θ_y

Error Motion	Description	Value	units	total
$\theta_{z_{\text{systematic}}}$	Wheel Mount Location Tolerance	**5.00E-02**	mm	**1.89E-03**
	Roller Roundness	**1.00E-02**	mm	
	Ramp Form Errors	**1.00E-02**	mm	
	Roller Spacing	**4.40E+01**	mm	
	t1	**1.59E-03**	rad	
	Base-Carriage Thickness Tolerance	**1.00E-02**	mm	
	Ramp Bearing Pad Spacing	**5.00E+01**	mm	
	t2	**2.00E-04**	rad	
	Nut Misalignment	**1.00E-04**	rad	
$\theta_{z_{\text{random}}}$	Roller Wheel ID	**1.00E-03**	mm	**1.88E-04**
	Roller Wheel OD	**1.00E-03**	mm	
	Ramp Peak-to-Valley Errors	**1.00E-03**	mm	
	Roller Spacing	**4.40E+01**	mm	
	t1	**6.82E-05**	rad	
	Base Carriage Peak-to-Valley Errors	**1.00E-03**	mm	
	Ramp Bearing Pad Spacing	**5.00E+01**	mm	
	t2	**2.00E-05**	rad	
	Nut Wiggle	**1.00E-04**	rad	

Table 4.14: CS2-CS3 Error Derivation; Angular θ_z

Sum Random Errors For Y-axis Motion in the Reference CS	
δX	**0.0151**
δY	**0.0265**
δZ	**0.0107**
ϵX (rad)	**0.0001**
ϵY (rad)	**0.0001**
ϵZ (rad)	**0.0002**

Table 4.15: Sum random errors for y axis

4.5.3 CS3-CS4

The transformation between CS3 and CS4, shown in Figure 4-35, details the error motions between the ballguide and the vee wheel. The Cartesian systematic errors stem from locational tolerances on the ballguide with respect to the base-carriage and the vee-wheel bearing mount with respect to the base-carriage. Random error motions along the Cartesian directions come from the angular-contact bearings in which the vee-wheel spins.
Rotational systematic errors are due to parallelism errors between the ballguide and angular-contact bearing-mount, also between the angular-contact bearing inner-race and outer-race. Random rotational errors stem from groove-wobble on the inner and outer bearing races. Table 4.16 presents the transformation results while detailed calculations can be found in Tables 4.17, 4.18, 4.19 and 4.20.

Axes	Actual Dims.	Random errors	Systematic Errors	Units
X	**1.35E+01**	**0.0076**	**0.5500**	**mm**
Y	**-4.09E+00**	**0.0025**	**0.2000**	**mm**
Z	**-1.03E+01**	**0.0076**	**0.5500**	**mm**
θ_x	**0.0000**	**0.0002**	**0.0023**	**rad**
θ_y	**0.0000**	**0.0000**	**0.0000**	**rad**
θ_z	**0.0000**	**0.0002**	**0.0016**	**rad**

Table 4.16: Ballguide to vee wheel error budget

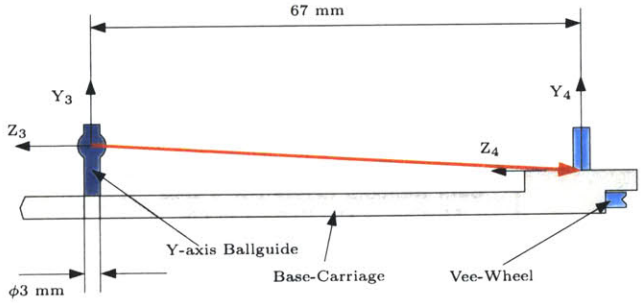

Figure 4-35: Pin 2 wheel

Error Motion	Description	Value	units	total
$X_{systematic}$	Guideball Locational Tolerance	**5.00E-01**	mm	**5.50E-01**
	Vee-Wheel Bearing Mount Locational Tolerance	**5.00E-02**	mm	
X_{random}	Bearing Outer Race Radial Runout	**3.81E-03**	mm	**7.62E-03**
	Bearing Inner Race Radial Runout	**1.27E-03**	mm	
	Bore Runout With side	**1.27E-03**	mm	
	Raceway Runout With Side	**1.27E-03**	mm	
$Y_{systematic}$	Guideball Height Tolerance	**1.00E-01**	mm	**2.00E-01**
	Base-Carriage Height Tolerance	**5.00E-02**	mm	
	Vee-Wheel Height Tolerance	**5.00E-02**	mm	
Y_{random}	Angular Contact Bearing Axial Runout of preloaded set	**2.54E-03**	mm	**2.54E-03**
$Z_{systematic}$	Guideball Locational Tolerance	**5.00E-01**	mm	**5.50E-01**
	Vee-Wheel Bearing Mount Locational Tolerance	**5.00E-02**	mm	
Z_{random}	Bearing Outer Race Radial Runout	**3.81E-03**	mm	**7.62E-03**
	Bearing Inner Race Radial Runout	**1.27E-03**	mm	
	Bore Runout With side	**1.27E-03**	mm	
	Raceway Runout With Side	**1.27E-03**	mm	

Table 4.17: CS3-CS4 Error Derivation; Cartesian

Error Motion	Description	Value	units	total
$\theta_{x_{\text{systematic}}}$	Bearing O.D. runout with side	**1.27E-03**	mm	**2.26E-03**
	Bearing ID runout with side	**1.27E-03**	mm	
	Outer race thickness	**2.78E+00**	mm	
	t1	**4.57E-04**	rad	
	Outer-Race Runout With side (Groove Wobble)	**0.00254**	mm	
	outer-Race OD	**6.35**	mm	
	t2	**4.00E-04**	rad	
	Inner-Race Runout With side (Groove Wobble)	**1.27E-03**	mm	
	Inner-Race OD	**3.18E+00**	mm	
	t3	**4.00E-04**	rad	
	Parallelism	**2.00E-04**	rad	
	Guideball Parallelism with Base-Carriage	**1.00E-03**	rad	
$\theta_{x_{\text{random}}}$	Bearing O.D. runout with side	**1.27E-04**	mm	**1.51E-04**
	Bearing ID runout with side	**1.27E-04**	mm	
	Outer race thickness	**2.78E+00**	mm	
	t1	**9.14E-05**	rad	
	Outer-Race Runout With side (Groove Wobble)	**0.000254**	mm	
	outer-Race OD	**6.35**	mm	
	t2	**4.00E-05**	rad	
	Inner-Race Runout With side (Groove Wobble)	**4.06E-03**	mm	
	Inner-Race OD	**3.18E+00**	mm	
	t3	**1.28E-03**	rad	
	Parallelism	**2.00E-05**	rad	

Table 4.18: CS3-CS4 Error Derivation; Angular θ_x

Error Motion	Description	Value	units	total
$\theta_{y_{\text{systematic}}}$	NA	**0.00E+00**	rad	**0.00E+00**
$\theta_{y_{\text{random}}}$	NA	**0.00E+00**	rad	**0.00E+00**

Table 4.19: CS3-CS4 Error Derivation; Angular θ_y

Error Motion	Description	Value	units	total
$\theta_{z_{\text{systematic}}}$	Bearing O.D. runout with side	**1.27E-03**	mm	**1.61E-03**
	Bearing ID runout with side	**1.27E-03**	mm	
	Outer race thickness	**2.78E+00**	mm	
	t1	**9.14E-04**	rad	
	Outer-Race Runout With side (Groove Wobble)	**0.00254**	mm	
	outer-Race OD	**6.35**	mm	
	t2	**4.00E-04**	rad	
	Inner-Race Runout With side (Groove Wobble)	**4.06E-02**	mm	
	Inner-Race OD	**3.18E+00**	mm	
	t3	**1.28E-02**	rad	
	Parallelism	**2.00E-04**	rad	
	Guideball Parallelism with Base-Carriage	**1.00E-04**	rad	
$\theta_{z_{\text{random}}}$	Bearing O.D. runout with side	**1.27E-04**	mm	**1.51E-04**
	Bearing ID runout with side	**1.27E-04**	mm	
	Outer race thickness	**2.78E+00**	mm	
	t1	**9.14E-05**	rad	
	Outer-Race Runout With side (Groove Wobble)	**0.000254**	mm	
	outer-Race OD	**6.35**	mm	
	t2	**4.00E-05**	rad	
	Inner-Race Runout With side (Groove Wobble)	**1.27E-04**	mm	
	Inner-Race OD	**3.18E+00**	mm	
	t3	**4.00E-05**	rad	
	Parallelism	**2.00E-05**	rad	

Table 4.20: CS3-CS4 Error Derivation; Angular θ_z

4.5.4 CS4-CS5

The transformation between CS4 and CS5 is shown in Figure 4-36. As before, systematic errors are generally based on geometrical tolerances, while random errors stem from peak-to-valley errors upon the geometrical tolerance, therefore for this transformation the error motions are defined as follows:

- $X_{systematic}$ errors are a function of the pinion's effective pitch diameter, while the X_{random} errors stem from random variations in the pinion's effective pitch diameter.
- $Y_{systematic}$ errors stem from the vee-wheel's and rack's dimensional tolerances, while the Y_{random} errors are a function of the vee-wheel's runout with height and the rack's peak-to-valley height error.
- $Z_{systematic}$ errors are the combination of vee-wheel radial tolerance and rack-width tolerance, while the Z_{random} error motions stem from vee-wheel radial runout and peak-to-valley rack-width errors.
- $\theta_{x_{systematic}}$ errors are a combination vee-wheel height tolerance across the three vee-wheels and rack parallelism errors, while $\theta_{x_{random}}$ errors are simply the equivalent peak-to-valley errors on the three vee-wheel heights and the rack parallelism.
- $\theta_{y_{systematic}}$ errors are a combination of the vee-wheels' radial tolerances, and the rack width, while $\theta_{y_{random}}$ error motions are due to the combination of the vee-wheel radial runout and peak-to-valley rack-width.
- $\theta_{z_{systematic}}$ errors are a combination of three vee-wheels height tolerance and the rack-height tolerance, while $\theta_{z_{random}}$ errors are the combination of vee-wheel runout with height and the peak-to-valley rack height.

Consult Table 4.21 for error motion quantification.

As previously discussed, the combination of transformations between CS3-CS4 and CS4-CS5 predict the x-axis error motions, as listed in Table 4.25. This axis should produce high Cartesian error motions on the order of ± 50 μm but rather low angular error motions. Experience with the bench-top system showed that we are mainly concerned about local resolution. If the error motions occur at low frequencies, then *dead reckoning* will still allow us to traverse to each fiber.

Axes	Actual Dims.	Random errors	Systematic Errors	Units
X	**0.00E+00**	**0.0100**	**0.1100**	**mm**
Y	**2.12E+00**	**0.0100**	**0.1000**	**mm**
Z	**1.96E+02**	**0.0100**	**0.1000**	**mm**
θ_x	**0.0000**	**0.0002**	**0.0020**	**rad**
θ_y	**0.0000**	**0.0002**	**0.0016**	**rad**
θ_z	**0.0000**	**0.0005**	**0.0053**	**rad**

Table 4.21: Vee-wheel to rack error budget

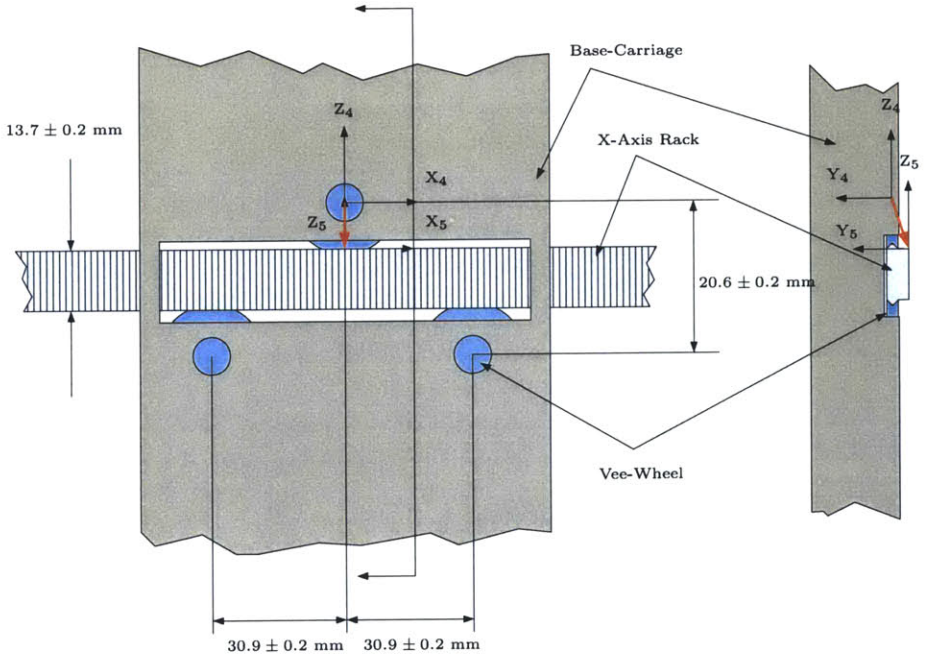

Figure 4-36: Error budget: rack/carriage interface

Error Motion	Description	Value	units	total
$X_{systematic}$	Pitch Diameter Tolerance	**1.00E-01**	mm	**1.10E-01**
X_{random}	Pitch Diameter Random Tolerance	**1.00E-02**	mm	**1.00E-02**
$Y_{systematic}$	Vee-Wheel Height Tolerance Rack Height Tolerance	**5.00E-02** **5.00E-02**	mm mm	**1.00E-01**
Y_{random}	Vee Wheel Runout with Side Rack Height Peak-to-Valley	**5.00E-03** **5.00E-03**	mm mm	**1.00E-02**
$Z_{systematic}$	Vee-Wheel Radial Tolerance Rack Width Tolerance	**5.00E-02** **5.00E-02**	mm mm	**1.00E-01**
Z_{random}	Vee-Wheel Radial Runout Rack Width Peak-to-Valley	**5.00E-03** **5.00E-03**	mm mm	**1.00E-02**

Table 4.22: CS4-CS5 Error Derivation; Cartesian

Error Motion	Description	Value	units	total
$\theta_x$systematic	Vee-Wheel Height Tolerance	**5.00E-02**	mm	**2.03E-03**
	Distance Between Wheels	**2.06E+01**	mm	
	t1	**2.43E-03**	rad	
	Rack Height Tolerance	**5.00E-02**	mm	
	Rack Width	**1.37E+01**	mm	
	t2	**3.65E-03**	rad	
	number of wheels	**3.00E+00**		
$\theta_x$random	Vee-Wheel Runout with Side	**5.00E-03**	mm	**2.03E-04**
	Distance Between Wheels	**2.06E+01**	mm	
	t1	**2.43E-04**	rad	
	Rack Height Peak-to-Valley Tolerance	**5.00E-03**	mm	
	Rack Width	**1.37E+01**	mm	
	t2	**3.65E-04**	rad	
	number of wheels	**3.00E+00**		
$\theta_y$systematic	Vee-Wheel Radial Tolerance	**5.00E-02**	mm	**1.62E-03**
	Rack Width Tolerance	**5.00E-02**	mm	
	Wheel Spacing	**6.18E+01**	mm	
	t1	**1.62E-03**	rad	

Table 4.23: CS4-CS5 Error Derivation; Angular θ_x and θ_y

Error Motion	Description	Value	units	total
$\theta_{y_{\text{random}}}$	Vee-Wheel Radial Runout	**5.00E-03**	mm	**1.62E-04**
	Rack Width Peak-to-Valley	**5.00E-03**	mm	
	wheel Spacing	**6.18E+01**	mm	
	t1	**1.62E-04**	rad	
$\theta_{z_{\text{systematic}}}$	Vee-Wheel Height Tolerance	**5.00E-02**	mm	**5.29E-03**
	Spacing	**3.09E+01**	mm	
	t1	**1.62E-03**	rad	
	Rack Height Tolerance	**5.00E-02**	mm	
	Rack Width	**1.36E+01**	mm	
	t2	**3.68E-03**	rad	
$\theta_{z_{\text{random}}}$	Vee-Wheel Runout with Height	**5.00E-03**	mm	**5.27E-04**
	Spacing	**3.09E+01**	mm	
	t1	**1.62E-04**	rad	
	Rack Height Peak-to-Valley	**5.00E-03**	mm	
	Rack Width	**1.37E+01**	mm	
	t2	**3.65E-04**	rad	

Table 4.24: CS4-CS5 Error Derivation; Angular θ_y and θ_z

Sum Random Errors For X-Axis Motion in the Reference CS	
δX	**0.0482**
δY	**0.0537**
δZ	**0.0560**
ϵX (rad)	**0.0004**
ϵY (rad)	**0.0002**
ϵZ (rad)	**0.0007**

Table 4.25: Sum random errors for x axis

4.6 Experimental Verification

4.6.1 Repeatability and Resolution

A Lion Precision capacitance gauge, model C1-A, recorded all measurements. It is capable of 0.5 μm resolution and 1.5 mm travel and its output voltage was recorded with a 12-bit A/D converter with ± 10 V range. Measurement accuracy is on the order of ± 1LSB $= 0.7$ μm. Unless otherwise stated, all measurements were recorded at the lens tip with the camera-tube in the fully extended position to include all Abbe errors in the measurement. For example, the $\hat{x}$ error motions measurement setup can be seen in Figure 4-37, that for $\hat{y}$ in Figure 4-38 and that for $\hat{z}$ in Figure 4-39.

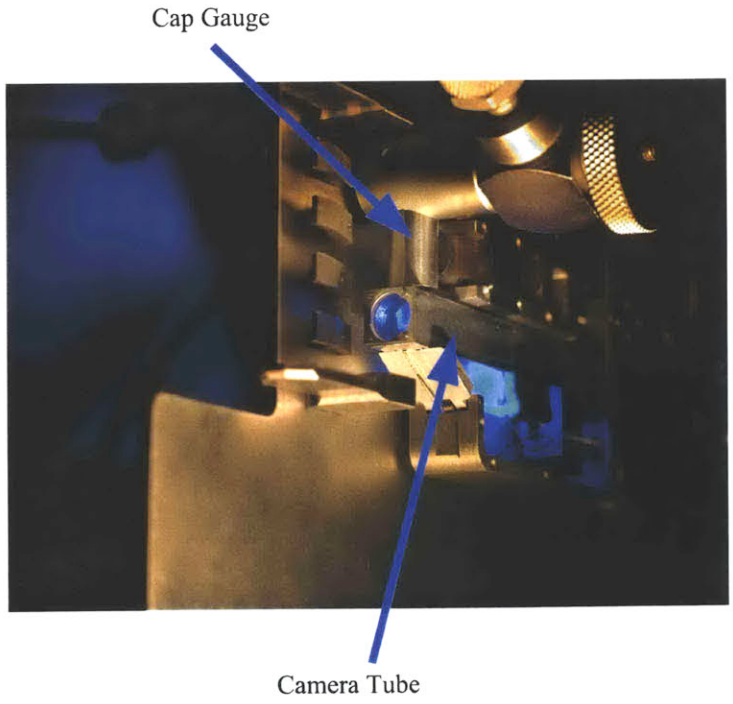

Figure 4-37: $\hat{x}$ motion measurement, capacitance gauge location

A typical repeatability test trajectory can be seen in Figure 4-40, consisting of the following steps:

1. start axis at encoder position 0

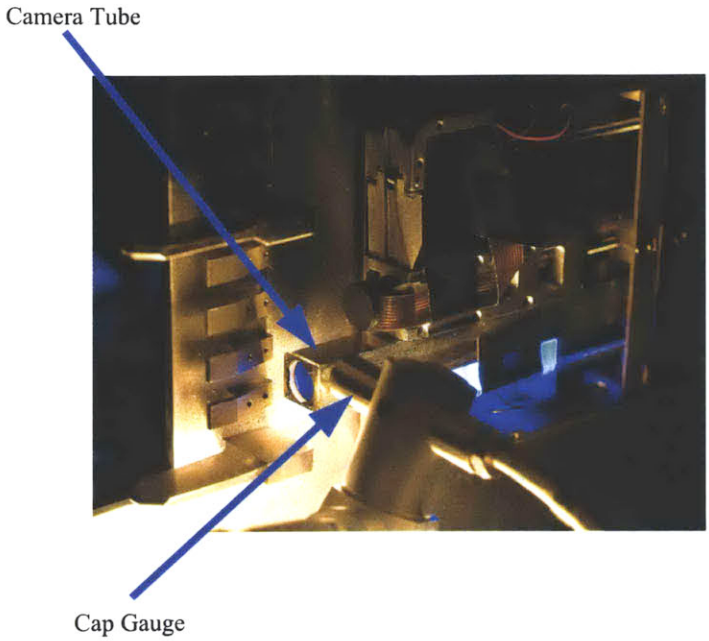

Figure 4-38: $\hat{y}$ motion measurement, capacitance gauge location

2. move axis to a positive random encoder position
3. move axis back to encoder position 0
4. move axis to a negative random encoder position
5. move axis back to encoder position 0
6. repeat steps 2 through 5

Resolution was measured by sweeping the axis through its travel while recording the lens tip position with the capacitance gauge and motor encoder position. Average resolution was computed as the measured capacitance gauge displacement divided by the measured encoder position.

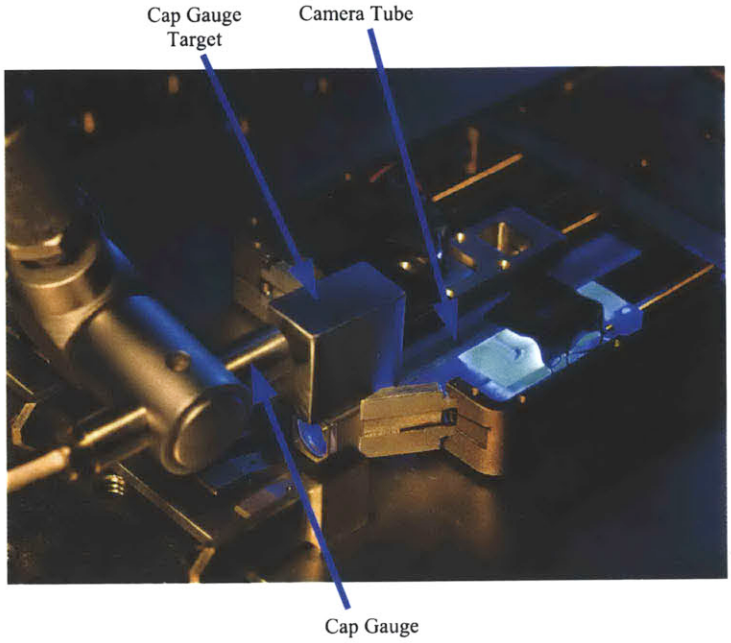

Figure 4-39: $\hat{z}$ motion measurement, capacitance gauge location

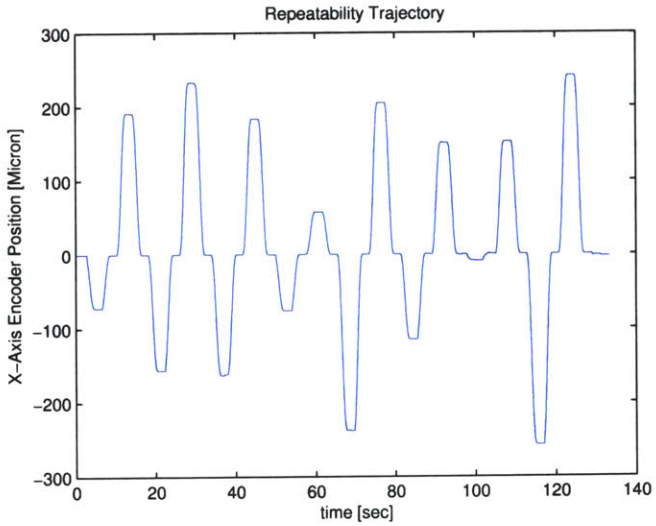

Figure 4-40: Repeatability trajectory

X Axis

The x-axis repeatability measurement results, Figure 4-41, show a clear bi-modal distribution with the two modes nearly straddling the zero-point. The two modes come from drive-train backlash. The small distribution in the middle is due to a random motion to a distance smaller than the backlash. The backlash specifications on the motor gear head predict 1.8° movement and with a 12 mm pitch-diameter pinion, x-axis backlash is predicted to be ± 94 μm. We are well below that and it is probably a combination of the manufacturer beating their specification and the moment loading on the pinion due to the rack being transmitted into the gearbox. Implementing backlash compensation reduces the repeatability from ± 15 μm down to ± 8 μm as shown in Figure 4-42, which is much better than the ± 25 μm repeatability from the functional requirements.

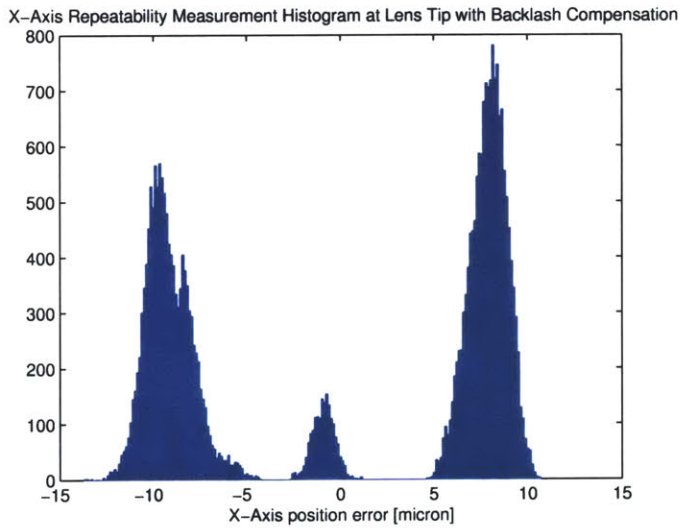

Figure 4-41: X-axis repeatability histogram

The average system resolution measured by sweeping the axis through its travel equals 0.138 ± 4 μm/cnt, where the theoretical is 0.134 ± 11 μm/cnt, which is clearly good enough for the functional requirements. The error motion from this measurement can be seen in Figure 4-43.

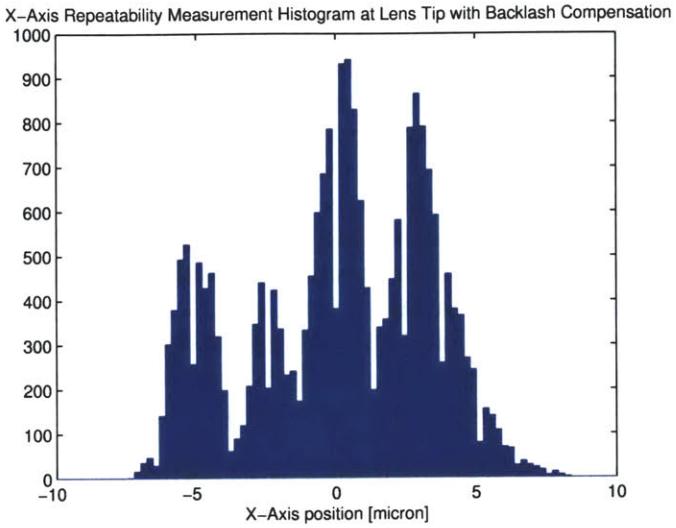

Figure 4-42: X-axis repeatability histogram with backlash compensation

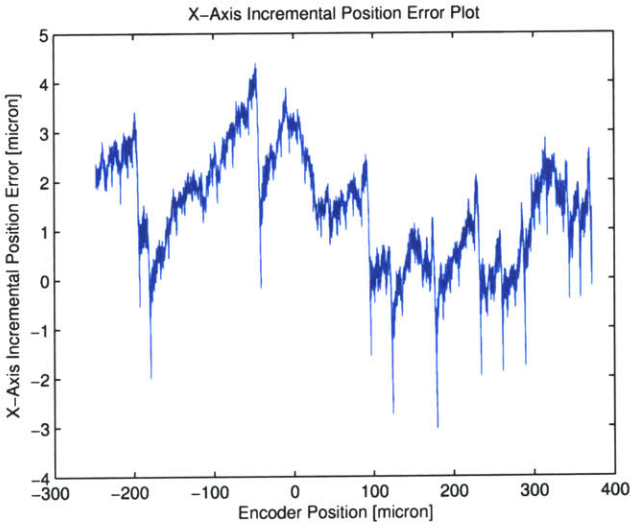

Figure 4-43: X axis average resolution error

Y Axis

The y-axis repeatability results, Figure 4-44, show a distinct bimodal distribution, due to actuator backlash. The gearhead backlash is on the order of 2.2° and passing through the leadscrew and roller ramps, the yz carriage should exhibit backlash on the order of ± 1.11 μm. The data shown below is much worse than this indicating that the leadscrew nut, hard mount coupling and setscrews may have loosened giving much higher backlash. Implementing blacklash motion control reduces the backlash from ± 45 μm to ± 4 μm, as shown in Figure 4-45, bringing the axis to well within the functional requirements.

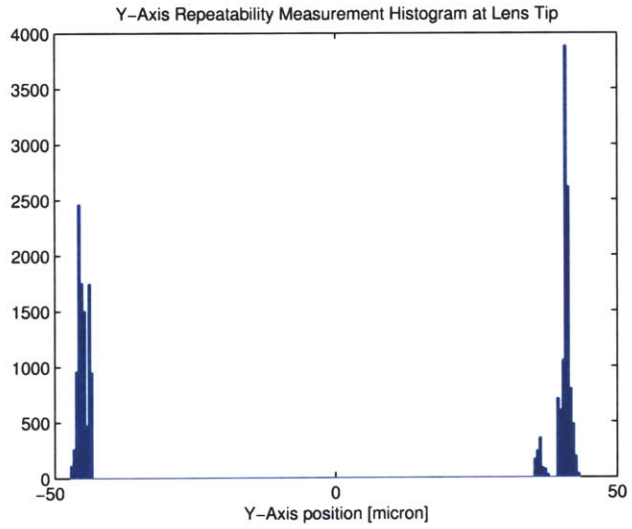

Figure 4-44: Y-axis repeatability histogram

Locking the y-axis rollers such that they effectively are sliding contact bearings drastically reduced the error motions. The average system resolution measured by sweeping the axis through its travel results in 0.0028 ± 4 μm, which meets the 5 μm functional requirement. The error motion measured during the resolution test can be seen in Figure 4-46.

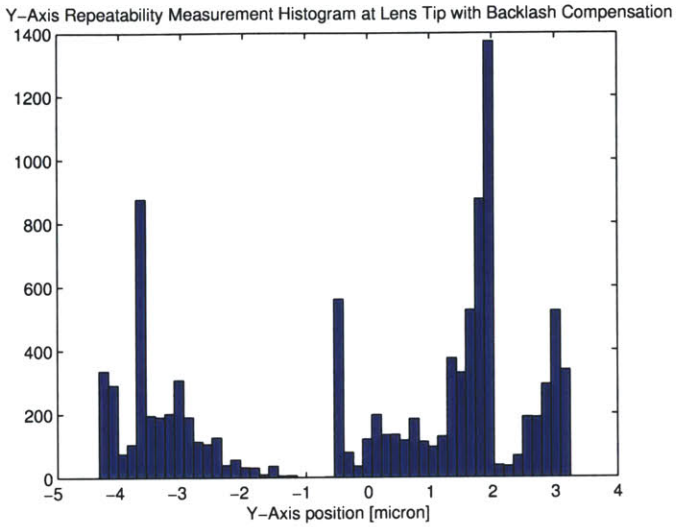

Figure 4-45: Y-axis repeatability histogram with backlash compensation

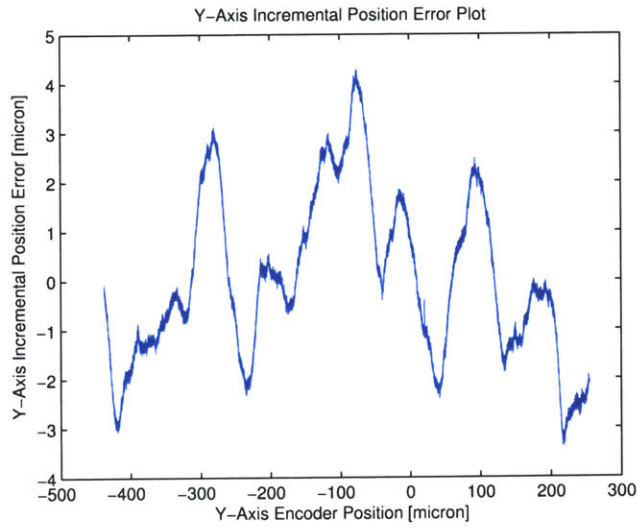

Figure 4-46: Y axis average resolution error

Z-Axis

The z-axis repeatability test results, Figure 4-47, show a clear bimodal distribution due to actuator backlash. The few points that lie between the two modes are due to movements smaller than the actuator backlash. The gearhead backlash specifications are 2.2°, therefore at the lens tip we should see 3 μm backlash. The data shown below indicates much worse backlash, the hard mount coupling and nut may have loosened up explaining the high backlash results. With backlash compensation, the repeatability is reduced from ± 150 μm to ± 4 μm, well within the ± 25 μm from functional requirements. This is due to backlash in from the motor gearhead and backlash in the coupling between the gearhead and the leadscrew.

The average z-axis resolution measured by sweeping the axis through its travel was found to be $0.0076 \pm 9\mu$m, which is also within the functional requirements. The error motion from this measurement can be seen in Figure 4-49. We see that the 0.5 mm lead of the leadscrew causing the majority of the error motion.

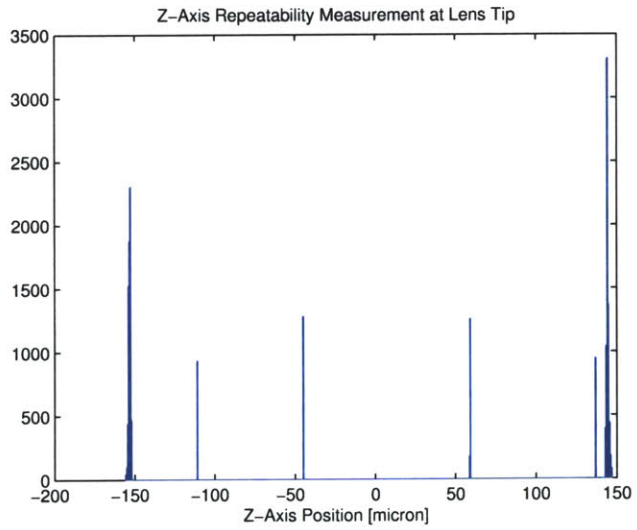

Figure 4-47: Z-axis repeatability histogram

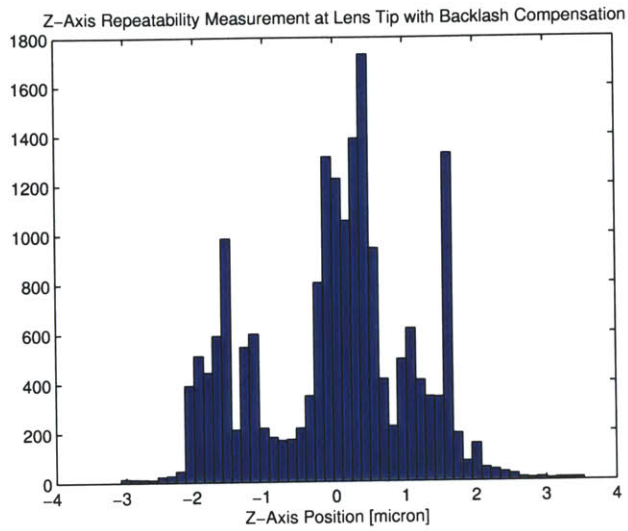

Figure 4-48: Z-axis repeatability histogram with backlash compensation

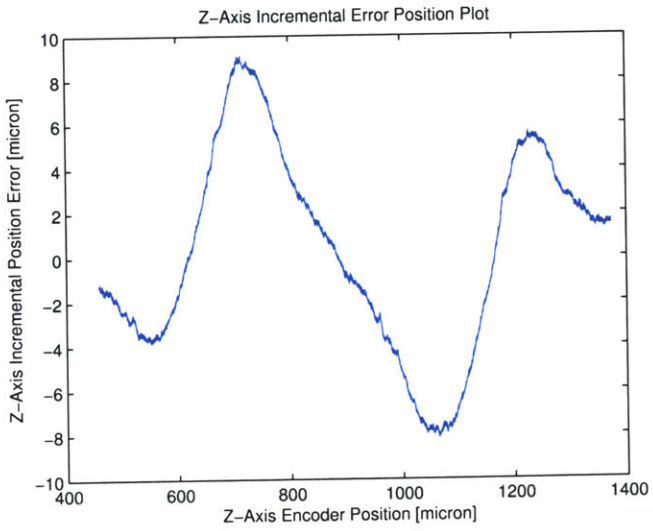

Figure 4-49: Z-axis average resolution error

4.6.2 System Dynamics

Experimental system identification was used to correlate system dynamics with the transfer functions presented earlier in the chapter. Sine-sweep tests are typically used for most mechanical system identification experiments [94], but in practice these proved difficult to accurately implement due to high actuator backlash. To ensure that the inertia dynamics are measured correctly, the actuator must move each axis substantially beyond the backlash. At higher frequencies this becomes difficult as the input torque required to move the axis beyond the backlash is rather high and the amplifier saturates and eventually shuts-down due to heat overload, thus giving inaccurate measurement results.

X Axis

System step response has been shown to be quite effective at measuring system performance such as bandwidth, damping and settling time [95]. An example of the x-axis velocity step-response can be seen in Figure 4-50, where the x's correspond to the measured data points and the line is the fitted model response.

The system has significant friction and dissipative effects, and for simplicity we'll model it as viscous damping. Recalling the model derived earlier in the chapter, Equation 4.1, and adding viscous damping terms between each mass and ground we arrive at

$$\frac{\dot{\theta}_1}{T_1} = \frac{s^2 J_2 + b_2 s + k}{s^3 J_1 J_2 + s^2(b_2 J_1 + b_1 J_2) + s(k(J_1 + J_2) + b_1 b_2) + k(b_1 + b_2)} \tag{4.4}$$

This transfer function was then fit to the data using b_1 and b_2 as the variables (J_1, J_2 and k were calculated based on the CAD models.)

The x-axis velocity step response appears to be 1^{st} order, dominated by the dissipative effects between the rack-and-pinion and the vee wheels, modeled as a viscous damper b_2, and the mass of the carriage J_2, as the time constant $\tau = J_2/b_2 = 0.0135$ seconds. The x-axis settling time is $4\tau = 0.05$ seconds which is close to the 0.05 second settling time from functional requirements. Being that the system has such high friction it is quite difficult to experimentally determine the system bandwidth from a step-response. We must reduce damping to increase the settling time, which can be accomplished by reducing pinion preload against the rack.

An example of a ferrule-to-ferrule x-axis movement can be seen in Fig-

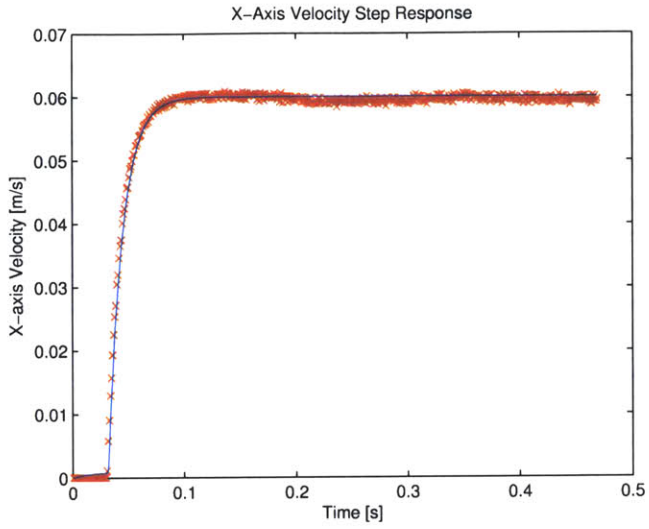

Figure 4-50: X-axis velocity step response

ure 4-51. Even though the x-axis's settling time is a little high, with a smooth position trajectory the axis meets the functional requirements. The measured motion shows the axis moves 6 mm in 1 second, which is significantly better than the 3 mm in 12 seconds specified by the functional requirements.

Y-Axis

The y-axis velocity step response can be seen in Figure 4-52. It appears to be first order due the high damping and friction between each of the moving components, the nut and bronze-gib, and the ramps and the base-carriage.

Recalling the system transfer function, Equation (4.2), we noted that the dynamics were dominated by the mass of the yz carriage and the effective stiffness of the four rollers on which it rides. The system simplifies as shown in Figure 4-53, giving the transfer function

$$\frac{\dot{y}_1}{F_1} = \frac{s^2 m_2 + b_2 s + k}{s^3 m_1 m_2 + s^2(b_2 m_1 + b_1 m_2) + s[k(m_1 + m_2) + b_1 b_2] + k(b_1 + b_2)} \tag{4.5}$$

where m_1 is the effective inertia of the leadscrew, motor shaft, gearhead, nut, nut-wing preload, and ramps, m_2 is the effective inertia of the yz carriage,

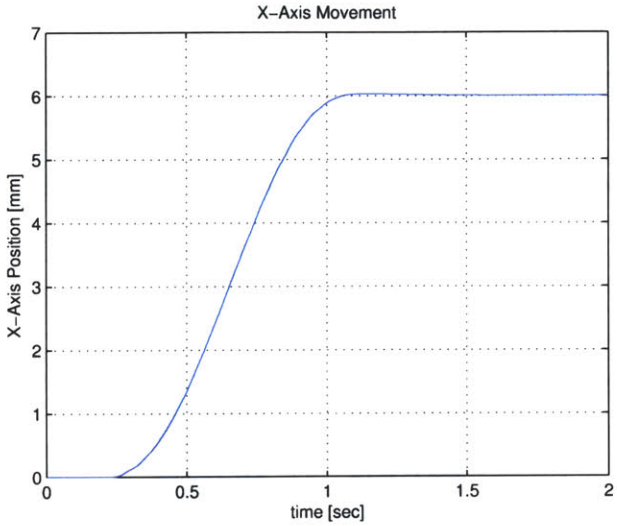

Figure 4-51: X-axis ferrule-to-ferrule motion

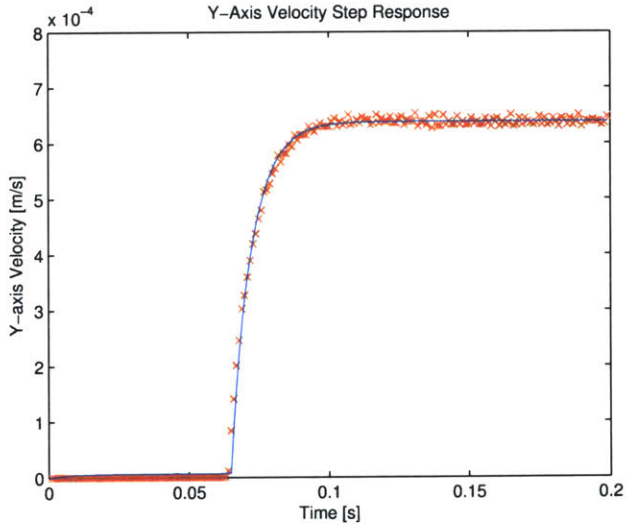

Figure 4-52: Y-axis velocity step response

k is the effective stiffness of the pins the rollers ride on, and b_1 and b_2 are viscous damping parameters acting on the two masses.

The transfer function was fit to the velocity step-response with b_1 and b_2 as the curve fitting parameters and has a good fit. The system dynamics are dominated by the mass of the yz carriage and damping giving a 1^{st}-order like time constant $\tau = 0.008$ second The settling time, $4\tau = 0.032$ second which is better than the 0.05 second from functional requirement.

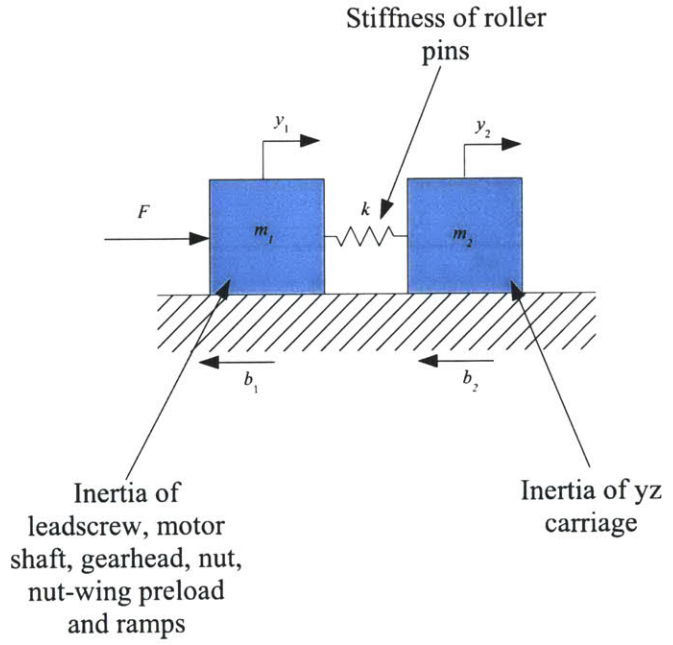

Figure 4-53: Y-axis simplified model

Y-axis motor position during a 250 μm fiber-to-fiber movement can be seen in Figure 4-54. From the motor's point of view, we meet the functional requirement of moving fiber-to-fiber within 1 second.

Z Axis

The z-axis velocity step-response can be seen in Figure 4-55. At first glance, the response appears 2^{nd}-order because of the oscillations. Closer inspection of the data shows that the oscillations occur at a period of 0.5 mm, same as the leadscrew lead. Thus the oscillations are not due to actuator dynamics but to leadscrew errors.

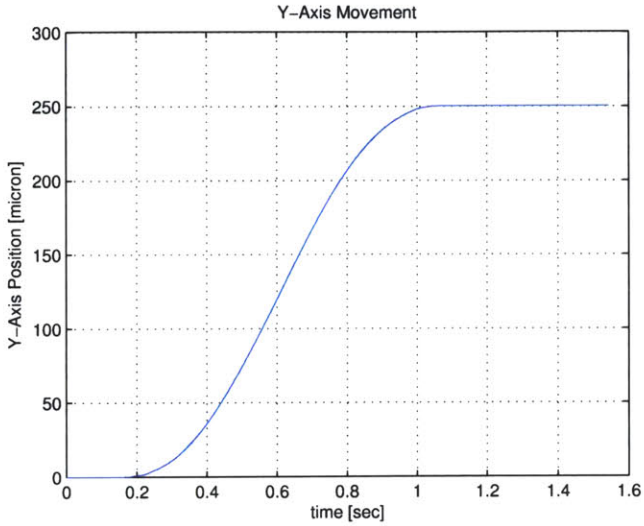

Figure 4-54: Y-axis ferrule-to-ferrule motion

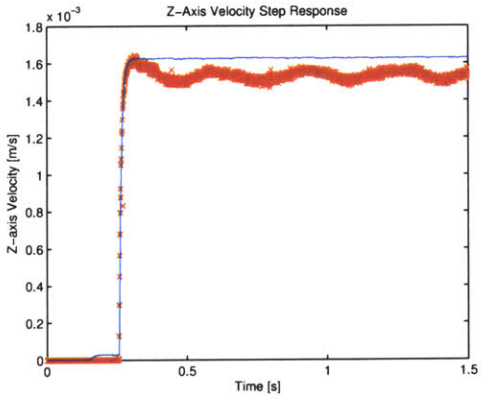

Figure 4-55: Z-axis velocity step-response

Recalling the transfer function Equation (4.3), the model is shown in Figure 4-29, and modeling friction effects as viscous damping terms b_1 and b_2 between each mass and ground, we obtain the transfer function in Equation (4.6). Again, modeling the dissipative friction effects as viscous damping may be incorrect but will suffice for the sake of simplicity. Fitting the transfer function only to the initial transient and not the oscillations shows that we have a highly damped system with settling time = 0.03 sec, which is well within the 0.05 sec functional requirement.

$$\frac{\dot{z}_1}{F_1} = \frac{s^2 m_2 + b_2 s + k}{s^3 m_1 m_2 + s^2(b_2 m_1 + b_1 m_2) + s[k(m_1 + m_2) + b_1 b_2] + k(b_1 + b_2)} \tag{4.6}$$

Z-axis motor position during a 200 μm traversal (focus motion) can be seen in Figure 4-56. From the motor's point of view, this axis is more then adequate to perform the 20 μm focus movement within 1 second.

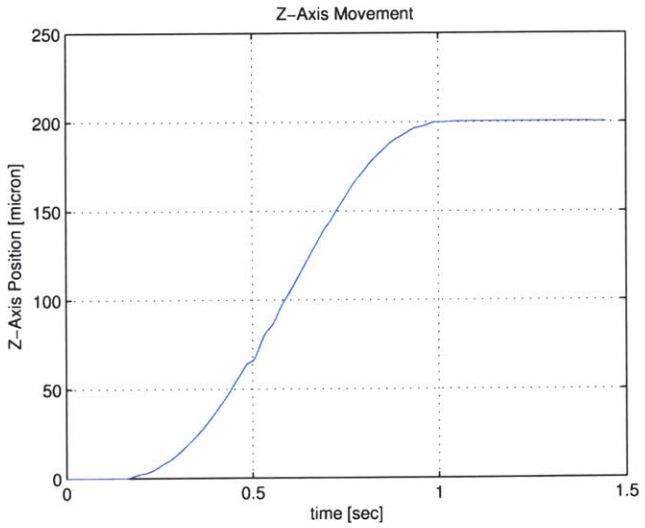

Figure 4-56: Z-axis focus motion

4.6.3 Error Budget Verification

The error motions for each axis were measured at the lens tip to verify the error budget calculations. The same capacitance-gauge and data-acquisition machine described earlier were use to record the motions.

CS1-CS2: Z-Axis Error Motions

Experimental verification of $\hat{x}$ error motions during a z-axis movement can be seen in Figure 4-57(a). The superposition of two separate phenomena occurs:

1. A linear error motion is most likely caused by the capacitance-gauge measurement-target not being truly square. As previously discussed, during z axis motion, the functional requirements for HDOF imaging only require $\hat{x}$ and $\hat{y}$ error motions to be less than 5 μm per mm traveled along $\hat{z}$. If the linear error motion is real instead of an artifact of the measurement technique, this measurement shows that the requirement is met.

2. The sinusoidal error of 0.5 mm period is the same as the 0.5 mm lead on the leadscrew driving the z axis. Close inspection of the camera-tube during z-axis traversal shows that the leadscrew is not quite straight and does cause the camera-tube to precess in accordance with the leadscrew lead. We can see that the z-axis leadscrew and nut over-constrain the z-axis bearings, hence the leadscrew motion along $\hat{x}$ and $\hat{y}$ imparts onto the camera tube. Later we will discuss how to design the nut so that the system is no longer over-constrained, which should remove the sinusoidal error motion.

By symmetry, $\hat{y}$ error motions are nearly identical to those along $\hat{x}$, so we neglect to present those here. Experimental verification of $\hat{z}$ error motions during a z-axis movement can be seen in Figure 4-57(b). The result is dominated by a sinusoidal motion with amplitude 9 μm and period 0.5 mm (again the same as the leadscrew lead), which is well within the ± 25 μm repeatability functional requirement. Interestingly, the measured error motions are well below those predicted by the error budget, as given in Table 4.9. Because we do not have exactly point contact at each bearing gib, the surface roughness errors are averaging out thus explaining why the system performance is better than expected.

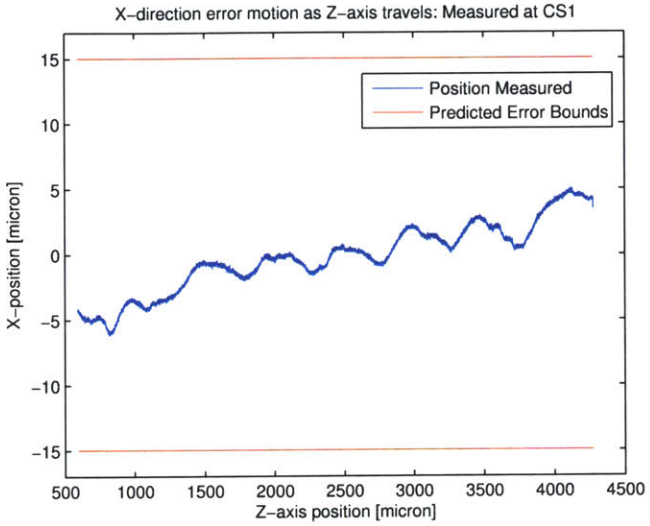

(a) X_{random} Error-Motion

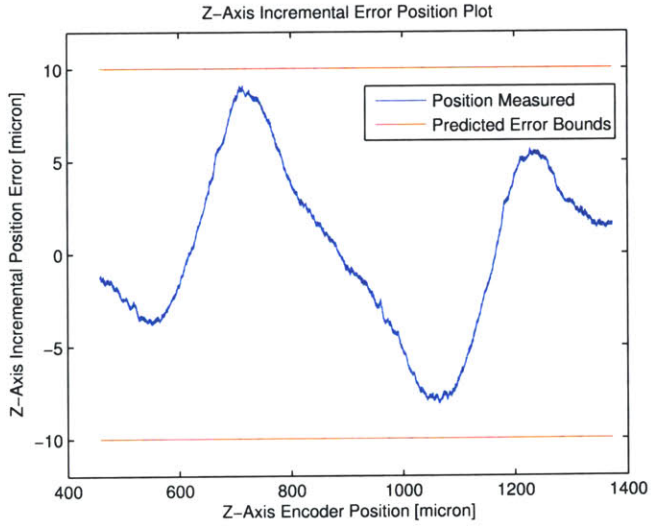

(b) Z_{random} Error-Motion

Figure 4-57: CS1-CS2 error-motions

CS2-CS3: Y-Axis Error Motions

Upon verifying the y-axis error motions, we found that the roller-wheels caused rather high random error motions due to stick-slip phenomena. For example, the Y_{random} motion shown in Figure 4-58(a) swings randomly ± 40 μm, whereas with the rollers locked so that they act as sliding-contact bearings the error motions are reduced by a factor of 10, Figure 4-58(b).

As can be seen in Figure 4-59, X_{random} error motion measured at the lens tip shows a linear trend with a sinusoidal oscillation. The linear trend is most likely due to the capacitance-gauge target not being fully square. The oscillation has amplitude approximately ± 2 μm, which is well within the error budget. Also, Z_{random} error motion is shown in Figure 4-60. There is a linear trend in this plot, which is probably due to the capacitance-gauge target not being fully square. Nevertheless, the error motion remains within the functional requirements, and in practice the axis behaves better than expected. See Table 4.15.

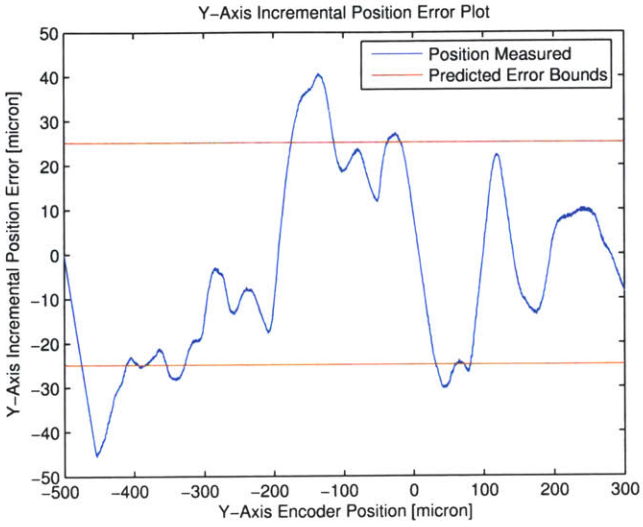

(a) Y_{random} Error-Motion

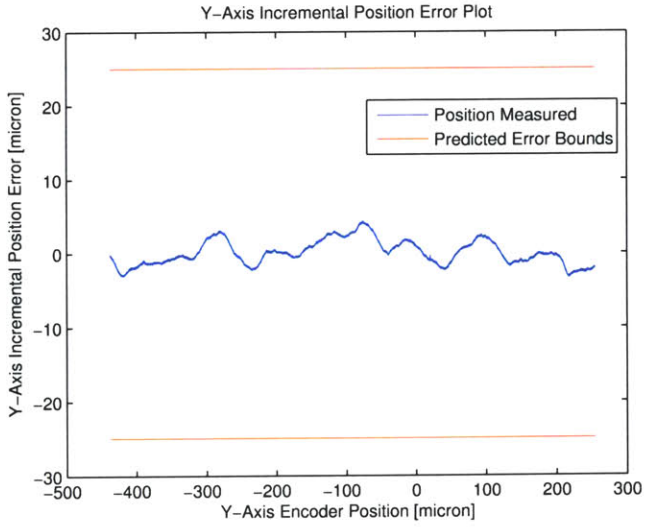

(b) Y_{random} Error-Motion With Rollers Locked

Figure 4-58: CS2 measured y error-motions

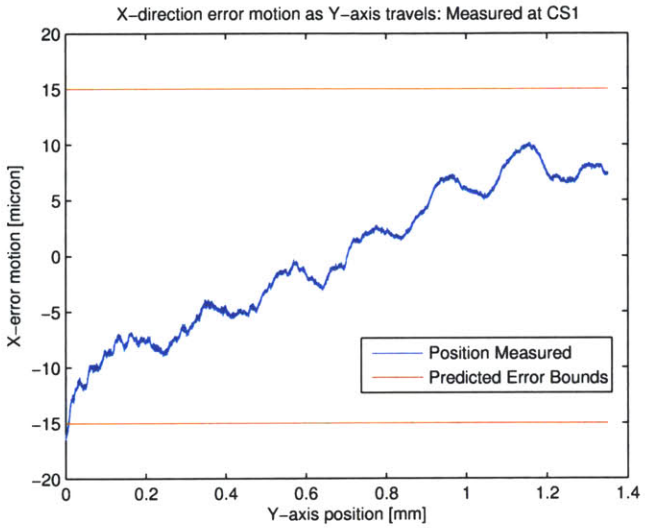

Figure 4-59: X_{random} error-motion measured at lens tip

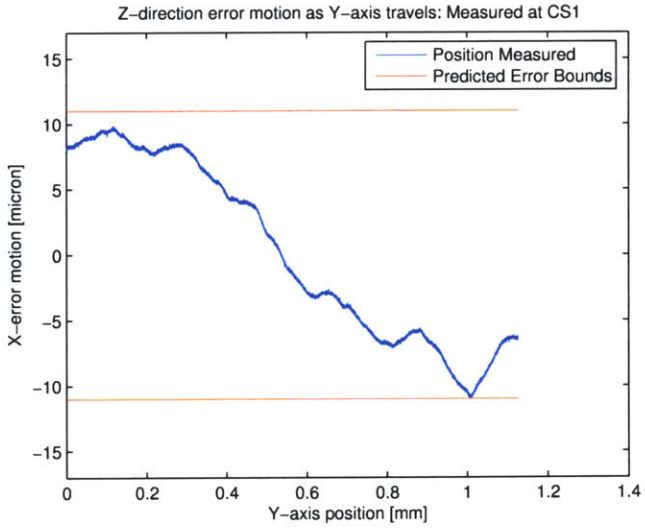

Figure 4-60: Z_{random} error-motion

CS3-CS5: X-Axis Error Motions

Experimental verification of the x-axis error motions measured at the lens-tip can be seen in Figures 4-61 4-62 and 4-63. The X_{random} is well within ± 25 μm required by the functional requirements and the ± 50 μm predicted from the error budget.

Y_{random} error motion can be seen in Figure 4-62. It appears to have a large "u" shape, with a maximum spread of ± 15 μm per 40 mm traveled, which is within the error budget and functional-requirements. A sinusoidal motion is superimposed upon the "u" and appears to come from the rack-and-pinion as it has the same period and has negligible effect as the amplitude is quite low.

Z_{random} error motion, as shown in Figure 4-63, is highly dominated by a sinusoid with approximately 5 μm amplitude and the 1.5 mm period (same as the rack-and-pinion tooth engagement). Over the 30 mm recorded, we see approximately ± 15 μm motion, which is well within the error budget and functional requirements.

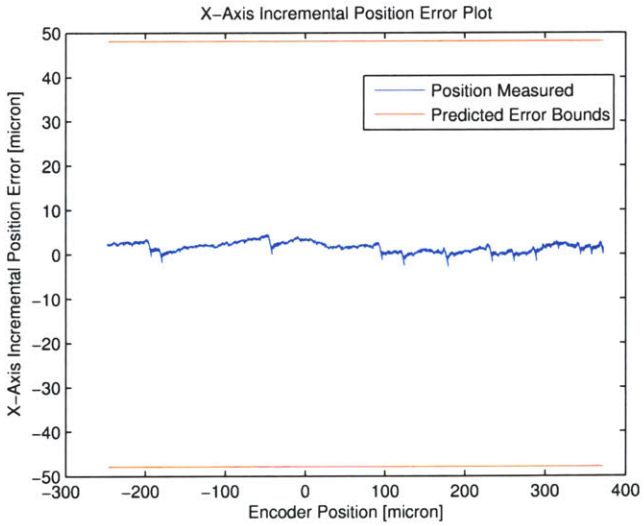

Figure 4-61: CS3-CS5: X_{random} error motions measured at lens tip

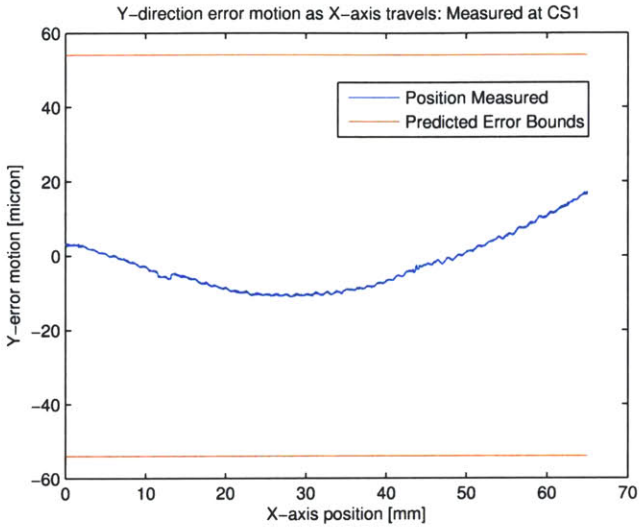

Figure 4-62: CS3-CS5: Y_{random} error motions measured at lens tip

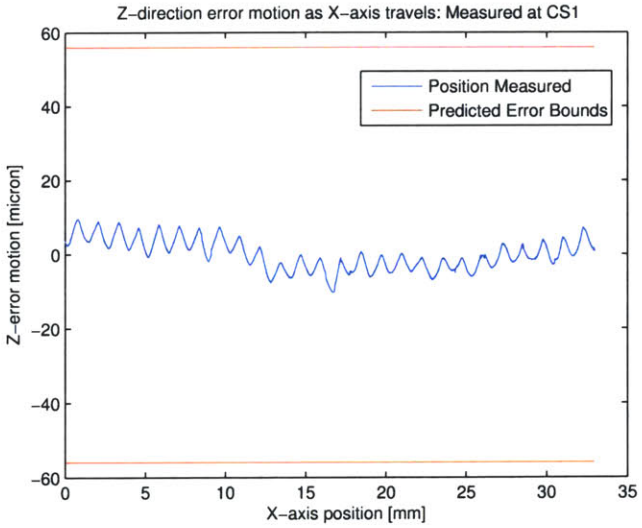

Figure 4-63: CS3-CS5: Z_{random} error motions measured at lens tip

4.7 Summary and Future Work

Through the use of an error budget and creative design, the mechanical design achieves all the functional requirements. The x axis has 0.05 second settling time, 0.124 ± 4 μm resolution and ± 8 μm repeatability. The y axis has 0.03 second settling time, 0.003 ± 4 μm resolution and ± 15 μm repeatability. The z axis has 0.03 second settling time and 0.00076 ± 10 μm resolution and ± 10 μm repeatability. Also, the system fits within the 15 x 80 x 300 mm envelope.

Simplifying parts, reducing part count, and reducing part tolerances may drastically reduce manufacturing costs. Frame-less motors, castings, extrusions and high-volume manufacturing are potential ideas for reducing costs.

This prototype is viewed as a successful enabling technology experiment. We were unable to test the inspection machine in a live router and so the affects of vibrations and temperature gradients have not been fully tested, and are left for future work. Even though this second prototype meets virtually all functional requirements, many improvements could be made. Assembling the system and performing the various error motion and system-identification measurements makes most of the needed improvements readily apparent. A short description of the most important improvements follow.

4.7.1 Z-Axis Leadscrew and Nut

As previously discussed the z-axis leadscrew and nut were over constrained and had an undoubtedly sinusoidal error motion. The first quick fix was to re-manufacture the screw with much tighter tolerances as the initial leadscrew was turned on a lathe and then the thread was cut with a die. The re-manufactured part was single-point turned on lathe. Each end of the screw was drilled out to support the free end during the turning process. The screw worked much better than the original but still did exhibit the sinusoidal error motion.

The support hole on the coupling end of the leadscrew created a rather thin section, on the order of 0.5 mm, and after a few swift runs hitting a hard stop the leadscrew broke at the coupling mount. A better solution is required.

As shown in Figure 4-64, the newly designed nut would allow for a "sloppy" leadscrew. The nut is only constrained along $\hat{z}$ by the the axial flexure preloading the nut against the bearing surface, which is attached the camera-tube. $\hat{\theta}_z$ is constrained by the rotational flexure; this nut allows for quite significant $\hat{x}$, $\hat{y}$, $\hat{\theta}_x$ and $\hat{\theta}_y$ error motions.

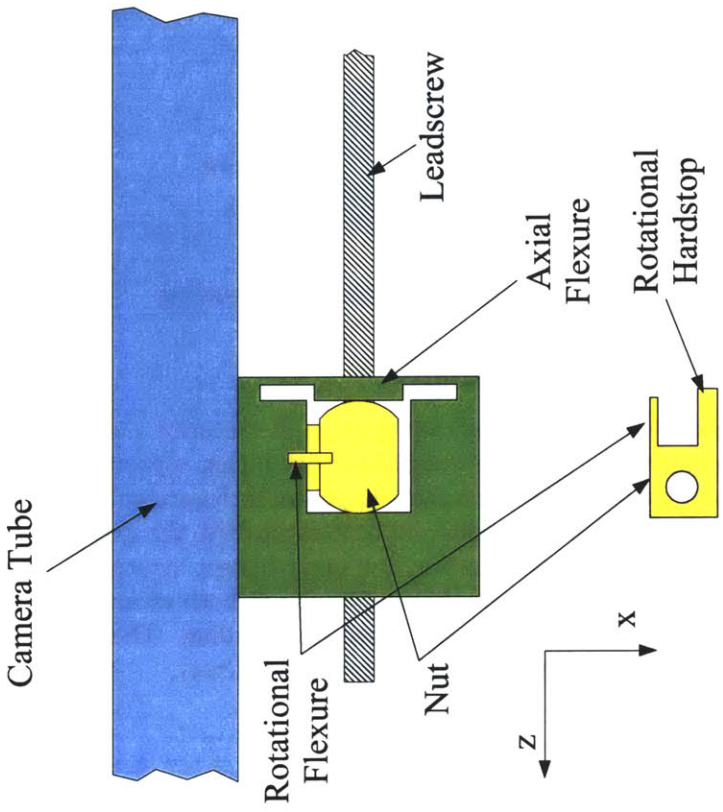

Figure 4-64: Redesigned z-axis nut

4.7.2 Coupling Set Screws

Another problem was high-backlash on each axis. A significant portion arose from the gearhead which could not be reduced. The remaining backlash came from the couplings which were connected to the motor-shafts and leadscrews by set screws. A considerable amount of backlash came from the coupling mounts as the set screws would back out even with Loctite, thus they definitely need to be redesigned for future machines. A split allows for much greater preload force upon the mounted shaft, as shown in Figure 4-65. With a socket-head cap-screw use lock washers prevent the screws from backing out.

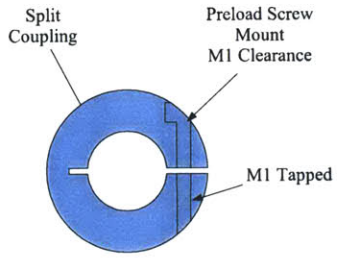

Figure 4-65: Redesigned coupling

4.7.3 Higher Repeatability

The x axis produces a significant portion of the error motions. If one desired to implement a similar design but with higher repeatability they could implement a system with two racks as shown in Figure 4-66. The front rack constrains the angular motions and both racks drive the system. Moving the rack forward drastically shortens the error budget structural loop, significantly improve x-axis repeatability. Driving at both racks effectively drives the system at its center of mass preventing binding. These benefits would have to be weighed against the increased complexity.

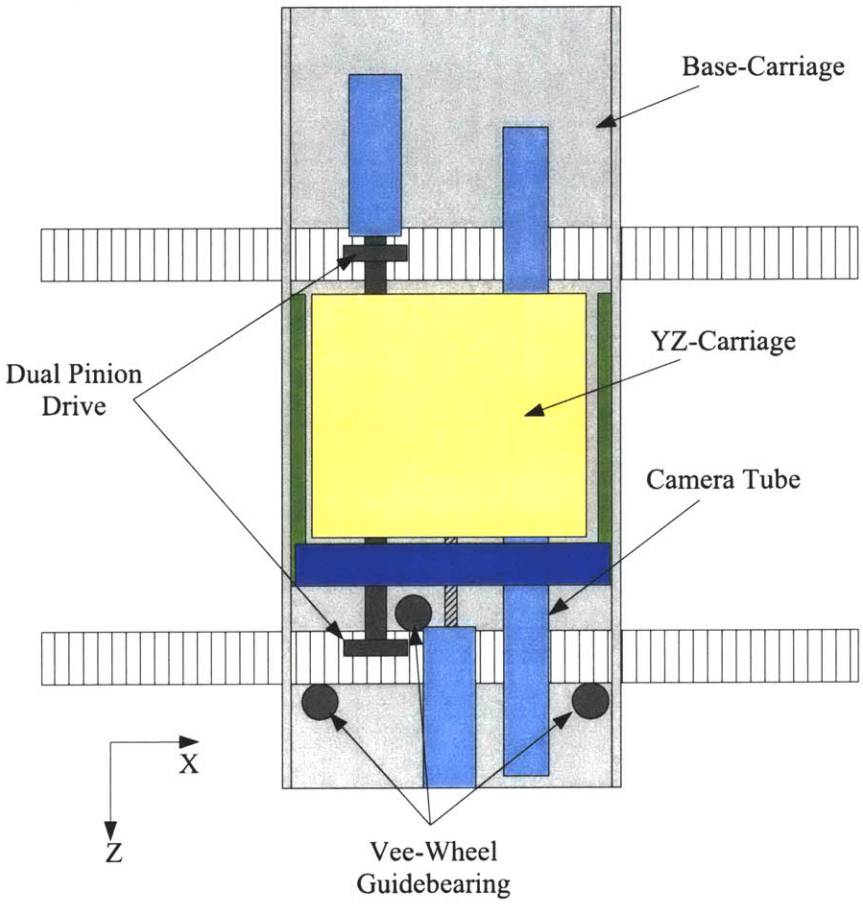

Figure 4-66: X-axis with higher performance

Chapter 5

System Testing

5.1 Introduction

The purpose of this chapter is to summarize the results of tests performed on the FOFIM system developed in this thesis, showing that the optical design meets the 1 μm Rayleigh resolution requirement through the use of image processing; virtually unlimited depth-of-field and dynamic range images capture all available intensity information; innovative machine vision algorithms successfully detect 1 μm detects and the mechanical design meets all functional requirements.

5.2 Optics

Due to lack of equipment, we do not have the capability to directly measure the optical system performance (MTF, PSF or OPD), but comparison between images collected from an inspection system with higher resolution shows that the designed optics behave as expected.

Examples of images taken with the designed optics can be seen in Figures 5-1(a), 5-2(a), and 5-3(a). Beside each is the deconvolved image and below each is an image taken from an inspection system with a higher (0.96 μm) resolution objective. Differences between the higher resolution image and the deconvolved FOFIM's image are due to focus position variances, illumination variances and obviously they are imaged via different lenses.

Manual, visual inspection of the fiber images shown in Figures 5-1, 5-2 and 5-3, shows that nearly all defects in the high-resolution images, appear in the deconvolved FOFIM images. The deconvolved FOFIM images even

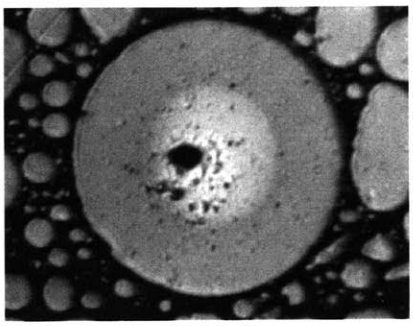

(a) Original image from FOFIM prototype

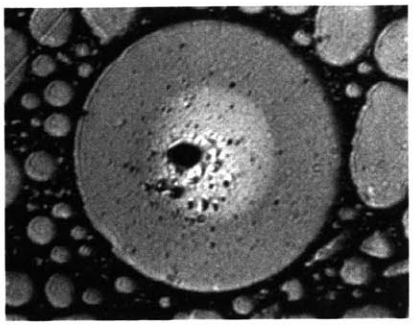

(b) Deconvolved image from FOFIM prototype

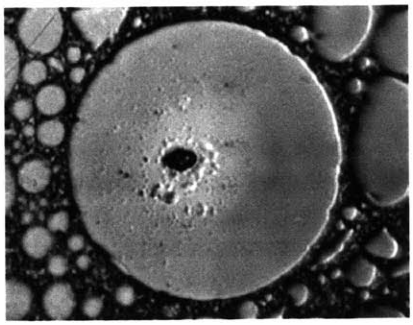

(c) Image by objective with 0.3 NA from bench top FOFIM

Figure 5-1: Fiber 1 Deconvolved

show slightly more contrast than the high-resolution images indicating that the FOFIM's optics perform very well. For example, the faint scratches and dust particles in Figure 5-2 are much easier to see in the deconvolved image than in the high-resolution image. One may object that the objects are slightly larger, and distorted due to diffraction effects, but we are not overly concerned with accurately measuring defect size. We simply must detect them, which the FOFIM optics do well.

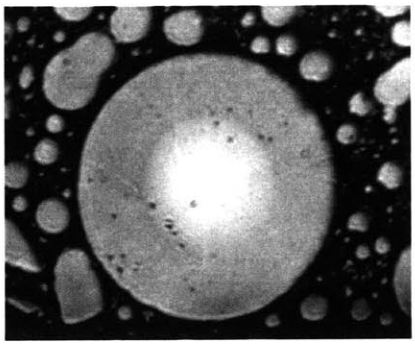

(a) Original image from FOFIM prototype

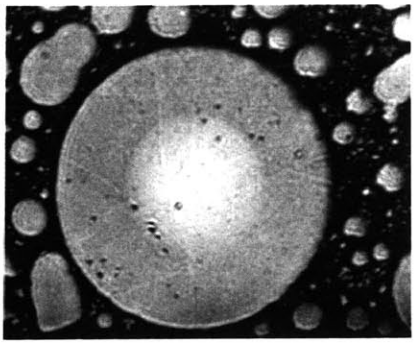

(b) Deconvolved image from FOFIM prototype

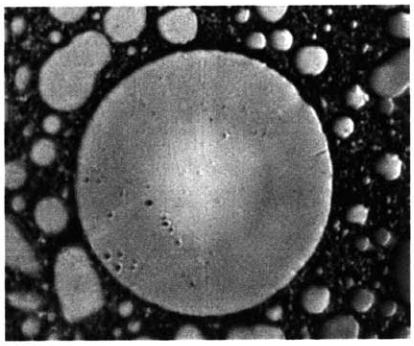

(c) Image by objective with 0.3 NA from bench top FOFIM

Figure 5-2: Fiber 2 Deconvolved

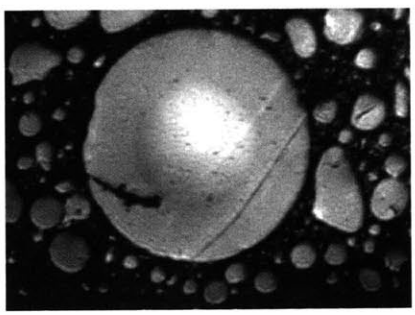

(a) Original image from FOFIM prototype

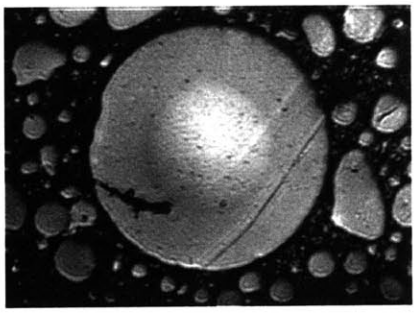

(b) Deconvolved image from FOFIM prototype

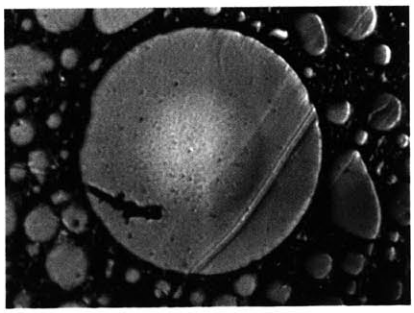

(c) Image by objective with 0.3 NA from bench top FOFIM

Figure 5-3: Fiber 3 Deconvolved

5.3 Machine Vision

Simulated fiber defects help determine appropriate image processing parameter settings. As shown in Figure 5-4(a), simulated particles of known size and contrast are passed through the defect detection algorithm. The particle sizes range from 0.5 μm to 5.5 μm and contrast range 2.2:1 to 1.2:1.

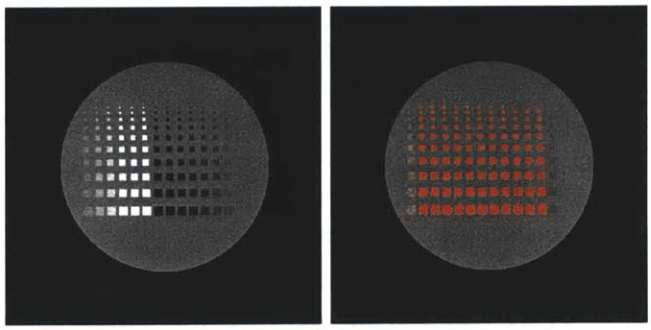

(a) Simulated Defects (b) Defect Detection

Figure 5-4: Particle Defect Sensitivity

As shown in Figure 5-4(b), the FOFIM easily detects 1 μm defects with minimum contrast of 1.5:1. iNEMI neglects to discuss defect contrast ratios, but the inspection machine is capable of detecting beyond the required 2 μm defect size.

Simulated scratches upon the fiber endface are shown in Figure 5-5(a), with scratch widths ranging from 1 μm down to 0.5 μm and contrast ratio ranges from 1.4:1 to 1.02:1. The proposed scratch detection algorithm detects the scratches as marked by the yellow lines in Figure 5-5(b). The FOFIM detects 1 μm wide scratches with contrast down to 1.1:1, thus beating the recommended iNEMI inspection guidelines.

These simulated fiber defect tests show that the proposed defect detection algorithms do detect 1 μm defects with sufficient contrast. Results from images taken by the FOFIM are shown in Figures 5-6, 5-7 and 5-8. All pertinent defects are detected within the image. Red blobs correspond to pits, chips and particles and the yellow lines correspond to scratch defects. The blue and green areas label the inspected core and cladding areas respectively.

Even though the proposed algorithms do meet the iNEMI specs, much improvement is needed. It appears the some of the dust particles on the fiber's core in Figure 5-6(b) have only their periphery marked. The contrast filling rule was not able to accurately measure its contrast to fill in the defect

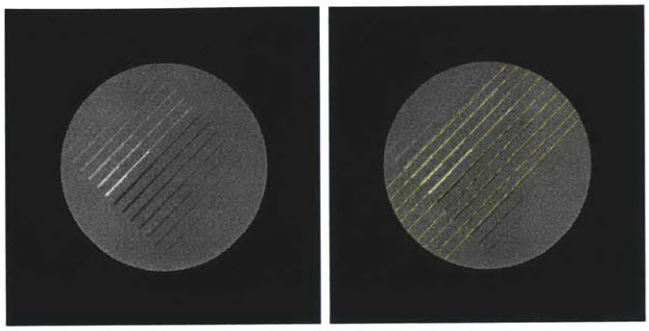

(a) Simulated Scratches (b) Scratch Detection

Figure 5-5: Scratch Defect Sensitivity

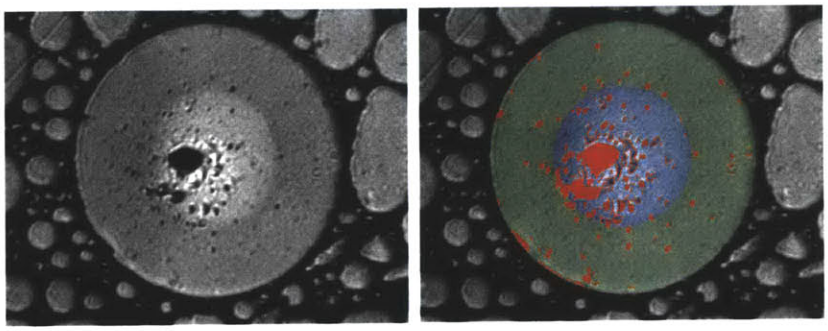

(a) Deconvolved Image (b) Detected Defects

Figure 5-6: Fiber 1 Defect Detection

due to the core being lit and the high density of defects. The lit core and high defect density confuse the local contrast measure.

For fiber 2, Figure 5-7(b), the contrast particle detection rule filled in some defects that do not exist near the very bottom center of the fiber. It is hard to accurately measure local contrast near the fiber edge as the ferrule surrounding may swing the measure quite far, thus resulting in mislabeled defects. Also, the scratch detection algorithm was able to detect a few of the scratches even though they are quite faint. It appears that slightly curved scratches are detected as two separate scratches though.

For fiber 3, Figure 5-8(b), we again see the mislabeled particle defect near the bottom left of the fiber, which is due to being near the fiber edge. Also it is noticed that the deep scratch is detected as both a scratch and particles by having both the yellow and red defect labels.

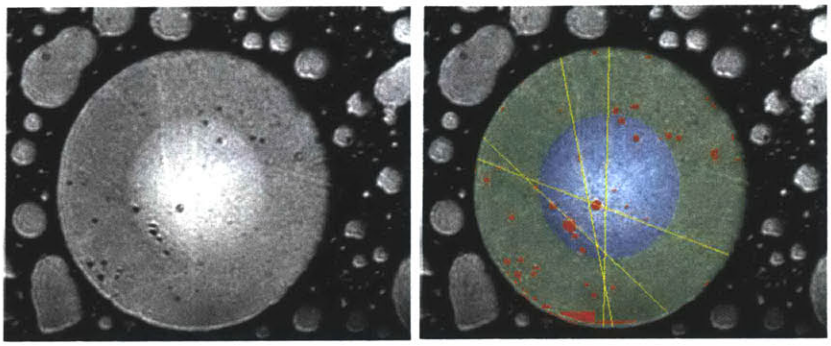

(a) Deconvolved Image (b) Detected Defects

Figure 5-7: Fiber 2 Defect Detection

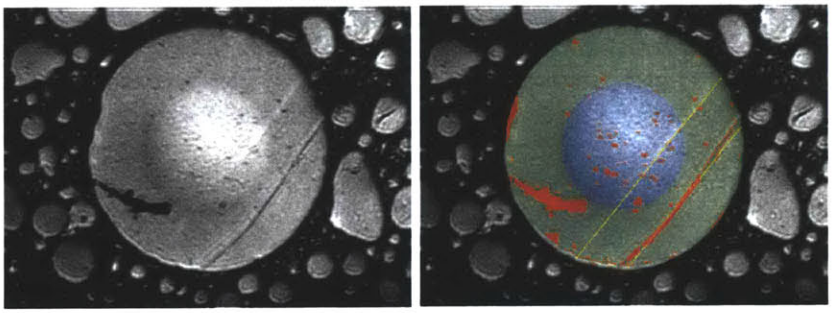

(a) Deconvolved Image (b) Detected Defects

Figure 5-8: Fiber 3 Deconvolved

The machine vision algorithms are more than adequate for inspecting fibers within the iNEMI guidelines. The mentioned mis-labeled defect problems err on the side of caution, thus they are not catastrophic failures.

5.4 Machine Design

Through the use of an error-budget and creative design the mechanical design meets all the functional requirements. the performance of each axis is summarized in Table 5.1.

We propose the following time line to inspect a 12-fiber MT ferrule in well under 2 minutes:

- center the system (2 sec.)

Axis	Settling Time	Resolution	Repeatability	Range
X-Axis	0.05 sec.	0.128 ± 4 μm	± 8 μm	NA
Y-Axis	0.03 sec.	0.003 ± 4 μm	± 15 μm	3.5 mm
Z-Axis	0.03 sec.	0.0076 ± 10 μm	± 10 μm	24 mm

Table 5.1: Final System Performance

- take HDR+HDOF Image (1 sec.)
- traverse to next fiber (1 sec.)
- repeat the previous steps until all 12 fibers are inspected

In our tests the FOFIM is found to inspect a 12-fiber MT ferrule in 222 sec. as shown in Table 5.2. The image capturing is slow because we are limited by the 30 frames/sec frame rate and the computer processing the images is quite slow (AMD Athlon 1800+ processor). The FOFIM mechanical hardware is more than capable of beating the 2-minute time schedule. A faster computer and more efficient computations will significantly reduce inspection time.

Step	**Time [sec]**	**Variance [sec]**
Focus Camera	4	± 0.1
Center the system	0.5	± 0.1
Take HDR + HDOF Image	13	± 0.5
Traverse to Next Fiber	1	± 0.1
total per fiber	18.5	± 0.8
number of fibers	12	
total	**222**	± 9.6

Table 5.2: Measured System Inspection Time

Chapter 6

Conclusion

6.1 Thesis Contributions

At the onset of this thesis it was uncertain if in-situ backplane inspection was feasible. This thesis has clearly shown that backplane inspection is quite practical and we presented a comprehensive study and method for in-situ backplane inspection. We also developed a fiber optic ferrule inspection machines (FOFIMs) for in situ backplane inspection where the inspection problem was framed by laying out the functional requirements:

- perform in situ inspection of back plane connectors
- 3-axis motion:
  - Ferrule-to-ferrule: Nominal range up to 700 mm with $\pm$ 20 μm repeatability and 5 μm resolution.
  - Fiber-to-fiber: Nominal range of 250 μm with $\pm$ 20 μm repeatability and 5 μm resolution.
  - Focus: Nominal range of 20 μm with $\pm$ 25 μm repeatability and 0.5 μm.
- 2 minute inspection time for 12 fiber MT ferrule
- detect 1-2 μm defects:
  - Scratches: location, width and contrast
  - Pits, Particles, and Oils: are, location and contrast
- priced for the market, being salable at \$5k-\$10k

- non destructive to the fiber endface

The key components solving the problem are optics, machine vision and mechanical design.

- Optics: We successfully designed an ultra-long working-distance microscope objective with 15X magnification and 0.2 NA. It uses two doublets and 2 singlets and is optimized for 470 nm light, thus giving 1.4 μm object Rayleigh resolution. Deconvolution methods further increased resolution to 1.1 μm, well within the 1-2 μm requirement by iNEMI[1].

- Machine Vision: A few methods to accurately and repeatably detect defects upon the fiber endface have been presented. We utilized a simple method of summing images of differing exposures that provides virtually limitless high-dynamic-range (HDR) images.

  We then employ high-depth-of-field (HDOF) imaging to extended the inherent 1 μm depth-of-field limit to inspect well beyond 20 μm required for APC[2] fiber inspection.

  Through capturing HDR and HDOF images all information needed to detect all defects is available. Edge finding, the Hough Transform, and various morphological operators accurately detect the fiber endface, particles and scratches.

- Machine Design: Through the use of an error-budget and creative deterministic design, the mechanical design achieves all the functional requirements. It is a simple mechanical system that is produced at relatively low cost, controllable, compact, gives good performance and is good for in-situ backplane inspection. The x-axis has 0.05 second settling time, $0.124 \pm 4\mu$m resolution and $\pm 8\mu$m repeatability. The y-axis has 0.03 second settling time, 0.003 ± 4 μm resolution and $\pm 15\mu$m repeatability. The z-axis has 0.03 second settling time and 0.00076 ± 10 μm resolution and $\pm 10\mu$m repeatability.

6.1.1 Future Work

This prototype is very promising; it has served as enabling technology proving that an automated backplane inspection machine is feasible, but in order

[1] International Electronics Manufacturing Initiative; they road map the needs of the global electronics industry providing standards and dissemination of efficient business practices

[2] Angled Physical Contact: reduces an interconnect's reflectance loss.

for it to become a salable product many improvements should be made. Decreasing manufacturing costs of the mechanical components even further is key. Total cost of the mechanical parts was $2500, and of course higher quantities should reduce the price but we do have a fundamental limit; manufacturing tolerance requirements on some parts are quite high. Instead of the standard machining operations, perhaps casting followed by milling or grinding could be used to ensure high-tolerance parts at lower cost.

To enhance repeatability, the z-axis leadscrew and nut should be redesigned to reduce backlash and error motions; The motor couplings need to be redesigned to reduce backlash and motor shaft loading; and a dual drive rack-and-pinion would reduce the Abbe error motions of the x-axis.

Sliding contact bearings will generate many particles that could fall onto the card-based machine or fiber endface while performing inspections. The use of a sticky grease at each bearing could help trap particles as well as placing a sticky patch on the underside of the FOFIM top.

The large cable connecting the FOFIM to the microcontroller and computer may accidentally be bumped. It is desirous to reduce these usability problems, therefore packaging the microcontroller, battery pack and wireless transmitter and receiver into the inspection system would be a nice feature for future machines. The host computer could then just send simple "GOTO" commands over a wireless network and the FOFIM would pick up the command with its receiver. There is existing technology for broadcasting live video feeds over an RF channel, the quality of this setup would need to be fully tested to maintain the high quality images for inspection.

The optics work very well, and when purchased in quantities of 100, the doublets cost $15.25 each and the singlets cost $7.50 each, totaling $45.50 per objective. Costs could possibly be minimized by reducing the lens count and loosening manufacturing tolerances. Also, high volume manufacturing allows cost effective use of aspherical lenses which can easily reduce lens count.

It has been proposed to use coherent lighting (i.e. a laser diode) but it is difficult to directly compare the coherent and incoherent lighting cases as the Rayleigh resolution, frequency content and PSF depend directly upon the phase distribution of the object [25]. The phase distribution of fiber endfaces can vary widely with different scratches and oils on the fiber endface, thus we should experiment with coherent lighting to determine its capabilities.

The proposed image processing algorithms work well, but due to imaging variations: uneven lighting, connector materials, and lit fiber cores; the detection algorithms may mislabel defects. They err on the side of caution and the code should be made more robust before being sold to the market.

Also it is desirous to reduce computation time, and experimentation with different algorithms such as active appearance models may be beneficial.

In order for the fiber optic industry to adopt this machine, total system cost should be approximately $5k-$10k, which at quantities of 100 the FOFIM should be profitable. As a cost study example, IBM's BlueGene/L supercomputer is leased at $0.50/cpu/hour, thus for 1 day downtime for 1000 processors, the total cost is $12,000. Perhaps the $5k-$10k price is a little low, but the FOFIM should be quite profitable when made in quantity 100 or more as shown in Table 6.1. Also, standard product design practices such as design for manufacture and aesthetics should be applied rigorously.

Description	**Quantity 1 Cost**	**Quantity 100 Cost**
Mechanical Parts	$3,000.00	$1,000.00
Optics	$300.00	$7.50
Motors	$450.00	$180.00
Computer	$2,000.00	$1,000.00
Microcontroller	$100.00	$20.00
total	$5,850.00	$2,207.50

Table 6.1: FOFIM Cost Structure

This thesis has shown that in-situ backplane inspection is quite feasible and for future work we may want to extend this platform to inspect other items such as planar wave-guides, ball lenses or even copper connectors.

Bibliography

[1] G. Keiser, *Optical Fiber Communications.* McGraw-Hill, Inc., 1991.

[2] C. L. Men, "Fibre characterization and measurements," *Trends in Optical fibre Metrology and Standards*, pp. 353–397, 1995.

[3] M. D. Rosa, J. Carberry, V. Bhagavatula, K. Wagner, and C. Saravanos, "High-power performance of single-mode fiber-optic connectors," *Journal of Lightwave Technology*, vol. 20, no. 5, pp. 879–885, 2002.

[4] K. Schmidt, "Automated inspection saves time, money," *Quality Magazine*, May 2003.

[5] Y. Kipman and D. Wolin, "Scanning machine vision for fiber optic connector inspection," *Machine Vision and Three-Dimensional Imaging Systems for Inspection Systems for Inspection and Metrology II, Proceedings of SPIE*, vol. 4567, pp. 216–223, 2002.

[6] Y. Yaguang and E. Sahinci, "Fiber connector inspection system," *Optical Fiber Communication Conference*, vol. 1.

[7] A. Wilson, "System examines fiberoptic assemblies," *Vision Systems Design*, 2002.

[8] A. Wilson, "Machine-vision system inspects fiber connectors," *Vision Systems Design*, 2003.

[9] http://www.westoverfiber.com/fiber/software/fiberChek2.htm, "webpage," 2005.

[10] D. Marcuse, "Loss of single-mode fiber splices," *The Bell System Technical Journal*, vol. 56, no. 5, pp. 703–718, 1977.

[11] *Preparation and Examination of Optical Fiber Endface for Testing Purposes.* Telecommunications Industry Association, 1994.

[12] *Visual and Mechanical Inspection of Fibers, Cables, Connectors, and/or Fiber Optic Devices.* Telecommunications Industry Association, 1996.

[13] *Inspection of Cleaved Fiber End Faces by Interferometry.* Telecommunications Industry Association, 1994.

[14] *Generic Specification for a Field Portable Optical Inspection Device.* Telecommunications Industry Association, 1994.

[15] W. Mahmood, M. Özer, and E. Avram, "Surface scratch and pit analysis on optical interfaces," *Proceedings of SPIE*, vol. 4532, pp. 323–329, 2001.

[16] E. Avram, W. Mahmood, and M. Özer, "Quantification of scattering from fiber surface irregularties," *Journal of Lightwave Technology*, vol. 20, no. 4, pp. 634–637, 2002.

[17] http://www.inemi.org/cms/projects/opto/fiber_signal.html, "webpage," 2005.

[18] R. Manning, "Optical connector contamination and its influence on optical signal performance," *IEC SC86B/WG6*, April 2004.

[19] T. Berdinskikh, H. Tkalec, and J. Nguyen, "At the core: how scratches, dust, and fingerprints affect optical connector performance," *Connector Specifier*, pp. 11–12, January 2004.

[20] N. Inc., "`http://www.microscopyu.com/museum/firstnikon.html`," 2005.

[21] L. C. Martin, "The theory of the microscope, ii: dark-ground illumination," *Proceedings of the Physical Society*, vol. 46, no. 2, pp. 231–251, 1934.

[22] C. Beck, "Modern methods of microscope illumination. i. high power dark ground illumination," *Journal of Scientific Instruments*, vol. 1, no. 5, pp. 148–149, 1924.

[23] M. W. Davidson, "`http://www.microscopyu.com/index.html`," 2005.

[24] http://www.nhm.ac.uk/hosted_sites/quekett/Technical/Rheinberg.html, "webpage," 2005.

[25] J. W. Goodman, *Introduction to Fourier Optics.* McGraw-Hill, 1988.

[26] J. A. Macdonald, "Apodization and frequency response with incoherent light," *Proceedings of the Physical Society*, vol. 72, no. 5, pp. 749–756, 1958.

[27] S. Bradbury, *The Microscope, Past and Present.* Pergamon Press, 1968.

[28] A. Dakoff, J. Gass, and M. K. Kim, "Microscopic three-dimensional imaging by digital interference holography," *Journal of Electronic Imaging*, vol. 12, pp. 643–647, 2003.

[29] W. J. Smith, *Modern Lens Design.* SPIE Press, 1992.

[30] A. E. Conrady, *Applied Optics and Optical Design.* Dover Publications, Inc., 1985.

[31] E. Hecht, *Optics.* Addison Wesley Publishing Company, 1997.

[32] M. Betrero and P. Boccacci, *Introduction to Inverse Problems in Imaging.* Institute of Physics Publishing, 1998.

[33] J. L. Starck, E. Pantin, and F. Murtagh, "Deconvolution in astronomy: A review," *Publications of the Astronomical Society of the Pacific*, vol. 114, pp. 1051–1069, 2002.

[34] M. Juric, "Deconvolution, regularization and maximum entropy methods," November 2005.

[35] V. K. Ivanov *Soviet Math. Dokl.*, vol. 3, p. 981, 1962.

[36] A. N. Tikhonov *Soviet Math. Dokl.*, vol. 4, p. 1035, 1963.

[37] C. Miller, B. R. Hunt, M. W. Marcelling, and M. A. Neifeld, "Image restoration with the viterbi algorithm," *Journal of the Optical Society of America A*, vol. 17, pp. 265–275, 2000.

[38] M. A. Neifeld and Y. Wu, "Parallel image restoration with a two-dimensional likelihood-based algorithm," *Journal of the Optical Society of America A*, vol. 41, pp. 4812–4824, 2002.

[39] E. T. Jaynes, "The rationale of maximum entropy methods," *Proc. IEEE*, vol. 70, pp. 939–952, 1982.

[40] E. Pantin and J. L. Starck, "Deconvolution of astronomical images using multiscale maximum entropy method," *Astronomy and Astrophysics*, vol. 118, pp. 575–585, 1996.

[41] S. E. Ferrando and L. A. Kolasa, "Averages of best wavelet basis estimates for denoising," *Journal of Computational And Applied Mathematics*, vol. 136, pp. 357–367, 2001.

[42] S. Bacchelli and S. Papi, "Filtered wavelet thresholding methods," *Journal of Computational And Applied Mathematics*, vol. 164-165, pp. 39–52, 2004.

[43] D. L. Donoho, "Nonlinear solution of linear inverse problems by wavelet-vaguelette decomposition," *Applied and Computational Harmonic Analysis*, vol. 2, pp. 101–126, 1995.

[44] R. Neelamani, H. Choi, and R. Baraniuk, "Forward: Fourier-wavelet regularized deconvolution for ill-conditioned systems," *IEEE Transactions on Signal Processing*, vol. 52, pp. 418–433, 2004.

[45] A. W. C. Liew, N. F. Law, and D. T. Nguyen, "Multiple resolution image restoration," *IEEE Proceedings Vis. Image Signal Process.*, vol. 144, pp. 199–206, 1997.

[46] M. D. Grossberg and S. K. Nayar, "High dynamic range from multiple images: Which exposures to combine?," *Ninth IEEE International Conference on Computer Vision*, 2003.

[47] P. J. Burt and R. J. Kolczynksi, "Enhance image capture through fusion," pp. 173–182, 1993.

[48] P. E. Debevec and J. Malik, "Recovering high dynamic range radiance maps from photographs," *Proc. of ACM SIGGRAPH*, pp. 369–378, 1997.

[49] B. C. Madden, "Extended intensity range image," *Technical Report 366, Grasp Lab, UPenn*, 1993.

[50] S. Mann and R. Picard, "Being 'undigital' with digital cameras: Extending dynamic range by combining differently exposed pictures," *In Proceedings of IS&T, 46th annual conference*, pp. 422–428, 1995.

[51] M. A. Robertson, S. Borman, and R. L. Stevenson, "Estimation theoretic approach to dynamic range improvement through multiple exposures," *In Proceedings of ICIP*, pp. 159–163, 1999.

[52] G. W. Larson, H. Rushmeier, and C. Piatko, "A visibility matching tone reproduction operator for high dynamic range scenes," *IEEE Transactions on Visualization and Computer Graphics*, vol. 3, no. 4, pp. 291–306, 1997.

[53] R. Fattal, D. Lischinski, and M. Werman, "Gradient domain high dynamic range compression," *Proceedings of the 29th annual conference on Computer graphics and interactive techniques*, pp. 249–256, 2002.

[54] J. Biemond, R. L. Lagendijk, and R. M. Mersereau, "Iterative methods for image deblurring," *Proc. IEEE*, vol. 78, pp. 865–883, 1990.

[55] W. T. Cathey and E. R. Dowski, "New paradigm for imaging systems," *Appl. Opt.*, vol. 41, pp. 6080–6092, 2002.

[56] H. Li, B. S. Manjunath, and S. K. Mitra, "Multisensor image fusion using the wavelet transform," *Graph Models Image Proc.*, vol. 57, pp. 235–245, 1995.

[57] B. Forster, D. V. D. Ville, J. Berent, D. Sage, and M. Unser, "Complex wavelets for extended depth-of-field: A new method for the fusion of multichannel microscopy images," *Microscopy Research and Technique*, vol. 65, pp. 33–42, 2004.

[58] A. G. Valdecasas, D. Marshall, J. M. Becerra, and J. J. Terrero, "On the extended depth of focus algorithms for bright field microscopy," *Micron*, vol. 32, pp. 559–569, 2001.

[59] R. J. Pieper and A. Korpel, "Image processing for extended depth of field," *Appl Opt*, vol. 22, pp. 1449–1453, 1983.

[60] S. A. Sugimoto and Y. Ichioka, "Digital composition of images with increased depth of focus considering depth information," *Appl Opt*, vol. 24, pp. 2076–2080, 1985.

[61] T. T. E. Yeo, S. H. Ong, and S. R. Jayasooriah, "Autofocusing for tissue microscopy," *Image Vis Comput*, vol. 11, pp. 629–639, 1993.

[62] Z. Zhang and R. S. Blum, "A categorization and study of multiscale-decomposition-based image fusion schemes," pp. 1315–1328, 1999.

[63] F. R. Boddeke, L. J. van Vliet, H. Netten, and I. T. Young, "Autofocusing in microscopy based on the otf and sampling," *Bioimaging*, vol. 2, pp. 193–203, 1994.

[64] E. K. Yen and R. G. Johnston, "The ineffectiveness of the correlation coefficient for image comparisons."

[65] M. Jenkin, A. D. Jepson, and J. Tsotsos, "Techniques for disparity measurement," *Image Understanding*, vol. 53, pp. 14–30, 1991.

[66] R. Y. W. E. L. Hall and J. Rouge, "Hierarchical search for image matching," pp. 405–408, 1976.

[67] J. P. Lewis, "Fast template matching," *Vision Interface*, pp. 120–123, 1995.

[68] G. S. Cox, "Template matching and measures of match in image processing," 1995.

[69] D. I. Barnea and H. F. Silverman, "A class of algorithms for fast digital image registration," *IEEE Transactions on Computers*, vol. C-21, pp. 179–186, 1972.

[70] N. Bennet, R. Burridge, and N. Saito, "A method to detect and characterize ellipses using the hough transform," *IEEE Transactions on Pattern Analysis and Machine Intelligence*, vol. 21, no. 7, pp. 652–657, 1999.

[71] J. G. Daugman, "High confidence visual recognition of persons by a test of statistical independence," *IEEE Transactions on Pattern Analysis and Machine Intelligence*, vol. 15, no. 11, pp. 1148–1161, 1993.

[72] J. Serra, *Image Analysis and Mathematical Morphology.* Academic Press, 1982.

[73] F. I. Parke, "`www-viz.tamu.edu/faculty/parke/ends489f00/notes/sec1_9.html`," 2005.

[74] R. Owens, "`http://homepages.inf.ed.ac.uk/rbf/CVonline/LOCAL_COPIES/OWENS/LECT3/node3.html`," 2005.

[75] R. van den Boomgard and R. van Balen, "Methods for fast morphological image transforms using bitmapped images," *Computer Vision, Graphics and Image Processing: Graphical Models and Image Processing*, vol. 54, no. 3, pp. 252–254, 1992.

[76] N. Otsu, "A threshold selection method from gray-level histograms," *IEEE Transactions on Systems, Man and Cybernetics*, vol. 9, no. 1, pp. 62–66, 1979.

[77] J. N. Kapur, P. K. Sahoo, and A. K. C. Wong, "A new method for gray-level picture thresholding using the entropy of the histogram," *Graphical Models and Image Processing*, vol. 29, pp. 273–285, 1985.

[78] T. W. Ridler and S. Calvard, "Picture thresholding using an iterative selection method," *IEEE Transactions on Systems, Man and Cybernetics*, vol. SMC-8, pp. 630–632, 1978.

[79] R. O. Duda and P. E. Hart, "Use of the hough transform to detect lines and curves in pictures," *Commun. ACM*, vol. 15, pp. 11–15, 1972.

[80] P. Hough, *Methods and Means for Recognizing Complex Patterns.* U.S. Patent No 3,069,654, 1962.

[81] D. M. Tsa and S. K. Wu, "Automated surface inspection using gabor filters," *The International Journal of Advanced Manufacturing Technology*, vol. 16, no. 7, pp. 474–482, 2000.

[82] M. A. Coulthard, "Image processing for automatic surface defect detection," *Third International Conference on Image Processing and its Applications*, pp. 192–196, 1989.

[83] P. Kovesi, "Image features from phase congruency," *Videre: A Journal of Computer Vision Research, MIT Press*, vol. 1, pp. 1–27, 1999.

[84] J. F. Canny, "A computational approach to edge detection," *IEEE Trans. Pattern Analysis and Machine Intelligence*, vol. 8, pp. 112–131, 1986.

[85] D. G. Daut and D. Zhao, "A flaw detection method based on morphological image processing," *IEEE Transactions on Circuits and Systems for Video Technology*, vol. 3, no. 6, pp. 389–398, 1993.

[86] G. Lambert and F. Bock, "Wavelet methods for texture defect detection," *International Conference on Image Processing*, vol. 3.

[87] A. U. Batur and M. H. Hayes, "Adaptive active appearance models," *IEEE Transactions on Image Processing*, vol. 14, no. 11, pp. 1707–1721, 2005.

[88] P. L. Palmer, J. Kittler, and M. Petrou, "An optimizing line finder using a hough transform algorithm," *Computer Vision and Image Understanding*, vol. 67, pp. 1–23, 1997.

[89] A. Storkey, "http://www.anc.ed.ac.uk/~amos/ hough.html," 2004.

[90] D. Marr and E. C. Hildreth, "Theory of edge detection," *Proceedings of the Royal Society, London B*, vol. 207, pp. 187–217, 1980.

[91] P. Kovesi, "http://www.csse.uwa.edu.au/~pk/Research/MatlabFns/index.html#phasecong," 2004.

[92] L. Vincent and P. Soille, "Watersheds in digital spaces: An efficient algorithm based on immersion simulations," *IEEE Trans. Pat. Anal. Mach. Intel.*, vol. 13, pp. 583–598, 1991.

[93] *Fibre Optic Connector Interfaces - Part 5: Type MT connector family.* International Electrotechnical Commission (IEC), 1996.

[94] L. Ljung, *System Identification, Theory for the User.* Prentice Hall PTR, 1998.

[95] H. Rake, "Step response and frequency response methods," *Automatica*, vol. 16, pp. 519–526, 1980.

Appendix A

Lens Detailed Drawings

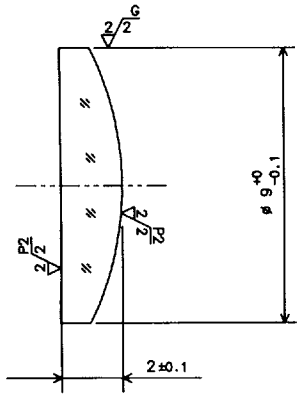

Left Surface:	Material Specification:	Right Surface:
R 319.761 CC ±0.319761 ø 9.0 Prot. Cham. 0.1 - 0.25 ~~Ⓛ MgF2 R<1.5%~~ 3/ 5(3) 4/ 1' 5/ 3x0.1; C 3x0.1; L 3x0.1; E 0.25 6/ -	Private LAF8_CHIN n(470 nm) 1.770766±0.001 v(470 nm) 470.9±0.8% 0/ 10 1/ 2x0.1 2/ 2;2	R 10.16 CX ±0.01016 ø 9.0 Prot. Cham. 0.1 - 0.25 ~~Ⓛ MgF2 R<1.5%~~ 3/ 5(3) 4/ 1' 5/ 3x0.1; C 3x0.1; L 3x0.1; E 0.25 6/ - To be cemented

Lens 1	
1	Ind. acc. ISO 10110

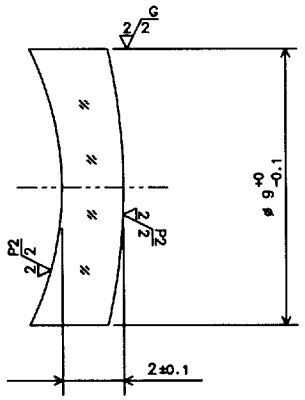

Left Surface:	Material Specification:	Right Surface:
R 10.16 CC ±0.01016 ø 9.0 Prot. Cham. 0.1 - 0.25 Ⓐ ~~MgF2 R<1.5%~~ 3/ 5(3) 4/ 1' 5/ 3x0.1; C 3x0.1; L 3x0.1; E 0.25 6/ - To be cemented	Private K20_CHIN n(470 nm) 1.540971±0.001 v(470 nm) 560.8±0.8% 0/ 10 1/ 2x0.1 2/ 2;2	R 20.193 CX ±0.020193 ø 9.0 Prot. Cham. 0.1 - 0.25 Ⓐ ~~MgF2 R<1.5%~~ 3/ 5(3) 4/ 1' 5/ 3x0.1; C 3x0.1; L 3x0.1; E 0.25 6/ -

Lens 2	
2	Ind. acc. ISO 10110

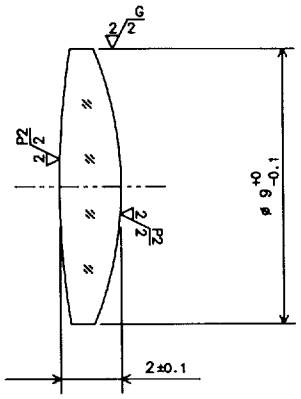

Left Surface:	Material Specification:	Right Surface:
R 28.6 CX ±0.0286 øe 9.0 Prot. Cham. 0.1 - 0.25 ~~(1) MgF2 R<1.5%~~ 3/ 5(3) 4/ 1' 5/ 3x0.1; C 3x0.1; L 3x0.1; E 0.25 6/ -	Private K20_CHN n(470 nm) 1.540971±0.001 v(470 nm) 560.8±0.8% 0/ 10 1/ 2x0.1 2/ 2;2	R 12.014 CX ±0.012014 øe 9.0 Prot. Cham. 0.1 - 0.25 ~~(1) MgF2 R<1.5%~~ 3/ 5(3) 4/ 1' 5/ 3x0.1; C 3x0.1; L 3x0.1; E 0.25 6/ - To be cemented

Lens 3	
3	Ind. acc. ISO 10110

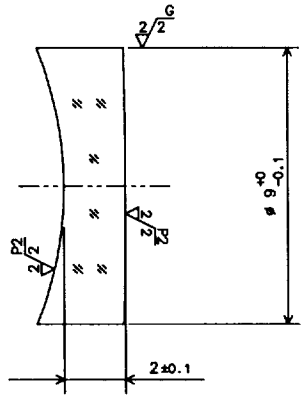

Left Surface:	Material Specification:	Right Surface:
R 12.014 CC ±0.012014 ø 9.0 Prot. Cham. 0.1 - 0.25 ~~① MgF2 R<1.5%~~ 3/ 5(3) 4/ 1' 5/ 3x0.1; C 3x0.1; L 3x0.1; E 0.25 6/ - To be cemented	Private ZF13_CHN n(470 nm) 1.811641±0.001 v(470 nm) 238.4±0.8% 0/ 10 1/ 2x0.1 2/ 2;2	R 202.66 CX ±0.20266 ø 9.0 Prot. Cham. 0.1 - 0.25 ~~① MgF2 R<1.5%~~ 3/ 5(3) 4/ 1' 5/ 3x0.1; C 3x0.1; L 3x0.1; E 0.25 6/ -

Lens 4	
4	Ind. acc. ISO 10110

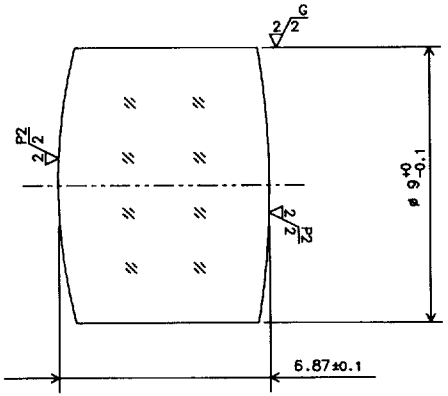

Left Surface:	Material Specification:	Right Surface:
R 18.155 CX ±0.018155 ø 9.0 Prot. Cham. 0.1 - 0.25 ~~1/ MgF2 R<1.5%~~ 3/ 5(3) 4/ 1' 5/ 3x0.1; C 3x0.1; L 3x0.1; E 0.25 6/ -	Private QF8_CHIN n(470 nm) 1.550577±0.001 v(470 nm) 461.6±0.8% 0/ 10 1/ 2x0.1 2/ 2;2	R 27.48 CX ±0.02748 ø 9.0 Prot. Cham. 0.1 - 0.25 ~~1/ MgF2 R<1.5%~~ 3/ 5(3) 4/ 1' 5/ 3x0.1; C 3x0.1; L 3x0.1; E 0.25 6/ -

Lens 5	
5	Ind. acc. ISO 10110

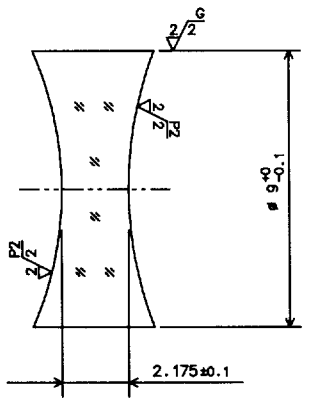

Left Surface:	Material Specification:	Right Surface:
R 11.172 CC ±0.011172 ø 9.0 Prot. Cham. 0.1 - 0.25 Ⓛ ~~Mgf 2~~ R<1.5% 3/ 5(3) 4/ 1' 5/ 3x0.1; C 3x0.1; L 3x0.1; E 0.25 6/ -	Private K20_CHN n(470 nm) 1.540971±0.001 v(470 nm) 580.8±0.8% 0/ 10 1/ 2x0.1 2/ 2:2	R 12.446 CC ±0.012446 ø 9.0 Prot. Cham. 0.1 - 0.25 Ⓛ ~~Mgf 2~~ R<1.5% 3/ 5(3) 4/ 1' 5/ 3x0.1; C 3x0.1; L 3x0.1; E 0.25 6/ -

Lens 6	
6	Ind. acc. ISO 10110

A.0.2 Glass Properties

Glass Name	LAF6_CHIN	K20_CHIN	ZF13_CHIN	QF8_CHIN
Index at 470 nm	1.770765868	1.540971076	1.811641047	1.550576636
Index at 465 nm	1.771597199	1.541444656	1.813391807	1.551183436
Index at 475 nm	1.769960523	1.540513191	1.809958075	1.549990777
Index at 454 nm	1.773524814	1.542545756	1.817498799	1.552597698
Index at 478 nm	1.769489295	1.540245684	1.808979615	1.549648886
Index at 447 nm	1.774829167	1.543292267	1.820311419	1.55355941
Index at 485 nm	1.768423342	1.539641588	1.806784176	1.548877875
V Number	470.9336839	580.7746079	236.3728186	461.6378707

Appendix B

Machine Detailed Drawings

DWG NO.	SH	REV
P1038-C3-Y-AXIS-GIB-DOWEL	1	0

ZONE	REV	DESCRIPTION	BY	DATE	APPROVED
-	-	-	-	-	-

QTY. 8

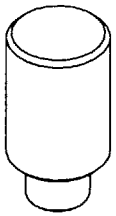

ISO VIEW
SCALE 15/1

SURFACE FINISH IN MICRONS

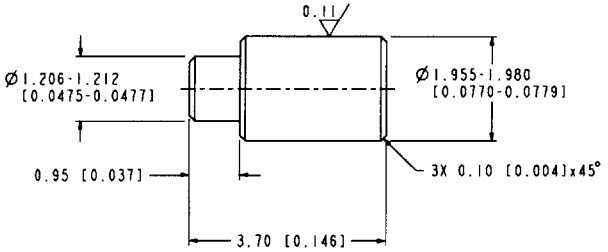

GENERAL NOTES (UNLESS OTHERWISE SPECIFIED):
1. REMOVE ALL BURRS AND SHARP EDGES.
2. TAPPED HOLES TO BE CLEARED AFTER HARDENING AND OR SURFACE FINISH.
3. MILLED SURFACES TO BE 63 RMS OR BETTER.
4. FLATNESS, PERPENDICULARITY AND PARALLELISM REQUIREMENTS MILLED SURFACES WITHIN .002"
5. NO MATERIAL AND OR PLATING SUBSTITUTIONS PERMITTED.

TOLERANCES	
.00	±0.15
.000	±0.05
.0000	± -
ANGLES	±1°

UNLESS OTHERWISE SPECIFIED DIMENSIONS ARE IN MM

FINISH:	-
HEAT TREAT:	-
MATERIAL:	303

INTERPRET PER ASME Y14.5M

CODE IDENT 31413

DESIGN 12/1/2003 A.WILSON
DRAWN 12-17-2003 M.DEROSA
CHK 01/03/2004 A.WILSON
APPD 12-17-2003 A.WILSON

[redacted]
TERADYNE CONNECTION SYSTEMS, INC
44 SIMON STREET, NASHUA, N.H. 03064 (603) 879-3000

TITLE
DOWEL FOR Y-AXIS GIB

PART NO.	REV
P1038-C3-Y-AXIS-GIB-DOWEL	0

PDM MODEL PART : P1038-C3-Y-AXIS-GIB-DOWEL 1.5
PDM DRAWING : P1038-C3-Y-AXIS-GIB-DOWEL 1.6

SIZE B | SCALE 15/1 | SHEET 1 OF 1

DWG NO P1038-C3-Y-AXIS-GIB-DOWEL
SH 1
REV 0

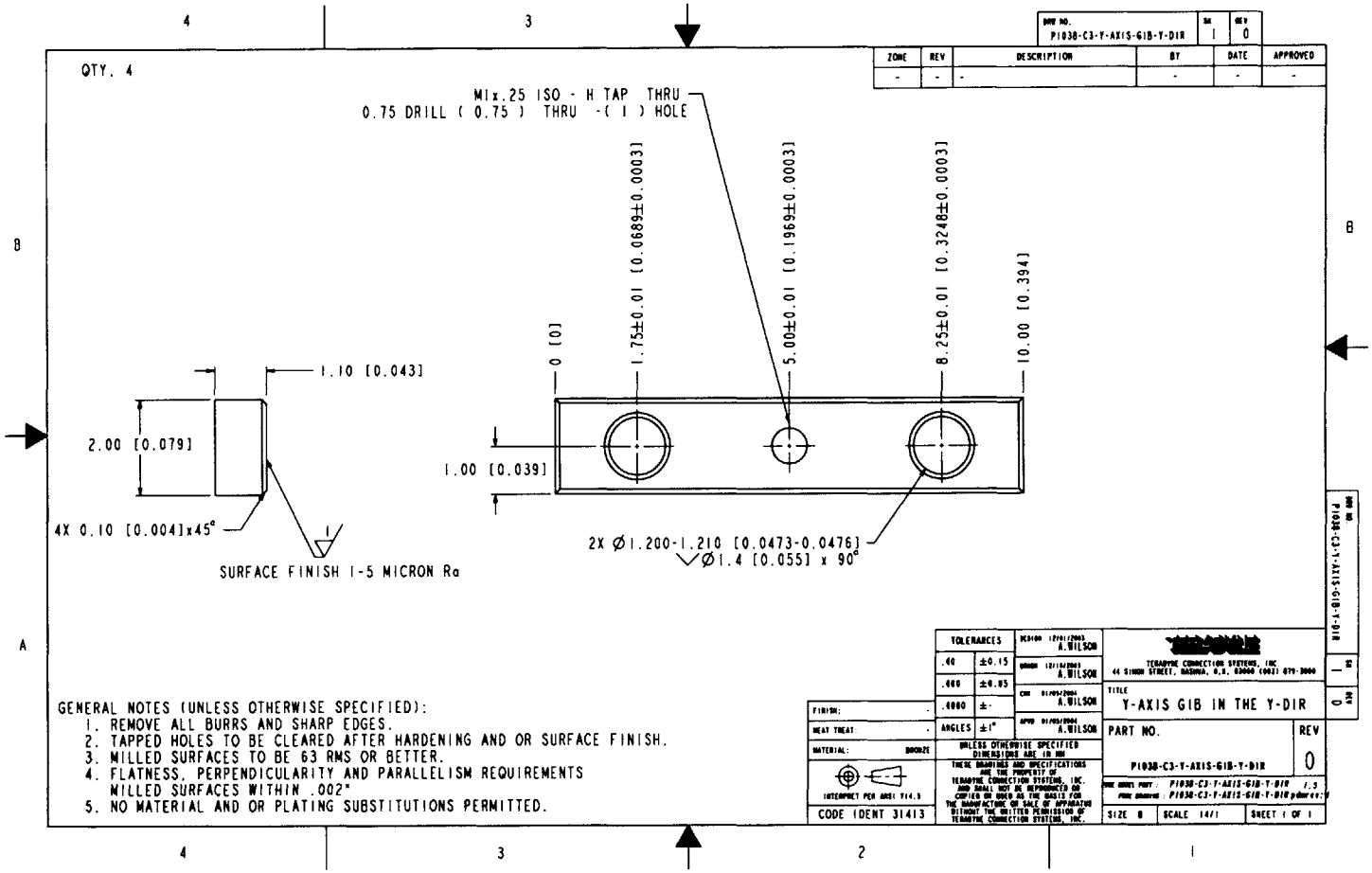
DWG NO. P1038-C3-Y-AXIS-GIB-Y-DIR
SH 1
REV 0
ZONE | REV | DESCRIPTION | BY | DATE | APPROVED
QTY. 4
M1x.25 ISO - H TAP THRU
0.75 DRILL (0.75) THRU -(1) HOLE
0 [0]
1.75±0.01 [0.0689±0.0003]
5.00±0.01 [0.1969±0.0003]
8.25±0.01 [0.3248±0.0003]
10.00 [0.394]
1.10 [0.043]
2.00 [0.079]
1.00 [0.039]
4X 0.10 [0.004]x45°
SURFACE FINISH 1-5 MICRON Ra
2X Ø1.200-1.210 [0.0473-0.0476]
Ø1.4 [0.055] x 90°
GENERAL NOTES (UNLESS OTHERWISE SPECIFIED):
1. REMOVE ALL BURRS AND SHARP EDGES.
2. TAPPED HOLES TO BE CLEARED AFTER HARDENING AND OR SURFACE FINISH.
3. MILLED SURFACES TO BE 63 RMS OR BETTER.
4. FLATNESS, PERPENDICULARITY AND PARALLELISM REQUIREMENTS MILLED SURFACES WITHIN .002"
5. NO MATERIAL AND OR PLATING SUBSTITUTIONS PERMITTED.
TOLERANCES
.XX ±0.15
.XXX ±0.05
.XXXX ±-
ANGLES ±1°
UNLESS OTHERWISE SPECIFIED DIMENSIONS ARE IN MM
A.WILSON
TERADYNE CONNECTION SYSTEMS, INC.
TITLE
Y-AXIS GIB IN THE Y-DIR
PART NO.
P1038-C3-Y-AXIS-GIB-Y-DIR
REV 0
SIZE B
SCALE 1:1
SHEET 1 OF 1
CODE IDENT 31413

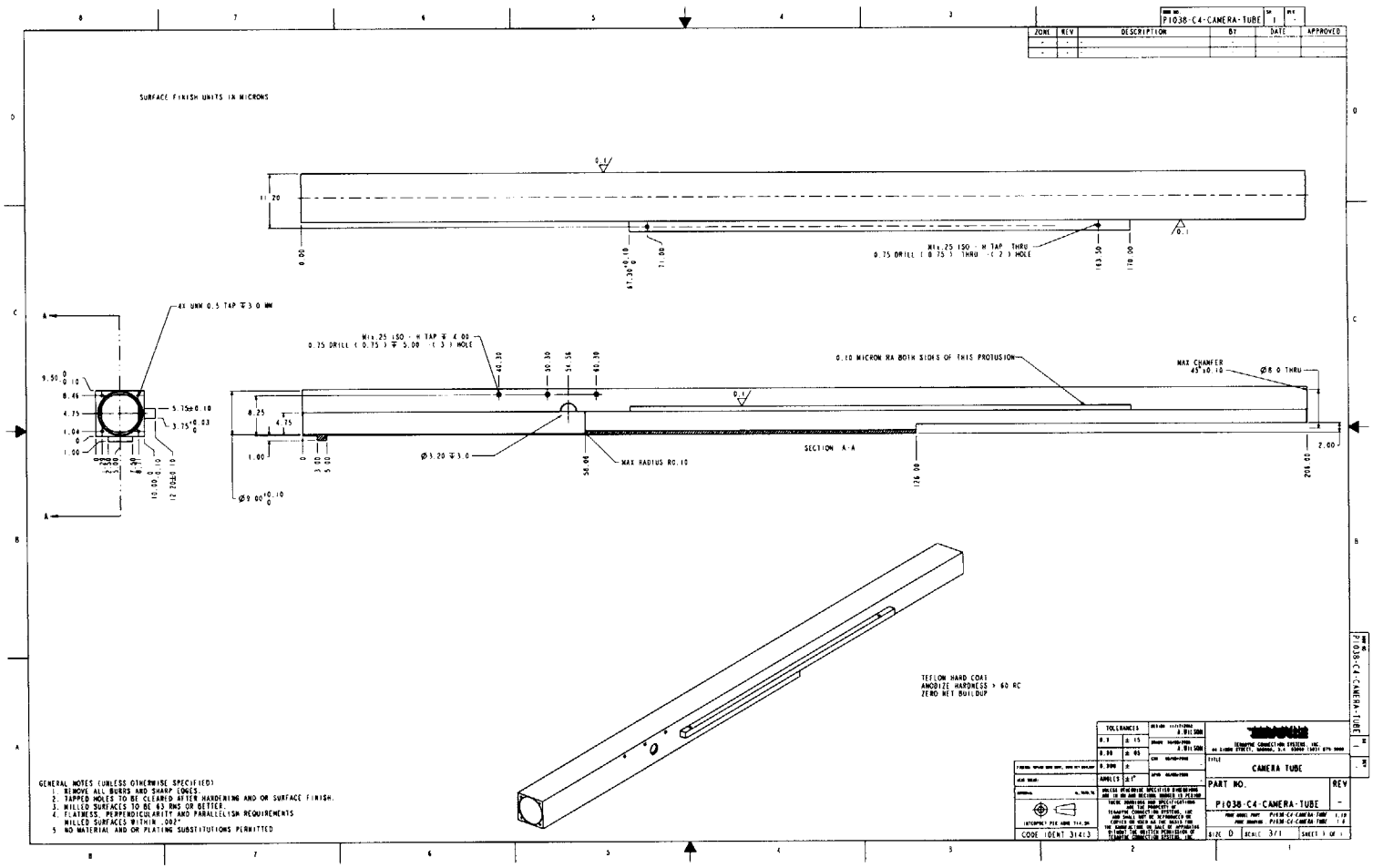
P1038-C4-CAMERA-TUBE
ZONE | REV | DESCRIPTION | BY | DATE | APPROVED
SURFACE FINISH UNITS IN MICRONS
4X UNM 0.5 TAP ↧3.0 MM
M1x.25 ISO - H TAP ↧ 4.00
0.75 DRILL (0.75) ↧ 5.00 (3) HOLE
M1x.25 ISO - H TAP THRU
0.75 DRILL (0.75) THRU (2) HOLE
0.10 MICRON RA BOTH SIDES OF THIS PROTUSION
MAX CHAMFER
45°±0.10
Ø8.0 THRU
Ø3.20 ↧3.0
MAX RADIUS R0.10
SECTION A-A
TEFLON HARD COAT
ANODIZE HARDNESS > 60 RC
ZERO NET BUILDUP
GENERAL NOTES (UNLESS OTHERWISE SPECIFIED)
1. REMOVE ALL BURRS AND SHARP EDGES.
2. TAPPED HOLES TO BE CLEARED AFTER HARDENING AND OR SURFACE FINISH.
3. MILLED SURFACES TO BE 63 RMS OR BETTER.
4. FLATNESS, PERPENDICULARITY AND PARALLELISM REQUIREMENTS
MILLED SURFACES WITHIN .002"
5. NO MATERIAL AND OR PLATING SUBSTITUTIONS PERMITTED
TOLERANCES
CAMERA TUBE
PART NO.
P1038-C4-CAMERA-TUBE
REV
CODE IDENT 31413
SIZE D
SCALE 3/1
SHEET 1 OF 1

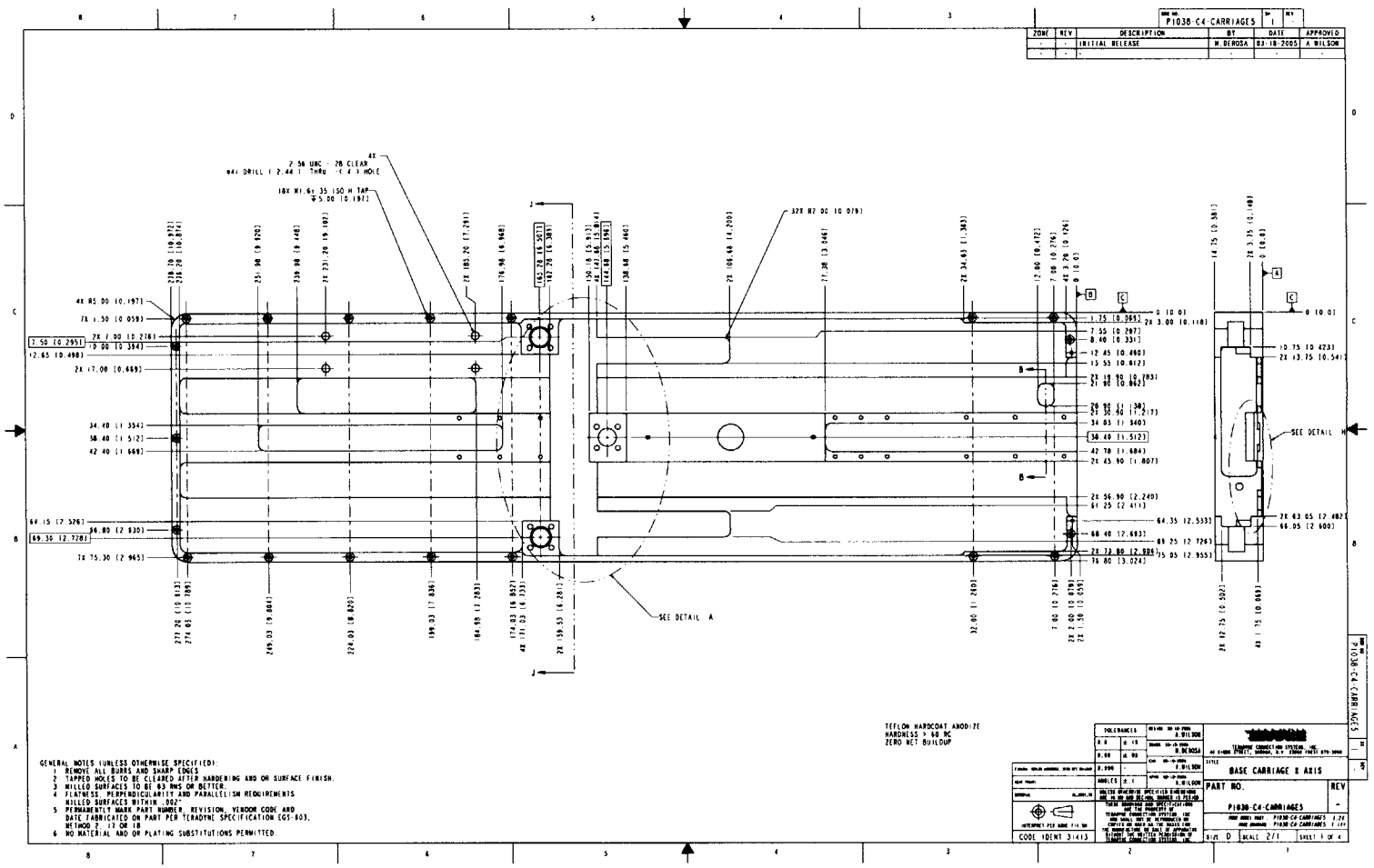
P1038-C4-CARRIAGE5
ZONE | REV | DESCRIPTION | BY | DATE | APPROVED
INITIAL RELEASE | M.DEROSA | 03-18-2005 | A.WILSON
4X 2.56 UNC - 2B CLEAR Ø4.1 DRILL (2.44) THRU - C & J - HOLE
18X M1.6x.35 -6H TAP Ø5.00 [0.197]
4X R5.00 [0.197]
7X 1.50 [0.059]
2X 7.00 [0.276]
7.50 [0.295]
9.00 [0.354]
12.65 [0.498]
2X 17.00 [0.669]
34.40 [1.354]
38.40 [1.512]
42.40 [1.669]
64.15 [2.526]
66.80 [2.630]
69.30 [2.728]
7X 75.30 [2.965]
SEE DETAIL A
SEE DETAIL B
TEFLON HARDCOAT ANODIZE HARDNESS > 60 RC ZERO NET BUILDUP
GENERAL NOTES (UNLESS OTHERWISE SPECIFIED):
1 REMOVE ALL BURRS AND SHARP EDGES
2 TAPPED HOLES TO BE CLEARED AFTER HARDENING AND OR SURFACE FINISH.
3 MILLED SURFACES TO BE 63 RMS OR BETTER.
4 FLATNESS, PERPENDICULARITY AND PARALLELISM REQUIREMENTS MILLED SURFACES WITHIN .002"
5 PERMANENTLY MARK PART NUMBER, REVISION, VENDOR CODE AND DATE FABRICATED ON PART PER TERADYNE SPECIFICATION EGS-603, METHOD 2, 17 OR 18
6 NO MATERIAL AND OR PLATING SUBSTITUTIONS PERMITTED
TOLERANCES
CODE IDENT 31413
BASE CARRIAGE X AXIS
PART NO. P1038-C4-CARRIAGE5
REV -
SIZE D | SCALE 2/1 | SHEET 1 OF 4

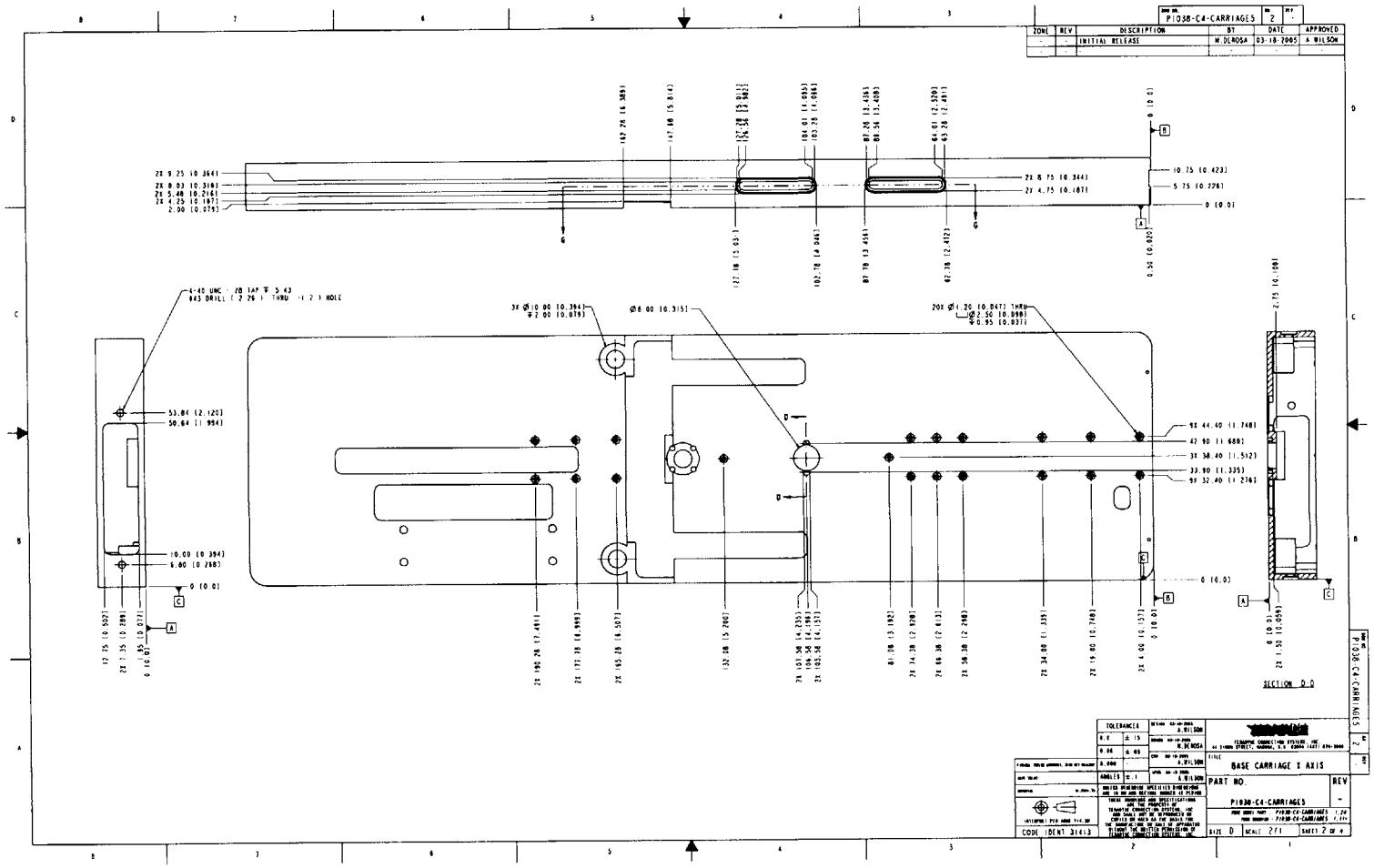
P1038-C4-CARRIAGES
ZONE | REV | DESCRIPTION | BY | DATE | APPROVED
INITIAL RELEASE | M.DEROSA | 03-18-2005 | A.WILSON
SECTION D-D
BASE CARRIAGE X AXIS
PART NO.
P1038-C4-CARRIAGES
REV
SIZE D SCALE 2/1 SHEETS 2 OF 4

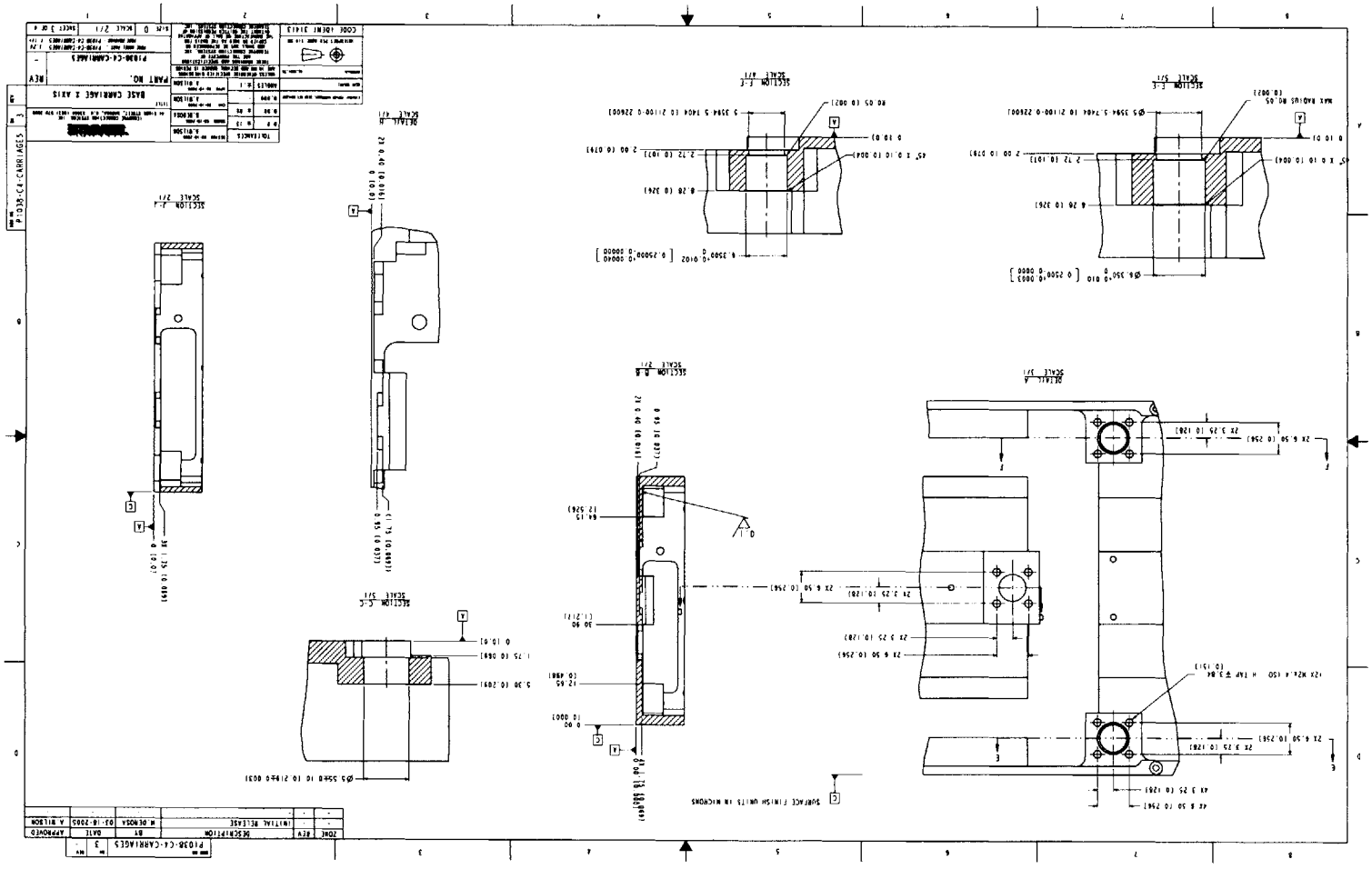

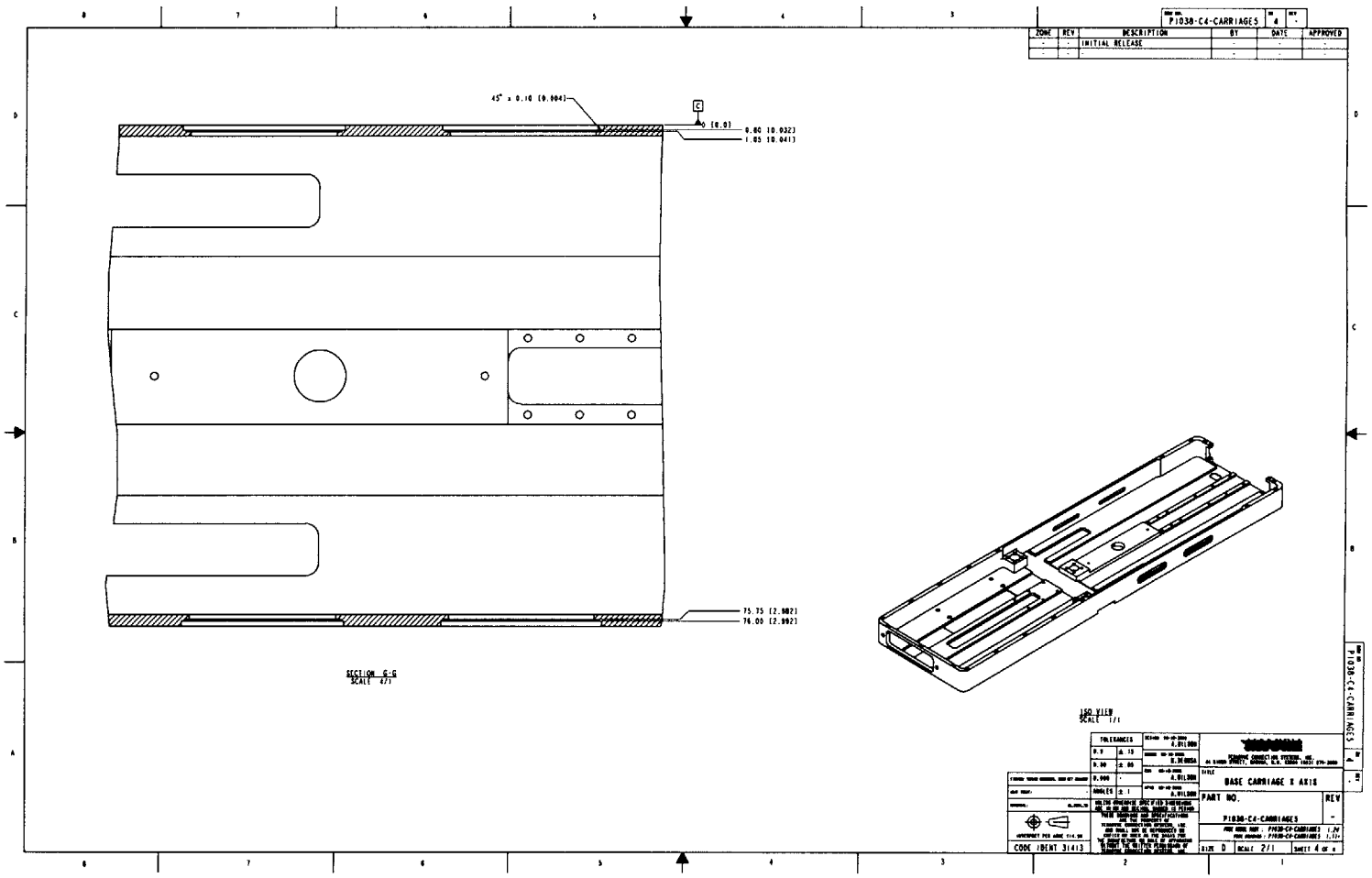
P1038-C4-CARRIAGE5
ZONE | REV | DESCRIPTION | BY | DATE | APPROVED
INITIAL RELEASE
45° x 0.10 [0.004]
C
0 [0.0]
0.80 [0.032]
1.05 [0.041]
75.75 [2.982]
76.00 [2.992]
SECTION G-G
SCALE 4/1
ISO VIEW
SCALE 1/1
TOLERANCES
CODE IDENT 31413
BASE CARRIAGE X AXIS
PART NO.
REV
P1038-C4-CARRIAGE5
SIZE D
SCALE 2/1
SHEET 4 OF 6

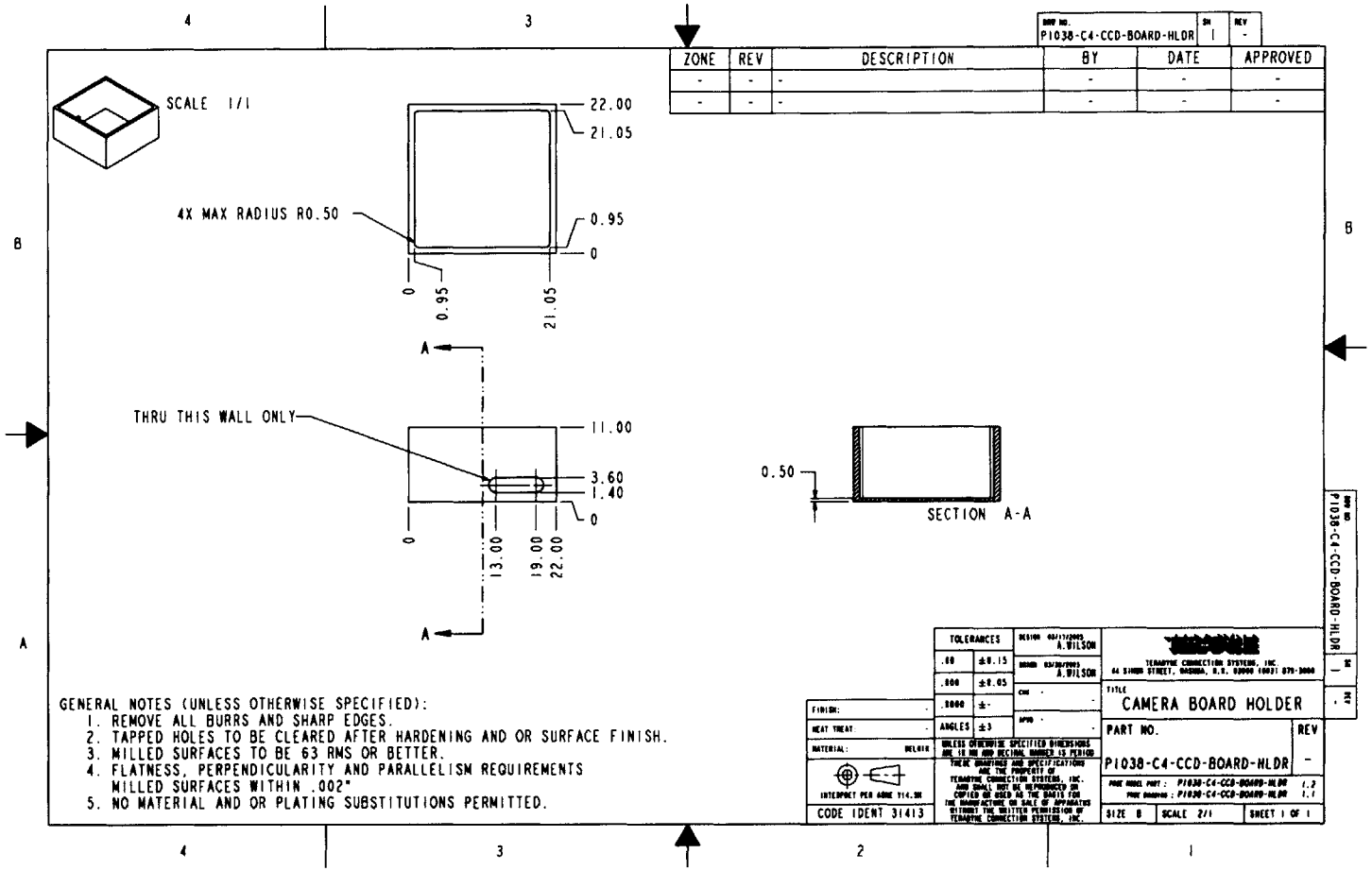

ZONE	REV	DESCRIPTION	BY	DATE	APPROVED
-	-	-	-	-	-
-	-	-	-	-	-

GENERAL NOTES (UNLESS OTHERWISE SPECIFIED):

1. REMOVE ALL BURRS AND SHARP EDGES.
2. TAPPED HOLES TO BE CLEARED AFTER HARDENING AND OR SURFACE FINISH.
3. MILLED SURFACES TO BE 63 RMS OR BETTER.
4. FLATNESS, PERPENDICULARITY AND PARALLELISM REQUIREMENTS MILLED SURFACES WITHIN .002"
5. NO MATERIAL AND OR PLATING SUBSTITUTIONS PERMITTED.

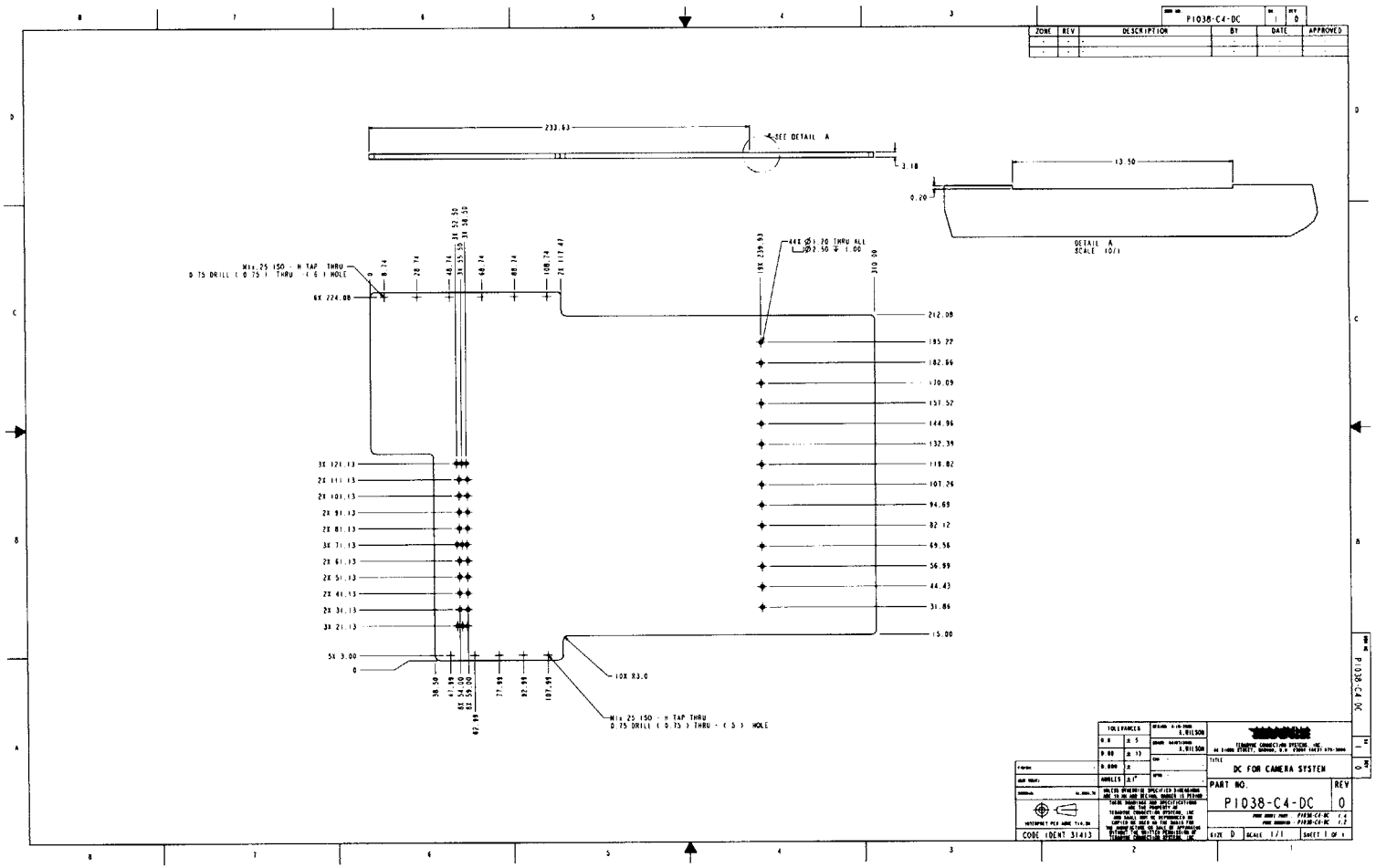
P1038-C4-DC
ZONE | REV | DESCRIPTION | BY | DATE | APPROVED
233.63
SEE DETAIL A
3.18
13.50
0.20
DETAIL A
SCALE 10/1
M4x.25 ISO - H TAP THRU
0.75 DRILL (0.75) THRU - (6) HOLE
6X 224.08
0
8.74
28.74
48.74
68.74
88.74
108.74
128.74
148.74
168.74
188.74
208.74
228.74
248.74
268.74
288.74
308.74
328.74
348.74
368.74
388.74
408.74
428.74
448.74
468.74
488.74
508.74
528.74
548.74
568.74
588.74
608.74
628.74
648.74
668.74
688.74
708.74
728.74
748.74
768.74
788.74

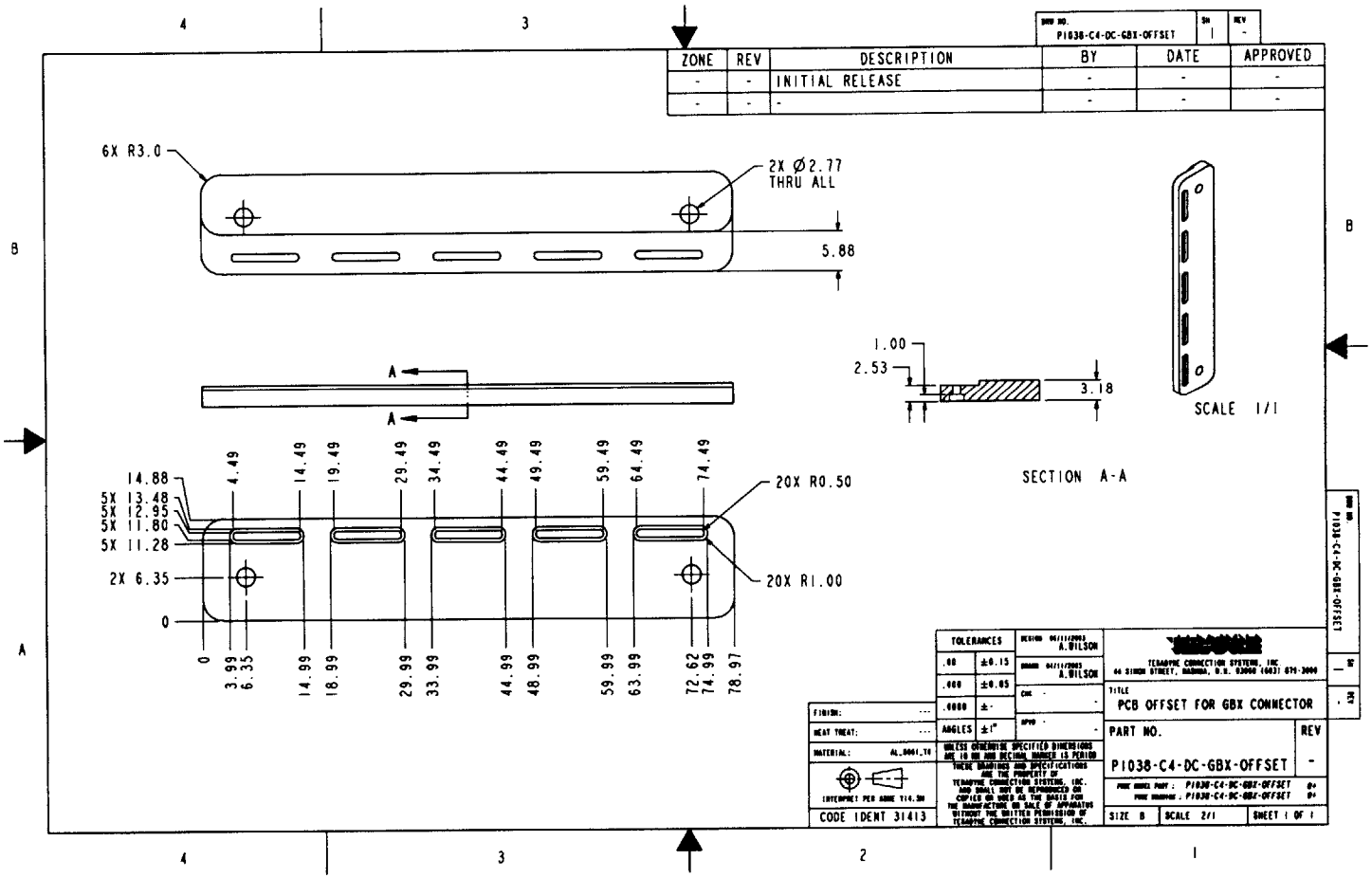
DWG NO. P1038-C4-DC-GBX-OFFSET
SH 1
REV -
ZONE | REV | DESCRIPTION | BY | DATE | APPROVED
- | - | INITIAL RELEASE | - | - | -
- | - | - | - | - | -
6X R3.0
2X Ø2.77 THRU ALL
5.88
1.00
2.53
3.18
SCALE 1/1
SECTION A-A
14.88
5X 13.48
5X 12.95
5X 11.80
5X 11.28
2X 6.35
0
4.49
14.49
19.49
29.49
34.49
44.49
49.49
59.49
64.49
74.49
20X R0.50
20X R1.00
0
3.99
6.35
14.99
18.99
29.99
33.99
44.99
48.99
59.99
63.99
72.62
74.99
78.97
TOLERANCES
.00 ±0.15
.000 ±0.05
.0000 ±-
ANGLES ±1°
UNLESS OTHERWISE SPECIFIED DIMENSIONS ARE IN DECIMAL MARKER IS PERIOD
THESE DRAWINGS AND SPECIFICATIONS ARE THE PROPERTY OF TERADYNE CONNECTION SYSTEMS, INC. AND SHALL NOT BE REPRODUCED OR COPIED OR USED AS THE BASIS FOR THE MANUFACTURE OR SALE OF APPARATUS WITHOUT THE WRITTEN PERMISSION OF TERADYNE CONNECTION SYSTEMS, INC.
FINISH: ---
HEAT TREAT: ---
MATERIAL: AL_6061_T6
INTERPRET PER ASME Y14.5M
CODE IDENT 31413
DESIGN 04/14/2003 A.WILSON
DRAWN 04/14/2003 A.WILSON
CHK -
APVD -
TERADYNE CONNECTION SYSTEMS, INC
TITLE PCB OFFSET FOR GBX CONNECTOR
PART NO. P1038-C4-DC-GBX-OFFSET
REV -
SIZE B SCALE 2/1 SHEET 1 OF 1

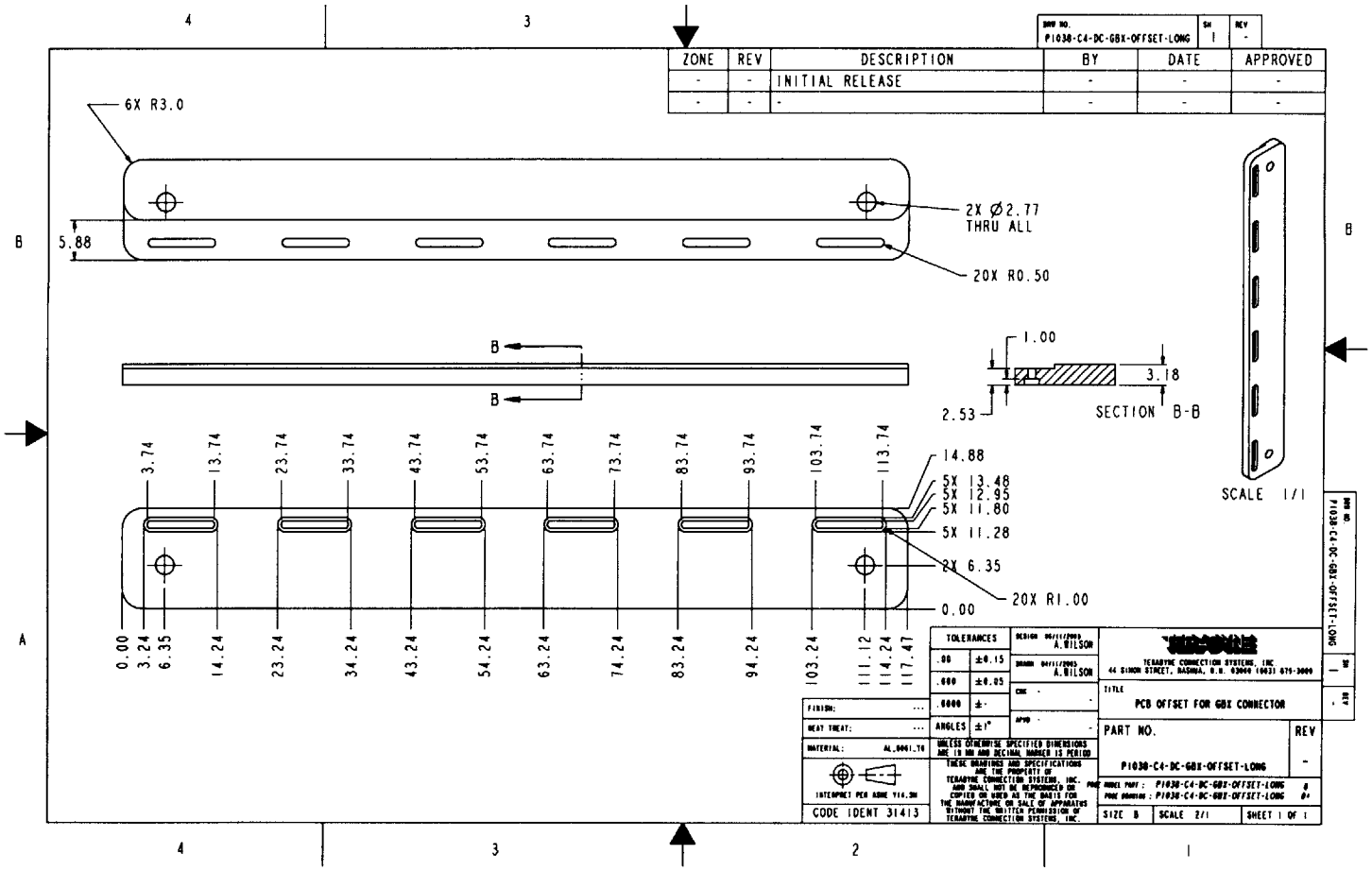
DWG NO. P1030-C4-DC-GBX-OFFSET-LONG
SH 1
REV -
ZONE | REV | DESCRIPTION | BY | DATE | APPROVED
- | - | INITIAL RELEASE | - | - | -
- | - | - | - | - | -
6X R3.0
5.88
2X Ø2.77 THRU ALL
20X R0.50
B
B
1.00
3.18
2.53
SECTION B-B
SCALE 1/1
3.74
13.74
23.74
33.74
43.74
53.74
63.74
73.74
83.74
93.74
103.74
113.74
14.88
5X 13.48
5X 12.95
5X 11.80
5X 11.28
2X 6.35
20X R1.00
0.00
0.00
3.24
6.35
14.24
23.24
34.24
43.24
54.24
63.24
74.24
83.24
94.24
103.24
111.12
114.24
117.47
TOLERANCES
.00 ±0.15
.000 ±0.05
.0000 ±.
ANGLES ±1°
FINISH:
HEAT TREAT:
MATERIAL:
INTERPRET PER ASME Y14.5M
CODE IDENT 31413
UNLESS OTHERWISE SPECIFIED DIMENSIONS ARE IN MM AND DECIMAL MARKER IS PERIOD
THESE DRAWINGS AND SPECIFICATIONS ARE THE PROPERTY OF TERADYNE CONNECTION SYSTEMS, INC. AND SHALL NOT BE REPRODUCED OR COPIED OR USED AS THE BASIS FOR THE MANUFACTURE OR SALE OF APPARATUS WITHOUT THE WRITTEN PERMISSION OF TERADYNE CONNECTION SYSTEMS, INC.
DESIGN 06/11/2003 A.WILSON
DRAWN 06/11/2003 A.WILSON
CHK -
APVD -
TERADYNE CONNECTION SYSTEMS, INC
44 SIMON STREET, NASHUA, N.H. 03060 (603) 879-3000
TITLE
PCB OFFSET FOR GBX CONNECTOR
PART NO.
P1030-C4-DC-GBX-OFFSET-LONG
REV -
MODEL PART : P1030-C4-DC-GBX-OFFSET-LONG
PROE DRAWING : P1030-C4-DC-GBX-OFFSET-LONG
SIZE B
SCALE 2/1
SHEET 1 OF 1
P1030-C4-DC-GBX-OFFSET-LONG

DWG NO. P1038-C4-DOOR	SH 1	REV -

ZONE	REV	DESCRIPTION	BY	DATE	APPROVED
-	-	-	-	-	-
-	-	-	-	-	-

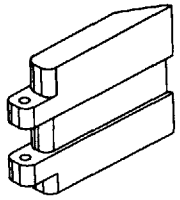

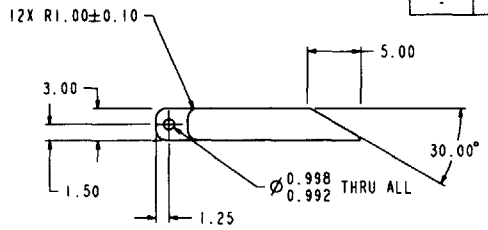

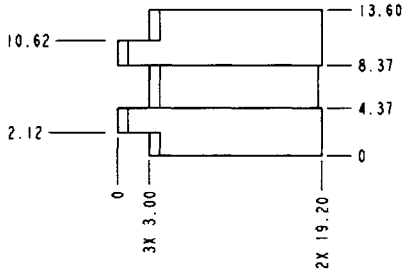

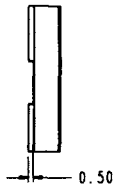

GENERAL NOTES (UNLESS OTHERWISE SPECIFIED):
1. REMOVE ALL BURRS AND SHARP EDGES.
2. TAPPED HOLES TO BE CLEARED AFTER HARDENING AND OR SURFACE FINISH.
3. MILLED SURFACES TO BE 63 RMS OR BETTER.
4. FLATNESS, PERPENDICULARITY AND PARALLELISM REQUIREMENTS MILLED SURFACES WITHIN .002"
5. NO MATERIAL AND OR PLATING SUBSTITUTIONS PERMITTED.

TOLERANCES	
.00	±0.15
.000	±0.05
.0000	±
ANGLES	±1°

UNLESS OTHERWISE SPECIFIED DIMENSIONS ARE IN MM AND SECTIONS DRAWN IN PERSPECTIVE

THESE DRAWINGS AND SPECIFICATIONS ARE THE PROPERTY OF TERADYNE CONNECTION SYSTEMS, INC. AND SHALL NOT BE REPRODUCED OR COPIED OR USED AS THE BASIS FOR THE MANUFACTURE OR SALE OF APPARATUS WITHOUT THE WRITTEN PERMISSION OF TERADYNE CONNECTION SYSTEMS, INC.

FINISH: -
HEAT TREAT: -
MATERIAL: AL.6061.T6

INTERPRET PER ASME Y14.5M

CODE IDENT 31413

DESIGN 11/04/2004 A.WILSON
DRAWN 03/23/2005 A.WILSON
CHK -
APVD -

TERADYNE CONNECTION SYSTEMS, INC.
44 SIMON STREET, NASHUA, N.H. 03060-1603 603-879-3000

TITLE: DOOR FOR FRONT OF SYSTEM

PART NO. P1038-C4-DOOR | REV -

PROE MODEL PART: P1038-C4-DOOR 1.17
PROE DRAWING: P1038-C4-DOOR 1.34

SIZE B | SCALE 3/1 | SHEET 1 OF 1

DWG NO. P1038-C4-DOOR | SH 1 | REV -

DWG NO.	SH	REV
P1038-C4-DOOR_2	1	-

ZONE	REV	DESCRIPTION	BY	DATE	APPROVED
-	-	-	-	-	-
-	-	-	-	-	-

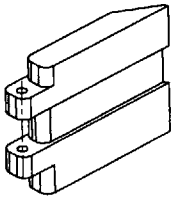

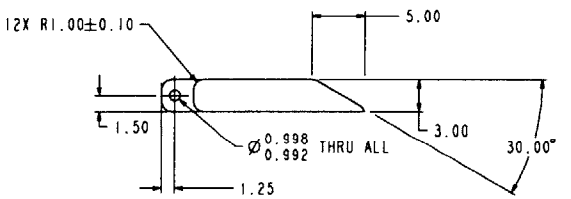

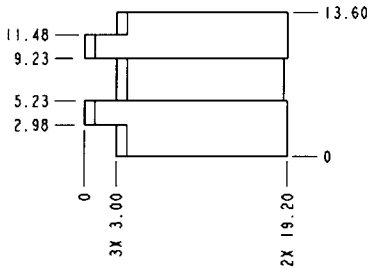

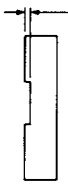

GENERAL NOTES (UNLESS OTHERWISE SPECIFIED):
1. REMOVE ALL BURRS AND SHARP EDGES.
2. TAPPED HOLES TO BE CLEARED AFTER HARDENING AND OR SURFACE FINISH.
3. MILLED SURFACES TO BE 63 RMS OR BETTER.
4. FLATNESS, PERPENDICULARITY AND PARALLELISM REQUIREMENTS MILLED SURFACES WITHIN .002"
5. NO MATERIAL AND OR PLATING SUBSTITUTIONS PERMITTED.

TOLERANCES	
.00	±0.15
.000	±0.05
.0000	± -
ANGLES	±3

UNLESS OTHERWISE SPECIFIED DIMENSIONS ARE IN INCHES AND DECIMAL MARKER IS PERIOD

THESE DRAWINGS AND SPECIFICATIONS ARE THE PROPERTY OF TERADYNE CONNECTION SYSTEMS, INC. AND SHALL NOT BE REPRODUCED OR COPIED OR USED AS THE BASIS FOR THE MANUFACTURE OR SALE OF APPARATUS WITHOUT THE WRITTEN PERMISSION OF TERADYNE CONNECTION SYSTEMS, INC.

DESIGN 11/04/2004 A.WILSON
DRAWN 03/23/2005 A.WILSON
CHK -
APPD -

FINISH: -
HEAT TREAT: -
MATERIAL: AL.6061.T6
INTERPRET PER ASME Y14.5M
CODE IDENT 31413

TERADYNE CONNECTION SYSTEMS, INC
44 SIMON STREET, NASHUA, N.H. 03060 (603) 879-3000

TITLE: DOOR FOR FRONT OF SYSTEM

PART NO.	REV
P1038-C4-DOOR_2	-

PROE MODEL PART : P1038-C4-DOOR_2 1.17
PROE DRAWING : P1038-C4-DOOR_2 1.3

SIZE B | SCALE 3/1 | SHEET 1 OF 1

DWG NO. P1038-C4-DOOR_2 | SH 1 | REV -

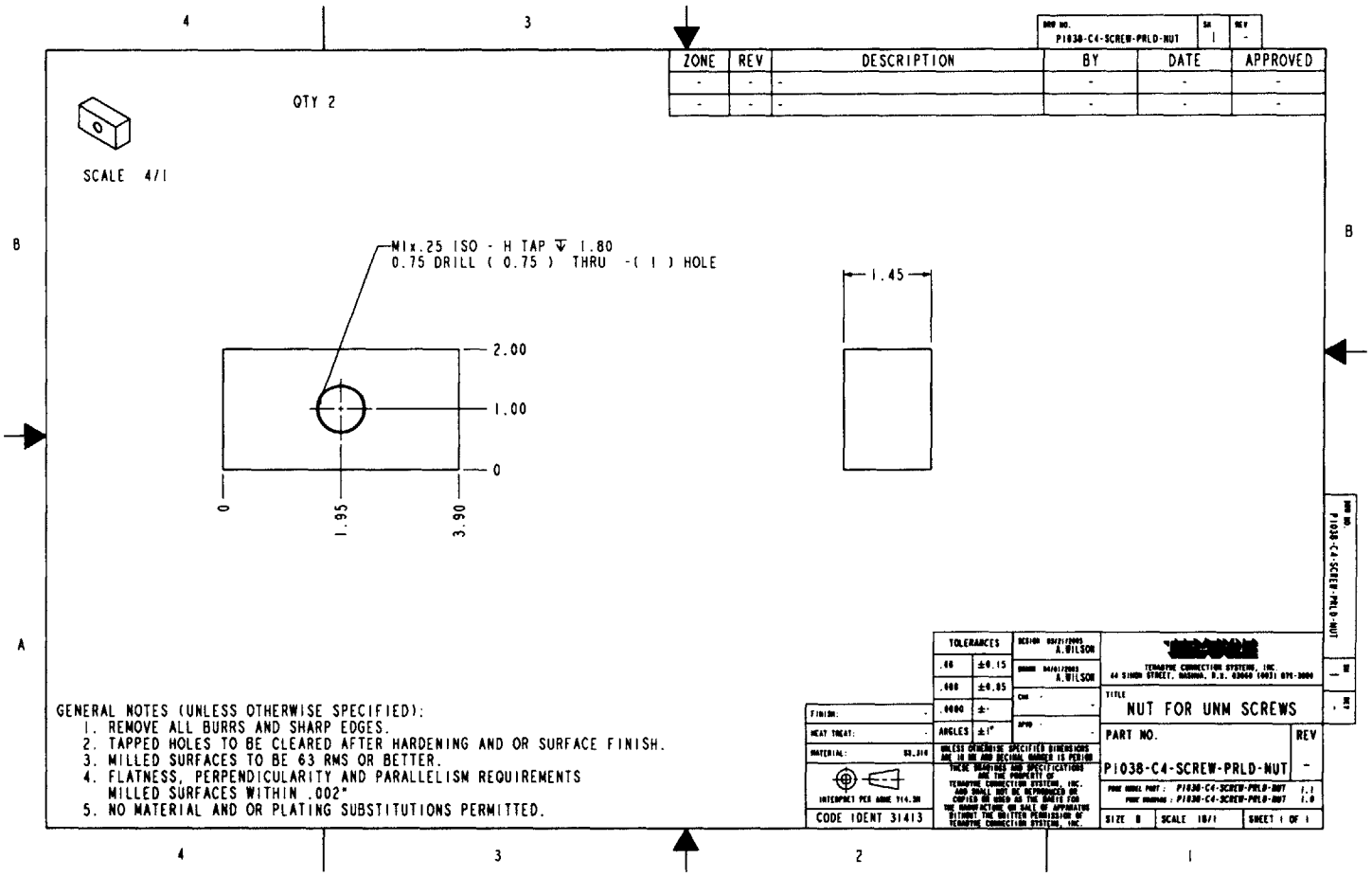
DRG NO. P1038-C4-SCREW-PRLD-NUT
SH 1
REV -
ZONE | REV | DESCRIPTION | BY | DATE | APPROVED
QTY 2
SCALE 4/1
M1x.25 ISO - H TAP ↧ 1.80
0.75 DRILL (0.75) THRU -(1) HOLE
2.00
1.00
0
0
1.95
3.90
1.45
GENERAL NOTES (UNLESS OTHERWISE SPECIFIED):
1. REMOVE ALL BURRS AND SHARP EDGES.
2. TAPPED HOLES TO BE CLEARED AFTER HARDENING AND OR SURFACE FINISH.
3. MILLED SURFACES TO BE 63 RMS OR BETTER.
4. FLATNESS, PERPENDICULARITY AND PARALLELISM REQUIREMENTS MILLED SURFACES WITHIN .002"
5. NO MATERIAL AND OR PLATING SUBSTITUTIONS PERMITTED.
TOLERANCES
.XX ±0.15
.XXX ±0.05
.XXXX ±.
ANGLES ±1°
FINISH:
HEAT TREAT:
MATERIAL:
INTERPRET PER ASME Y14.3M
CODE IDENT 31413
DESIGN 05/21/2003 A.WILSON
DRAWN 06/01/2003 A.WILSON
CHK
APVD
TERADYNE CONNECTION SYSTEMS, INC
TITLE
NUT FOR UNM SCREWS
PART NO.
REV
P1038-C4-SCREW-PRLD-NUT
-
SIZE B
SCALE 10/1
SHEET 1 OF 1

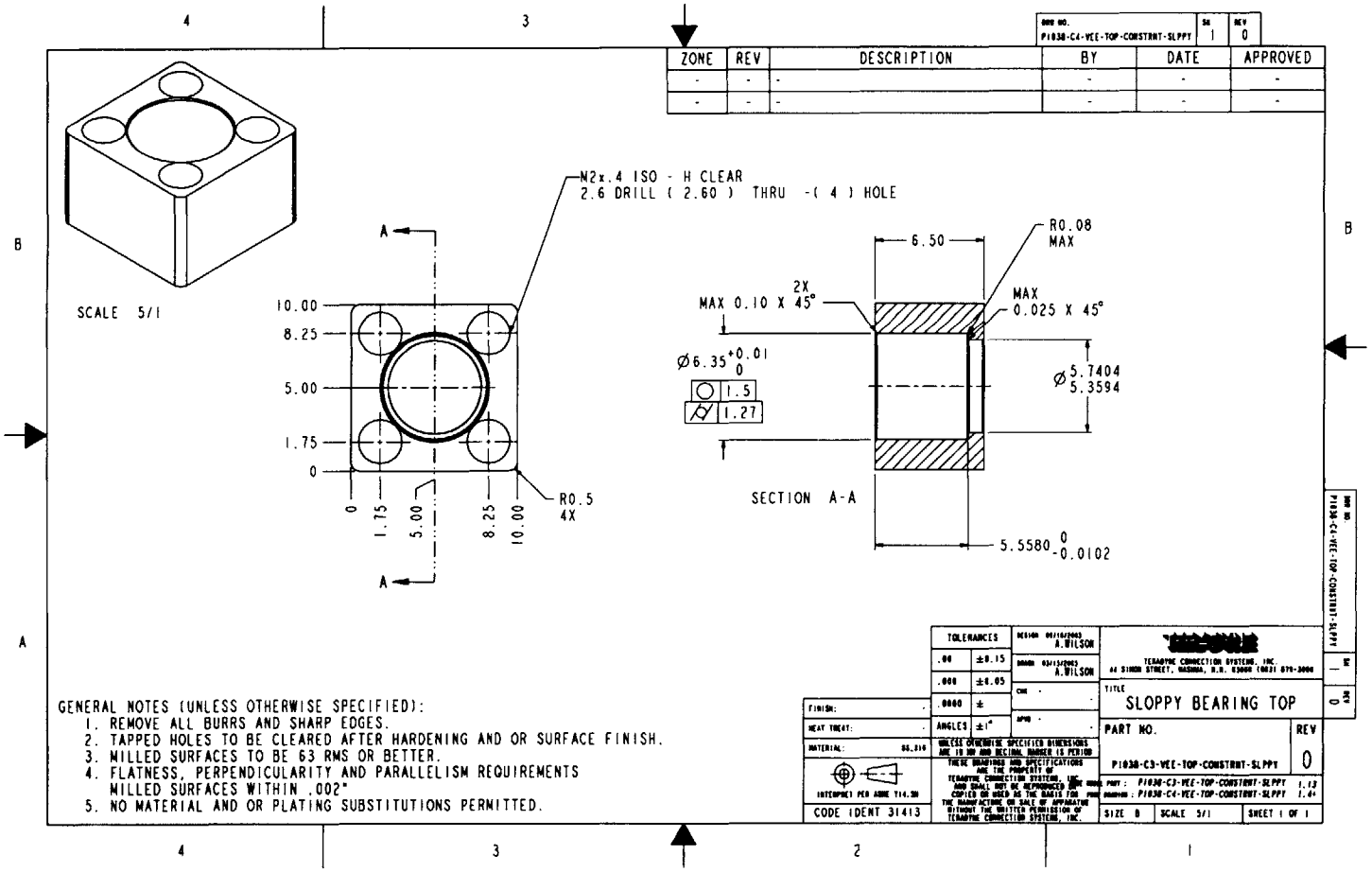
DWG NO. P1038-C4-VEE-TOP-CONSTRNT-SLPPY
SH 1
REV 0
ZONE | REV | DESCRIPTION | BY | DATE | APPROVED
SCALE 5/1
M2x.4 ISO - H CLEAR
2.6 DRILL (2.60) THRU -(4) HOLE
10.00
8.25
5.00
1.75
0
R0.5
4X
6.50
R0.08
MAX
2X
MAX 0.10 X 45°
MAX
0.025 X 45°
Ø6.35 +0.01 0
1.5
1.27
Ø5.7404
5.3594
SECTION A-A
5.5580 0 -0.0102
GENERAL NOTES (UNLESS OTHERWISE SPECIFIED):
1. REMOVE ALL BURRS AND SHARP EDGES.
2. TAPPED HOLES TO BE CLEARED AFTER HARDENING AND OR SURFACE FINISH.
3. MILLED SURFACES TO BE 63 RMS OR BETTER.
4. FLATNESS, PERPENDICULARITY AND PARALLELISM REQUIREMENTS MILLED SURFACES WITHIN .002"
5. NO MATERIAL AND OR PLATING SUBSTITUTIONS PERMITTED.
TOLERANCES
.00 ±0.15
.000 ±0.05
.0000 ±
ANGLES ±1°
FINISH:
HEAT TREAT:
MATERIAL:
INTERPRET PER ASME Y14.5M
CODE IDENT 31413
A.WILSON
TERADYNE CONNECTION SYSTEMS, INC.
TITLE
SLOPPY BEARING TOP
PART NO.
REV
P1038-C3-VEE-TOP-CONSTRNT-SLPPY
0
SIZE B
SCALE 5/1
SHEET 1 OF 1

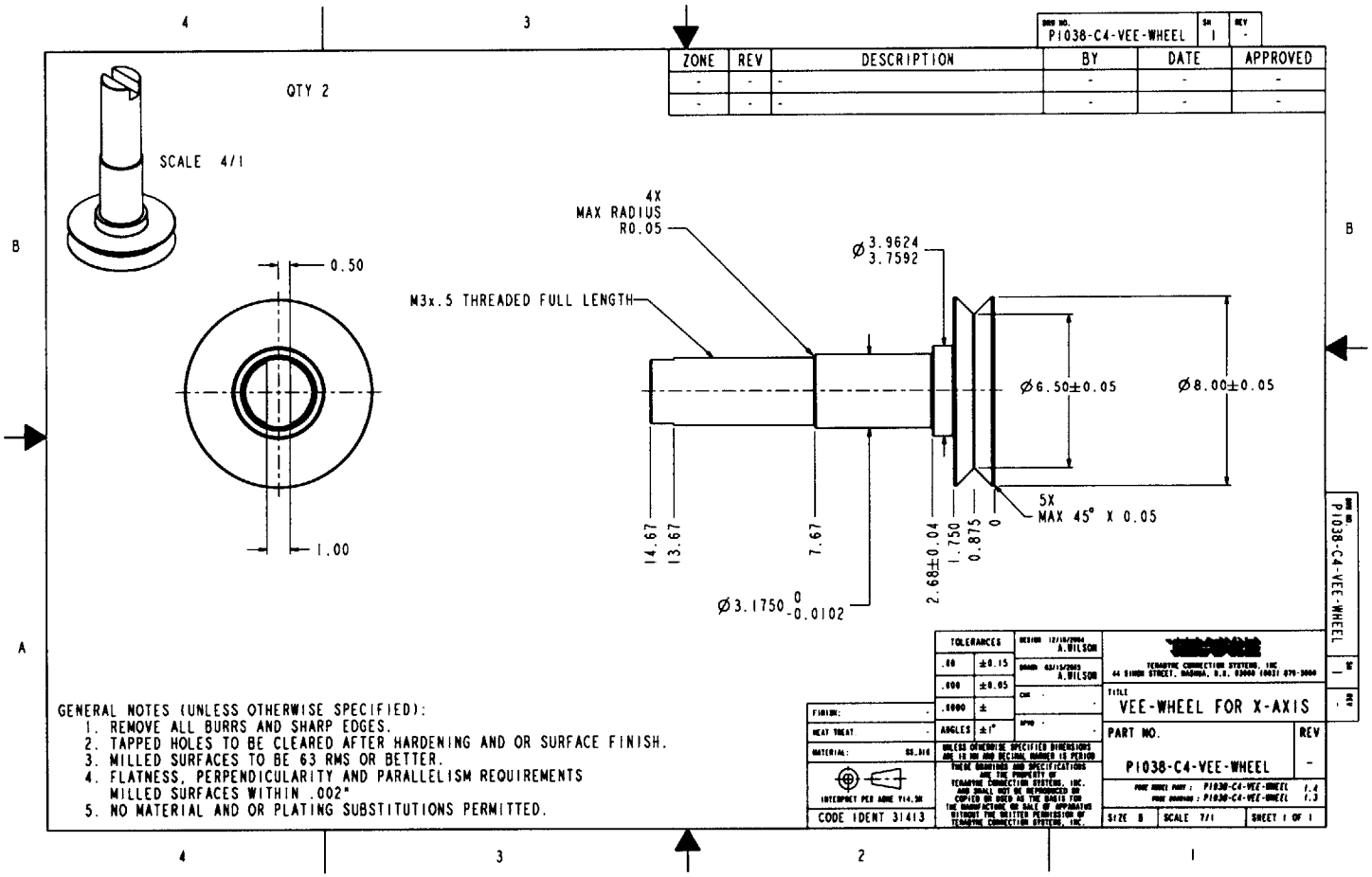
DWG NO. P1038-C4-VEE-WHEEL
SH 1
REV -
ZONE | REV | DESCRIPTION | BY | DATE | APPROVED
QTY 2
SCALE 4/1
4X MAX RADIUS R0.05
M3x.5 THREADED FULL LENGTH
Ø3.9624 3.7592
Ø6.50±0.05
Ø8.00±0.05
5X MAX 45° X 0.05
0.50
1.00
14.67
13.67
7.67
2.68±0.04
1.750
0.875
0
Ø3.1750 0 -0.0102
TOLERANCES
.00 ±0.15
.000 ±0.05
.0000 ±
ANGLES ±1°
FINISH:
HEAT TREAT:
MATERIAL: SS.316
INTERPRET PER ASME Y14.5M
CODE IDENT 31413
UNLESS OTHERWISE SPECIFIED DIMENSIONS ARE IN INCHES AND DECIMAL MARKED IS PERINCH
THESE DRAWINGS AND SPECIFICATIONS ARE THE PROPERTY OF TERADYNE CONNECTION SYSTEMS, INC. AND SHALL NOT BE REPRODUCED OR COPIED OR USED AS THE BASIS FOR THE MANUFACTURE OR SALE OF APPARATUS WITHOUT THE WRITTEN PERMISSION OF TERADYNE CONNECTION SYSTEMS, INC.
DESIGN 12/10/2004 A.WILSON
DRAWN 03/15/2005 A.WILSON
CHK -
APVD -
[redacted]
TERADYNE CONNECTION SYSTEMS, INC
44 SIMON STREET, NASHUA, N.H. 03060 (603) 879-3000
TITLE VEE-WHEEL FOR X-AXIS
PART NO. P1038-C4-VEE-WHEEL
REV -
PROE MODEL PART : P1038-C4-VEE-WHEEL 1.4
PROE DRAWING : P1038-C4-VEE-WHEEL 1.3
SIZE B SCALE 7/1 SHEET 1 OF 1
P1038-C4-VEE-WHEEL
SH 1
REV -
4 3 2 1
A B

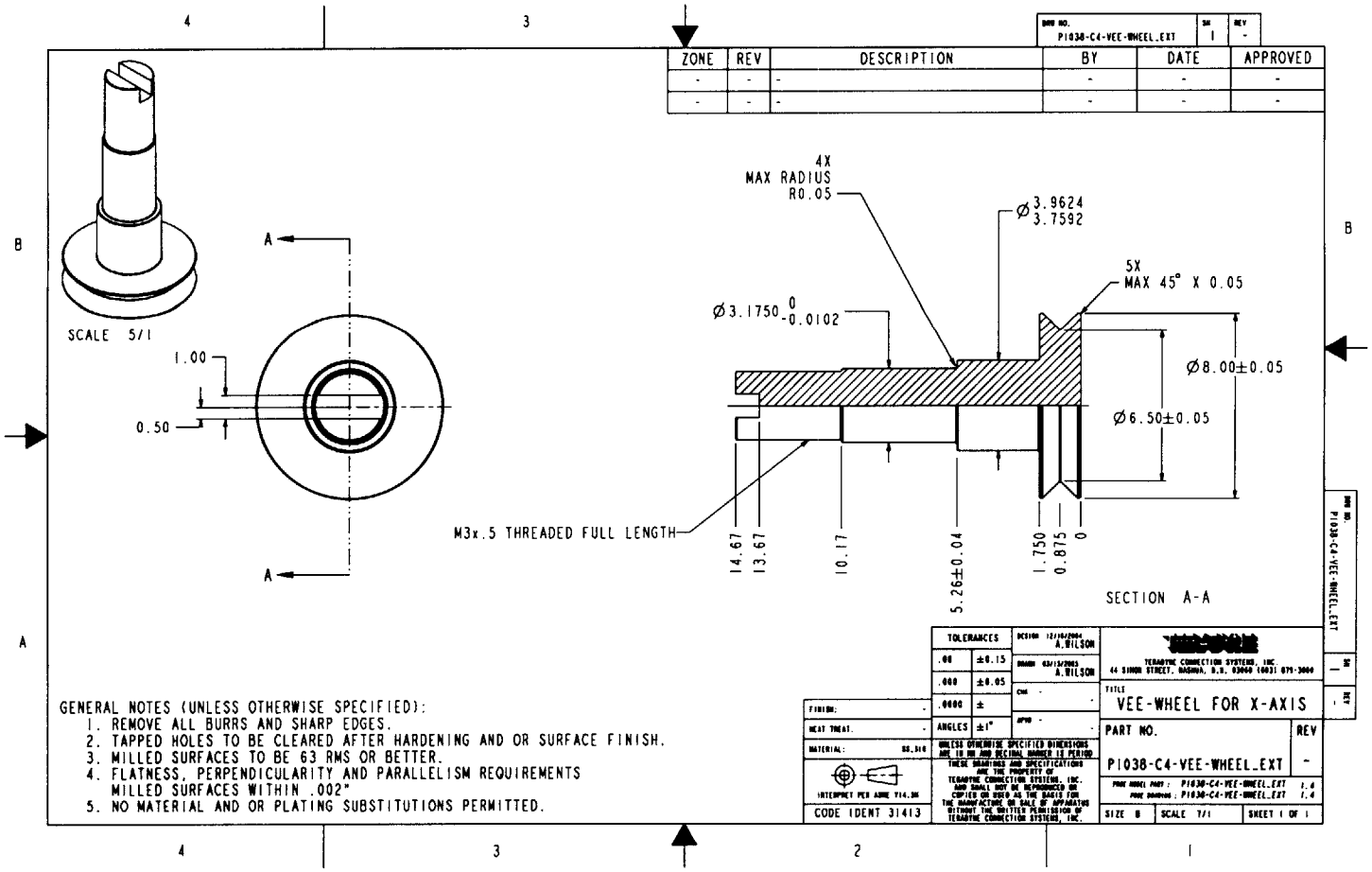
DWG NO. P1038-C4-VEE-WHEEL_EXT
SH 1
REV -
ZONE | REV | DESCRIPTION | BY | DATE | APPROVED
SCALE 5/1
1.00
0.50
A
4X MAX RADIUS R0.05
Ø3.9624
3.7592
5X MAX 45° X 0.05
Ø3.1750 0 -0.0102
Ø8.00±0.05
Ø6.50±0.05
M3x.5 THREADED FULL LENGTH
14.67
13.67
10.17
5.26±0.04
1.750
0.875
0
SECTION A-A
GENERAL NOTES (UNLESS OTHERWISE SPECIFIED):
1. REMOVE ALL BURRS AND SHARP EDGES.
2. TAPPED HOLES TO BE CLEARED AFTER HARDENING AND OR SURFACE FINISH.
3. MILLED SURFACES TO BE 63 RMS OR BETTER.
4. FLATNESS, PERPENDICULARITY AND PARALLELISM REQUIREMENTS MILLED SURFACES WITHIN .002"
5. NO MATERIAL AND OR PLATING SUBSTITUTIONS PERMITTED.
TOLERANCES
.00 ±0.15
.000 ±0.05
.0000 ±
ANGLES ±1°
FINISH:
HEAT TREAT.
MATERIAL:
INTERPRET PER ASME Y14.5M
CODE IDENT 31413
DESIGN 12/10/2004 A.WILSON
DRAWN 03/15/2005 A.WILSON
CHK -
APVD -
UNLESS OTHERWISE SPECIFIED DIMENSIONS ARE IN INCHES AND DECIMAL MARKER IS PERIOD
THESE DRAWINGS AND SPECIFICATIONS ARE THE PROPERTY OF TERADYNE CONNECTION SYSTEMS, INC. AND SHALL NOT BE REPRODUCED OR COPIED OR USED AS THE BASIS FOR THE MANUFACTURE OR SALE OF APPARATUS WITHOUT THE WRITTEN PERMISSION OF TERADYNE CONNECTION SYSTEMS, INC.
TERADYNE CONNECTION SYSTEMS, INC
44 SIMON STREET, NASHUA, N.H. 03060 (603) 879-3000
TITLE
VEE-WHEEL FOR X-AXIS
PART NO.
P1038-C4-VEE-WHEEL_EXT
REV -
PROE MODEL PART : P1038-C4-VEE-WHEEL_EXT 1.4
PROE DRAWING : P1038-C4-VEE-WHEEL_EXT 1.4
SIZE B
SCALE 7/1
SHEET 1 OF 1
DWG NO. P1038-C4-VEE-WHEEL_EXT
SH 1
REV -

ZONE	REV	DESCRIPTION	BY	DATE	APPROVED
-	-	-	-	-	-
-	-	-	-	-	-

QTY 3

SCALE 5/1

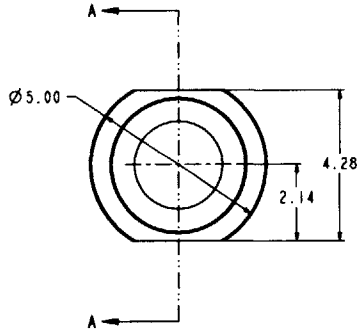

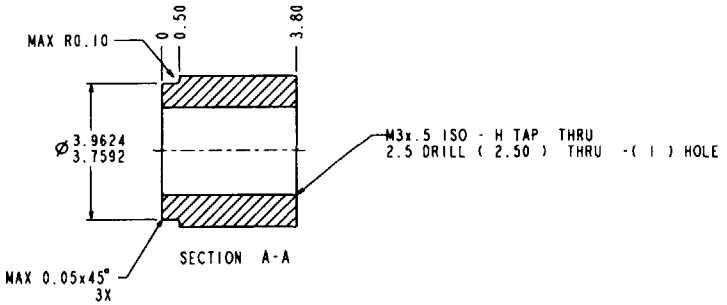

GENERAL NOTES (UNLESS OTHERWISE SPECIFIED):
1. REMOVE ALL BURRS AND SHARP EDGES.
2. TAPPED HOLES TO BE CLEARED AFTER HARDENING AND OR SURFACE FINISH.
3. MILLED SURFACES TO BE 63 RMS OR BETTER.
4. FLATNESS, PERPENDICULARITY AND PARALLELISM REQUIREMENTS MILLED SURFACES WITHIN .002"
5. NO MATERIAL AND OR PLATING SUBSTITUTIONS PERMITTED.

TOLERANCES	
.00	±0.15
.000	±0.05
.0000	±
ANGLES	±1°

FINISH: -
HEAT TREAT: -
MATERIAL: 6061-T6

INTERPRET PER ASME Y14.5M

CODE IDENT 31413

DESIGN 12/16/2004 A.WILSON
DRAWN 02/15/2005 A.WILSON
CHK -
APVD -

UNLESS OTHERWISE SPECIFIED DIMENSIONS ARE IN INCH AND DECIMAL MARKER IS PERIOD

THESE DRAWINGS AND SPECIFICATIONS ARE THE PROPERTY OF TERADYNE CONNECTION SYSTEMS, INC. AND SHALL NOT BE REPRODUCED OR COPIED OR USED AS THE BASIS FOR THE MANUFACTURE OR SALE OF APPARATUS WITHOUT THE WRITTEN PERMISSION OF TERADYNE CONNECTION SYSTEMS, INC.

TERADYNE CONNECTION SYSTEMS, INC.
44 SIMON STREET, NASHUA, N.H. 03060 (603) 879-3000

TITLE
VEE WHEEL SPACER

PART NO.	REV
P1038-C4-VEE-WHEEL-SPCR	1

PART NAME PART : P1038-C4-VEE-WHEEL-SPCR 1.0
PART DRAWING : P1038-C4-VEE-WHEEL-SPCR 1.0

SIZE B | SCALE 10/1 | SHEET 1 OF 1

P1038-C4-VEE-WHEEL-SPCR

ZONE	REV	DESCRIPTION	BY	DATE	APPROVED
-	-	-	-	-	-
-	-	-	-	-	-

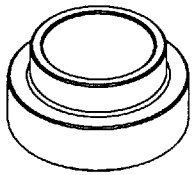

QTY 2

SCALE 10/1

SURFACE FINISH UNITS IN MICRONS

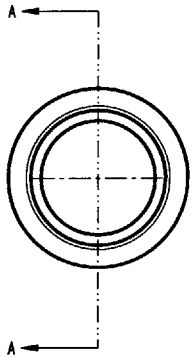

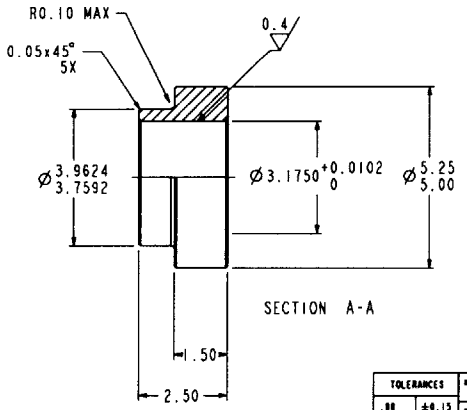

SECTION A-A

GENERAL NOTES (UNLESS OTHERWISE SPECIFIED):
1. REMOVE ALL BURRS AND SHARP EDGES.
2. TAPPED HOLES TO BE CLEARED AFTER HARDENING AND OR SURFACE FINISH.
3. MILLED SURFACES TO BE 63 RMS OR BETTER.
4. FLATNESS, PERPENDICULARITY AND PARALLELISM REQUIREMENTS MILLED SURFACES WITHIN .002"
5. NO MATERIAL AND OR PLATING SUBSTITUTIONS PERMITTED.

TOLERANCES	
.00	±0.15
.000	±0.05
.0000	±
ANGLES	±1°

FINISH: -
HEAT TREAT: -
MATERIAL: 65.310

INTERPRET PER ASME Y14.5M

UNLESS OTHERWISE SPECIFIED DIMENSIONS ARE IN INCH AND DECIMAL MARKER IS PERIOD

THESE DRAWINGS AND SPECIFICATIONS ARE THE PROPERTY OF TERADYNE CONNECTION SYSTEMS, INC. AND SHALL NOT BE REPRODUCED OR COPIED OR USED AS THE BASIS FOR THE MANUFACTURE OR SALE OF APPARATUS WITHOUT THE WRITTEN PERMISSION OF TERADYNE CONNECTION SYSTEMS, INC.

CODE IDENT 31413

DRAWN 03/16/2005 A.WILSON
CHK -
APVD -

TERADYNE CONNECTION SYSTEMS, INC.
44 SIMON STREET, NASHUA, N.H. 03060 (603) 879-3000

TITLE: WORM PRELOAD

PART NO. P1038-C4-WORM-PRELOAD

REV -

SIZE B | SCALE 10/1 | SHEET 1 OF 1

P1038-C4-WORM-PRELOAD | SH 1 | REV -

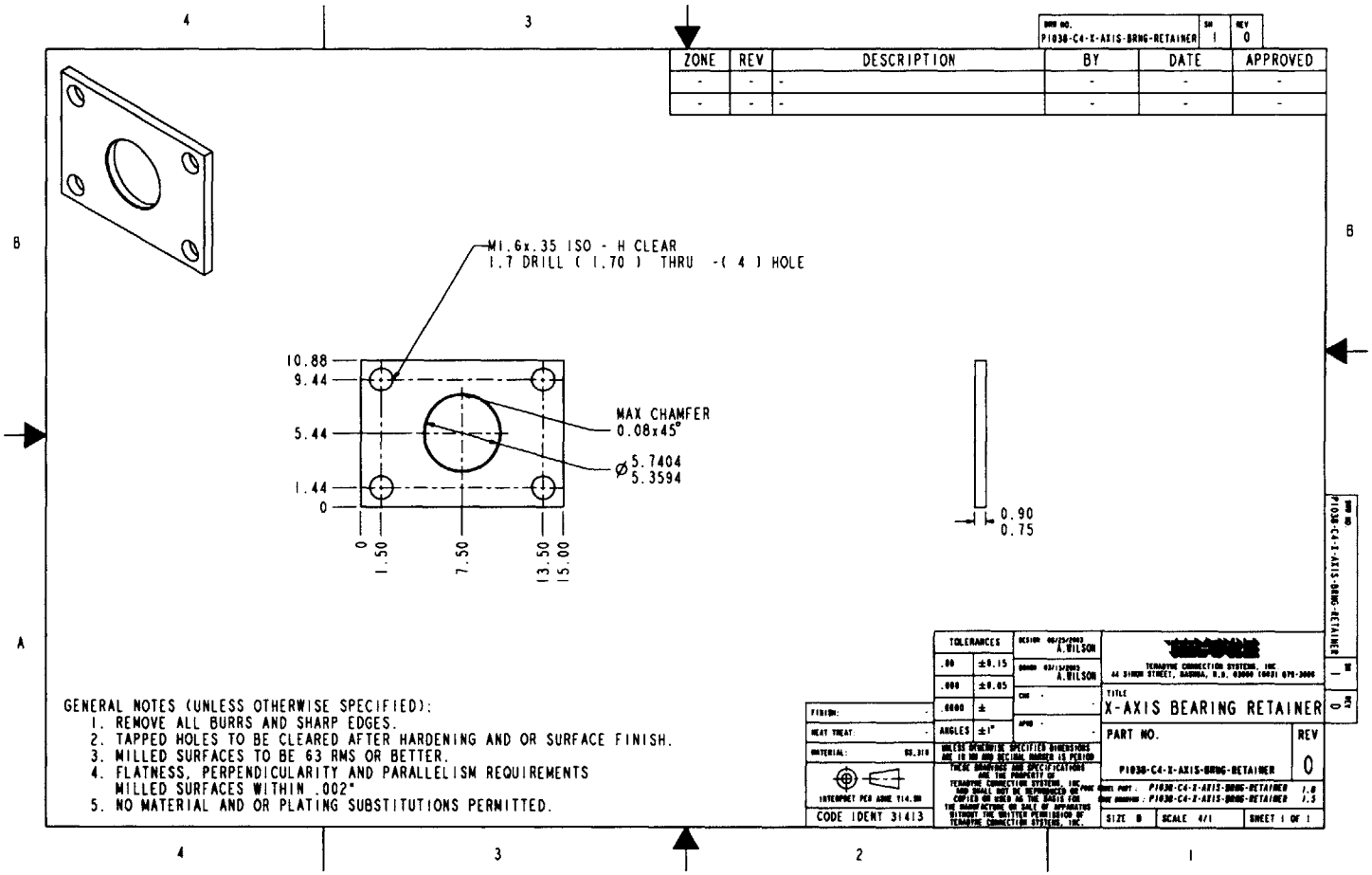
M1.6x.35 ISO - H CLEAR
1.7 DRILL (1.70) THRU -(4) HOLE
10.88
9.44
5.44
1.44
0
0
1.50
7.50
13.50
15.00
MAX CHAMFER
0.08x45°
Ø5.7404
5.3594
0.90
0.75
ZONE | REV | DESCRIPTION | BY | DATE | APPROVED
P1030-C4-X-AXIS-BRNG-RETAINER
GENERAL NOTES (UNLESS OTHERWISE SPECIFIED):
1. REMOVE ALL BURRS AND SHARP EDGES.
2. TAPPED HOLES TO BE CLEARED AFTER HARDENING AND OR SURFACE FINISH.
3. MILLED SURFACES TO BE 63 RMS OR BETTER.
4. FLATNESS, PERPENDICULARITY AND PARALLELISM REQUIREMENTS MILLED SURFACES WITHIN .002"
5. NO MATERIAL AND OR PLATING SUBSTITUTIONS PERMITTED.
TOLERANCES
.00 ±0.15
.000 ±0.05
.0000 ±
ANGLES ±1°
A.WILSON
TERADYNE CONNECTION SYSTEMS, INC
TITLE
X-AXIS BEARING RETAINER
PART NO.
REV
P1030-C4-X-AXIS-BRNG-RETAINER
0
CODE IDENT 31413
SIZE B
SCALE 4/1
SHEET 1 OF 1

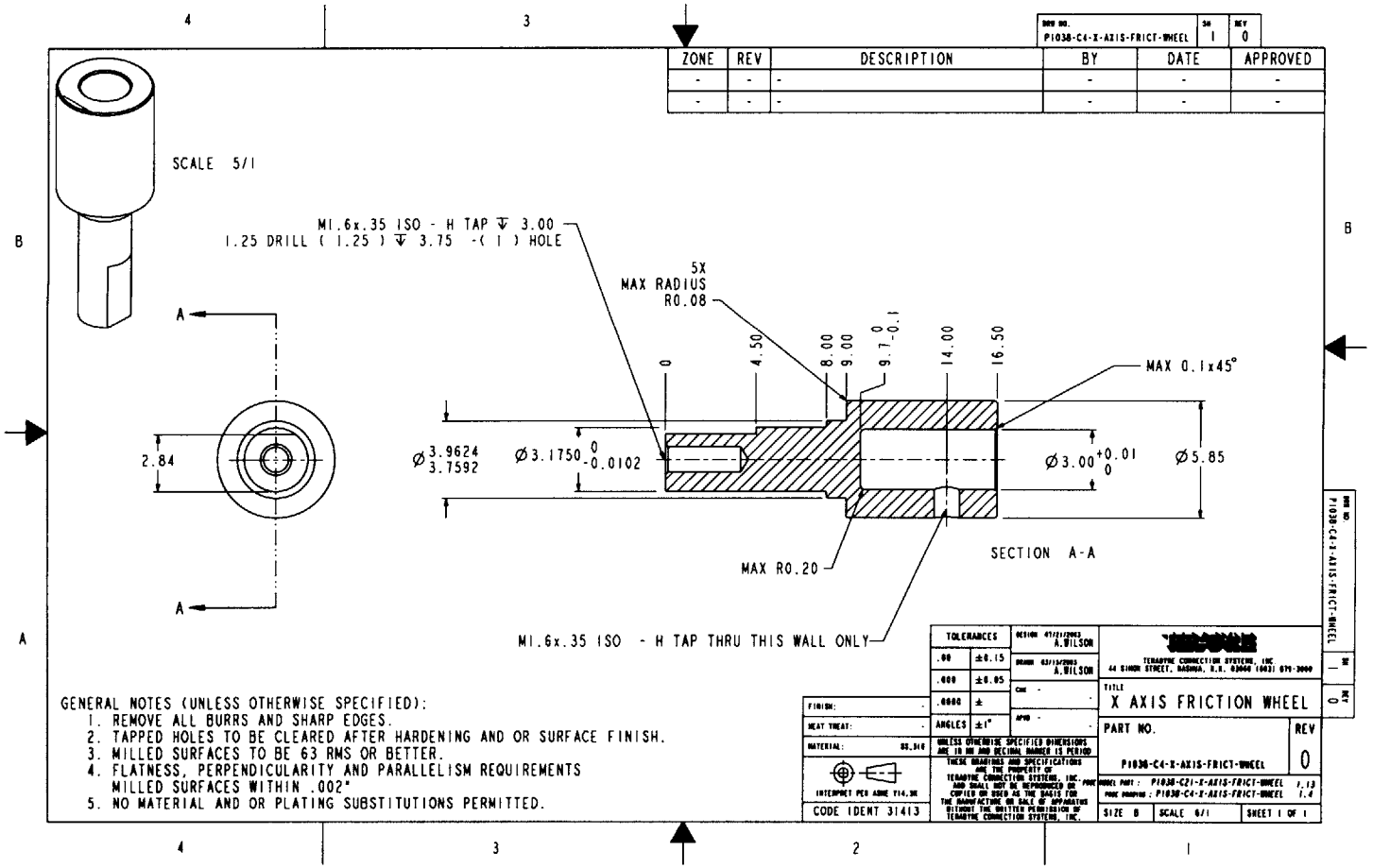
DWG NO. P1038-C4-X-AXIS-FRICT-WHEEL
SH 1
REV 0
ZONE | REV | DESCRIPTION | BY | DATE | APPROVED
SCALE 5/1
M1.6x.35 ISO - H TAP ↧ 3.00
1.25 DRILL (1.25) ↧ 3.75 -(1) HOLE
5X
MAX RADIUS
R0.08
0
4.50
8.00
9.00
9.7 0 -0.1
14.00
16.50
MAX 0.1x45°
2.84
Ø3.9624
3.7592
Ø3.1750 0 -0.0102
Ø3.00 +0.01 0
Ø5.85
MAX R0.20
SECTION A-A
M1.6x.35 ISO - H TAP THRU THIS WALL ONLY
GENERAL NOTES (UNLESS OTHERWISE SPECIFIED):
1. REMOVE ALL BURRS AND SHARP EDGES.
2. TAPPED HOLES TO BE CLEARED AFTER HARDENING AND OR SURFACE FINISH.
3. MILLED SURFACES TO BE 63 RMS OR BETTER.
4. FLATNESS, PERPENDICULARITY AND PARALLELISM REQUIREMENTS MILLED SURFACES WITHIN .002"
5. NO MATERIAL AND OR PLATING SUBSTITUTIONS PERMITTED.
TOLERANCES
.00 ±0.15
.000 ±0.05
.0000 ±
ANGLES ±1°
FINISH:
HEAT TREAT:
MATERIAL:
INTERPRET PER ASME Y14.5M
CODE IDENT 31413
DESIGN 07/21/2003 A.WILSON
DRAWN 03/13/2003 A.WILSON
CHK -
APVD -
UNLESS OTHERWISE SPECIFIED DIMENSIONS ARE IN INCH AND DECIMAL MARKER IS PERIOD
THESE DRAWINGS AND SPECIFICATIONS ARE THE PROPERTY OF TERADYNE CONNECTION SYSTEMS, INC. AND SHALL NOT BE REPRODUCED OR COPIED OR USED AS THE BASIS FOR THE MANUFACTURE OR SALE OF APPARATUS WITHOUT THE WRITTEN PERMISSION OF TERADYNE CONNECTION SYSTEMS, INC.
TERADYNE CONNECTION SYSTEMS, INC
44 SIMON STREET, NASHUA, N.H. 03060 (603) 879-3000
TITLE
X AXIS FRICTION WHEEL
PART NO.
P1038-C4-X-AXIS-FRICT-WHEEL
REV 0
MODEL PART : P1038-C21-X-AXIS-FRICT-WHEEL 1.13
PROC PROFILE : P1038-C4-X-AXIS-FRICT-WHEEL 1.4
SIZE B
SCALE 6/1
SHEET 1 OF 1
P1038-C4-X-AXIS-FRICT-WHEEL
DWG NO
REV
0 INC

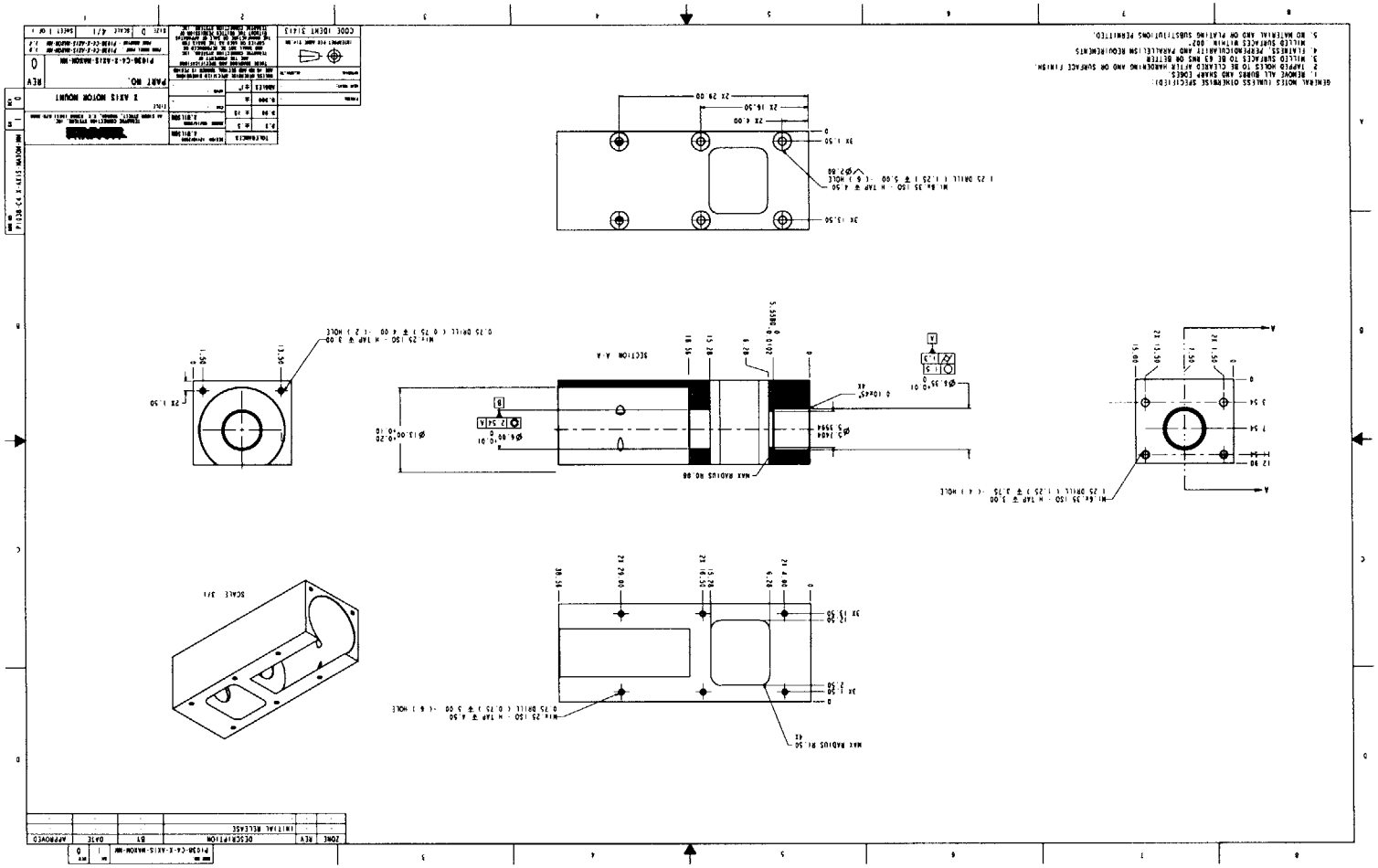
PART NO.
P10B-C4-A01S-MAXON-MM
REV
0
X AXIS MOTOR MOUNT
SCALE 1/1
SECTION A-A
MAX RADIUS R0.50
MAX RADIUS R0.80

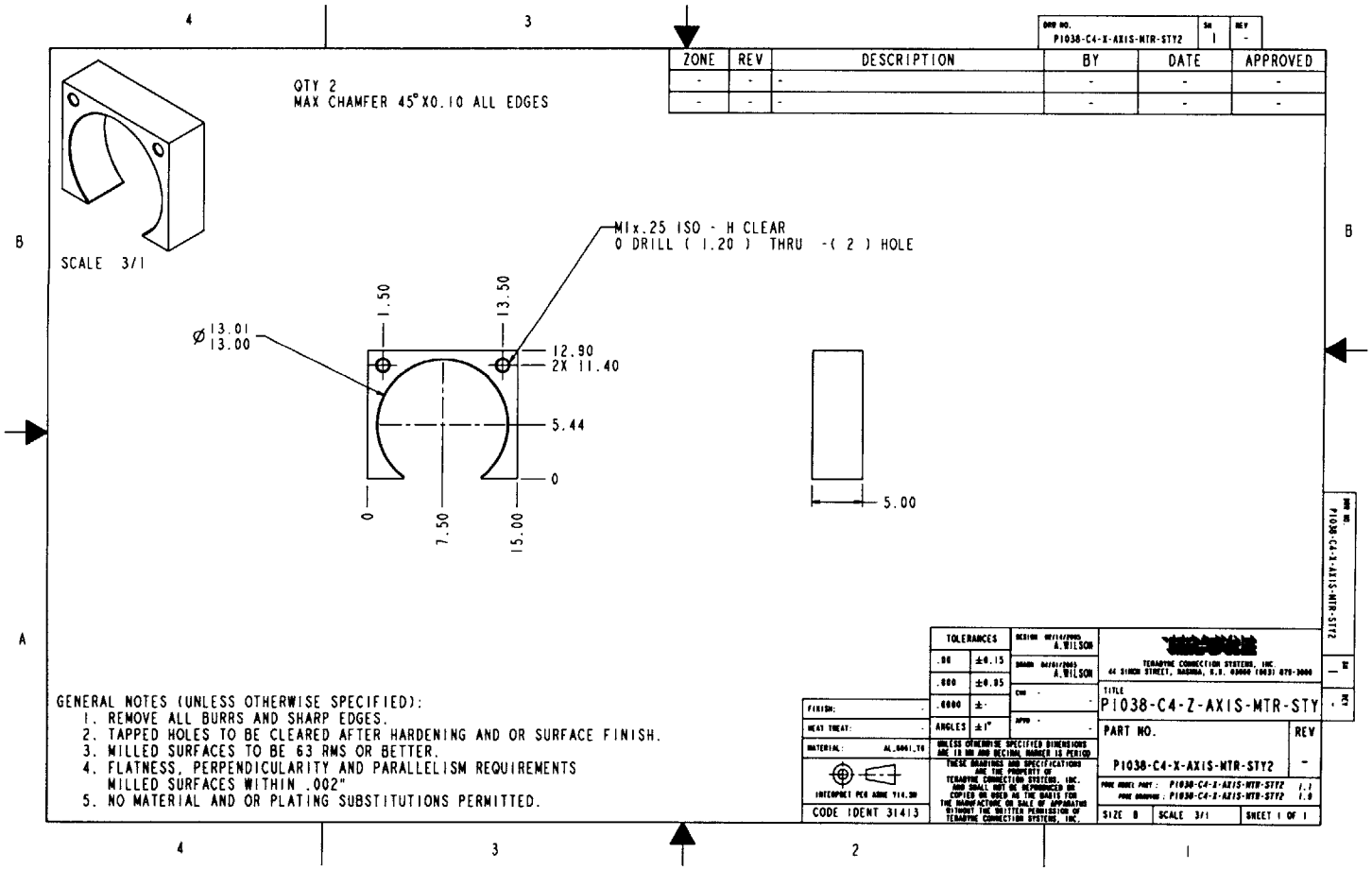
DWG NO. P1038-C4-X-AXIS-MTR-STY2
SH 1
REV -
ZONE | REV | DESCRIPTION | BY | DATE | APPROVED
QTY 2
MAX CHAMFER 45°X0.10 ALL EDGES
SCALE 3/1
M1x.25 ISO - H CLEAR
Ø DRILL (1.20) THRU -(2) HOLE
Ø13.01
13.00
1.50
13.50
12.90
2X 11.40
5.44
0
0
7.50
15.00
5.00
GENERAL NOTES (UNLESS OTHERWISE SPECIFIED):
1. REMOVE ALL BURRS AND SHARP EDGES.
2. TAPPED HOLES TO BE CLEARED AFTER HARDENING AND OR SURFACE FINISH.
3. MILLED SURFACES TO BE 63 RMS OR BETTER.
4. FLATNESS, PERPENDICULARITY AND PARALLELISM REQUIREMENTS MILLED SURFACES WITHIN .002"
5. NO MATERIAL AND OR PLATING SUBSTITUTIONS PERMITTED.
TOLERANCES
.00 ±0.15
.000 ±0.05
.0000 ±-
ANGLES ±1°
UNLESS OTHERWISE SPECIFIED DIMENSIONS ARE IN MM AND DECIMAL MARKER IS PERIOD
THESE DRAWINGS AND SPECIFICATIONS ARE THE PROPERTY OF TERADYNE CONNECTION SYSTEMS, INC. AND SHALL NOT BE REPRODUCED OR COPIED OR USED AS THE BASIS FOR THE MANUFACTURE OR SALE OF APPARATUS WITHOUT THE WRITTEN PERMISSION OF TERADYNE CONNECTION SYSTEMS, INC.
FINISH: -
HEAT TREAT: -
MATERIAL: AL_6061_T6
INTERPRET PER ASME Y14.5M
CODE IDENT 31413
DESIGN 09/14/2005 A.WILSON
DRAWN 04/01/2005 A.WILSON
CHK -
APPD -
TERADYNE CONNECTION SYSTEMS, INC
44 SIMON STREET, NASHUA, N.H. 03060 (603) 879-3000
TITLE
P1038-C4-Z-AXIS-MTR-STY
PART NO.
P1038-C4-X-AXIS-MTR-STY2
REV -
FROM ASSY PART: P1038-C4-Z-AXIS-MTR-STY2 1.1
FROM DRAWING: P1038-C4-Z-AXIS-MTR-STY2 1.0
SIZE B
SCALE 3/1
SHEET 1 OF 1
DWG NO. P1038-C4-X-AXIS-MTR-STY2
SH 1
REV -

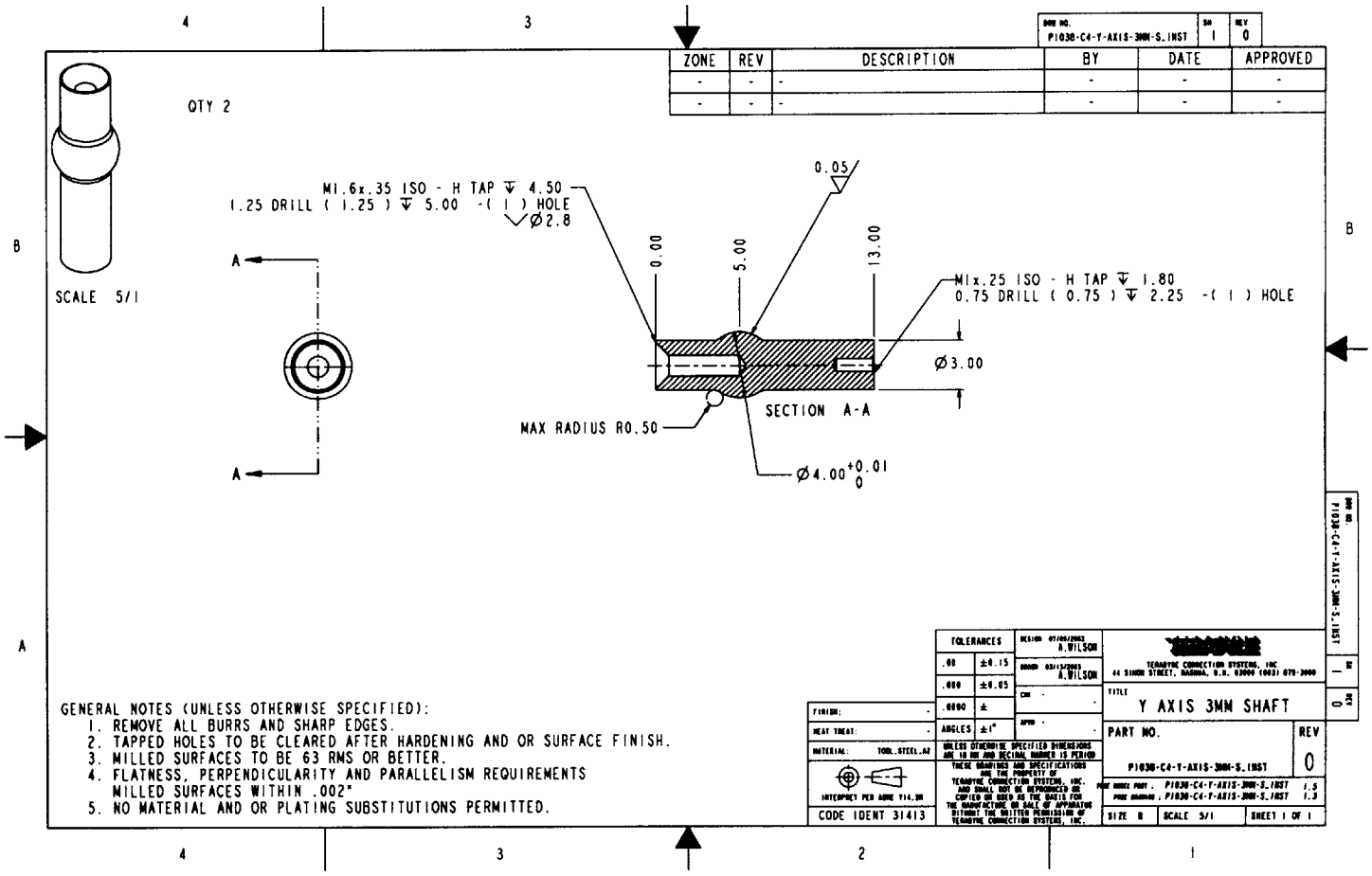
DWG NO. P1030-C4-Y-AXIS-3MM-S.INST
SH 1
REV 0
ZONE | REV | DESCRIPTION | BY | DATE | APPROVED
QTY 2
SCALE 5/1
M1.6x.35 ISO - H TAP ↧ 4.50
1.25 DRILL (1.25) ↧ 5.00 -(1) HOLE
⌵ Ø2.8
0.05
0.00
5.00
13.00
M1x.25 ISO - H TAP ↧ 1.80
0.75 DRILL (0.75) ↧ 2.25 -(1) HOLE
Ø3.00
SECTION A-A
MAX RADIUS R0.50
Ø4.00 +0.01 0
GENERAL NOTES (UNLESS OTHERWISE SPECIFIED):
1. REMOVE ALL BURRS AND SHARP EDGES.
2. TAPPED HOLES TO BE CLEARED AFTER HARDENING AND OR SURFACE FINISH.
3. MILLED SURFACES TO BE 63 RMS OR BETTER.
4. FLATNESS, PERPENDICULARITY AND PARALLELISM REQUIREMENTS MILLED SURFACES WITHIN .002"
5. NO MATERIAL AND OR PLATING SUBSTITUTIONS PERMITTED.
TOLERANCES
.00 ±0.15
.000 ±0.05
.0000 ±
ANGLES ±1°
FINISH:
HEAT TREAT:
MATERIAL: TOOL STEEL A2
INTERPRET PER ASME Y14.5M
CODE IDENT 31413
A.WILSON
A.WILSON
TERADYNE CONNECTION SYSTEMS, INC
TITLE
Y AXIS 3MM SHAFT
PART NO.
P1030-C4-Y-AXIS-3MM-S.INST
REV 0
SIZE B
SCALE 5/1
SHEET 1 OF 1

DWG NO. P1038-C4-Y-AXIS-BRNG-PRLD	SH 1	REV -

ZONE	REV	DESCRIPTION	BY	DATE	APPROVED
-	-	-	-	-	-
-	-	-	-	-	-

SCALE 4/1

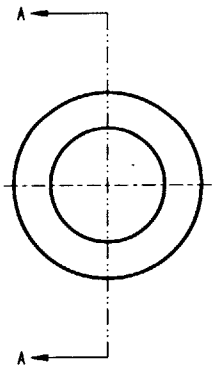

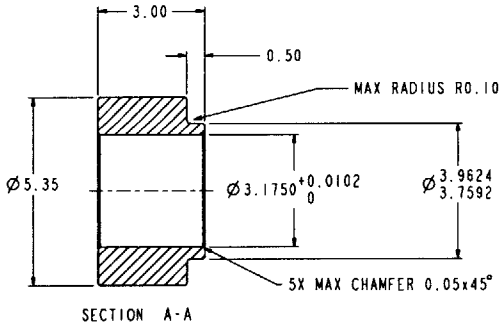

SECTION A-B

GENERAL NOTES (UNLESS OTHERWISE SPECIFIED):
1. REMOVE ALL BURRS AND SHARP EDGES.
2. TAPPED HOLES TO BE CLEARED AFTER HARDENING AND OR SURFACE FINISH.
3. MILLED SURFACES TO BE 63 RMS OR BETTER.
4. FLATNESS, PERPENDICULARITY AND PARALLELISM REQUIREMENTS MILLED SURFACES WITHIN .002"
5. NO MATERIAL AND OR PLATING SUBSTITUTIONS PERMITTED.

TOLERANCES	
.00	±0.15
.000	±0.05
.0000	±
ANGLES	±1°

DESIGN 01/06/2005 A.WILSON
DRAWN 02/23/2005 A.WILSON
CHK -
APVD -

FINISH: -
HEAT TREAT: -
MATERIAL: 66.316

INTERPRET PER ASME Y14.5M

CODE IDENT 31413

UNLESS OTHERWISE SPECIFIED DIMENSIONS ARE IN INCH AND DECIMAL MARKER IS PERIOD

THESE DRAWINGS AND SPECIFICATIONS ARE THE PROPERTY OF TERADYNE CONNECTION SYSTEMS, INC. AND SHALL NOT BE REPRODUCED OR COPIED OR USED AS THE BASIS FOR THE MANUFACTURE OR SALE OF APPARATUS WITHOUT THE WRITTEN PERMISSION OF TERADYNE CONNECTION SYSTEMS, INC.

[redacted]
TERADYNE CONNECTION SYSTEMS, INC
44 SIMON STREET, NASHUA, N.H. 03060 (603) 879-3000

TITLE
P1038-C4-Y-AXIS-BRNG-PRLD

PART NO. P1038-C4-Y-AXIS-BRNG-PRLD
REV -

SIZE B | SCALE 10/1 | SHEET 1 OF 1

P1038-C4-Y-AXIS-BRNG-PRLD | SH 1 | REV -

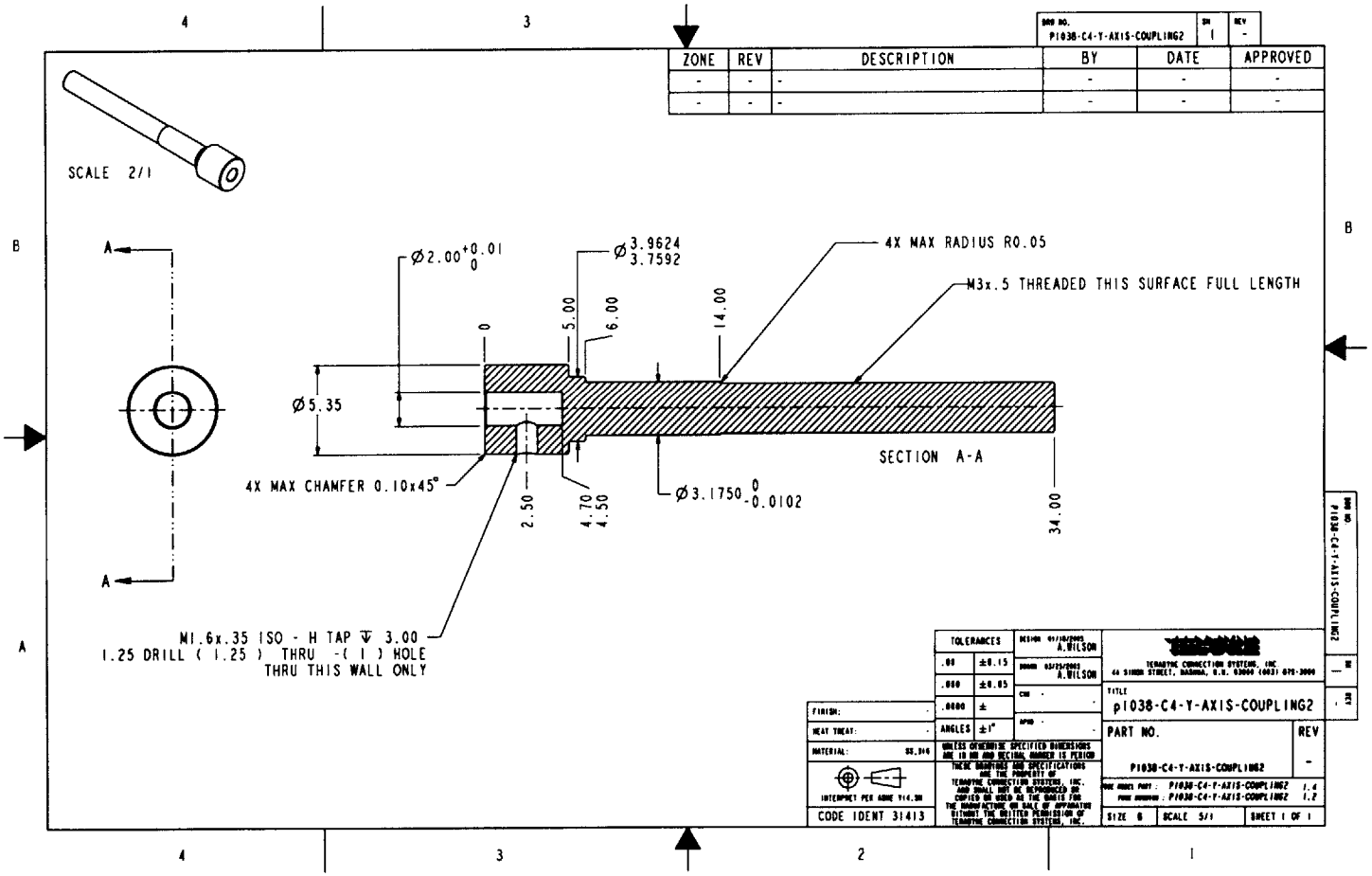
DWG NO. P1038-C4-Y-AXIS-COUPLING2
SN 1
REV -
ZONE | REV | DESCRIPTION | BY | DATE | APPROVED
SCALE 2/1
Ø2.00 +0.01 0
Ø3.9624 3.7592
4X MAX RADIUS R0.05
M3x.5 THREADED THIS SURFACE FULL LENGTH
5.00
6.00
14.00
Ø5.35
SECTION A-A
4X MAX CHAMFER 0.10x45°
2.50
4.70 4.50
Ø3.1750 0 -0.0102
34.00
M1.6x.35 ISO - H TAP ↧ 3.00
1.25 DRILL (1.25) THRU -(1) HOLE
THRU THIS WALL ONLY
TOLERANCES
.00 ±0.15
.000 ±0.05
.0000 ±
ANGLES ±1°
FINISH:
HEAT TREAT:
MATERIAL:
INTERPRET PER ASME Y14.5M
CODE IDENT 31413
UNLESS OTHERWISE SPECIFIED DIMENSIONS ARE IN INCHES DECIMAL NUMBER IS FINISH
THESE DRAWINGS AND SPECIFICATIONS ARE THE PROPERTY OF TERADYNE CONNECTION SYSTEMS, INC. AND SHALL NOT BE REPRODUCED OR COPIED OR USED AS THE BASIS FOR THE MANUFACTURE OR SALE OF APPARATUS WITHOUT THE WRITTEN PERMISSION OF TERADYNE CONNECTION SYSTEMS, INC.
DESIGN 01/15/2003 A.WILSON
DRAWN 02/25/2003 A.WILSON
CHK
APVD
TERADYNE CONNECTION SYSTEMS, INC. 44 SIMON STREET, NASHUA, N.H. 03060 (603) 879-3000
TITLE p1038-C4-Y-AXIS-COUPLING2
PART NO. P1038-C4-Y-AXIS-COUPLING2
REV -
NEXT ASSY P1038-C4-Y-AXIS-COUPLING2 1.4
USED ON P1038-C4-Y-AXIS-COUPLING2 1.2
SIZE B
SCALE 5/1
SHEET 1 OF 1
P1038-C4-Y-AXIS-COUPLING2

DWG NO.	SH	REV
P1038-C4-Y-AXIS-CPLNG	1	-

ZONE	REV	DESCRIPTION	BY	DATE	APPROVED
-	-	-	-	-	-
-	-	-	-	-	-

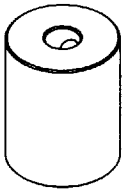

QTY 2

SCALE 5/1

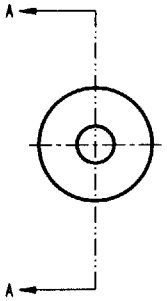

SECTION A-A

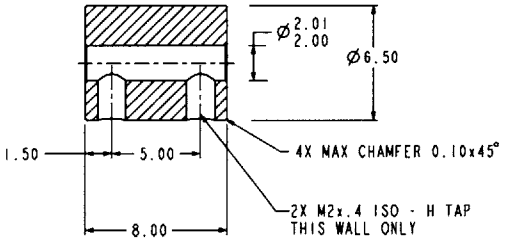

GENERAL NOTES (UNLESS OTHERWISE SPECIFIED):
1. REMOVE ALL BURRS AND SHARP EDGES.
2. TAPPED HOLES TO BE CLEARED AFTER HARDENING AND OR SURFACE FINISH.
3. MILLED SURFACES TO BE 63 RMS OR BETTER.
4. FLATNESS, PERPENDICULARITY AND PARALLELISM REQUIREMENTS MILLED SURFACES WITHIN .002"
5. NO MATERIAL AND OR PLATING SUBSTITUTIONS PERMITTED.

TOLERANCES	
.00	±0.15
.000	±0.05
.0000	±
ANGLES	±1°

FINISH: -
HEAT TREAT: -
MATERIAL: 6061-T6

INTERPRET PER ASME Y14.5M

CODE IDENT 31413

DESIGN 03/10/2005 A.WILSON
DRAWN 03/10/2005 A.WILSON
CHK -
APPD -

UNLESS OTHERWISE SPECIFIED DIMENSIONS ARE IN INCHES AND DECIMAL MARKER IS PERIOD

TERADYNE CONNECTION SYSTEMS, INC.
44 SIMON STREET, NASHUA, N.H. 03060 (603) 879-3000

TITLE
P1038-C4-Y-AXIS-CPLNG

PART NO.
P1038-C4-Y-AXIS-CPLNG

REV -

PROE MODEL PART : P1038-C4-Y-AXIS-CPLNG 1.4
PROE DRAWING : P1038-C4-Y-AXIS-CPLNG 1.3

SIZE B | SCALE 5/1 | SHEET 1 OF 1

P1038-C4-Y-AXIS-CPLNG | SH 1 | REV -

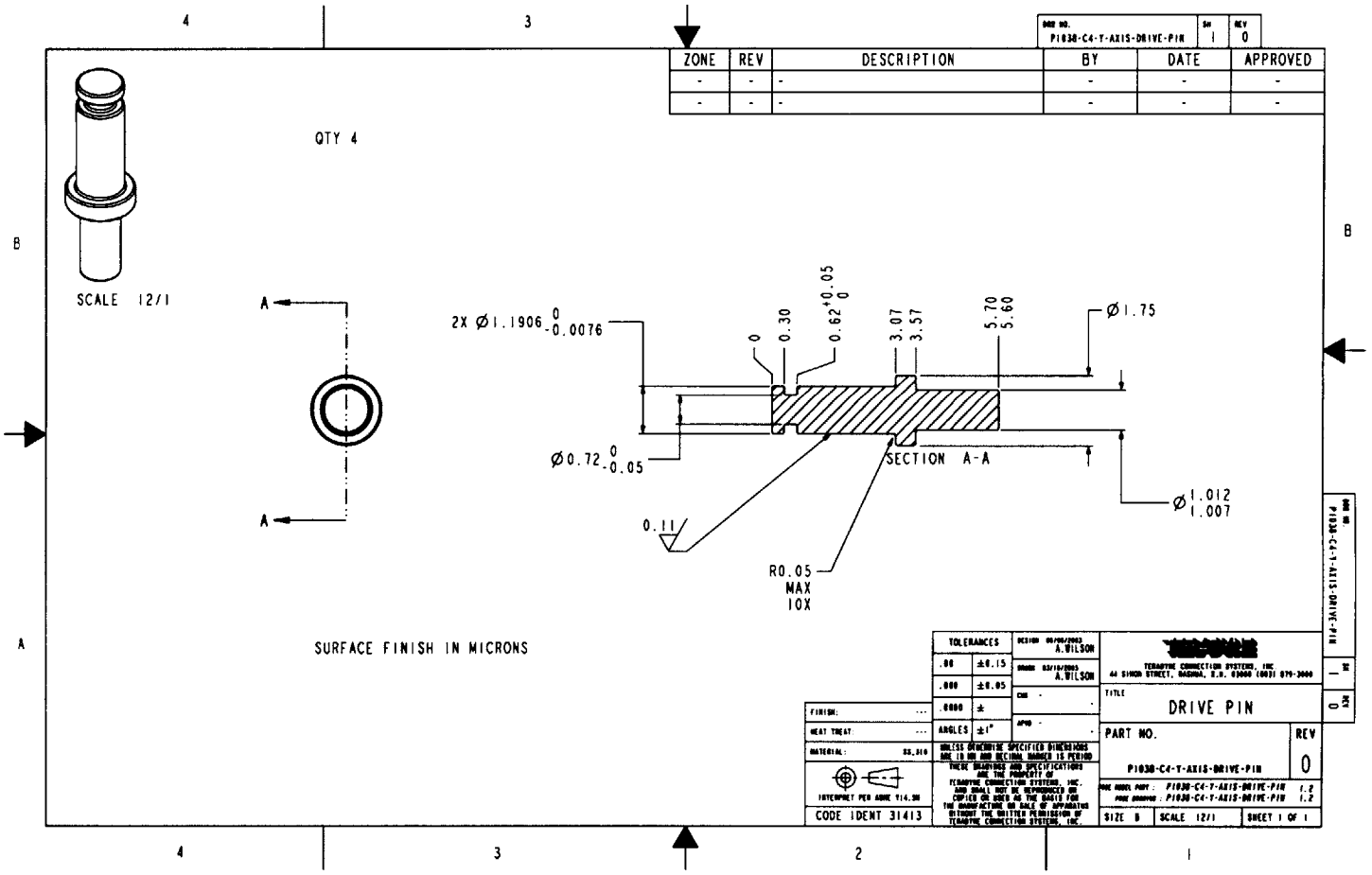
P1030-C4-Y-AXIS-DRIVE-PIN
SH 1
REV 0
ZONE REV DESCRIPTION BY DATE APPROVED
QTY 4
SCALE 12/1
2X Ø1.1906 0 -0.0076
0
0.30
0.62 +0.05 0
3.07
3.57
5.70
5.60
Ø1.75
Ø0.72 0 -0.05
SECTION A-A
Ø1.012 1.007
0.11
R0.05 MAX 10X
SURFACE FINISH IN MICRONS
TOLERANCES
.00 ±0.15
.000 ±0.05
.0000 ±
ANGLES ±1°
FINISH: ---
HEAT TREAT: ---
MATERIAL: SS,316
INTERPRET PER ASME Y14.5M
CODE IDENT 31413
DESIGN 09/06/2003 A.WILSON
DRAWN 03/10/2004 A.WILSON
CHK -
APVD -
UNLESS OTHERWISE SPECIFIED DIMENSIONS ARE IN INCH AND DECIMAL MARKER IS PERIOD
THESE DRAWINGS AND SPECIFICATIONS ARE THE PROPERTY OF TERADYNE CONNECTION SYSTEMS, INC. AND SHALL NOT BE REPRODUCED OR COPIED OR USED AS THE BASIS FOR THE MANUFACTURE OR SALE OF APPARATUS WITHOUT THE WRITTEN PERMISSION OF TERADYNE CONNECTION SYSTEMS, INC.
[redacted]
TERADYNE CONNECTION SYSTEMS, INC
44 SIMON STREET, NASHUA, N.H. 03060 (603) 879-3000
TITLE
DRIVE PIN
PART NO.
REV 0
P1030-C4-Y-AXIS-DRIVE-PIN
SIZE B SCALE 12/1 SHEET 1 OF 1

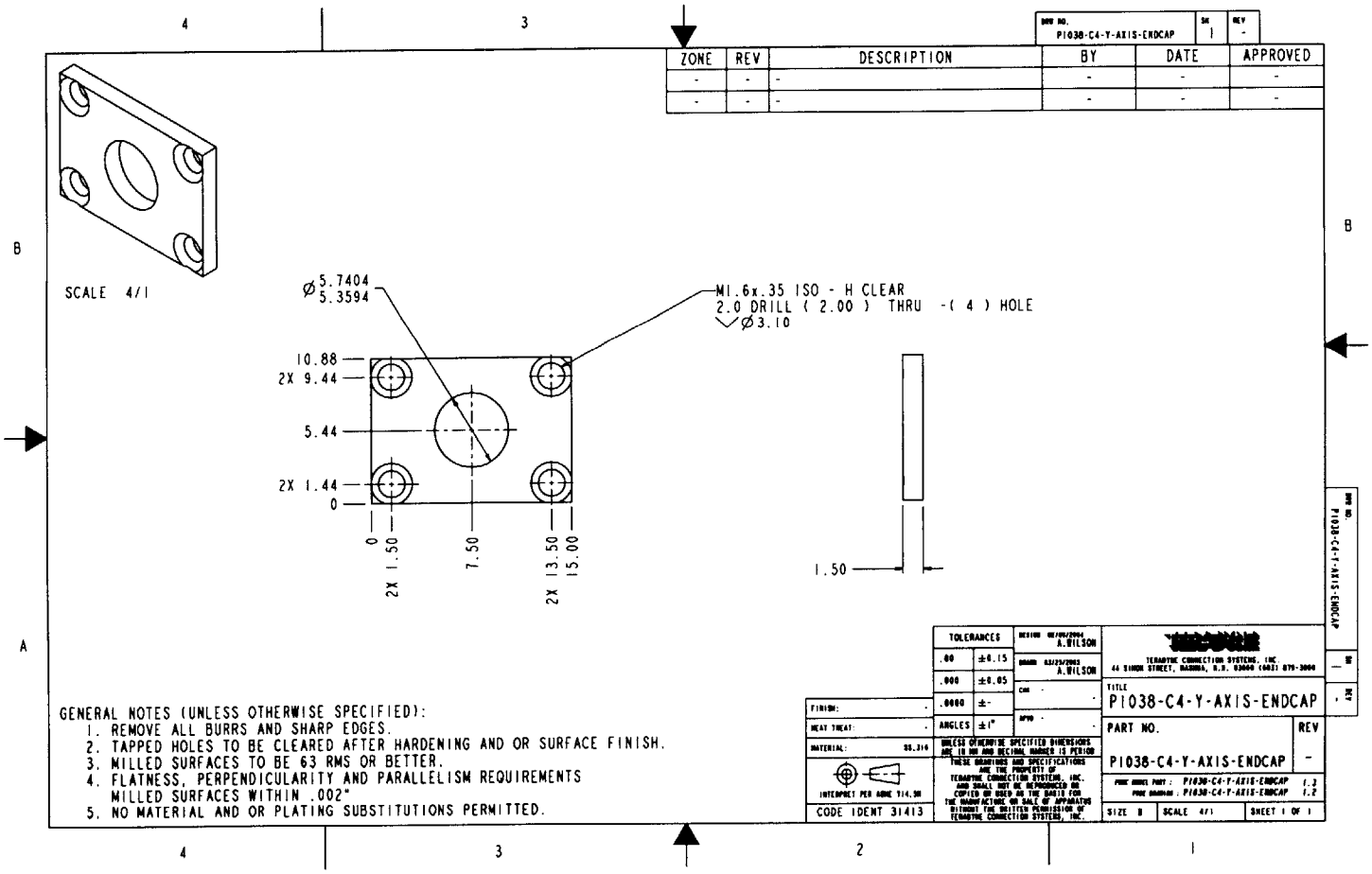
DWG NO. P1038-C4-Y-AXIS-ENDCAP
SH 1
REV -
ZONE | REV | DESCRIPTION | BY | DATE | APPROVED
SCALE 4/1
Ø5.7404
5.3594
M1.6x.35 ISO - H CLEAR
2.0 DRILL (2.00) THRU -(4) HOLE
Ø3.10
10.88
2X 9.44
5.44
2X 1.44
0
0
2X 1.50
7.50
2X 13.50
15.00
1.50
GENERAL NOTES (UNLESS OTHERWISE SPECIFIED):
1. REMOVE ALL BURRS AND SHARP EDGES.
2. TAPPED HOLES TO BE CLEARED AFTER HARDENING AND OR SURFACE FINISH.
3. MILLED SURFACES TO BE 63 RMS OR BETTER.
4. FLATNESS, PERPENDICULARITY AND PARALLELISM REQUIREMENTS MILLED SURFACES WITHIN .002"
5. NO MATERIAL AND OR PLATING SUBSTITUTIONS PERMITTED.
TOLERANCES
.00 ±0.15
.000 ±0.05
.0000 ±-
ANGLES ±1°
FINISH:
HEAT TREAT:
MATERIAL:
INTERPRET PER ASME Y14.5M
CODE IDENT 31413
A.WILSON
A.WILSON
TERADYNE CONNECTION SYSTEMS, INC
TITLE
P1038-C4-Y-AXIS-ENDCAP
PART NO.
P1038-C4-Y-AXIS-ENDCAP
REV -
SIZE B
SCALE 4/1
SHEET 1 OF 1

ZONE	REV	DESCRIPTION	BY	DATE	APPROVED
-	-	-	-	-	-
-	-	-	-	-	-

QTY 2

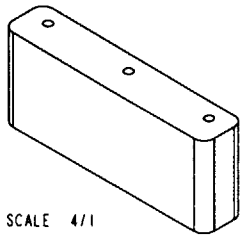

SCALE 4/1

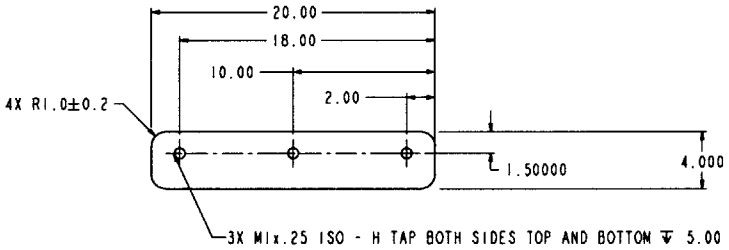

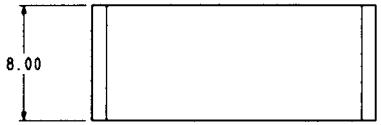

GENERAL NOTES (UNLESS OTHERWISE SPECIFIED):
1. REMOVE ALL BURRS AND SHARP EDGES.
2. TAPPED HOLES TO BE CLEARED AFTER HARDENING AND OR SURFACE FINISH.
3. MILLED SURFACES TO BE 63 RMS OR BETTER.
4. FLATNESS, PERPENDICULARITY AND PARALLELISM REQUIREMENTS MILLED SURFACES WITHIN .002"
5. NO MATERIAL AND OR PLATING SUBSTITUTIONS PERMITTED.

TOLERANCES	
.XX	±0.15
.XXX	±0.05
.XXXX	±
ANGLES	±1°

FINISH: -
HEAT TREAT: -
MATERIAL: BRONZE

INTERPRET PER ASME Y14.5M

CODE IDENT 31413

DESIGN 09/29/2004 A.WILSON
DRAWN 09/29/2004 A.WILSON
CHK -
APPD -

UNLESS OTHERWISE SPECIFIED DIMENSIONS ARE IN INCHES AND DECIMAL NUMBER IS PERIOD

THESE DRAWINGS AND SPECIFICATIONS ARE THE PROPERTY OF TERADYNE CONNECTION SYSTEMS, INC. AND SHALL NOT BE REPRODUCED OR COPIED OR USED AS THE BASIS FOR THE MANUFACTURE OR SALE OF APPARATUS WITHOUT THE WRITTEN PERMISSION OF TERADYNE CONNECTION SYSTEMS, INC.

[redacted]
TERADYNE CONNECTION SYSTEMS, INC.
44 SIMON STREET, NASHUA, N.H. 03060 (603) 879-3000

TITLE
LINEAR BEARING FOR Y-AXIS RAMP

PART NO.
P1038-C4-Y-AXIS-L-BRNG

REV
-

YOUR MODEL PART : P1038-C4-Y-AXIS-L-BRNG 1.12
YOUR DRAWING : P1038-C4-Y-AXIS-L-BRNG 1.1

SIZE B | SCALE 4/1 | SHEET 1 OF 1

DWG NO. P1038-C4-Y-AXIS-L-BRNG | SH 1 | REV -

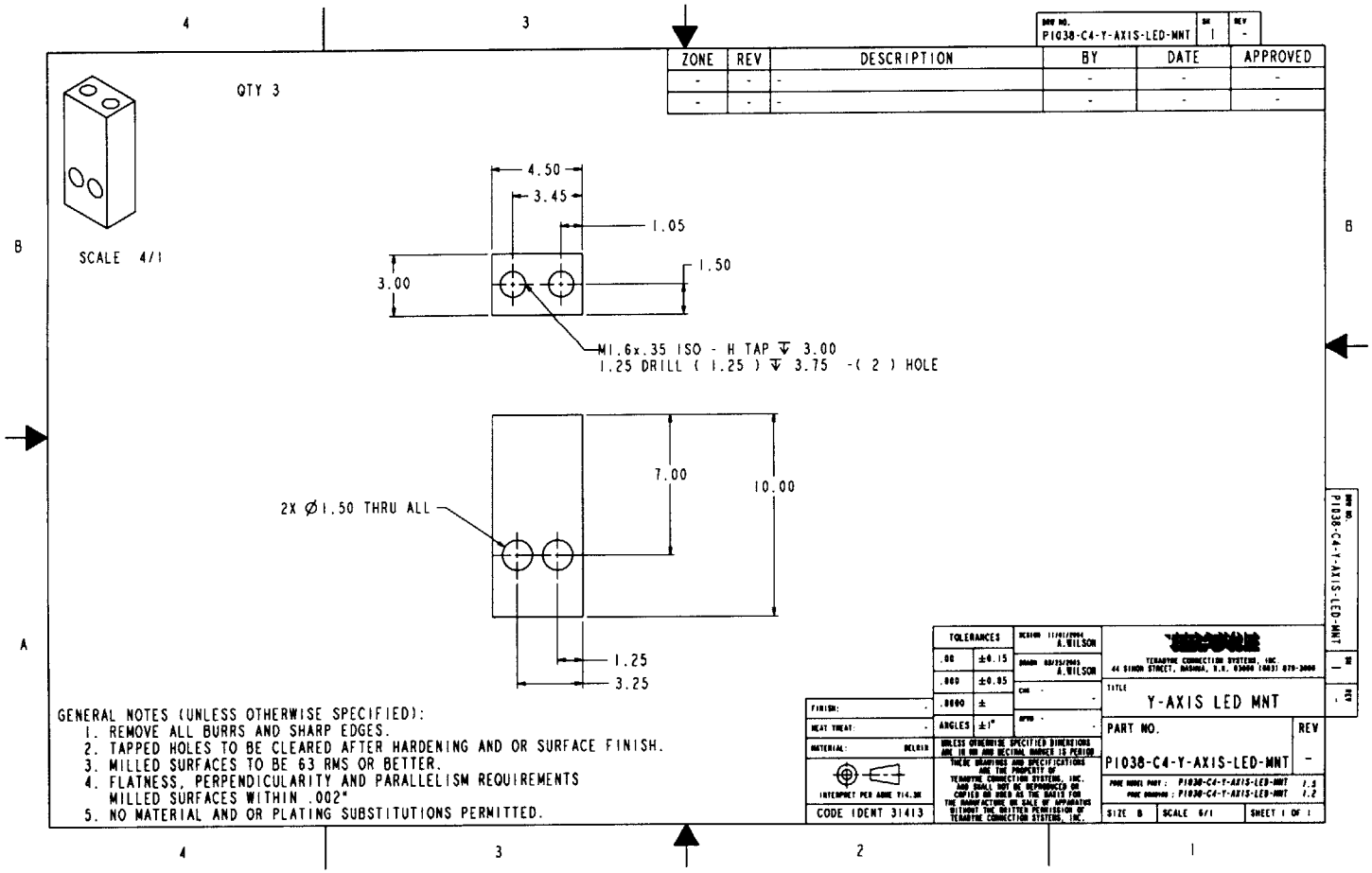
QTY 3
SCALE 4/1
4.50
3.45
1.05
1.50
3.00
M1.6x.35 ISO - H TAP ↧ 3.00
1.25 DRILL (1.25) ↧ 3.75 -(2) HOLE
2X Ø1.50 THRU ALL
7.00
10.00
1.25
3.25
GENERAL NOTES (UNLESS OTHERWISE SPECIFIED):
1. REMOVE ALL BURRS AND SHARP EDGES.
2. TAPPED HOLES TO BE CLEARED AFTER HARDENING AND OR SURFACE FINISH.
3. MILLED SURFACES TO BE 63 RMS OR BETTER.
4. FLATNESS, PERPENDICULARITY AND PARALLELISM REQUIREMENTS MILLED SURFACES WITHIN .002"
5. NO MATERIAL AND OR PLATING SUBSTITUTIONS PERMITTED.
ZONE | REV | DESCRIPTION | BY | DATE | APPROVED
DWG NO. P1038-C4-Y-AXIS-LED-MNT
TOLERANCES
.00 ±0.15
.000 ±0.05
.0000 ±
ANGLES ±1°
FINISH:
HEAT TREAT:
MATERIAL: DELRIN
INTERPRET PER ASME Y14.5M
CODE IDENT 31413
TERADYNE CONNECTION SYSTEMS, INC
TITLE Y-AXIS LED MNT
PART NO. P1038-C4-Y-AXIS-LED-MNT
REV -
SIZE B
SCALE 6/1
SHEET 1 OF 1

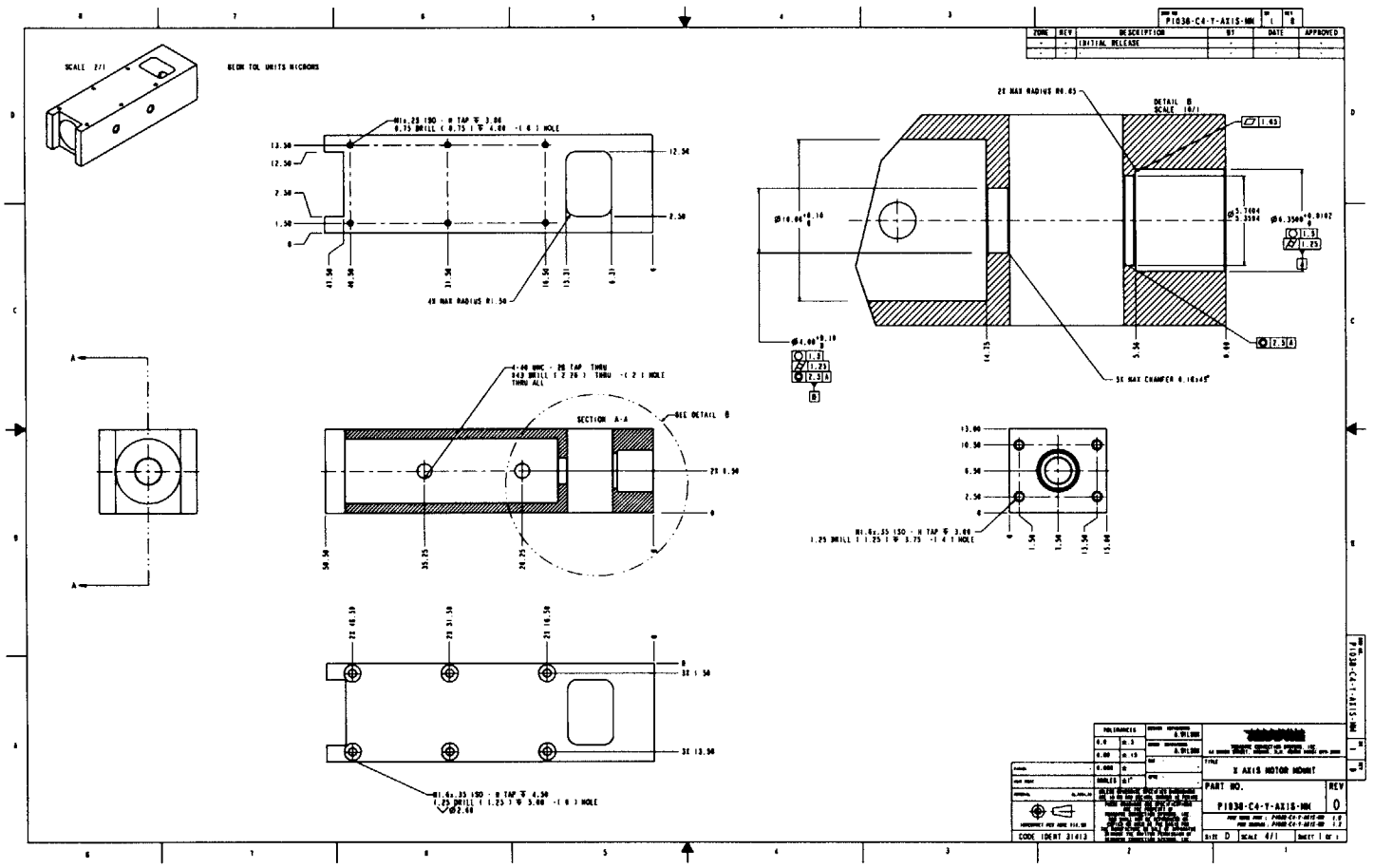
P1038-C4-Y-AXIS-MM
DESCRIPTION
INITIAL RELEASE
SCALE 2/1
DETAIL B
SCALE 10/1
SECTION A-A
SEE DETAIL B
X AXIS MOTOR MOUNT
PART NO.
P1038-C4-Y-AXIS-MM
REV
0
SIZE D
SCALE 4/1

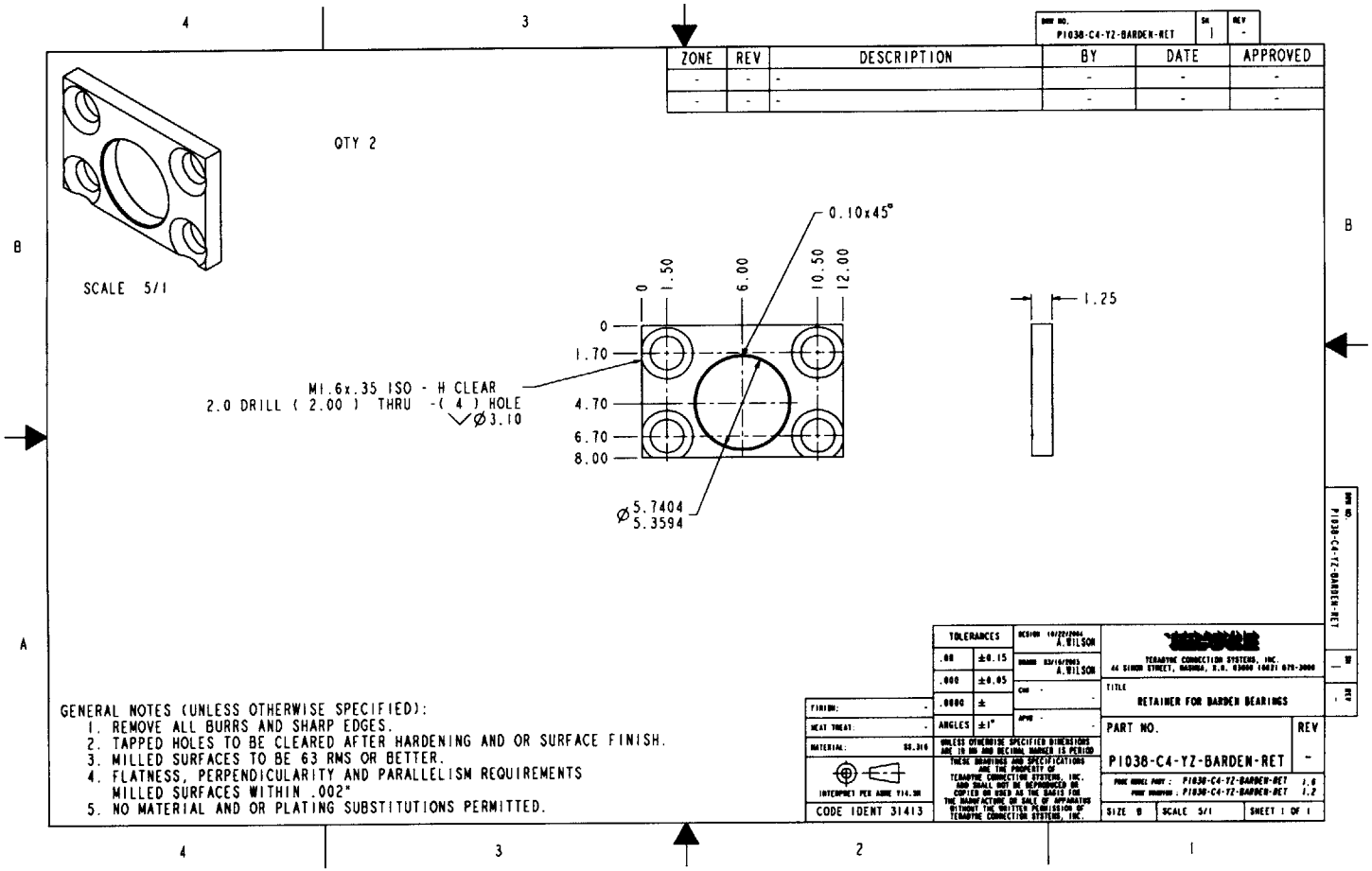
DWG NO. P1038-C4-YZ-BARDEN-RET
SH 1
REV -
ZONE | REV | DESCRIPTION | BY | DATE | APPROVED
QTY 2
SCALE 5/1
0.10x45°
0
1.50
6.00
10.50
12.00
0
1.70
4.70
6.70
8.00
M1.6x.35 ISO - H CLEAR
2.0 DRILL (2.00) THRU -(4) HOLE
Ø3.10
Ø5.7404
5.3594
1.25
GENERAL NOTES (UNLESS OTHERWISE SPECIFIED):
1. REMOVE ALL BURRS AND SHARP EDGES.
2. TAPPED HOLES TO BE CLEARED AFTER HARDENING AND OR SURFACE FINISH.
3. MILLED SURFACES TO BE 63 RMS OR BETTER.
4. FLATNESS, PERPENDICULARITY AND PARALLELISM REQUIREMENTS MILLED SURFACES WITHIN .002"
5. NO MATERIAL AND OR PLATING SUBSTITUTIONS PERMITTED.
TOLERANCES
.00 ±0.15
.000 ±0.05
.0000 ±
ANGLES ±1°
UNLESS OTHERWISE SPECIFIED DIMENSIONS ARE IN MM AND DECIMAL MARKER IS PERIOD
FINISH: -
HEAT TREAT: -
MATERIAL: SS 316
INTERPRET PER ASME Y14.5M
CODE IDENT 31413
DESIGN 10/22/2004 A.WILSON
DRAWN 03/16/2005 A.WILSON
CHK -
APVD -
THESE DRAWINGS AND SPECIFICATIONS ARE THE PROPERTY OF TERADYNE CONNECTION SYSTEMS, INC. AND SHALL NOT BE REPRODUCED OR COPIED OR USED AS THE BASIS FOR THE MANUFACTURE OR SALE OF APPARATUS WITHOUT THE WRITTEN PERMISSION OF TERADYNE CONNECTION SYSTEMS, INC.
TERADYNE CONNECTION SYSTEMS, INC.
44 SIMON STREET, NASHUA, N.H. 03060 (603) 879-3000
TITLE
RETAINER FOR BARDEN BEARINGS
PART NO.
REV
P1038-C4-YZ-BARDEN-RET
-
PROE MODEL NAME : P1038-C4-YZ-BARDEN-RET 1.0
PROE DRAWING : P1038-C4-YZ-BARDEN-RET 1.2
SIZE B
SCALE 5/1
SHEET 1 OF 1
DWG NO. P1038-C4-YZ-BARDEN-RET
REV -

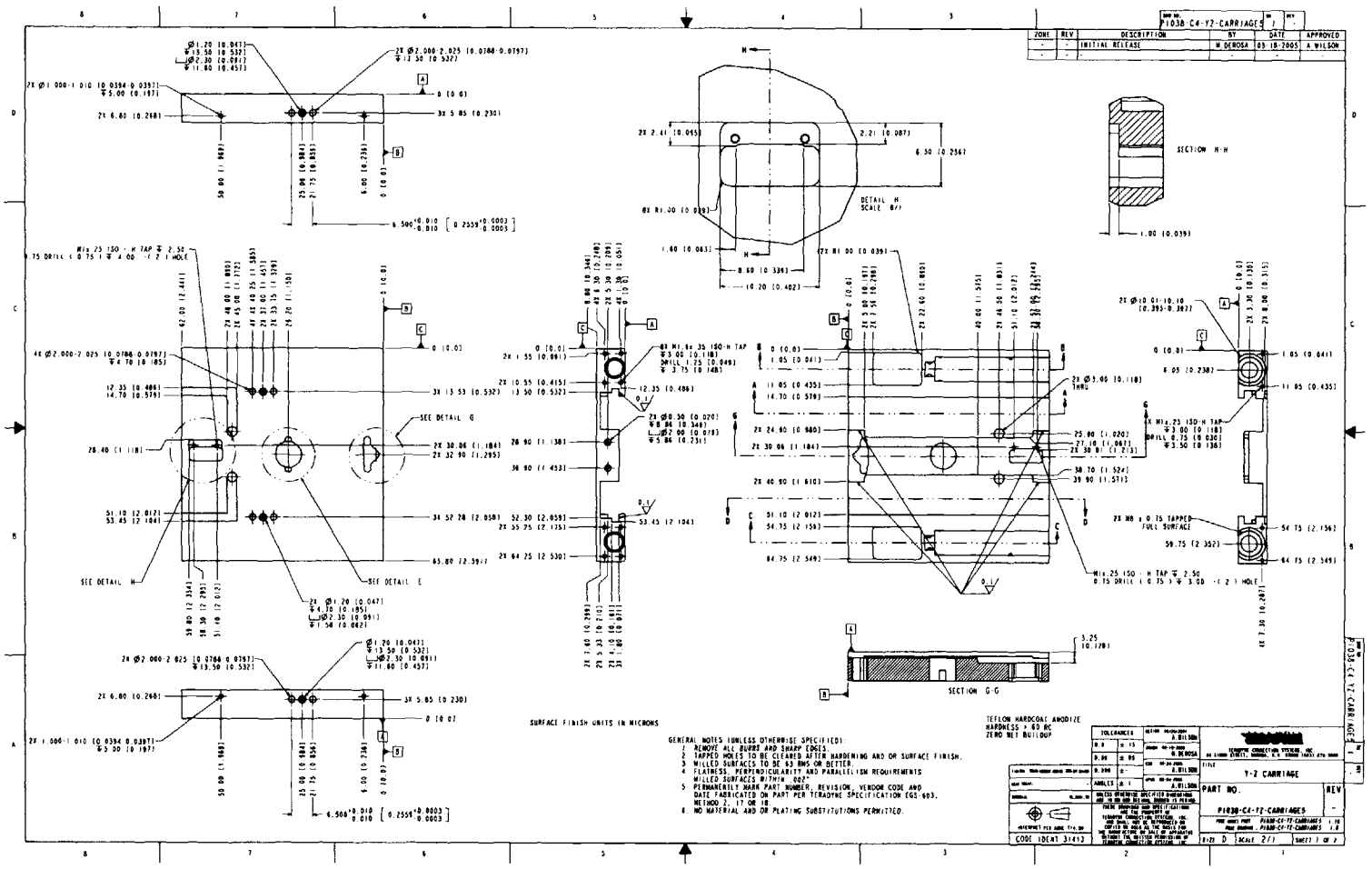
P1038-C4-Y2-CARRIAGE
ZONE | REV | DESCRIPTION | BY | DATE | APPROVED
INITIAL RELEASE | M.DEROSA | 05-18-2005 | A.WILSON
DETAIL H
SCALE 8/1
SECTION H-H
SECTION G-G
SURFACE FINISH UNITS IN MICRONS
TEFLON HARDCOAT ANODIZE
HARDNESS > 60 RC
ZERO NET BUILDUP
GENERAL NOTES (UNLESS OTHERWISE SPECIFIED):
1. REMOVE ALL BURR AND SHARP EDGES.
2. TAPPED HOLES TO BE CLEARED AFTER HARDENING AND OR SURFACE FINISH.
3. MILLED SURFACES TO BE 63 RMS OR BETTER.
4. FLATNESS, PERPENDICULARITY AND PARALLELISM REQUIREMENTS
MILLED SURFACES WITHIN .002"
5. PERMANENTLY MARK PART NUMBER, REVISION, VENDOR CODE AND
DATE FABRICATED ON PART PER TERADYNE SPECIFICATION EGS 603,
METHOD 2, 17 OR 18.
6. NO MATERIAL AND OR PLATING SUBSTITUTIONS PERMITTED.
TOLERANCES
CODE IDENT 31413
TITLE
Y-2 CARRIAGE
PART NO.
P1038-C4-Y2-CARRIAGES
REV
SIZE D
SCALE 2/1

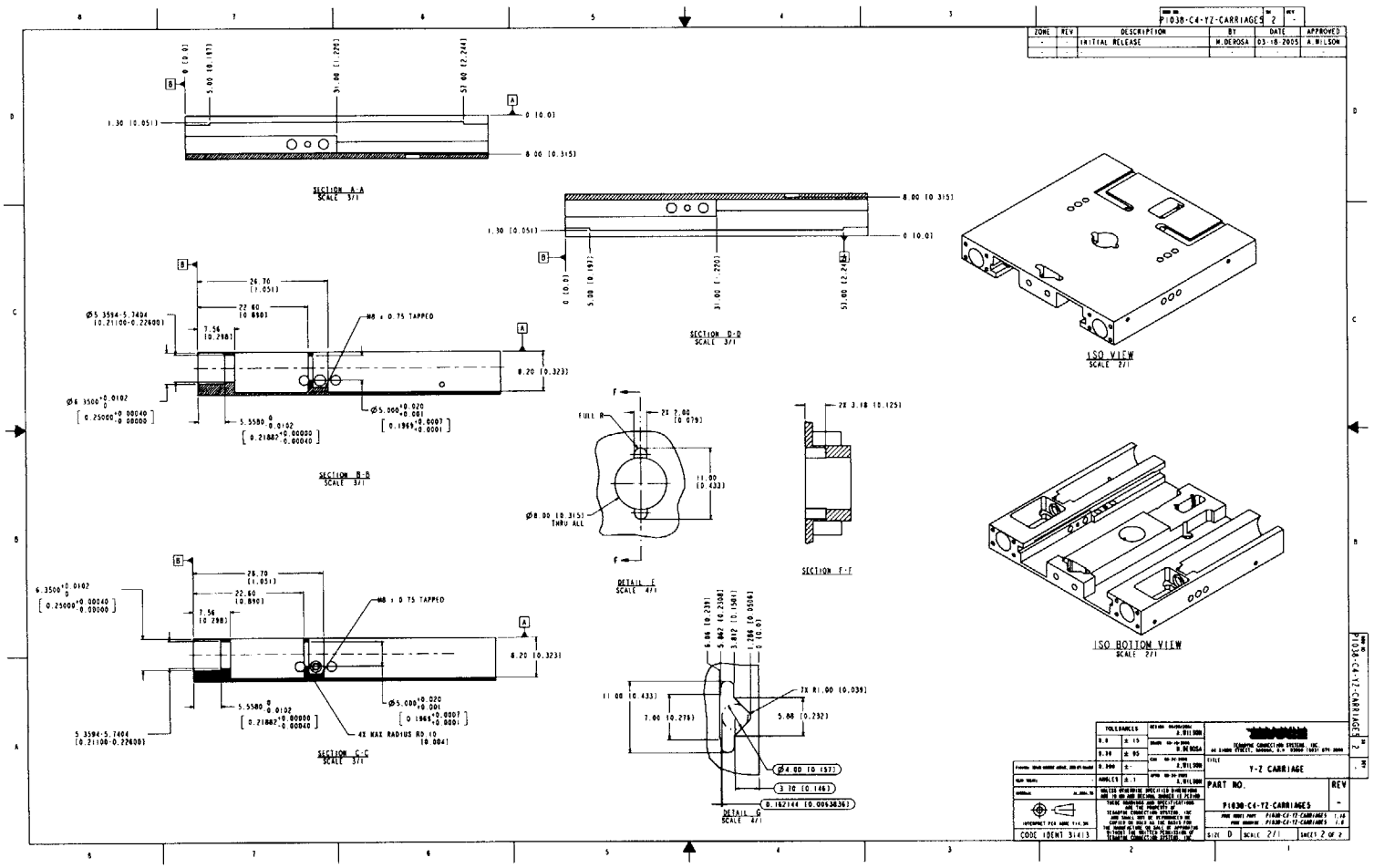
P1030-C4-YZ-CARRIAGES 2
ZONE | REV | DESCRIPTION | BY | DATE | APPROVED
- | - | INITIAL RELEASE | M.DEPOSA | 03.18.2005 | A.WILSON
SECTION A-A
SCALE 3/1
SECTION D-D
SCALE 3/1
ISO VIEW
SCALE 2/1
SECTION B-B
SCALE 3/1
DETAIL C
SCALE 4/1
SECTION F-F
ISO BOTTOM VIEW
SCALE 2/1
SECTION C-C
SCALE 3/1
DETAIL D
SCALE 4/1
TOLERANCES
Y-Z CARRIAGE
PART NO.
P1030-C4-YZ-CARRIAGES
REV
CODE IDENT 31413
SIZE D
SCALE 2/1
SHEET 2 OF 2
P1030-C4-YZ-CARRIAGES 2

DWG NO. P1038-C4-YZ-PRELOAD-PIN	SH 1	REV -

ZONE	REV	DESCRIPTION	BY	DATE	APPROVED
-	-	-	-	-	-
-	-	-	-	-	-

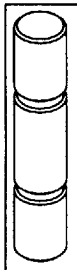

QTY 2

SCALE 8/1

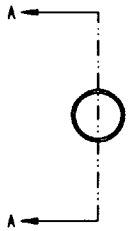

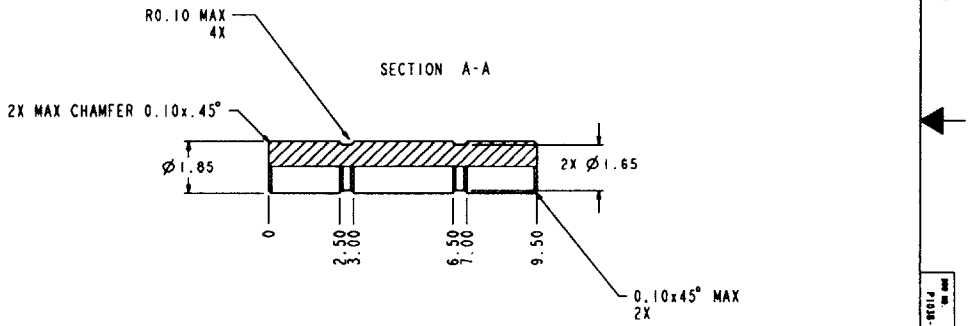

GENERAL NOTES (UNLESS OTHERWISE SPECIFIED):
1. REMOVE ALL BURRS AND SHARP EDGES.
2. TAPPED HOLES TO BE CLEARED AFTER HARDENING AND OR SURFACE FINISH.
3. MILLED SURFACES TO BE 63 RMS OR BETTER.
4. FLATNESS, PERPENDICULARITY AND PARALLELISM REQUIREMENTS MILLED SURFACES WITHIN .002"
5. NO MATERIAL AND OR PLATING SUBSTITUTIONS PERMITTED.

TOLERANCES	
.00	±0.15
.000	±0.05
.0000	±
ANGLES	±1°

UNLESS OTHERWISE SPECIFIED DIMENSIONS ARE IN MM AND DECIMAL MARKED IS PERIOD

THESE DRAWINGS AND SPECIFICATIONS ARE THE PROPERTY OF TERADYNE CONNECTION SYSTEMS, INC. AND SHALL NOT BE REPRODUCED OR COPIED OR USED AS THE BASIS FOR THE MANUFACTURE OR SALE OF APPARATUS WITHOUT THE WRITTEN PERMISSION OF TERADYNE CONNECTION SYSTEMS, INC.

FINISH: -
HEAT TREAT: -
MATERIAL: SS,316

INTERPRET PER ASME Y14.5M

CODE IDENT 31413

DESIGN 10/20/2004 A.WILSON
DRAWN 03/10/2005 A.WILSON
CHK -
APVD -

TERADYNE CONNECTION SYSTEMS, INC.
44 SIMON STREET, NASHUA, N.H. 03060 (603) 879-3000

TITLE
P1038-C4-YZ-PRELOAD-PIN

PART NO.
P1038-C4-YZ-PRELOAD-PIN

REV
-

PROE MODEL PART : P1038-C4-YZ-PRELOAD-PIN 1.5
PROE DRAWING : P1038-C4-YZ-PRELOAD-PIN 1.2

SIZE B | SCALE 8/1 | SHEET 1 OF 1

P1038-C4-YZ-PRELOAD-PIN

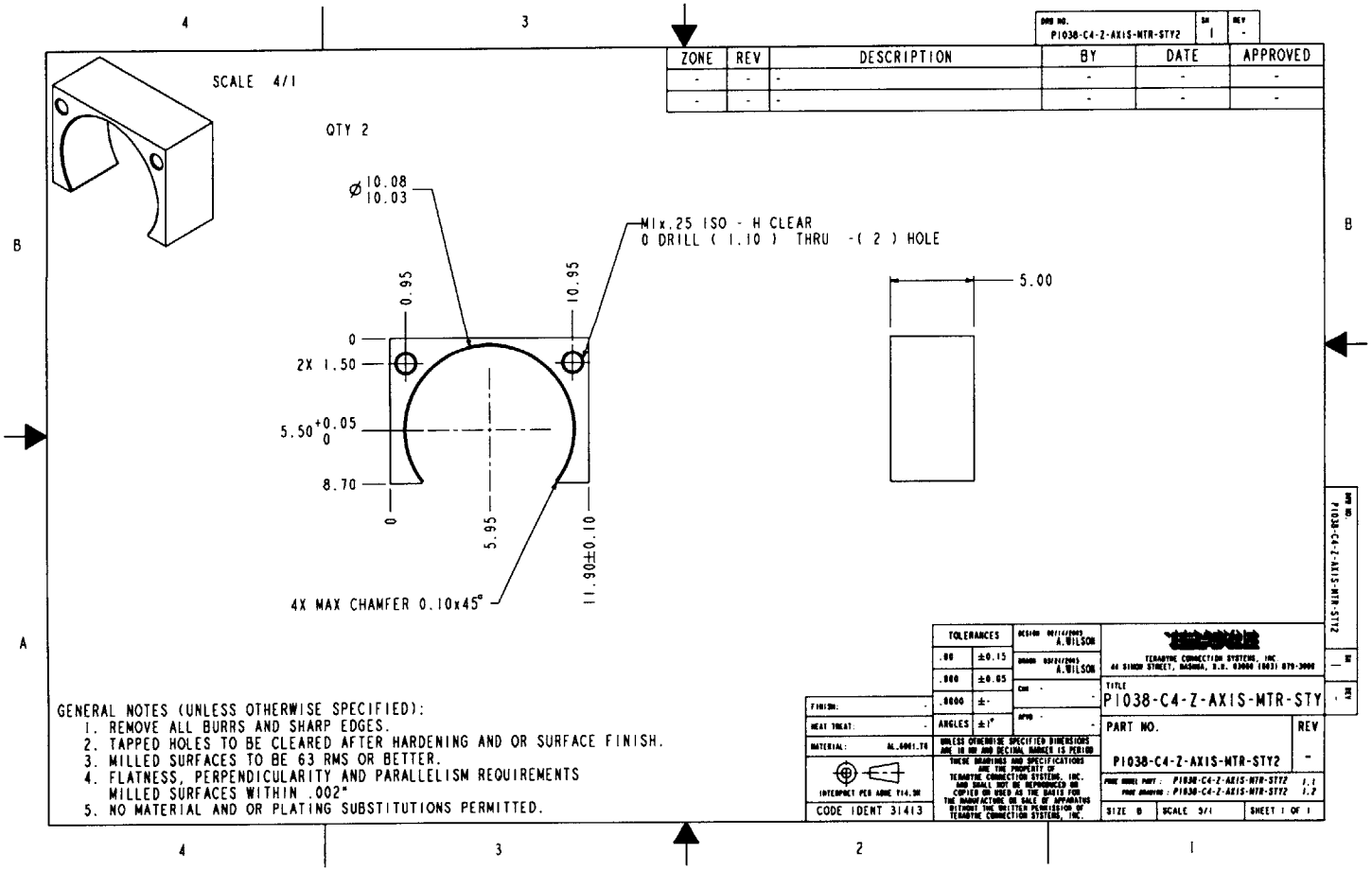

ZONE	REV	DESCRIPTION	BY	DATE	APPROVED
-	-	-	-	-	-
-	-	-	-	-	-

DRG NO. P1038-C4-Z-AXIS-MTR-STY2 | SH 1 | REV -

GENERAL NOTES (UNLESS OTHERWISE SPECIFIED):
1. REMOVE ALL BURRS AND SHARP EDGES.
2. TAPPED HOLES TO BE CLEARED AFTER HARDENING AND OR SURFACE FINISH.
3. MILLED SURFACES TO BE 63 RMS OR BETTER.
4. FLATNESS, PERPENDICULARITY AND PARALLELISM REQUIREMENTS MILLED SURFACES WITHIN .002"
5. NO MATERIAL AND OR PLATING SUBSTITUTIONS PERMITTED.

TOLERANCES	
.00	±0.15
.000	±0.05
.0000	± -
ANGLES	±1°

UNLESS OTHERWISE SPECIFIED DIMENSIONS ARE IN MM AND DECIMAL MARKER IS PERIOD

FINISH: -
HEAT TREAT: -
MATERIAL: AL.6061-T6

INTERPRET PER ASME Y14.5M

CODE IDENT 31413

DESIGN 09/14/2005 A.WILSON
DRAWN 09/21/2005 A.WILSON
CHK -
APVD -

TERADYNE CONNECTION SYSTEMS, INC
44 SIMON STREET, NASHUA, N.H. 03060 (603) 879-3000

TITLE
P1038-C4-Z-AXIS-MTR-STY

PART NO.	REV
P1038-C4-Z-AXIS-MTR-STY2	-

PRIME MODEL PART : P1038-C4-Z-AXIS-MTR-STY2 1:1
PRIME DRAWING : P1038-C4-Z-AXIS-MTR-STY2 1:2

SIZE B | SCALE 5/1 | SHEET 1 OF 1

DRG NO. P1038-C4-Z-AXIS-MTR-STY2 | SH — | REV -

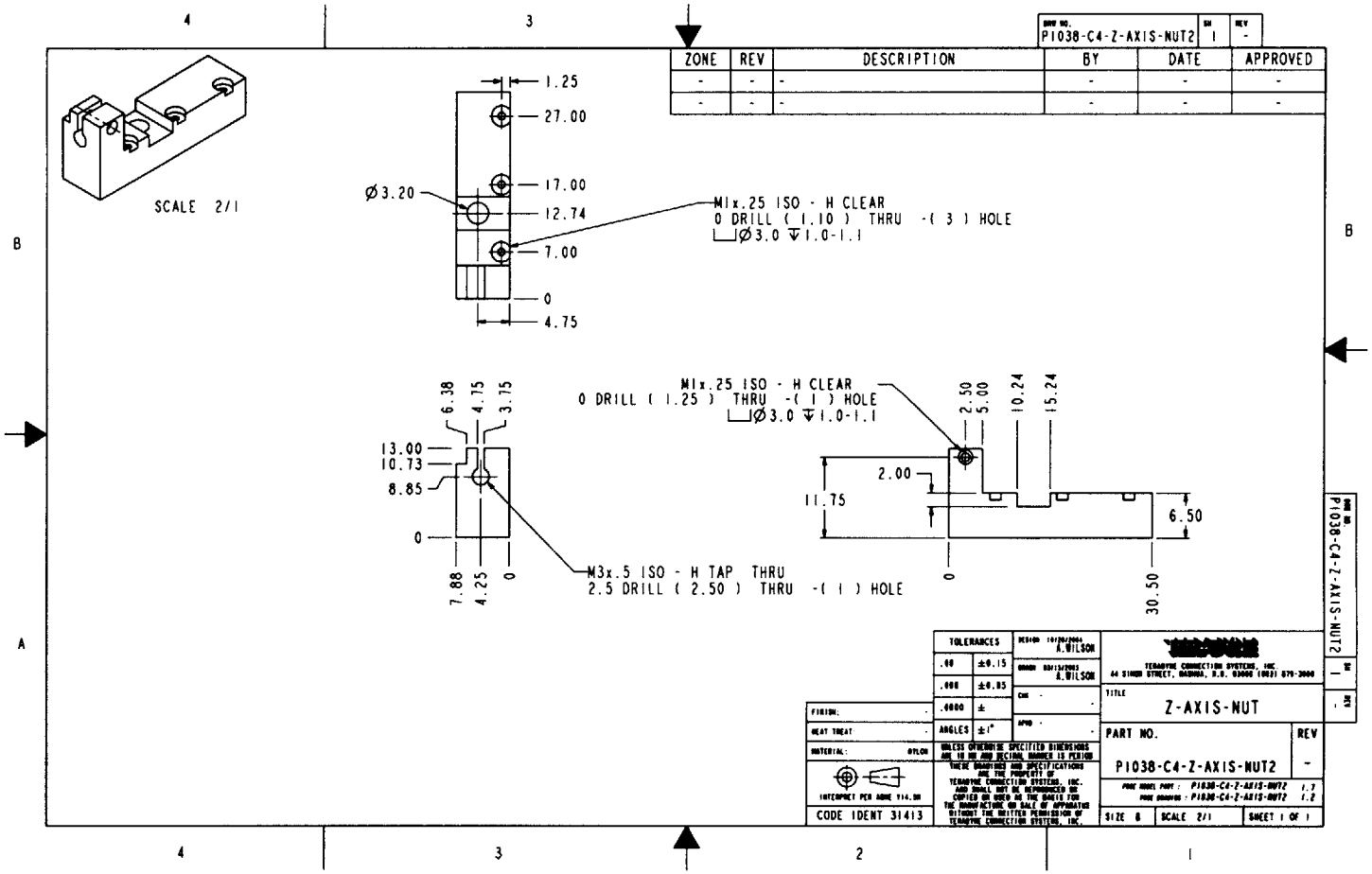
DWG NO. P1038-C4-Z-AXIS-NUT2
SH 1
REV -
ZONE | REV | DESCRIPTION | BY | DATE | APPROVED
SCALE 2/1
1.25
27.00
17.00
12.74
7.00
0
4.75
Ø3.20
M1x.25 ISO - H CLEAR
0 DRILL (1.10) THRU -(3) HOLE
⌴Ø3.0 ↧1.0-1.1
6.38
4.75
3.75
13.00
10.73
8.85
0
7.88
4.25
0
M3x.5 ISO - H TAP THRU
2.5 DRILL (2.50) THRU -(1) HOLE
M1x.25 ISO - H CLEAR
0 DRILL (1.25) THRU -(1) HOLE
⌴Ø3.0 ↧1.0-1.1
2.50
5.00
10.24
15.24
2.00
11.75
6.50
0
30.50
TOLERANCES
.00 ±0.15
.000 ±0.05
.0000 ±
ANGLES ±1°
FINISH:
HEAT TREAT:
MATERIAL: NYLON
INTERPRET PER ASME Y14.5M
CODE IDENT 31413
UNLESS OTHERWISE SPECIFIED DIMENSIONS ARE IN INCH AND DECIMAL ENGINEER IS PERSON
THESE DRAWINGS AND SPECIFICATIONS ARE THE PROPERTY OF TERADYNE CONNECTION SYSTEMS, INC. AND SHALL NOT BE REPRODUCED OR COPIED OR USED AS THE BASIS FOR THE MANUFACTURE OR SALE OF APPARATUS WITHOUT THE WRITTEN PERMISSION OF TERADYNE CONNECTION SYSTEMS, INC.
A.WILSON
TERADYNE CONNECTION SYSTEMS, INC
TITLE
Z-AXIS-NUT
PART NO.
P1038-C4-Z-AXIS-NUT2
REV -
SIZE B
SCALE 2/1
SHEET 1 OF 1
P1038-C4-Z-AXIS-NUT2

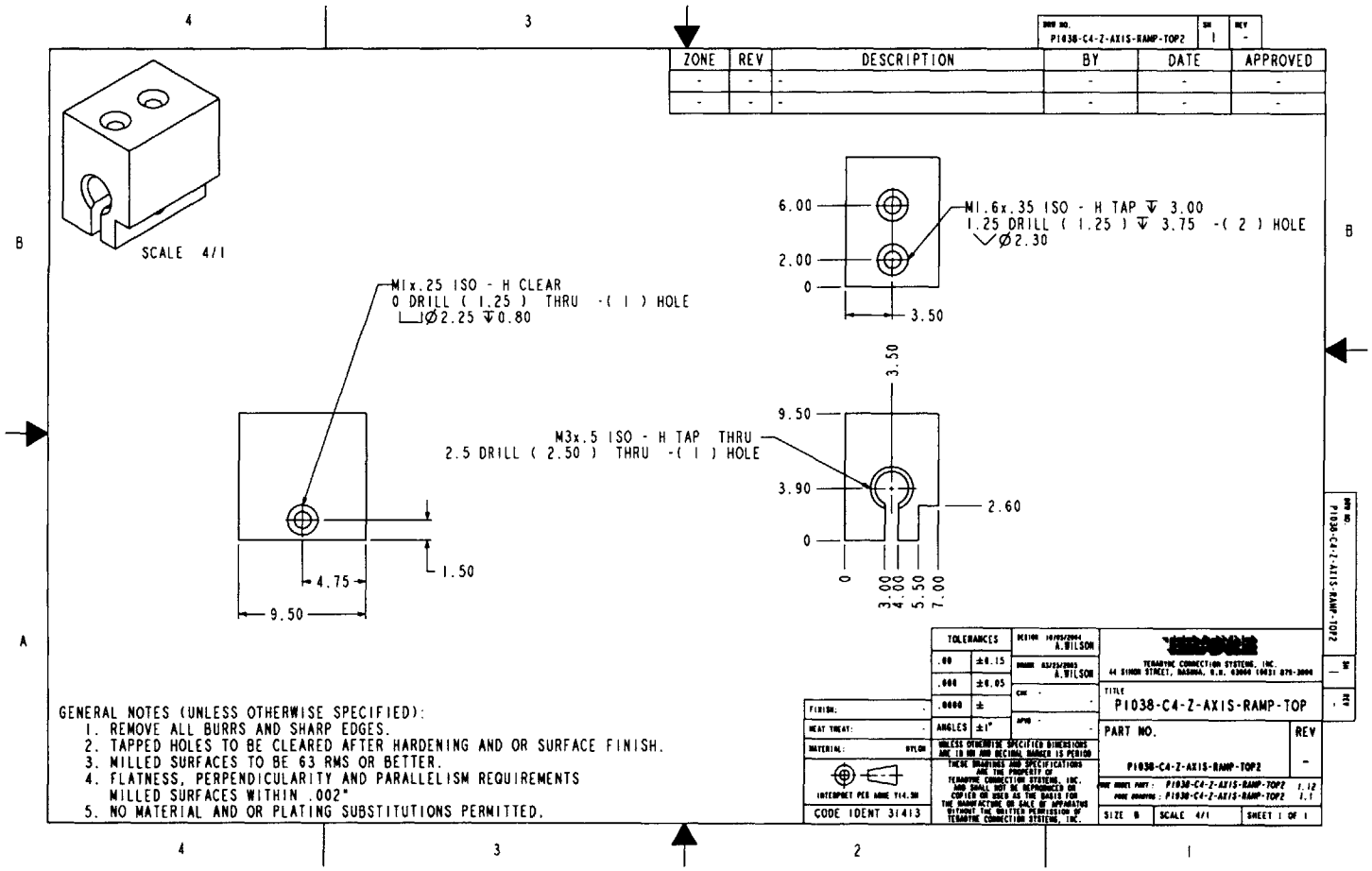
DWG NO. P1038-C4-Z-AXIS-RAMP-TOP2
SH 1
REV -
ZONE | REV | DESCRIPTION | BY | DATE | APPROVED
SCALE 4/1
M1.6x.35 ISO - H TAP ↧ 3.00
1.25 DRILL (1.25) ↧ 3.75 -(2) HOLE
⌵Ø2.30
6.00
2.00
0
3.50
M1x.25 ISO - H CLEAR
0 DRILL (1.25) THRU -(1) HOLE
⌴Ø2.25 ↧0.80
M3x.5 ISO - H TAP THRU
2.5 DRILL (2.50) THRU -(1) HOLE
9.50
3.90
0
2.60
3.00
4.00
5.50
7.00
4.75
1.50
9.50
GENERAL NOTES (UNLESS OTHERWISE SPECIFIED):
1. REMOVE ALL BURRS AND SHARP EDGES.
2. TAPPED HOLES TO BE CLEARED AFTER HARDENING AND OR SURFACE FINISH.
3. MILLED SURFACES TO BE 63 RMS OR BETTER.
4. FLATNESS, PERPENDICULARITY AND PARALLELISM REQUIREMENTS MILLED SURFACES WITHIN .002"
5. NO MATERIAL AND OR PLATING SUBSTITUTIONS PERMITTED.
TOLERANCES
.00 ±0.15
.000 ±0.05
.0000 ±
ANGLES ±1°
FINISH:
HEAT TREAT:
MATERIAL:
INTERPRET PER ANSI Y14.5M
CODE IDENT 31413
DESIGN 10/05/2004 A.WILSON
DRAWN 03/25/2005 A.WILSON
CHK -
APVD -
UNLESS OTHERWISE SPECIFIED DIMENSIONS ARE IN MM AND DECIMAL MARKER IS PERIOD
THESE DRAWINGS AND SPECIFICATIONS ARE THE PROPERTY OF TERADYNE CONNECTION SYSTEMS, INC. AND SHALL NOT BE REPRODUCED OR COPIED OR USED AS THE BASIS FOR THE MANUFACTURE OR SALE OF APPARATUS WITHOUT THE WRITTEN PERMISSION OF TERADYNE CONNECTION SYSTEMS, INC.
[redacted]
TERADYNE CONNECTION SYSTEMS, INC.
44 SIMON STREET, NASHUA, N.H. 03060 (603) 879-2000
TITLE
P1038-C4-Z-AXIS-RAMP-TOP
PART NO.
P1038-C4-Z-AXIS-RAMP-TOP2
REV -
SIZE B
SCALE 4/1
SHEET 1 OF 1
P1038-C4-Z-AXIS-RAMP-TOP2

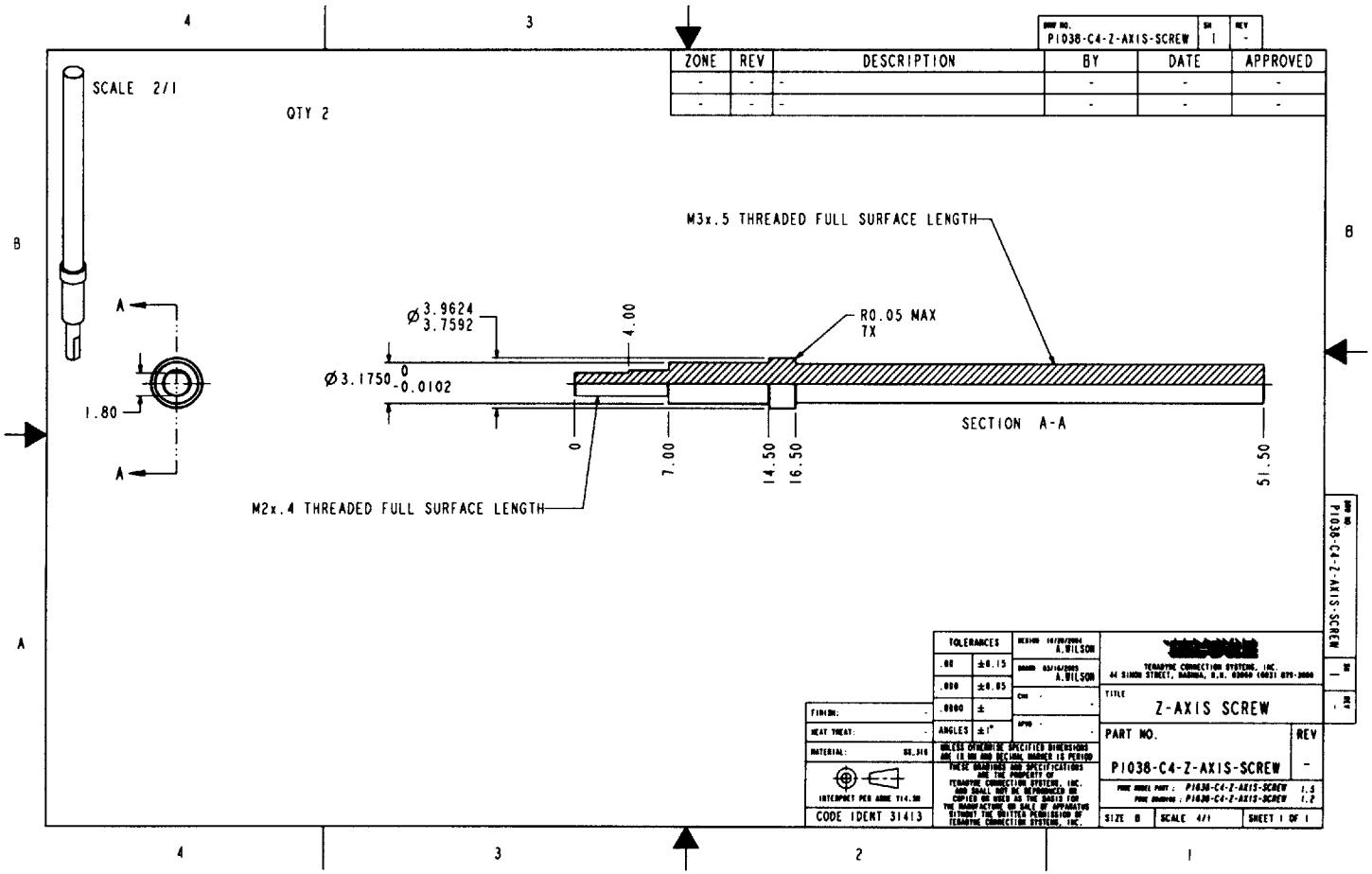
DWG NO. P1038-C4-Z-AXIS-SCREW
SH 1
REV -
ZONE | REV | DESCRIPTION | BY | DATE | APPROVED
SCALE 2/1
QTY 2
M3x.5 THREADED FULL SURFACE LENGTH
Ø3.9624
3.7592
4.00
R0.05 MAX
7X
Ø3.1750 0 -0.0102
SECTION A-A
1.80
0
7.00
14.50
16.50
51.50
M2x.4 THREADED FULL SURFACE LENGTH
TOLERANCES
.00 ±0.15
.000 ±0.05
.0000 ±
ANGLES ±1°
FINISH:
HEAT TREAT:
MATERIAL:
INTERPRET PER ASME Y14.5M
CODE IDENT 31413
UNLESS OTHERWISE SPECIFIED DIMENSIONS ARE IN INCHES AND DECIMAL MARKED IS PERIOD
THESE DRAWINGS AND SPECIFICATIONS ARE THE PROPERTY OF TERADYNE CONNECTION SYSTEMS, INC. AND SHALL NOT BE REPRODUCED OR COPIED OR USED AS THE BASIS FOR THE MANUFACTURE OR SALE OF APPARATUS WITHOUT THE WRITTEN PERMISSION OF TERADYNE CONNECTION SYSTEMS, INC.
A.WILSON
A.WILSON
TERADYNE CONNECTION SYSTEMS, INC.
44 SIMON STREET, NASHUA, N.H. 03060-1003 (603) 879-3000
TITLE
Z-AXIS SCREW
PART NO.
P1038-C4-Z-AXIS-SCREW
REV -
SIZE B
SCALE 4/1
SHEET 1 OF 1
P1038-C4-Z-AXIS-SCREW

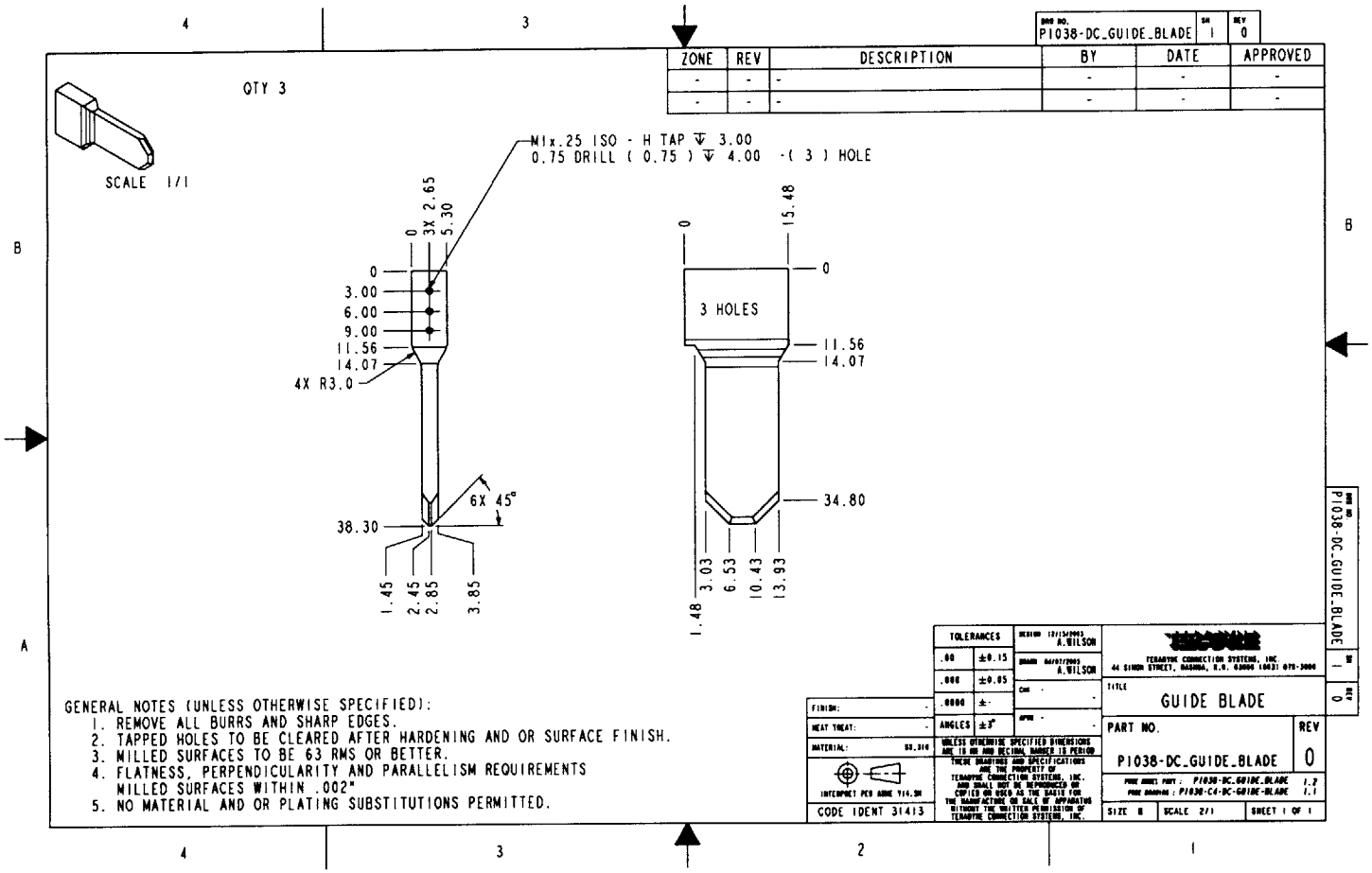
PART NO. P1038-DC_GUIDE_BLADE SH 1 REV 0
ZONE REV DESCRIPTION BY DATE APPROVED
QTY 3
SCALE 1/1
M1x.25 ISO - H TAP ⌀ 3.00
0.75 DRILL (0.75) ⌀ 4.00 -(3) HOLE
3X 2.65
5.30
0
3.00
6.00
9.00
11.56
14.07
4X R3.0
6X 45°
38.30
1.45
2.45
2.85
3.85
15.48
3 HOLES
34.80
1.48
3.03
6.53
10.43
13.93
GENERAL NOTES (UNLESS OTHERWISE SPECIFIED):
1. REMOVE ALL BURRS AND SHARP EDGES.
2. TAPPED HOLES TO BE CLEARED AFTER HARDENING AND OR SURFACE FINISH.
3. MILLED SURFACES TO BE 63 RMS OR BETTER.
4. FLATNESS, PERPENDICULARITY AND PARALLELISM REQUIREMENTS MILLED SURFACES WITHIN .002"
5. NO MATERIAL AND OR PLATING SUBSTITUTIONS PERMITTED.
TOLERANCES
.00 ±0.15
.000 ±0.05
.0000 ±.
ANGLES ±1°
FINISH:
HEAT TREAT:
MATERIAL:
INTERPRET PER ASME Y14.5M
CODE IDENT 31413
A.WILSON
TERADYNE CONNECTION SYSTEMS, INC.
TITLE
GUIDE BLADE
PART NO.
P1038-DC_GUIDE_BLADE
REV 0
SIZE B
SCALE 2/1
SHEET 1 OF 1
P1038-DC_GUIDE_BLADE

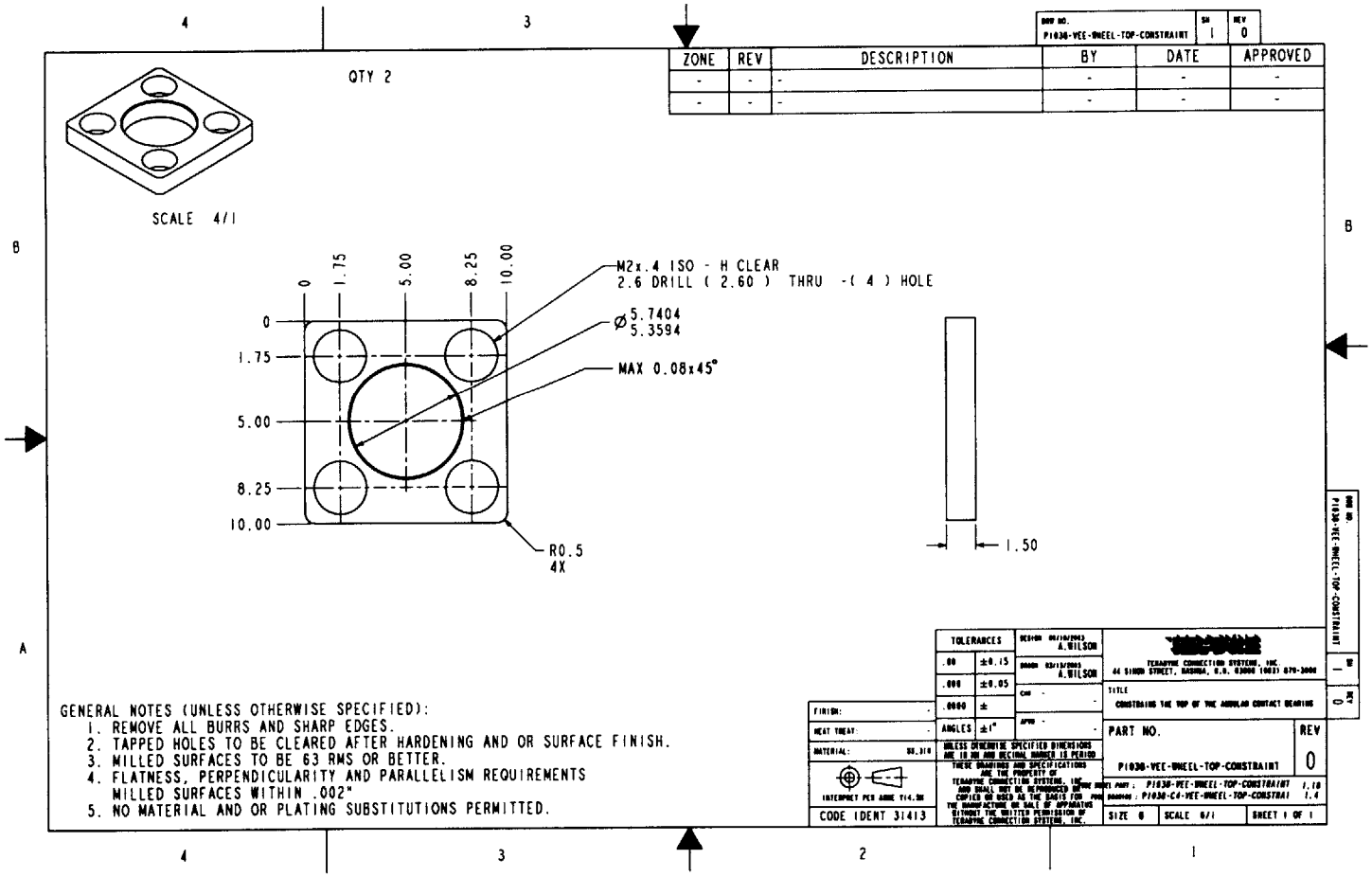
DWG NO. P1030-VEE-WHEEL-TOP-CONSTRAINT
SH 1
REV 0
ZONE | REV | DESCRIPTION | BY | DATE | APPROVED
QTY 2
SCALE 4/1
0
1.75
5.00
8.25
10.00
M2x.4 ISO - H CLEAR
2.6 DRILL (2.60) THRU -(4) HOLE
Ø5.7404
5.3594
MAX 0.08x45°
R0.5
4X
1.50
GENERAL NOTES (UNLESS OTHERWISE SPECIFIED):
1. REMOVE ALL BURRS AND SHARP EDGES.
2. TAPPED HOLES TO BE CLEARED AFTER HARDENING AND OR SURFACE FINISH.
3. MILLED SURFACES TO BE 63 RMS OR BETTER.
4. FLATNESS, PERPENDICULARITY AND PARALLELISM REQUIREMENTS MILLED SURFACES WITHIN .002"
5. NO MATERIAL AND OR PLATING SUBSTITUTIONS PERMITTED.
TOLERANCES
.00 ±0.15
.000 ±0.05
.0000 ±
ANGLES ±1°
UNLESS OTHERWISE SPECIFIED DIMENSIONS ARE IN INCH AND DECIMAL ENDINGS IS PERIOD
FINISH:
HEAT TREAT:
MATERIAL:
INTERPRET PER ANSI Y14.5M
CODE IDENT 31413
DESIGN 05/10/2002 A.WILSON
DRAWN 05/13/2002 A.WILSON
CHK -
APVD -
TERADYNE CONNECTION SYSTEMS, INC.
TITLE
CONSTRAINS THE TOP OF THE ANNULAR CONTACT BEARING
PART NO.
P1030-VEE-WHEEL-TOP-CONSTRAINT
REV 0
SIZE B
SCALE 4/1
SHEET 1 OF 1
P1030-VEE-WHEEL-TOP-CONSTRAINT

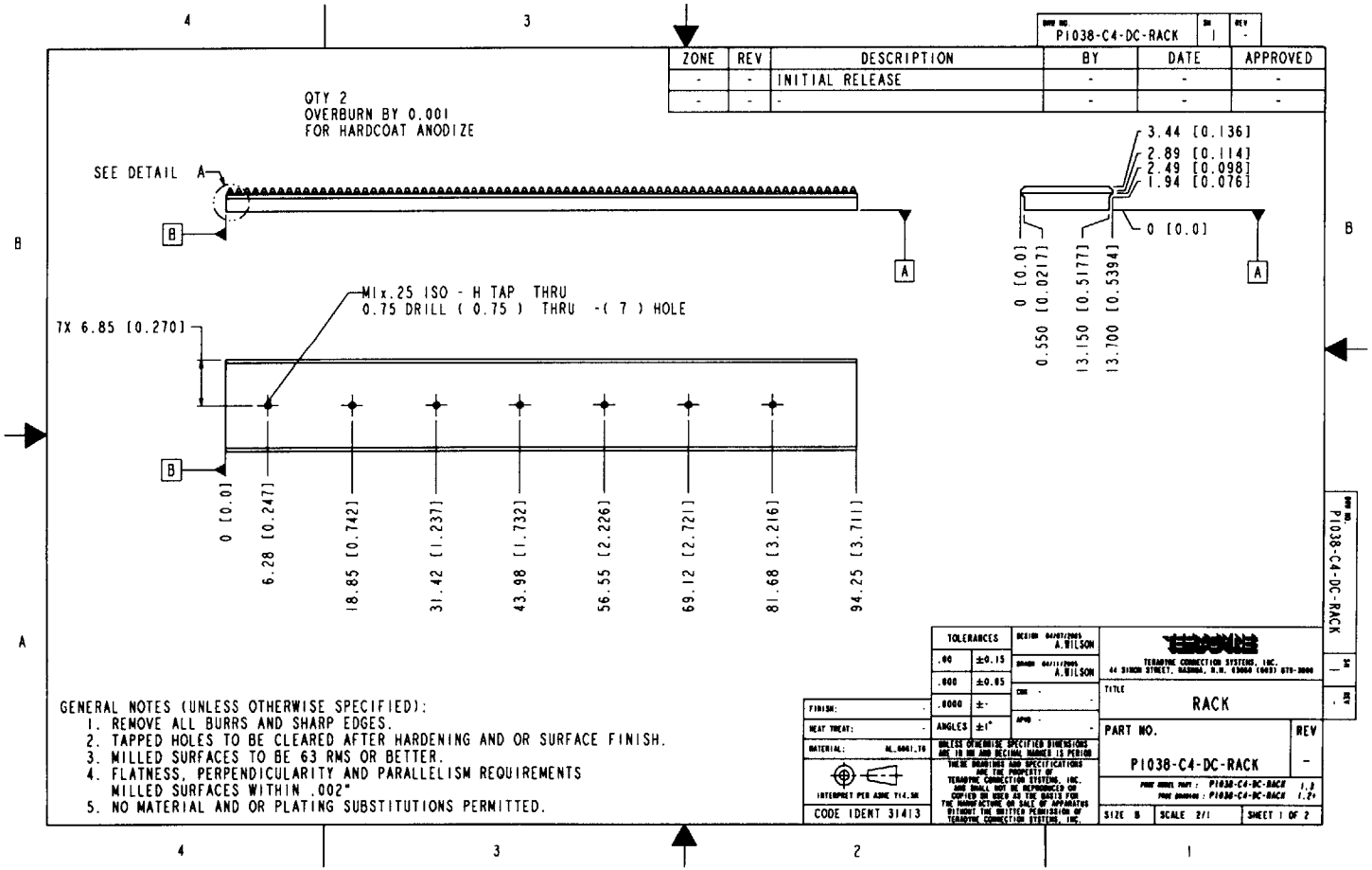
DWG NO P1038-C4-DC-RACK
SH 1
REV -
ZONE | REV | DESCRIPTION | BY | DATE | APPROVED
- | - | INITIAL RELEASE | - | - | -
- | - | - | - | - | -
QTY 2
OVERBURN BY 0.001
FOR HARDCOAT ANODIZE
SEE DETAIL A
B
A
3.44 [0.136]
2.89 [0.114]
2.49 [0.098]
1.94 [0.076]
0 [0.0]
0 [0.0]
0 [0.0217]
0.550 [0.5177]
13.150 [0.5394]
13.700
7X 6.85 [0.270]
M1x.25 ISO - H TAP THRU
0.75 DRILL (0.75) THRU -(7) HOLE
0 [0.0]
6.28 [0.247]
18.85 [0.742]
31.42 [1.237]
43.98 [1.732]
56.55 [2.226]
69.12 [2.721]
81.68 [3.216]
94.25 [3.711]
GENERAL NOTES (UNLESS OTHERWISE SPECIFIED):
1. REMOVE ALL BURRS AND SHARP EDGES.
2. TAPPED HOLES TO BE CLEARED AFTER HARDENING AND OR SURFACE FINISH.
3. MILLED SURFACES TO BE 63 RMS OR BETTER.
4. FLATNESS, PERPENDICULARITY AND PARALLELISM REQUIREMENTS MILLED SURFACES WITHIN .002"
5. NO MATERIAL AND OR PLATING SUBSTITUTIONS PERMITTED.
TOLERANCES
.00 ±0.15
.000 ±0.05
.0000 ±-
ANGLES ±1°
FINISH:
HEAT TREAT:
MATERIAL:
INTERPRET PER ASME Y14.5M
CODE IDENT 31413
DESIGN 04/07/2005 A.WILSON
DRAWN 04/11/2005 A.WILSON
CHK -
APVD -
UNLESS OTHERWISE SPECIFIED DIMENSIONS ARE IN INCH AND DECIMAL MARKER IS PERIOD
THESE DRAWINGS AND SPECIFICATIONS ARE THE PROPERTY OF TERADYNE CONNECTION SYSTEMS, INC. AND SHALL NOT BE REPRODUCED OR COPIED OR USED AS THE BASIS FOR THE MANUFACTURE OR SALE OF APPARATUS WITHOUT THE WRITTEN PERMISSION OF TERADYNE CONNECTION SYSTEMS, INC.
TERADYNE CONNECTION SYSTEMS, INC.
44 SIMON STREET, NASHUA, N.H. 03060 (603) 879-3000
TITLE
RACK
PART NO.
P1038-C4-DC-RACK
REV -
SIZE B
SCALE 2/1
SHEET 1 OF 2
P1038-C4-DC-RACK
1
-

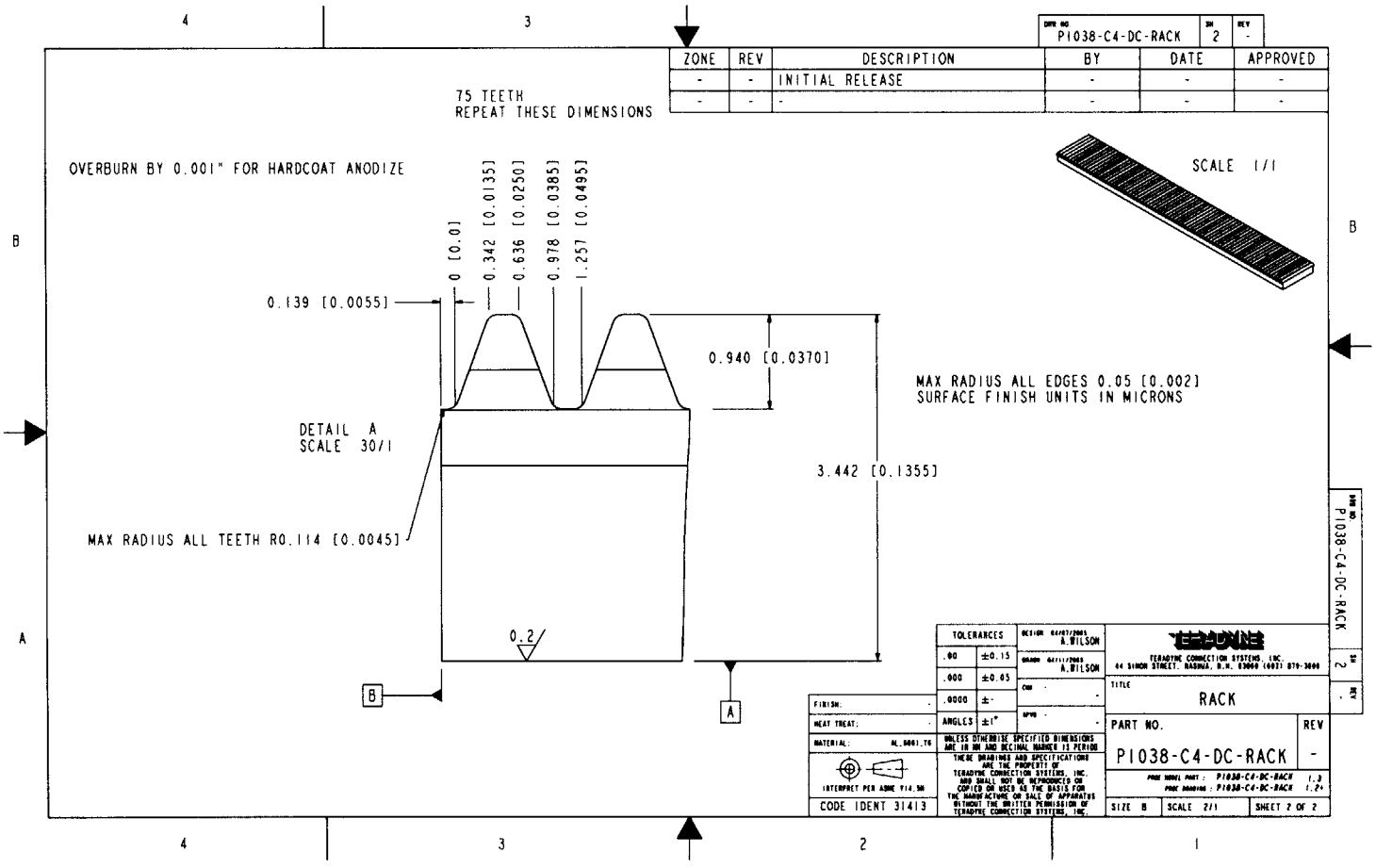
P1038-C4-DC-RACK
2
-
ZONE | REV | DESCRIPTION | BY | DATE | APPROVED
- | - | INITIAL RELEASE | - | - | -
- | - | - | - | - | -
75 TEETH
REPEAT THESE DIMENSIONS
OVERBURN BY 0.001" FOR HARDCOAT ANODIZE
SCALE 1/1
0 [0.0]
0.342 [0.0135]
0.636 [0.0250]
0.978 [0.0385]
1.257 [0.0495]
0.139 [0.0055]
0.940 [0.0370]
3.442 [0.1355]
MAX RADIUS ALL EDGES 0.05 [0.002]
SURFACE FINISH UNITS IN MICRONS
DETAIL A
SCALE 30/1
MAX RADIUS ALL TEETH R0.114 [0.0045]
0.2
B
A
TOLERANCES
.00 ±0.15
.000 ±0.05
.0000 ±-
ANGLES ±1°
FINISH: -
HEAT TREAT: -
MATERIAL: AL,6061,T6
INTERPRET PER ASME Y14.5M
CODE IDENT 31413
UNLESS OTHERWISE SPECIFIED DIMENSIONS ARE IN INCH AND DECIMAL MARKER IS PERIOD
THESE DRAWINGS AND SPECIFICATIONS ARE THE PROPERTY OF TERADYNE CONNECTION SYSTEMS, INC. AND SHALL NOT BE REPRODUCED OR COPIED OR USED AS THE BASIS FOR THE MANUFACTURE OR SALE OF APPARATUS WITHOUT THE WRITTEN PERMISSION OF TERADYNE CONNECTION SYSTEMS, INC.
DESIGN 04/07/2005 A.WILSON
DRAWN 04/11/2005 A.WILSON
CHK -
APVD -
TERADYNE
TERADYNE CONNECTION SYSTEMS, INC.
44 SIMON STREET, NASHUA, N.H. 03060 (603) 879-3000
TITLE
RACK
PART NO.
P1038-C4-DC-RACK
REV
-
PROE MODEL PART : P1038-C4-DC-RACK 1.3
PROE DRAWING : P1038-C4-DC-RACK 1.24
SIZE B
SCALE 2/1
SHEET 2 OF 2
P1038-C4-DC-RACK
SH 2
REV -

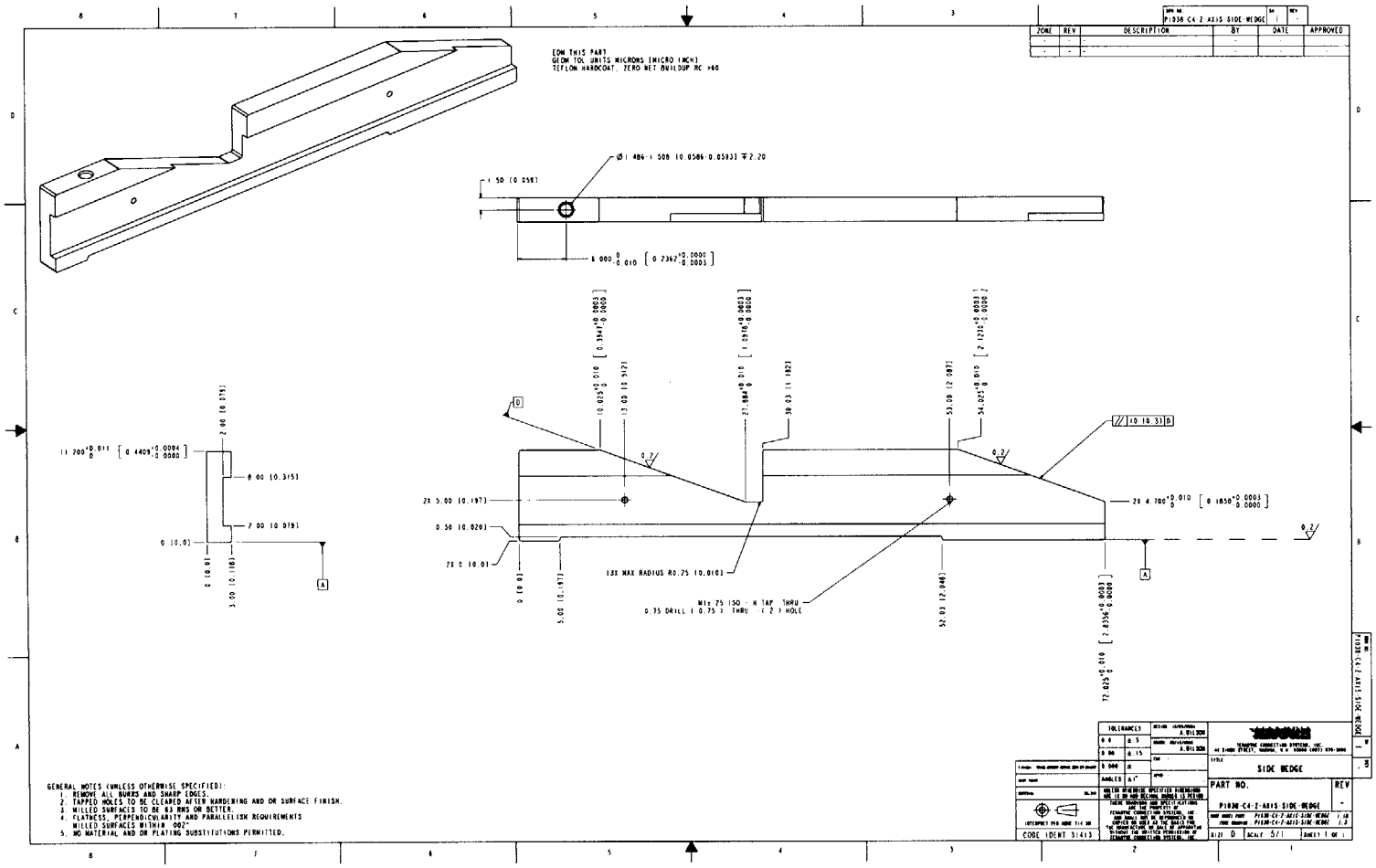
EDM THIS PART
GEOM TOL UNITS MICRONS [MICRO INCH]
TEFLON HARDCOAT. ZERO NET BUILDUP RC >60
P1036 C4-Z AXIS SIDE-WEDGE
ZONE REV DESCRIPTION BY DATE APPROVED
GENERAL NOTES (UNLESS OTHERWISE SPECIFIED):
1. REMOVE ALL BURRS AND SHARP EDGES.
2. TAPPED HOLES TO BE CLEARED AFTER HARDENING AND OR SURFACE FINISH.
3. MILLED SURFACES TO BE 63 RMS OR BETTER.
4. FLATNESS, PERPENDICULARITY AND PARALLELISM REQUIREMENTS
MILLED SURFACES WITHIN .002"
5. NO MATERIAL AND OR PLATING SUBSTITUTIONS PERMITTED.
SIDE WEDGE
PART NO.
P1036-C4-Z-AXIS-SIDE-WEDGE
REV
SIZE D SCALE 5/1 SHEET 1 OF 1
CODE IDENT 31413

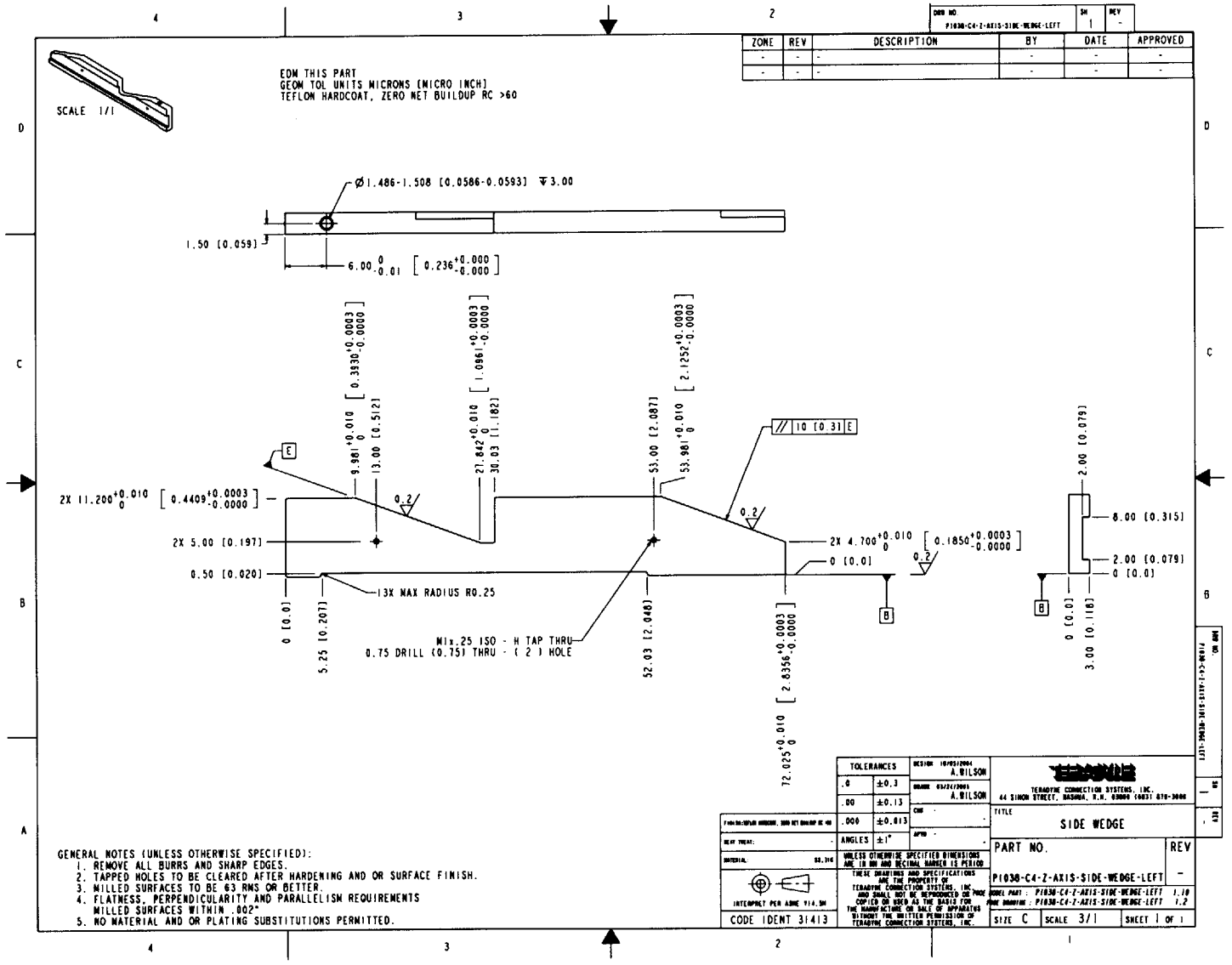

ZONE	REV	DESCRIPTION	BY	DATE	APPROVED
-	-	-	-	-	-
-	-	-	-	-	-

DWG NO P1038-C4-Z-AXIS-SIDE-WEDGE-LEFT | SH 1 | REV -

GENERAL NOTES (UNLESS OTHERWISE SPECIFIED):
1. REMOVE ALL BURRS AND SHARP EDGES.
2. TAPPED HOLES TO BE CLEARED AFTER HARDENING AND OR SURFACE FINISH.
3. MILLED SURFACES TO BE 63 RMS OR BETTER.
4. FLATNESS, PERPENDICULARITY AND PARALLELISM REQUIREMENTS
   MILLED SURFACES WITHIN .002"
5. NO MATERIAL AND OR PLATING SUBSTITUTIONS PERMITTED.

TOLERANCES	
.0	±0.3
.00	±0.13
.000	±0.013
ANGLES	±1°

WHEN OTHERWISE SPECIFIED DIMENSIONS ARE IN MM AND DECIMAL MARKER IS PERIOD

INTERPRET PER ASME Y14.5M

CODE IDENT 31413

DESIGN 10/03/2004 A.WILSON
DRAWN 03/24/2005 A.WILSON
CHK -
APPD -

TERADYNE CONNECTION SYSTEMS, INC.
44 SIMON STREET, NASHUA, N.H. 03060 (603) 879-3000

TITLE: SIDE WEDGE

PART NO. P1038-C4-Z-AXIS-SIDE-WEDGE-LEFT | REV -

MODEL PART : P1038-C4-Z-AXIS-SIDE-WEDGE-LEFT 1.10
DWG DRAWING : P1038-C4-Z-AXIS-SIDE-WEDGE-LEFT 1.2

SIZE C | SCALE 3/1 | SHEET 1 OF 1